technische universität
dortmund

From Spectroscopy to Coherent Control:

Photon Echoes of Excitons in Organic-Inorganic Perovskites and (In, Ga)As Quantum Dots

Stefan Grisard
2023

A document submitted in partial fulfillment of the requirements for the degree of
Doctor rerum naturalium
at
Fakultät Physik, Technische Universität Dortmund

Supervised by
Ilya A. Akimov and Artur V. Trifonov

Accepted by the Faculty of Physics of the TU Dortmund University, Germany.

Day of the oral examination: January 16th, 2024.

Examination board:
Ilya A. Akimov
Doris E. Reiter
Jacek Kasprzak
Frithjof B. Anders
Chris M. Delitzsch

Abstract

Photon echoes emerge from the delayed optical response of inhomogeneous ensembles of emitters upon resonant laser excitation. In semiconductors, they allow to uncover internal scattering and interaction dynamics on the picosecond timescale, while also holding promise as the realization of quantum optical memories in future quantum networks. Based on these two fields of application, this work uses photon echoes to investigate two material systems: Organic-inorganic perovskites and (In,Ga)As quantum dots. Organic-inorganic perovskites have attracted significant attention for their exceptional performance in photovoltaics and light-emitting applications. However, a comprehensive understanding of coherent light-matter interactions in this material class and in particular the role of excitons close to the band gap remained elusive. This work reveals that excitons dominate the nonlinear optical response of $MAPbI_3$ and $FAPbI_3$ single crystals and are subject to strong inhomogeneous broadening even at cryogenic temperatures. Compositional substitution is found to induce spatial band gap fluctuations on the nanometer scale that localize excitons accompanied by an extension of their coherence time by two orders of magnitude. Furthermore, exciton interactions are studied through polarization-dependent photon echoes, uncovering the formation of a biexciton state and the contribution of spin-dependent many-body interactions to nonlinear optical spectra. Subsequently, the focus shifts to confined excitons in (In,Ga)As semiconductor quantum dot ensembles, that represent an ideal platform to explore new approaches on how to coherently transfer, manipulate, and retrieve optical information to a solid state on picosecond timescales. First, it is demonstrated that collective Rabi rotations of the photon echoes from a quantum dot ensemble can be observed when a spatially uniform excitation profile is used. In this way, internal mechanisms of decoherence under strong laser excitation are identified. Thereafter, the photon echo sequence is expanded by two control pulses, providing all-optical control over the emission time, spectral response, and polarization state of photon echoes from quantum dots. Here, the interplay of temporally sorted multi-wave-mixing signals is exploited.

Kurzfassung

Photonen-Echos entstehen aus der verzögerten optischen Antwort von inhomogenen Ensembles von Emittern bei resonanter Laseranregung. In Halbleitern ermöglichen sie es, interne Streu- und Wechselwirkungsdynamiken auf der Pikosekundenskala aufzudecken und könnten einen wichtigen Beitrag zu der Realisierung von quantenoptischen Speichern in zukünftigen Quantennetzwerken leisten. Basierend auf diesen beiden Anwendungsbereichen nutzt diese Arbeit Photonen-Echos, um zwei Materialsysteme zu untersuchen: Organisch-anorganische Perovskite und (In,Ga)As-Quantenpunkte. Organisch-anorganische Perovskite haben aufgrund ihrer außergewöhnlichen Leistung in der Photovoltaik und bei lichtemittierenden Anwendungen große Aufmerksamkeit erregt. Ein umfassendes Verständnis der kohärenten Licht-Materie-Wechselwirkungen in dieser Materialklasse und insbesondere die Rolle von Exzitonen nahe der Bandlücke blieben jedoch bisher unklar. Diese Arbeit zeigt, dass Exzitonen die nichtlineare optische Antwort von $MAPbI_3$ und $FAPbI_3$ Einkristallen dominieren und selbst bei kryogenen Temperaturen einer starken inhomogenen Verbreiterung unterliegen. Es wird gezeigt, dass kompositionelle Substitutionen räumliche Bandlückenfluktuationen im Nanometerbereich verursachen, die Exzitonen lokalisieren und ihre Kohärenzzeit um zwei Größenordnungen verlängern. Darüber hinaus werden Exzitonenwechselwirkungen durch polarisationsabhängige Photonen-Echos untersucht, wobei die Bildung eines Biexzitonzustands und der Beitrag von spinabhängigen Vielteilchenwechselwirkungen zu nichtlinearen optischen Spektren beobachtet werden. Anschließend verlagert sich der Fokus auf lokalisierte Exzitonen in (In,Ga)As-Halbleiter-Quantenpunktensembles, die eine ideale Plattform darstellen, um neue Ansätze zur kohärenten Übertragung, Manipulation und Rückgewinnung von optischen Informationen im Festkörper auf Pikosekunden-Zeitskalen zu erforschen. Es wird demonstriert, dass kollektive Rabi-Rotationen der Photonen-Echos aus dem Quantenpunktensemble beobachtet werden können, wenn ein räumlich homogenes Anregungsprofil verwendet wird. Auf diese Weise werden interne Dekohärenzmechanismen unter starker Laseranregung identifiziert. Anschließend wird die Photonen-Echo-Sequenz um zwei Kontrollpulse erweitert, was eine optische Kontrolle der Emissionszeit, der spektralen Antwort und des Polarisationszustands der Photonen-Echos von Quantenpunkten ermöglicht. Hierbei wird das Zusammenspiel von zeitlich sortierten Multi-Wellen-Mischsignalen ausgenutzt.

Contents

Introduction

Direct band gap semiconductors are the fundamental components of modern light-emitting devices, sensors, and solar cells [1, 2]. The ongoing pursuit of more efficient and low-cost semiconductors with improved light emission and absorption properties is the driving force behind fundamental research, including the field of laser spectroscopy [3]. The most fascinating properties of light-matter interaction are revealed close to the band gap, where Coulomb interactions between photo-excited carriers lead to the formation of excitons – bound electron-hole pairs [2–5]. Of particular interest are the dynamics on a picosecond time scale during which the light emitted by the recombination of excitons remains coherent with the resonant excitation light source [3]. These dynamics can be temporally resolved using transient four-wave-mixing spectroscopy, where the optical resonance is resonantly excited by two short laser pulses with an adjustable delay. Here, the temporal resolution is solely limited by the duration of the pulses and therefore nowadays lies in the femtosecond regime [6]. In most semiconductor systems, the coherent dynamics of excitons is hidden by the inhomogeneous broadening of their optical transition energy. This obstacle can be circumvented using photon echoes, being the delayed four-wave-mixing response of an inhomogeneous ensemble of emitters [7]. The theoretical foundations and experimental methods of photon echo spectroscopy, critical for understanding the phenomena discussed in this thesis, are covered in Chapters 1 and 2. There are two motivations for the interest in photon echoes of excitons. First, temporally resolving the coherent dynamics offers the possibility to gain insight into fundamental scattering processes and quantum mechanical interactions in unexplored semiconductors [3]. Second, semiconductor nanostructures where excitons are weakly bound to their environment, and thus exhibit long coherence times, are appealing for completely new functionalities in the field of quantum optics [8, 9]. Here, systems with large inhomogeneous broadening are especially interesting for high-capacity storage and coherent control of large bandwidth non-classical light states [10, 11]. Motivated by these two fields of application, this work uses photon echoes to investigate two material systems: Organic-inorganic perovskites and (In, Ga)As quantum dots. In the following, a historical overview of the development of the experimental techniques used in this thesis is given.

The evolution of coherent spectroscopic techniques has been closely tied to advances in laser technology starting in the mid-20th century. Rapidly following the realization of laser pulses with nanosecond durations, photon echoes of a ruby crystal were observed for the first time in 1964 [12]. The progress of lasers generating picosecond or even femtosecond pulses [6, 13] opened up the possibility of investigating coherent dynamics in semiconductors starting in the 1980s. Initial studies observed the decoherence of excitons in bulk crystals of gallium arsenide (GaAs) on a picosecond timescale [14] and on a femtosecond time scale for free electron-hole pairs [15]. Many of the early experiments were applied to semiconductor heterostructures such as group III-V quantum wells that confine excitons in two dimensions [16, 17]. By performing measurements as a function of temperature [18] or using additional optical illumination [19], the contribution of phonons or carrier scattering to the decoherence of excitons was analyzed. The ability to temporally resolve the non-linear optical response using streak cameras [20] or the superposition with a reference pulse [21] was of major importance to identify photon echo formation and thus the impact of inhomogeneous broadening. In this way, the effect of structural disorder in

mixed bulk semiconductors [20] or quantum wells with spatially varying thickness [21] and its interconnection to extended coherence times of localized excitons were identified. Furthermore, the time-resolved photon echo technique enables to observe quantum beats resulting from the superposition of optical resonances whose energetic splitting is small compared to the inhomogeneous broadening of the system. For example, quantum beats resulting from the superposition of light-hole and heavy-hole excitons were observed [22]. An intriguing topic in coherent spectroscopy results from the effect of many-body Coulomb effects in semiconductors which lead to significant modifications in the temporal dynamics or the dependence on the polarization of the exciting laser pulses that were expected for ensembles of non-interacting excitons [23, 24]. In this context, also the contribution of the biexciton, a bound state of two excitons, was observed in quantum wells based on its characteristic polarization dependence and quantum beats revealing the biexciton binding energy [25]. Starting in the late 1990s, the first coherent experiments on fully localized excitons in epitaxially grown indium gallium arsenide quantum dots were performed [26]. Measurements at cryogenic temperatures revealed that excitons in quantum dots can exhibit coherence times in the range of 1 ns that are only limited by radiative recombination [27, 28]. The increased sensitivity of heterodyne techniques in combination with microscopy methods offered the possibility to study spectra of single quantum dots [29]. At that time, phase-stabilized coherent techniques were developed that include information about the absolute values of absorption and emission frequencies and their correlations, which forms the basis of two-dimensional Fourier transform spectroscopy [30]. Nowadays, photon echo spectroscopy and related techniques represent a well-established toolbox contributing to the understanding of exciton dynamics and interactions in a variety of modern semiconductors such as monolayer transition metal dichalcogenides [31], exciton-polaritons [32] or perovskites [33]. The latter are subject to Part I of the experimental investigation presented in this thesis.

Hybrid organic-inorganic perovskites gained substantial attraction considering their remarkable performance in photovoltaics and light-emitting applications [34–37]. Two prominent examples are methylammonium- and formamidinium lead tri-iodide ($MAPbI_3$ and $FAPbI_3$). The efficiency of these compounds in prototype solar cells rapidly increased from 4 % in 2009 [38] to 26 % in 2021 [39]. Furthermore, the quantum yields of light-emitting diodes nowadays exceed 20% [40]. Hybrid perovskites thus approach the performance of conventional inorganic materials such as gallium arsenide or silicon while providing substantial benefits in terms of tunability, reduced processing complexity, and lower production cost [37].

These technological advancements have sparked significant interest in exploring the fundamental aspects of light-matter interactions within hybrid organic-inorganic perovskites. In particular, photo-excitations close to the band gap and their dynamics are key to light absorption and charge transport [41]. At cryogenic temperatures, the optical spectra in this energy range are dominated by excitons [42]. Observing the decoherence of excitons using photon echo spectroscopy is a sensitive probe to structural inhomogeneities on the nanometer scale and thus directly related to technological applications. However, the available studies of coherent exciton phenomena are mainly concentrated on low-dimensional systems such as nanocrystals or thin films [43–46]. Exciton properties in bulk hybrid perovskites that underlie those in low-dimensional systems are in turn poorly understood, which is attributed to short coherence times as well as crystal instabilities. In Chapter 3 of this thesis, the photon echo spectroscopy is therefore applied to single crystals of the perovskites $MAPbI_3$ and $FA_{0.9}Cs_{0.1}PbI_{2.8}Br_{0.2}$. Here, the influence of inhomogeneous broadening on the emission properties of excitons is investigated. It is found that an inherent property of both perovskites is the inhomogeneous broadening of the exciton resonance, occurring on a scale of 10 meV. However, the compositional substitution in the mixed $FAPbI_3$ crystal is found to induce band gap fluctuations that lead to the localization of

excitons. Remarkably, the localized excitons exhibit coherence times of roughly 80 ps, which is by two orders of magnitudes larger than found in $MAPbI_3$. This finding not only provides valuable information about the effect of compositional substitutions on the energy structure of perovskites but also suggests new potential applications of perovskite crystals as bright quantum light sources.

Building upon these initial characterizations of the coherent exciton properties, Chapter 4 sets a focus on the interactions of excitons. Based on pronounced dependences of the photon echoes on the polarization of the applied lasers, conclusions are drawn on the interactions of coherently excited excitons. In $MAPbI_3$, a bound state of two excitons, the biexciton, is observed. A detailed modeling of the polarization dependences of the exciton-biexciton system is applied, which allows a comparison between experimental and theoretical predictions across various polarization configurations. The biexciton binding energy of 2.4 meV is extracted using quantum beats of the photon echo polarization state. This approach turns out to offer a higher resolution as compared to quantum beats of the photon echo amplitude and thus allows to resolve quantum beats when the binding energy is comparable to the homogeneous exciton linewidth. The long coherence times in $FA_{0.9}Cs_{0.1}PbI_{2.8}Br_{0.2}$ associated with the localization of excitons offer great potential to study weak interactions among excitons and their influence the nonlinear optical response of the system. Through a detailed analysis of polarization characteristics as well as polarization-dependent decoherence times, it is concluded that exciton interactions have a spin selectivity. These results are interpreted in terms of a spin-selective excitation-induced broadening of the resonance. By employing a model that takes into account correlated excitonic states, the experimental results are reproduced and an understanding of localized excitons in perovskites is developed.

Part II of the thesis is dedicated to the coherent control of photon echoes from an ensemble of self-assembled (In,Ga)As semiconductor quantum dots placed in a planar microcavity. Quantum dots confine excitons in a nanometer-sized volume, which leads to a full quantization of their energy spectrum just as in natural atoms. In contrast to atoms, the energy spectrum of quantum dots is tunable by adjusting their size, shape, or composition [47]. Quantum dots already find their application in classical devices such as lasers that benefit from the increased temperature stability of zero-dimensional systems [48, 49]. Moreover, due to their large oscillator strength, well-defined optical selection rules, and lifetime-limited coherence times, quantum dots are regarded as a versatile platform for future applications in quantum networks. Those applications include the creation of entangled photons [50, 51] or the efficient transfer between stationary and photonic qubits as needed for quantum communication [52]. Coherent spectroscopic techniques have been of major importance in understanding the microscopic sources of decoherence in quantum dots within the last 20 years [27, 53, 54]. On a single dot level, it has been widely demonstrated that quantum dots can be prepared in a targeted state on the sub-picosecond timescale using Rabi oscillations [9, 55–57]. Extending these coherent control experiments to ensembles of quantum dots remains challenging due to unavoidable inhomogeneities of the system. The particular interest in ensembles of quantum dots is motivated by the realization of optical quantum memories that store and retrieve non-classical light states on demand using the photon echo effect [11]. For example, quantum memories are needed to synchronize single photons that result from spontaneous emission processes [11, 58] and as the key element of quantum repeaters [59]. In this context, special interest arises from charged quantum dots whose lifetimes, which limit potential storage times, can be extended to several nanoseconds through the transfer between optical and spin coherence [60, 61]. Therefore, exploring further methods to control the optical coherence stored within an ensemble of charged quantum dots is an intriguing topic covered in Chapters 5 and 6.

One of the major problems of observing collective Rabi rotations of an ensemble of quantum dots results from the inhomogeneity of laser intensities within the excitation area [62]. In Chapter 5, refractive beam shaping optics are implemented to resolve this issue and excite a quantum dot ensemble with a uniform distribution of laser intensities. In this way, collective Rabi rotations of the ensemble are observed in intensity-dependent photon echoes. Further, Rabi rotations arising from charged and uncharged quantum dots are distinguished using specific polarization configurations of the exciting laser pulses. A detailed analysis of the remaining decoherence mechanisms is applied which reveals the efficient coupling to acoustic phonons as the main source in the regime of strong laser excitation. Chapter 6 explores further possibilities to optically manipulate the coherent response of the quantum dot ensemble. A sequence of two control pulses is added to the photon echo scheme that allows to temporally control the photon echo emission or manipulate its spectrum using Ramsey interference. By addressing the specific dipole selection rules of charged quantum dots, additional possibilities for the control of the photon echo's polarization state are demonstrated. Furthermore, the effect of the dephasing dynamic of the quantum dot ensemble during the action of picosecond laser pulses is analyzed using a multi-wave-mixing expansion.

List of publications

Parts of the content presented in this thesis have been published in the following articles:

A. V. Trifonov, S. Grisard, A. N. Kosarev, I. A. Akimov, D. R. Yakovlev, J. Höcker, V. Dyakonov, and M. Bayer, "Photon echo polarimetry of excitons and biexcitons in a $CH_3NH_3PbI_3$ perovskite single crystal", ACS Photonics **9**, 621 (2022)
DOI: 10.1021/acsphotonics.1c01603,

S. Grisard, H. Rose, A. V. Trifonov, R. Reichhardt, D. E. Reiter, M. Reichelt, C. Schneider, M. Kamp, S. Höfling, M. Bayer, T. Meier, and I. A. Akimov, "Multiple Rabi rotations of trions in InGaAs quantum dots observed by photon echo spectroscopy with spatially shaped laser pulses", Physical Review B **106**, 205408 (2022)
DOI: 10.1103/PhysRevB.106.205408,

S. Grisard, A. V. Trifonov, I. A. Solovev, D. R. Yakovlev, O. Hordiichuk, M. V. Kovalenko, M. Bayer, and I. A. Akimov, "Long-Lived Exciton Coherence in Mixed-Halide Perovskite Crystals", Nano Letters **23**, 7397 (2023)
DOI: 10.1021/acs.nanolett.3c01817,

S. Grisard, A. V. Trifonov, H. Rose, R. Reichhardt, M. Reichelt, C. Schneider, M. Kamp, S. Höfling, M. Bayer, T. Meier, and I. A. Akimov, "Temporal Sorting of Optical Multiwave-Mixing Processes in Semiconductor Quantum Dots", ACS Photonics **10**, 3161 (2023)
DOI: 10.1021/acsphotonics.3c00530,

S. Grisard, A. V. Trifonov, D. R. Yakovlev, O. Hordiichuk, M. V. Kovalenko, M. Bayer, and I. A. Akimov, "Spin-dependent excitation-induced dephasing of excitons in a $FA_{0.9}Cs_{0.1}PbI_{2.8}Br_{0.2}$ crystal", In preparation (2023)

1 Theoretical background

This chapter introduces the relevant theoretical background for coherent spectroscopy in semiconductors. Section 1.1 presents the basic electronic properties of group III–V and perovskite semiconductors involving excitons and semiconductor nanostructures. Thereafter, in Section 1.2, we establish the theoretical framework for photon echo spectroscopy. This framework forms the basis for modeling results that accompany the experimental observations presented in Parts I and II. Finally, Section 1.3 introduces Rabi rotations that are experimentally studied in Chapters 5 and 6.

1.1 Electronic structure of semiconductors

The optical properties of semiconductors are determined by their band structure that exhibits a characteristic energy gap in the order of 1 eV between the highest occupied band (valence band) and lowest unoccupied band (conduction band). The band structure defines the dispersion relation of electrons in a crystal upon interaction with a periodic lattice formed by the nuclei. In real space, the band structure corresponds to quasi-continuous allowed energy intervals separated by the band gap. The formation of bands can be understood by considering the hybridization of atoms when they are brought close to each other. Through the finite overlap of the valence electronic orbitals, bonding and antibonding molecular states are formed that are separated by an energetic gap as imposed by the Pauli principle. Arranging more atoms in a crystal lattice leads to a broadening of the bonding and antibonding molecular orbitals into bands. Generally, valence bands are called hole bands, where holes refer to empty electronic states that can be treated as quasiparticles with a positive charge. Introducing the concept of holes strongly simplifies the treatment of the modified carrier distribution in the valence band upon excitation of an electron from the valence band to the conduction band. We can understand the optical excitation of an electron from the valence band to the conduction band equivalently as the creation of an electron-hole pair. Of special interest for optical applications are direct semiconductors, where the valence band maximum and conduction band minimum appear at the same position in momentum-space. Here, electron-hole pair excitation/recombination can be efficiently mediated by the absorption/emission of a photon. Among those semiconductors are III–V semiconductors like gallium-arsenide (GaAs) and hybrid organic-inorganic perovskite semiconductors based on $MAPbI_3$ or $FAPbI_3$, which are subject to the investigations presented in this thesis. The most important properties of the band structure of these two types of semiconductors are reviewed in the following. [5, 68]

The crystal structure of the III–V semiconductor GaAs is based on two face-centered cubic lattices of Ga and As that are shifted along the main diagonal by 1/4 of the diagonal length as visualized in Figure 1.1a. Here, the bonding of the atoms is mediated by the valence electrons that are in the configuration $4s^2 4p$ for Ga and $4s^2 4p^3$ for As. The difference in electronegativity of Ga and As leads to a partial transfer of one electron from As to Ga. Forming sp^3 hybrid orbitals with their four nearest neighbors arranged in a tetragon, the four electrons per atom tend to create covalent

bonds, resulting in a zinc-blende structure. The valence and conduction bands of GaAs are formed from the three bonding and one antibonding sp^3 orbitals that have strong p- and s-character at the band edge, respectively. This leads to a band structure close to the band gap as shown in Figure 1.1b. Here, the bands have a nearly quadratic dispersion and carriers behave similarly to free particles with an effective mass determined by the inverse second derivative of the band dispersion. As a result of the spin-orbit coupling, the orbital angular momentum L couples to the electron spin S resulting in the total angular momentum $J = L + S$ [68]. For the conduction band ($L = 0$), the eigenstates are $|j = 1/2, j_z = \pm 1/2\rangle$, where j_z is the z-component of J. For the valence bands ($L = 1$), the eigenstates are $|3/2, \pm 3/2\rangle$ (heavy-hole), $|3/2, \pm 1/2\rangle$ (light-hole), and $|1/2, \pm 1/2\rangle$ (split-off). The spin-orbit coupling leads to the energetic splitting between the bands with $j = 3/2$ and the split-off band with $j = 1/2$. Thus, for the optical properties near the band edge, only the heavy- and light-hole bands are relevant. In low dimensional systems, the degeneracy between light- and heavy-hole bands at $k = 0$ is usually lifted [5].

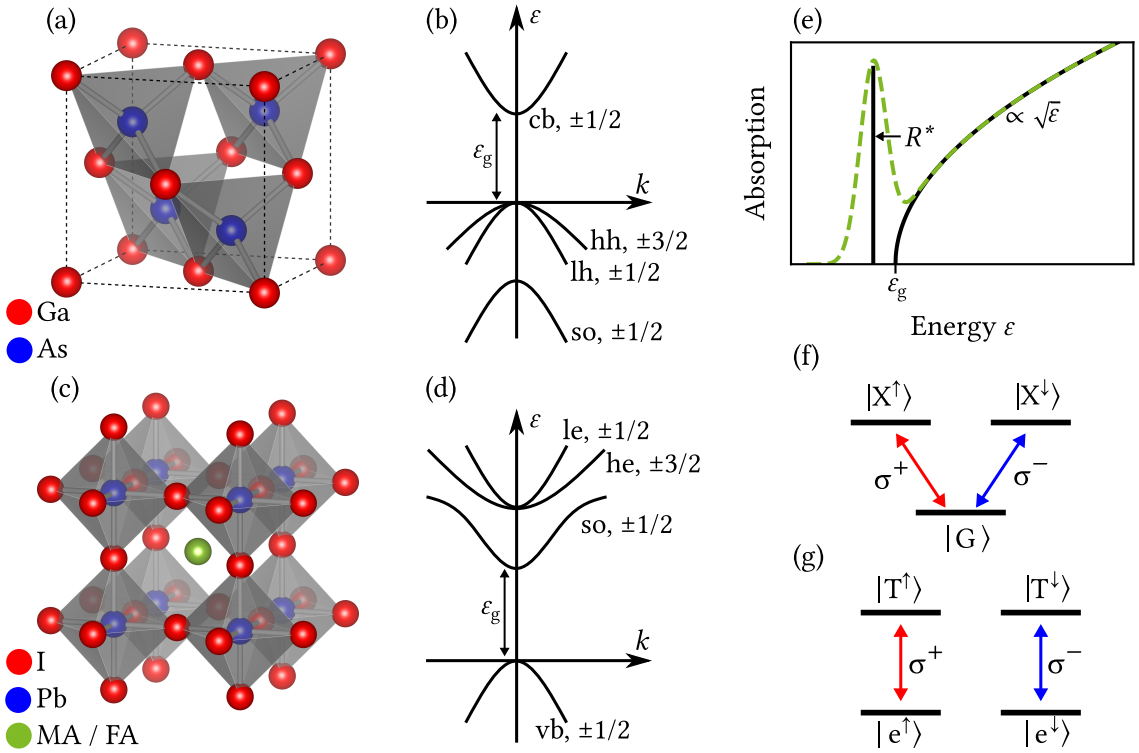

Figure 1.1: (a) Visualization of the zinc-blende structure of GaAs. (b) Simplified band structure $\varepsilon(k)$ of GaAs close to the direct band gap at $k = 0$ with an s-type conduction band and a p-type valence band. The bands are denoted as conduction band (cb), heavy-hole (hh), light-hole (lh), and split-off (so). (c) Perovskite crystal structure of $MAPbI_3$ and $FAPbI_3$. (d) Simplified perovskite band structure with s-type valence band and p-type conduction band. The bands are denoted as light-electron (le), heavy-electron (he), split-off (so), and valence band (vb). (e) The schematic absorption spectrum of a semiconductor taking into account the lowest lying exciton state split by the Rydberg energy R^* from the band gap ε_g. The black line shows the idealized situation with a delta-like exciton absorption and $\sqrt{\varepsilon}$-behavior of interband transitions. The green line shows schematically the effect of inhomogeneous broadening. (f) Optical excitation selection rules for the generation of bright exciton states $|X^{\uparrow\downarrow}\rangle$ from the crystal's ground state $|G\rangle$. (g) Optical selection rules for the excitation of trions. Here, $|e^{\uparrow\downarrow}\rangle$ and $|T^{\uparrow\downarrow}\rangle$ denote the degenerate ground and excited states of the resident electron and excited trion, respectively.

Perovskites denote materials that share the composition ABX_3. Within this thesis, the focus is set on hybrid organic-inorganic lead halide perovskites where A is an organic molecule such

as formadinium (FA, NH_2CH) or methylammonium (MA, CH_3NH_3), B is lead (Pb), and X is a halide like iodine (I). The crystal structure is formed by a lead-halide ionic cage PbI_3^-, where Pb is surrounded by six halide atoms in an octahedral arrangement as visualized in Figure 1.1c. Here, the organic cations A^+ are located in between the octahedra. The Pb and I ions with valence configurations $5d^{10}6s^26p^0$ and $5p^6$, respectively, are dominantly responsible for the highest valence and lowest conduction band states [69]. In particular, the valence band is formed from hybridized lead 6s and iodine 5p orbitals, where the 6s orbital dominates close to the band gap while the conduction band is formed from unoccupied lead 6p orbitals [69, 70]. Thus, the simplified band structure appears reversed compared to the aforementioned III–V semiconductors, i.e. the valence band is s-type, whereas the conduction band is p-type, compare Figure 1.1d. Due to the spin-orbit coupling, the lowest energy optical transition takes place between the valence band states with the total angular momentum of $j = 1/2$ and the conduction band. The band gap of organic-inorganic perovskites can be tuned in a wide range by changing the halide content. For example, the band gap of crystals with the composition $FAPbI_{3-x}Br_x$ can be adjusted between roughly 1.5 eV for $x = 0$ and 2.5 eV for $x = 3$ [71]. The organic molecule in the perovskites has profound influences on their electronic and crystallographic structure [72, 73]. These influences mainly result from the static dipole moment of the molecules that can lead to deformations of the Pb-halide octahedra depending on the rotation of the molecule. Due to the coexistence of multiple crystallographic phases, spatial fluctuations of the band gap occur that cause inhomogeneous broadening [74, 75]. This additional source of inhomogeneous broadening is absent in perovskites with rotational isotropic cations, for example $CsPbI_3$ [76].

1.1.1 Excitons

For both III–V and perovskite semiconductors, the concept of excitons is of great importance for the nonlinear optical properties close to the band gap. Exciton states result from the attractive Coulomb interaction between electrons and holes and thus represent a semiconductor analogy to hydrogen atoms. Regarding the absorption spectrum of semiconductors, schematically shown in Figure 1.1e, excitons manifest themselves as additional absorption peaks below the band gap. The lowest energy state is shifted by the Rydberg energy R^* from the band gap. Highly excited exciton states that follow a hydrogen-like series R^*/n^2, where n is an integer, are rarely observable only in selected semiconductor systems like CuO_2 [77] or two-dimensional transition metal dichalcogenides [78]. In most semiconductors, excited exciton states are spectrally too close to each other and the continuum transitions to be resolved. Moreover, as shown by the green line in Figure 1.1e, the energetic position of the exciton resonance is typically subject to statistical fluctuations induced by crystallographic disorder, which leads to an overall inhomogeneously broadened line that overlaps with the continuum.

Nonlinear optical phenomena are associated with excitation-induced changes in the absorption of optical resonances [79]. Due to their discrete energy state structure and strong oscillator strengths, exciton resonances typically dominate the nonlinear response of semiconductors as they are sensitive to light-induced saturation or energetic shifts and broadenings [3, 79, 80]. Moreover, the coherence time of excitons (proportional to the inverse spectral width) is substantially longer (picosecond-regime) compared to unbound electron-hole pairs (femtosecond-regime) [81]. Therefore, monitoring the exciton dynamics by nonlinear spectroscopic techniques is a sensitive tool to study various interaction mechanisms in semiconductors [3], as we explore within this thesis.

Optically bright excitons require a z-component of their total angular momentum of $j_z = \pm 1$. In III–V semiconductors, two of these exciton states are formed by antiparallel electron ($j_z = \pm 1/2$)

and heavy hole spins ($j_z = \mp 3/2$). In perovskites instead, the bright exciton states are formed by parallel electron ($j_z = \pm 1/2$) and hole spins ($j_z = \pm 1/2$). Optically dark exciton states with spin projections of ± 2 or 0, respectively, cannot be directly excited but may become important in correctly interpreting spin relaxation mechanisms or magnetic field dynamics of excitons [82, 83]. The dipole selection rules of the two bright exciton configurations, denoted as $|X^{\uparrow}\rangle$ and $|X^{\downarrow}\rangle$, are summarized by the V-scheme shown in Figure 1.1f, where the two exciton states can be excited from a common ground state $|G\rangle$ using circularly polarized light $\sigma^{\pm}$. As is discussed in Section 1.2.3, the scheme has important implications on polarization selection rules in nonlinear optical spectra of excitons.

The interaction of excitons with carriers can give rise to the formation of charged excitons (trions) [47]. To optically excite a trion, a resident electron (or hole) in the ground state of the crystal is required, which may result for example from doping of the sample. Thus, the ground state is doubly degenerate with respect to the two spin configurations of the resident carrier, as exemplary shown for the presence of a resident electron in Figure 1.1g. The two optically bright trion states with angular momentum of $\pm 3/2$ for III-V structures (or $\mp 1/2$ for perovskites) result from antiparallel electron spins and one hole spin and can be excited by the circular polarizations as depicted by the arrows in Figure 1.1g. Further excitonic complexes such as doubly charged excitons [84] or a bound state of two excitons (biexciton) [63] can be found in semiconductor structures. The biexciton state, in particular, is investigated in Section 4.1.

1.1.2 Semiconductor quantum dots

The lifetime of excitons and their light interaction strength can be enhanced in low-dimensional systems because excitons are more isolated from their environment and electron-hole pairs are closer to each other. Modern growth techniques such as molecular beam epitaxy enable the fabrication of semiconductor heterostructures with atomic precision [47]. Heterostructures are composed of multiple layers of semiconductor materials with different band gaps and thus exhibit a spatially modified electronic structure. When a layer of a lower band gap material like InAs is surrounded by two layers of a higher band gap material like GaAs, electrons and holes can be spatially confined in the inner layer. The spatial variation of the band gap for such a so-called quantum well structure is schematically shown in Figure 1.2a. When the spatial confinement is comparable to the de Broglie wavelength of the carriers, the energy states become quantized perpendicular to the confinement direction, whereas the movement perpendicular to the growth direction is free. In quantum dots (QDs), the spatial confinement is realized in all three dimensions which leads to a full quantization of energy levels similar to natural atoms. Within this thesis, we study ensembles of self-assembled (In,Ga)As QDs. Those QDs are formed by the Stranski-Krastanov method [85], where InAs is deposited on a GaAs substrate. The mismatch of 7 % of the lattice constant between both materials leads to strain that favors the spontaneous formation of nanometer-sized islands on a thin layer of InAs (wetting layer) [47], as depicted in Figure 1.2b. Subsequently, the islands are capped by a GaAs layer which leads to spatial confinement of carriers in the InAs islands in all three dimensions.

QDs exhibit strong oscillator strengths due to the spatial confinement of electrons and holes. Further, the discretization of energy levels minimizes the number of allowed inelastic scattering events and thus strongly increases the coherence time of electron-hole pairs as compared to bulk materials. Equivalently, the emission line shape of a single QD is more narrow. However, due to the self-organized growth technique, different QDs on one substrate typically differ in size and shape, as can be seen in Figure 1.2c. Consequently, the lineshape of an ensemble of QDs is usually several orders of magnitude broader than the lineshape of a single QD. Studying the

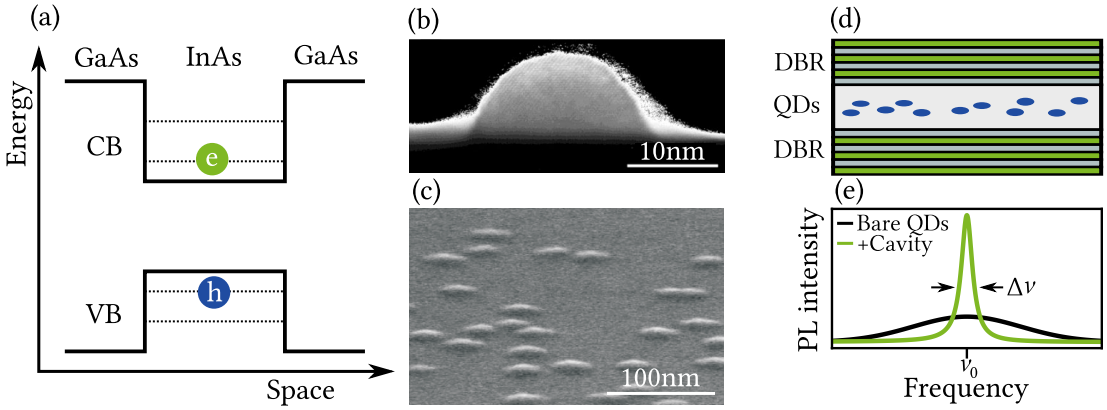

Figure 1.2: (a) Band alignment in a GaAs/InAs/GaAs heterostructure forming a quantum well for electrons and holes in the growth direction. (b) Transmission electron microscopy image of a single self-assembled QD, reprinted from [86, 87]. (c) Scanning electron microscopy image of several QDs formed by the Stranski-Krastanov method, reprinted from [88]. The QDs differ in size and shape leading to an inhomogeneous broadening. (d) Schematic of a QD–cavity system. The cavity is formed by two distributed Bragg reflectors (DBRs). (e) Effect of the cavity as enhanced photoluminescence of those QDs that are in resonance with the cavity mode with central frequency ν_0 and width $\Delta\nu$.

coherence properties of single QDs, therefore, requires either microscopic techniques (single QD spectroscopy [89]) or the use of nonlinear techniques that allow overcoming inhomogeneous broadening as described below.

The light-matter interaction of QDs can be further enhanced using optical microcavities. A planar microcavity confines light to small volumes by resonant recirculation between two reflecting surfaces [90]. When placing an optical emitter in the cavity (e.g. a QD), the cavity effectively wraps a large light-matter interaction distance into a tiny volume [91]. Therefore, the intracavity field at the position of the QD is enhanced which strongly increases optical nonlinearities. The efficiency of a microcavity is expressed by the Q-factor that measures the ratio between the stored energy and the energy loss per oscillation cycle. The Q-factor is given by the ratio between the central resonator frequency ν_0 and the bandwidth $\Delta\nu$, $Q = \frac{\nu_0}{\Delta\nu}$. Microcavities can be formed by distributed Bragg reflectors (DBRs) consisting of alternating layers of two materials with different refractive indices, such as AlAs and GaAs [92]. The distance between the DBRs defines the central resonance frequency ν_0 of the cavity. When placing the QD ensemble inside the cavity, Figure 1.2d, the optical response of the QDs which are in resonance with the cavity is strongly enhanced. This effect can be seen for example in the photoluminescence of the system, schematically shown in Figure 1.2e. We use a QD–cavity system to drive high-order optical nonlinearities from a QD ensemble as will be discussed in Section 1.3. Note that the regime of strong coupling between the cavity mode and the exciton resonance, achieved in high-Q cavities [90, 93], is not considered within this thesis.

1.2 Dynamics of Optical Excitations – Bloch equations

Coherent spectroscopic techniques are a powerful tool to gain insight into the dynamics and interactions of optical excitations in semiconductors [3]. Those techniques investigate the temporal regime during which photoexcited carriers remain in phase with the resonant excitation source. By monitoring the optically induced macroscopic polarization P, being itself a source of

radiation, valuable information about scattering events or quantum mechanical superpositions of photo-excitations can be extracted. Importantly, the loss of macroscopic polarization caused by the dephasing of individual excitations within an inhomogeneously broadened ensemble can be overcome by nonlinear techniques, as will be shown in Section 1.2.1. In the following, we will first describe theoretical approaches to quantify the dynamics of optical excitations in a semiconductor.

A comprehensive theoretical description of the coherent light-matter interaction in semiconductors is governed by the semiconductor Bloch equations, see for example References [3–5, 94]. The term Bloch equations is adopted from the equations describing the dynamic of an isolated optical two-level system (TLS) interacting with a nearly resonant light field [95]. The semiconductor Bloch equations further take into account many-body Coulomb interactions among carriers in solids which strongly increases the complexity of the problem. A full discussion of the semiconductor Bloch equations is beyond the scope of the theoretical considerations made within this thesis. However, a critical consequence of Coulomb interaction between photo-excited carriers is the formation of excitons. As mentioned above, excitons typically dominate the optical response of semiconductors close to the band edge. In nonlinear optical spectra, excitons may even exceed the optical response of unbound electron-hole pairs by several orders of magnitude due to the strong oscillator strength and long coherence time [3].

To introduce the most important concepts of coherent spectroscopy on semiconductors relevant to this thesis, we neglect Coulomb interactions beyond the formation of bound electron-hole pairs. When first neglecting the polarization state of the excitation source, the crystal ground state $|\mathrm{G}\rangle$ and a single excited exciton state $|\mathrm{X}\rangle$ can be treated as a TLS with energy splitting $\hbar\omega_0$. We exclusively consider dipole transitions between these two states. The interaction between the TLS and a light field with scalar electric field $E(t)$ is given by the Hamiltonian (written in 2×2 base of the eigenstates $|\mathrm{G}\rangle$ and $|\mathrm{X}\rangle$)

$$\mathbf{H}_{\mathrm{int}} = -\boldsymbol{\mu} \cdot \mathbf{E} = -\begin{pmatrix} 0 & \mu E \\ \mu^* E & 0 \end{pmatrix}, \tag{1.1}$$

where $\boldsymbol{\mu}$ denotes the dipole operator with the non-zero matrix element $\mu = \langle \mathrm{G}|\boldsymbol{\mu}|\mathrm{X}\rangle$. The optical response of the system results from the expectation value of the dipole operator $\langle\psi|\mathbf{d}|\psi\rangle$, where $|\psi\rangle = c_{\mathrm{g}}|\mathrm{G}\rangle + c_{\mathrm{x}}|\mathrm{X}\rangle$ denotes an arbitrary superposition of ground and excited states with complex state amplitudes c_{g} and c_{x}. Since this expectation value is related to the bilinear products $c_{\mathrm{g}}^* c_{\mathrm{x}}$ and $c_{\mathrm{g}} c_{\mathrm{x}}^*$, it is more convenient to deal with the density matrix $\boldsymbol{\rho}_{\mathrm{ij}} = c_{\mathrm{i}}^* c_{\mathrm{j}}$ $(i, j = g, x)$ of the system than with the state amplitudes. Moreover, the use of the density matrix formalism is unavoidable when considering an ensemble of TLS that is subject to random scattering events that affect the relative phase of the state amplitudes (discussed below) [96]. The dynamic of the density matrix results from the Liouville-von Neumann equation

$$i\hbar \frac{d}{dt}\boldsymbol{\rho} = [\mathbf{H}, \boldsymbol{\rho}], \tag{1.2}$$

where $\mathbf{H} = \mathbf{H}_0 + \mathbf{H}_{\mathrm{int}}$, with the unperturbed Hamiltonian $\mathbf{H}_0 = \mathrm{diag}(0, \hbar\omega_0)$. Equation (1.2) leads to the optical Bloch equations for the two independent elements of the density matrix $p = \boldsymbol{\rho}_{\mathrm{gx}} = \boldsymbol{\rho}_{\mathrm{xg}}^*$ and $n = \boldsymbol{\rho}_{\mathrm{xx}} = 1 - \boldsymbol{\rho}_{\mathrm{gg}}$

$$\frac{d}{dt}p = i\omega_0 p - i\frac{\mu E}{\hbar}(1 - 2n) \tag{1.3a}$$

$$\frac{d}{dt}n = 2\mathrm{Im}\left[\frac{\mu^* E}{\hbar} p\right], \tag{1.3b}$$

where p is referred to as the (microscopic) polarization and n the population of the excited state $|\mathrm{X}\rangle$. The macroscopic polarization of an ensemble of N identical TLS is given by

$$P = N\mathrm{Tr}\left(\boldsymbol{\rho}\,\boldsymbol{\mu}\right) \propto p. \tag{1.4}$$

Consequently, the microscopic polarization p contains the physics of (nonlinear) optical properties of the TLS [94]. Equation (1.3a) contains the free oscillation of the polarization with eigenfrequency ω_0 as well as a driving term proportional to the external electric field E. The latter decreases with the increasing population of the upper state n as a consequence of the Pauli exclusion principle. This nonlinear response to the external electric field is often called phase-space filling and gives rise to nonlinear optical effects, for example, excitation-induced saturation or four-wave mixing [97]. It should be noted that in semiconductors not only the Pauli exclusion principle but also Coulomb interactions with the many-body environment of an exciton can have a significant impact on the saturation of the absorption, which is a major difference to atomic systems [24]. We can therefore regard the term $(1-2n)$ in Equation (1.3a) as a phenomenological approach that takes into account various contributions that lead to a saturation of the resonance. Other influences of many-body interactions that are not governed by Equations (1.3), can be tackled by mean-field approaches as we will discuss in Section 4.2.

The Bloch equations (1.3) are expanded phenomenologically by decay rates Γ_2 and Γ_1 for the polarization and population to account for relaxation processes that contribute to the equilibration of the optical transition

$$\frac{d}{dt}p = i\omega_0 p - i\frac{\mu E}{\hbar}(1-2n) - \Gamma_2 p \tag{1.5a}$$

$$\frac{d}{dt}n = 2\mathrm{Im}\left[\frac{\mu^* E}{\hbar}p\right] - \Gamma_1 n. \tag{1.5b}$$

We denote the corresponding time constants $T_2 = \Gamma_2^{-1}$ and $T_1 = \Gamma_1^{-1}$ as decoherence time and population decay time. The population decay time may include energy relaxation through scattering events as well as the finite radiative lifetime of excitons that is inversely proportional to the dipole moment squared [28, 98]. As a consequence of the definition of the polarization p through the probability amplitudes $p \propto \sqrt{|c_\mathrm{x}|^2} \propto \exp(-t/2T_1)$, the decoherence time T_2 is ultimately limited by the population decay through $T_2 = 2T_1$. Moreover, T_2 can account for pure decoherence mechanisms that leave the excited state population unaffected while changing the phase between the ground and the excited state. Thus, we define

$$\frac{1}{T_2} = \frac{1}{2T_1} + \frac{1}{T_2'}, \tag{1.6}$$

where T_2' is the timescale of pure decoherence. The limiting case $T_2 = 2T_1$ can be found in isolated systems where elastic scattering events with phonons are minimized at low temperatures (compare Chapter 5). It is one of the tasks of four-wave-mixing spectroscopy to measure the decay times and thus gain insights into the efficiency of the underlying scattering mechanisms. We describe the working principle of this technique in the following section.

1.2.1 Four-wave-mixing spectroscopy and photon echoes

The induced polarization P in a semiconductor depends in general in a nonlinear fashion on the exciting electric field $\mathcal{E}$. Nonlinear components can be classified by expanding the polarization in a Taylor series

$$P = \chi^{(1)}\mathcal{E} + \chi^{(2)}\mathcal{E}^2 + \chi^{(3)}\mathcal{E}^3 + \dots, \tag{1.7}$$

where $\chi^{(m)}$ is the m-th order susceptibility [99]. In inversion symmetric systems, the lowest nonlinear component is given by the third order $\propto \chi^{(3)}\mathcal{E}^3$, which forms the basis of transient four-wave mixing (FWM) spectroscopy. Linear spectroscopic techniques such as linear absorption spectroscopy rely on a spectrally or time-resolved observation of the linear polarization $P^{(1)} \propto \mathcal{E}$. In principle, when temporally resolving the linear polarization after excitation with a short laser pulse, the loss of coherence caused by elastic or inelastic scattering events can be measured [7]. However, optical resonances like excitons in semiconductors are often subject to inhomogeneous broadening, as schematically shown in Figure 1.3a. Here, the spectral width of single resonance $\propto T_2^{-1}$ is hidden under a distribution of resonance frequencies ω_0. When temporally resolving the linear response $P^{(1)}$, a rapid decay of the macroscopic polarization will be observed due to the dephasing of the ensemble, which is known as free induction decay, Figure 1.3b. The timescale of the free induction decay, i.e. the dephasing time T_2^*, can be significantly shorter than the decoherence time T_2 of an individual optical excitation. Nonlinear FWM spectroscopy allows overcoming the reversible loss of macroscopic polarization due to dephasing as will be explained in the following.

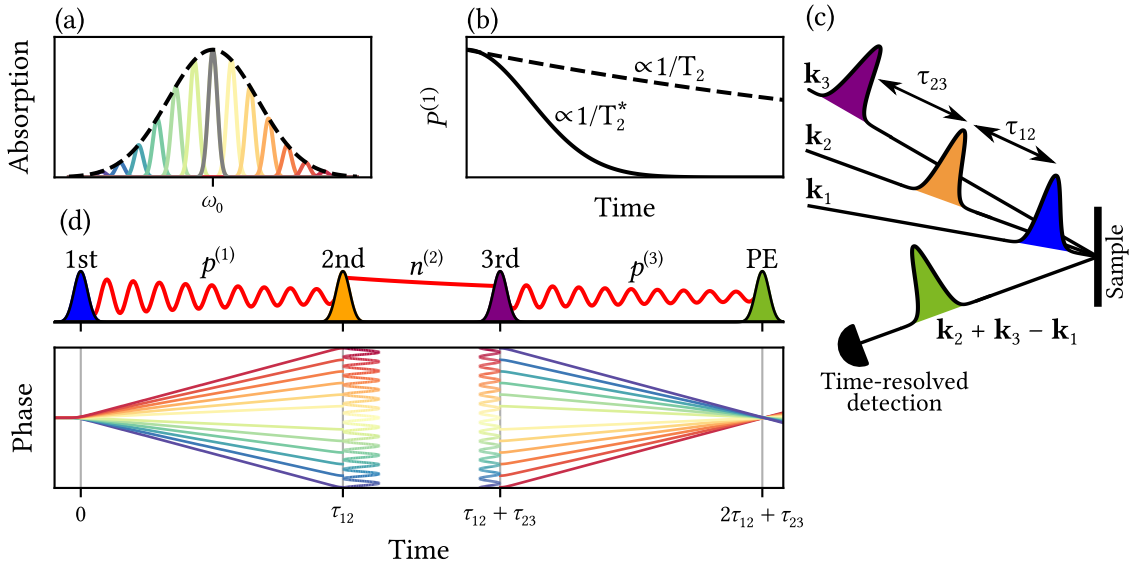

Figure 1.3: (a) Schematic absorption spectrum of an inhomogeneously broadened resonance. Here the statistical distribution of resonance frequencies (black dashed line) exceeds the width of the homogeneous lines of individual resonances (colored lines). (b) Temporal behavior of linear polarization for an inhomogeneously broadened resonance. The macroscopic polarization (solid) dephases on a shorter time scale as the microscopic polarization of an individual oscillator (free induction decay). (c) Pulse arrangement for a three-pulse photon echo (PE) experiment in reflection geometry. (d) Visualization of the three-pulse PE formation within a third-order nonlinear process as explained in the text.

The standard experimental geometry of transient FWM spectroscopy is depicted in Figure 1.3c. Here, the laser field $\mathcal{E}$ is in general split into three laser pulses $\mathcal{E}_i$ with relative delays τ_{12} and τ_{23} and wavevectors $\mathbf{k}_i$. We exclusively consider degenerate FWM spectroscopy, where all pulses share the same central optical frequency ω_L. We write the electric fields as

$$\mathcal{E}_i(t) = \frac{1}{2}E_i(t)e^{i\mathbf{k}\cdot\mathbf{r}+i\omega_L t} + \text{c.c.}, \tag{1.8}$$

where $E_i(t)$ denotes a slowly varying pulse envelope. The nonlinear response of the sample gives rise to a third-order polarization component $\propto E_1^* E_2 E_3$ being the source of a fourth optical field

emitted in the direction $\mathbf{k}_3 + \mathbf{k}_2 - \mathbf{k}_1$ (phase-matching condition). Using different wavevectors of the excitation pulses is advantageous from an experimental point of view since it leads to a spatial separation of the FWM response from other (nonlinear) signals. The temporal characteristic of the FWM response as a function of the relative delays between the exciting pulses τ_{ij} and real-time can be obtained from a perturbative expansion of the optical Bloch equations (1.3). For this purpose, the microscopic polarization p and population n are expanded in perturbative orders $p^{(m)}$ and $n^{(m)}$ with respect to the order m of the electric field. This procedure leads to the following set of coupled equations of motion [3]

$$\frac{d}{dt}p^{(1)} = \left(i\Delta - \frac{1}{T_2}\right)p^{(1)} + i\frac{\mu E}{\hbar} \tag{1.9a}$$

$$\frac{d}{dt}n^{(2)} = -\frac{1}{T_1}n^{(2)} - \frac{i}{\hbar}\left(\mu E p^{*(1)} - \mu^* E^* p^{(1)}\right) \tag{1.9b}$$

$$\frac{d}{dt}p^{(3)} = \left(i\Delta - \frac{1}{T_2}\right)p^{(3)} - 2\frac{i}{\hbar}\mu E n^{(2)}. \tag{1.9c}$$

Here, we introduced the detuning $\Delta = \omega_0 - \omega_L$ between resonance and laser frequency and neglected terms that oscillate at $\omega_0 + \omega_L$ (rotating wave approximation). Even orders of p and odd orders of n vanish when assuming that the system is initially in the ground state [3]. The time dependence of the FWM response is obtained by subsequently solving the set of Equations (1.9). For simplicity, we assume that the slowly varying envelopes of the three pulses are given by delta functions. The first pulse induces a linear polarization given by

$$p^{(1)}(t) = i\frac{\mu E_1}{\hbar}H(t)\exp\left[i\mathbf{k}_1\mathbf{r} + i\Delta t - \frac{t}{T_2}\right], \tag{1.10}$$

where $H(t)$ denotes the Heaviside function. The polarization freely oscillates with the detuning Δ associated with the oscillator and exponentially decays with T_2. Averaging over a distribution of detunings leads to a decay of the macroscopic linear polarization $P^{(1)}$ on a timescale given by T_2^*. This dephasing motion is visualized in Figure 1.3d. The linear polarization $p^{(1)}$ represents a source term $\propto p^{*(1)}E_2$ in the second order population $n^{(2)}$ of Equation (1.9b), which results in

$$n^{(2)}(t) = -\frac{|\mu|^2 E_1^* E_2}{\hbar^2}H(\tau_{12})H(t-\tau_{12})\exp\left[i(\mathbf{k}_2 - \mathbf{k}_1)\mathbf{r} - i\Delta\tau_{12} - \frac{\tau_{12}}{T_2} - \frac{t-\tau_{12}}{T_1}\right]. \tag{1.11}$$

The second-order interaction of the first and second pulses results in a spatial and spectral modulation of the second-order population at frequencies $\mathbf{k}_2 - \mathbf{k}_1$ and τ_{12}^{-1}, which is referred to as a population grating. The amplitude of the population grating decays with the population decay time T_1. The second-order population finally results in a source term $\propto E_3 n^{(2)}$ in the third-order polarization

$$\begin{aligned} p^{(3)} = i\frac{\mu|\mu|^2 E_1^* E_2 E_3}{\hbar^3}&H(\tau_{12})H(\tau_{23})H(t-\tau_{12}-\tau_{23})\times \\ &\times\exp\left[i(\mathbf{k}_2 + \mathbf{k}_3 - \mathbf{k}_1)\mathbf{r} + i\Delta(t-\tau_{23}-\tau_{12}) - i\Delta\tau_{12} - \frac{\tau_{23}}{T_1} - \frac{t-\tau_{23}}{T_2}\right]. \end{aligned} \tag{1.12}$$

The third-order optical response of the system $\propto p^{(3)}$ can be interpreted as the diffraction of the third pulse on the population grating created by the first and second pulse. In Equation (1.12), it can be seen that the phase of the linear polarization $\Delta\tau_{12}$, acquired during the time interval τ_{12}, is subtracted from the phase evolution in the time interval after the third pulse. Therefore, the free evolution of the system after the action of the third pulse leads to a reformation of the

macroscopic polarization at time $t = 2\tau_{12} + \tau_{23}$, as visualized in Figure 1.3d. When averaging over a Gaussian distribution of detunings, the macroscopic third-order polarization $P^{(3)}$ is given by a Gaussian laser pulse centered at $t = 2\tau_{12} + \tau_{23}$

$$P^{(3)} \propto \exp\left[-\frac{\tau_{23}}{T_1} - \frac{2\tau_{12}}{T_2}\right] \exp\left[-\frac{(t - \tau_{23} - 2\tau_{12})^2}{2T_2^{*2}}\right], \tag{1.13}$$

which we call the three-pulse PE. When measuring the amplitude of the three-pulse PE as a function of τ_{12} or τ_{23}, we can access the decoherence time T_2 and population decay time T_1, while a measurement of its duration includes information of the dephasing time T_2^*. It is therefore of striking importance to establish a time-resolved detection technique, as will be introduced in Section 2.1, to independently study homogeneous and inhomogeneous decoherence effects. A measurement of T_2 can also be performed using only two pulses resulting in the two-pulse PE at $t = 2\tau_{12}$. The derivation of the corresponding third-order nonlinearity $p^{(3)} \propto E_1^* E_2^2$ is equivalent when replacing E_3 by E_2 and setting $\tau_{23} = 0$ in Equation (1.12). In our experiments, we choose $\mathbf{k}_2 = \mathbf{k}_3$. Thus, the two-pulse PE and three-pulse PE share the same phase-matching condition.

1.2.2 Diagrammatic perturbation theory

The perturbative expansion of the optical Bloch equations presented in the previous section for a TLS up to the third order can be analogously continued up to an arbitrary perturbative order to describe the formation of multi-wave-mixing signals. Moreover, similar equations of motion can be obtained for few-level absorbers such as the V-scheme for excitons as presented in Figure 1.1f, where the spin degree of freedom is incorporated in the dipole selection rules. An elegant formalism to keep track of all terms contributing to a certain nonlinear optical response is diagrammatic perturbation theory [99, 100]. Here, each summand contributing to an m-th order polarization has a representation as a double-sided Feynman diagram. These diagrams are especially useful to easily check dipole selection rules in multi-level systems within a particular multi-wave-mixing process. We define these diagrams in the following according to Refs. [100, 101]. Here, we also take into account non-vanishing pulse durations, which lead to multivariate time integrals. Those are used to obtain the modeling results presented in Chapters 4 and 6.

We consider the interaction of N laser pulses with a general multi-level system with energy levels ε_n and corresponding density matrix $\boldsymbol{\rho}$. The dynamic of the density matrix is described by the Liouville-von Neumann equation (1.2). Decay rates are added phenomenologically through $\dot{\rho}_\mathrm{ij} \propto -\Gamma_\mathrm{ij}\rho_\mathrm{ij}$ as shown in Equations (1.5) for the TLS where population decays with T_1 and coherence with T_2. The m-th order expansion of the density matrix with respect to the external optical field is then recursively obtained from

$$\boldsymbol{\rho}_\mathrm{ij}^{(\mathrm{m})}(t) = \int_{-\infty}^{t} \frac{i}{\hbar}\left[\boldsymbol{\rho}^{(m-1)}(\tau), \mathbf{V}(\tau)\right]_\mathrm{ij} \mathrm{e}^{-i\Omega_\mathrm{ij}(t-\tau)} d\tau, \tag{1.14}$$

where $\Omega_\mathrm{ij} = \omega_\mathrm{ij} - i\Gamma_\mathrm{ij}$ with $\omega_\mathrm{ij} = (\varepsilon_\mathrm{i} - \varepsilon_\mathrm{j})/\hbar$. In a multi-wave-mixing experiment, the external electric field is given by a train of laser pulses with field envelopes $E_\mathrm{j}(t)$ and corresponding wavevectors $\mathbf{k}_\mathrm{j}$. The interaction operator $\mathbf{V}(t)$ thus reads as

$$\mathbf{V}(t) = -\frac{\boldsymbol{\mu}(t)}{2} \sum_{\mathrm{j}=0}^{N} \left(E_\mathrm{j}(t)\mathrm{e}^{-i\mathbf{k}_\mathrm{j}\cdot\mathbf{r}} + E_\mathrm{j}^*(t)\mathrm{e}^{i\mathbf{k}_\mathrm{j}\cdot\mathbf{r}}\right). \tag{1.15}$$

As a result of the nested commutators in Equasion (1.14), the m-th order expansion of the density matrix consists of $2^{2\mathrm{m}}N^\mathrm{m}$ summands. Each of these summands has a representation as a double-sided Feynman diagram that illustrates the different pathways by which the external electric

fields mediate between populations and coherences in the multi-level system. Any diagram can be obtained by vertically stacking together the following four unique elements with corresponding contributions to the m-th order density matrix element [101]:

$$\left|\begin{matrix}|i\rangle\langle j|\\|i\rangle\langle l|\end{matrix}\right| \leftarrow \mathbf{k}_\mathrm{n} \qquad \boldsymbol{\rho}_{\mathrm{il}}^{(\mathrm{m})}(t) = -i\frac{\mu_{\mathrm{jl}}}{2\hbar}\mathrm{e}^{-i\mathbf{k}_\mathrm{m}\cdot\mathbf{r}}\int_{\infty}^{t} E_\mathrm{m}^{*}(\tau)\mathrm{e}^{-i\Omega_{\mathrm{il}}(t-\tau)}\boldsymbol{\rho}_{\mathrm{ij}}^{(\mathrm{m}-1)}(\tau)d\tau \tag{1.16a}$$

$$\mathbf{k}_\mathrm{n} \leftarrow \left|\begin{matrix}|i\rangle\langle j|\\|l\rangle\langle j|\end{matrix}\right| \qquad \boldsymbol{\rho}_{\mathrm{lj}}^{(\mathrm{m})}(t) = +i\frac{\mu_{\mathrm{il}}}{2\hbar}\mathrm{e}^{-i\mathbf{k}_\mathrm{m}\cdot\mathbf{r}}\int_{\infty}^{t} E_\mathrm{m}^{*}(\tau)\mathrm{e}^{-i\Omega_{\mathrm{lj}}(t-\tau)}\boldsymbol{\rho}_{\mathrm{ij}}^{(\mathrm{m}-1)}(\tau)d\tau \tag{1.16b}$$

$$\left|\begin{matrix}|i\rangle\langle j|\\|i\rangle\langle l|\end{matrix}\right| \rightarrow \mathbf{k}_\mathrm{n} \qquad \boldsymbol{\rho}_{\mathrm{il}}^{(\mathrm{m})}(t) = -i\frac{\mu_{\mathrm{jl}}}{2\hbar}\mathrm{e}^{+i\mathbf{k}_\mathrm{m}\cdot\mathbf{r}}\int_{\infty}^{t} E_\mathrm{m}(\tau)\mathrm{e}^{-i\Omega_{\mathrm{il}}(t-\tau)}\boldsymbol{\rho}_{\mathrm{ij}}^{(\mathrm{m}-1)}(\tau)d\tau \tag{1.16c}$$

$$\mathbf{k}_\mathrm{n} \rightarrow \left|\begin{matrix}|i\rangle\langle j|\\|l\rangle\langle j|\end{matrix}\right| \qquad \boldsymbol{\rho}_{\mathrm{lj}}^{(\mathrm{m})}(t) = +i\frac{\mu_{\mathrm{il}}}{2\hbar}\mathrm{e}^{+i\mathbf{k}_\mathrm{m}\cdot\mathbf{r}}\int_{\infty}^{t} E_\mathrm{m}(\tau)\mathrm{e}^{-i\Omega_{\mathrm{lj}}(t-\tau)}\boldsymbol{\rho}_{\mathrm{ij}}^{(\mathrm{m}-1)}(\tau)d\tau. \tag{1.16d}$$

For example, one contribution to the FWM response of a TLS, as discussed in Section 1.2.1, is illustrated by the following diagram:

$$\begin{matrix}\mathbf{k}_2 \rightarrow \\ 2\mathbf{k}_2-\mathbf{k}_1 \leftarrow\end{matrix}\left|\begin{matrix}|\mathrm{G}\rangle\langle\mathrm{G}|\\|\mathrm{G}\rangle\langle\mathrm{X}|\\|\mathrm{X}\rangle\langle\mathrm{X}|\\|\mathrm{X}\rangle\langle\mathrm{G}|\end{matrix}\right|\begin{matrix}\leftarrow \mathbf{k}_1\\ \\ \\ \rightarrow \mathbf{k}_2\end{matrix}. \tag{1.17}$$

Here, time evolves from top to bottom, and arrows indicate interactions with the fields. The direction of the arrows with label $\mathbf{k}_\mathrm{j}$ indicates whether $E_\mathrm{j}e^{-i\mathbf{k}_\mathrm{j}\cdot\mathbf{r}}$ or $E_\mathrm{j}^{*}e^{i\mathbf{k}_\mathrm{j}\cdot\mathbf{r}}$ contributes. Here, the final emission is marked by a differently styled arrow. Note that the number of relevant Feynman diagrams $2^{2\mathrm{m}}N^\mathrm{m}$ is strongly reduced when the optical pulses are strictly temporally ordered and only a particular phase-matching condition is filtered. In this case, the temporal dynamic of a particular wave-mixing process as a function of temporal delays, polarizations or electric field amplitudes can be conveniently calculated by constructing all dipole-allowed Feynman diagrams and subsequently using the calculation rules given in Equations (1.16). The magnitude of the emitted signal field, which is the measured quantity in our experiments, is assumed to be proportional to the microscopic polarization.

1.2.3 Photon echo polarimetry

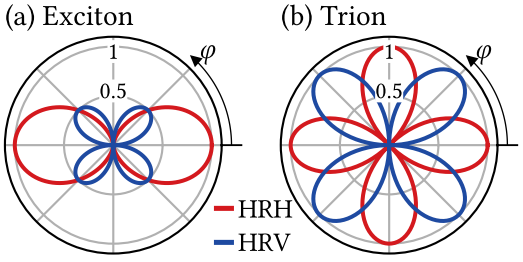

Figure 1.4: Polarimetric behavior of exciton (a) and trion (b) as described by the level schemes in Figures 1.1f and 1.1g within the PE polarimetry technique. The red and blue lines show the magnitude of the H and V polarized FWM signal as a function of the relative polarization angle φ between the first and second pulse, respectively.

A powerful degree of freedom in FWM spectroscopy is given by the relative polarization of the excitation pulses that allows to analyze polarization selection rules of the investigated optical resonance. The PE polarimetry technique, introduced in Reference [102], makes use of this degree of freedom to distinguish different excitonic complexes like excitons and trions in CdTe quantum wells. We actively apply the technique throughout the thesis to gain additional information

about excitons in perovskites and QDs. Here, we detect the horizontally (H) and vertically (V) polarized components of the PE amplitude as a function of the relative polarization angle φ between the horizontally polarized first pulse and second pulse. The choice of horizontal polarization for the first pulse is arbitrary since only the relative polarization angles are relevant. The two measurement routines are denoted as HRH and HRV, respectively. As an example, we compare the polarimetric behavior of trions and excitons with the dipole selection rules as depicted in Figure 1.1f and 1.1g. The theoretical polar dependences of the FWM signal fields in the configuration HRH and HRV are given by [102]

$$|E^{\mathrm{X}}_{\mathrm{HRH}}| \propto \cos^2(\varphi) \qquad |E^{\mathrm{X}}_{\mathrm{HRV}}| \propto \frac{1}{2}|\sin(2\varphi)| \tag{1.18a}$$

$$|E^{\mathrm{T}}_{\mathrm{HRH}}| \propto |\cos(2\varphi)| \qquad |E^{\mathrm{T}}_{\mathrm{HRV}}| \propto |\sin(2\varphi)|, \tag{1.18b}$$

with superscript X and T for exciton and trion. The dependences are visualized in Figures 1.4a and 1.4b in polar coordinates. We call these figures polar rosettes throughout the thesis.

Through the measurement in horizontal and vertical detection (HRH/HRV), we can also calculate the linear polarization angle of the signal φ_{S} and the total signal amplitude $|E_{\mathrm{tot}}|$ as given by

$$\varphi_{\mathrm{S}} = \arctan\left(\frac{E_{\mathrm{HRV}}}{E_{\mathrm{HRH}}}\right) \tag{1.19a}$$

$$|E_{\mathrm{tot}}| = \left(|E_{\mathrm{HRH}}|^2 + |E_{\mathrm{HRV}}|^2\right)^{1/2}. \tag{1.19b}$$

For the exciton, the signal polarization is directly set by the polarization angle of the second pulse, i.e. $\varphi_{\mathrm{S}} = \varphi$. Moreover, the total signal amplitude vanishes in cross-polarized configuration $\varphi = \pi/2$. This property intrinsically results from the fact that the two exciton transitions are not two independent TLS, but share a common ground state $|\mathrm{G}\rangle$. Thus, a population of one spin species also results in a nonlinear response from the second spin species as a consequence of the depletion of the ground state. Further, the superposition of the two excited states gives rise to a FWM response. For linearly cross-polarized excitation pulses, the multiple contributions to the FWM process cancel each other such that the total signal amplitude is zero. For the trion, consisting of two independent TLS instead, the total signal amplitude is fully independent of the polarization angle φ and the polarization angle of the signal is given by $\varphi_{\mathrm{S}} = 2\varphi$. Thus, the signal dependences in HRH and HRV are simply given by projections on the horizontal and vertical axis, as described by Equation (1.18b). Note that two configurations play an essential role in distinguishing between excitons and trions. For $\varphi = \pi/2$, only the trion gives a signal, while for $\varphi = \pi/4$, only the exciton gives a horizontally polarized signal. In Chapter 5, we make use of this property to independently study the FWM response of excitons and trions in an inhomogeneously broadened QD ensemble where the two resonances cannot be spectrally distinguished from each other.

1.3 Rabi rotations

Rabi rotations are a fundamental non-classical phenomenon of light-matter interaction that arises for field strengths strongly exceeding the limits of perturbation theory presented in the previous sections. Here, the coupling between the ground and excited state of a TLS, mediated by a nearly resonant optical field, reaches the regime of strong coupling which manifests in oscillations of the inversion of the system [95]. When applying a temporally limited optical field, i.e. a laser pulse, with a certain duration, strength, detuning, and optical phase, the system can be prepared in an arbitrary state. We are interested in the application of this approach to an inhomogeneously

broadened ensemble, where Rabi rotations have to be considered in a PE configuration. The relevant equations for Rabi rotations are presented in the following.

As for the derivation of the optical Bloch equations in Section 1.2, we start from the Hamiltonian that takes into account the dipole interaction between a TLS and an optical field of constant amplitude

$$\mathbf{H} = \frac{\hbar}{2}\begin{pmatrix} -\Delta & -\Omega_\mathrm{R} \\ -\Omega_\mathrm{R} & \Delta \end{pmatrix}, \tag{1.20}$$

formulated in the rotating frame. Here, $\Omega_\mathrm{R} = \mu E/\hbar$ denotes the Rabi frequency. We consider E as constant, spatially isotropic, and real in the following. This Hamiltonian is diagonal in the so-called dressed state base spanned by

$$|l\rangle = \frac{1}{\sqrt{2\Omega}}\left(\sqrt{\Omega-\Delta}|\mathrm{G}\rangle + \sqrt{\Omega+\Delta}|\mathrm{X}\rangle\right) \tag{1.21a}$$

$$|u\rangle = \frac{1}{\sqrt{2\Omega}}\left(\sqrt{\Omega+\Delta}|\mathrm{G}\rangle - \sqrt{\Omega-\Delta}|\mathrm{X}\rangle\right), \tag{1.21b}$$

where $\Omega = \sqrt{\Omega_\mathrm{R}^2 + \Delta^2}$ is the generalized Rabi frequency and the corresponding eigenvalues are given by $\pm\Omega/2$. The dressing of the energy states by the interaction with the light field is visualized in Figure 1.5a. Dashed lines show the energy states in the absence of the optical field in the rotating frame as a function of detuning. When turning on the optical field, the splitting between the upper and lower dressed state is given by Ω, which leads to an avoided crossing behavior at $\Delta = 0$, where the splitting is given by the Rabi frequency Ω_R. The dynamics of the independent density matrix elements in the dressed base are given by

$$p_\mathrm{uu}(t) = p_\mathrm{uu}(0), \quad p_\mathrm{lu}(t) = p_\mathrm{lu}(0)\exp(i\Omega t). \tag{1.22}$$

We expand these equations of motion when taking into account the interaction of QDs with acoustic phonons in Chapter 5.

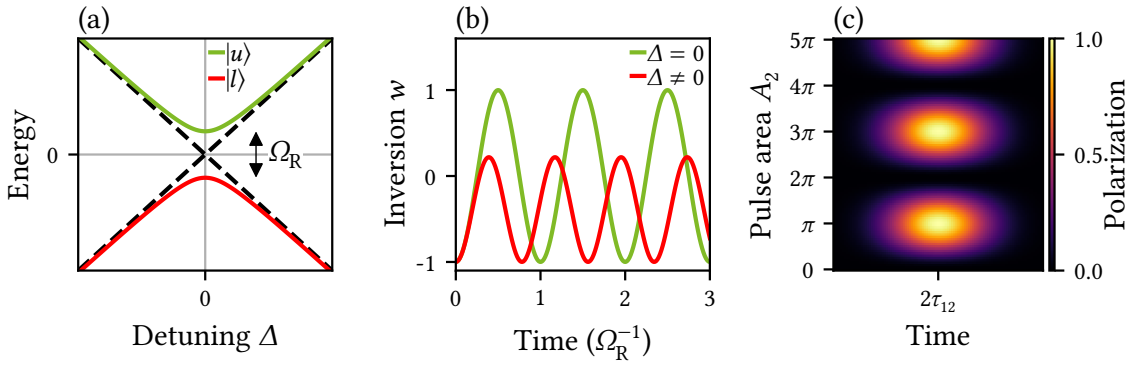

Figure 1.5: (a) Dressing of energy states of a TLS by interaction with a nearly resonant light field with constant magnitude. (b) Rabi oscillations of the inversion w of the two-level system for zero and non-zero detuning. (c) Manifestation of Rabi rotations in a PE protocol where the magnitude of the PE light pulse, centered at $2\tau_{12}$, oscillates as a function of the second pulse's area.

Transforming back to the undressed base leads to dynamics of both the polarization and occupation of the system. Those dynamics can be geometrically analyzed by introducing the Bloch vector with real entries

$$\begin{pmatrix} u \\ v \\ w \end{pmatrix} = \begin{pmatrix} p + p^* \\ i(p - p^*) \\ 2n - 1 \end{pmatrix}, \tag{1.23}$$

where u and v characterize the real and imaginary part of the complex-valued polarization and w is the real-valued inversion of the system. Using Equations (1.21), (1.22), and (1.23), the temporal evolution of the Bloch vector can be written as a matrix operation

$$\begin{pmatrix} u(t) \\ v(t) \\ w(t) \end{pmatrix} = \begin{pmatrix} \frac{\Omega_R^2+\Delta^2\cos(\Omega t)}{\Omega^2} & -\frac{\Delta}{\Omega}\sin(\Omega t) & -\frac{\Delta\Omega_R}{\Omega^2}[1-\cos(\Omega t)] \\ \frac{\Delta}{\Omega}\sin(\Omega t) & \cos(\Omega t) & \frac{\Omega_R}{\Omega}\sin(\Omega t) \\ -\frac{\Delta\Omega_R}{\Omega^2}[1-\cos(\Omega t)] & -\frac{\Omega_R}{\Omega}\sin(\Omega t) & \frac{\Delta^2+\Omega_R^2\cos(\Omega t)}{\Omega^2} \end{pmatrix} \begin{pmatrix} u(0) \\ v(0) \\ w(0) \end{pmatrix}. \tag{1.24}$$

As a special case, we consider the dynamic of the inversion $w(t)$ for a system that is initially in the ground state ($w(0) = -1$)

$$w(t) = -\frac{\Omega_R^2\cos(\Omega t) + \Delta^2}{\Omega^2}. \tag{1.25}$$

As plotted in Figure 1.5b for resonant excitation ($\Delta = 0$), the population inversion performs temporal oscillations between -1 and $+1$ at the Rabi frequency Ω_R (Rabi oscillations). For off-resonant excitation $\Delta \neq 0$, the oscillation frequency is faster but the system is not fully inverted, i.e. $w < 1$.

In general, the matrix in Equation (1.24) describes rotations of the Bloch vector as directly follows from the fact that the optical Bloch equations can be rewritten as a torque equation for the Bloch vector

$$\frac{d}{dt}\begin{pmatrix} u \\ v \\ w \end{pmatrix} = \begin{pmatrix} \Omega_R \\ 0 \\ \Delta \end{pmatrix} \times \begin{pmatrix} u \\ v \\ w \end{pmatrix}. \tag{1.26}$$

Thus, light geometrically acts as a torque on the Bloch vector and leads to a rotation by an angle of Ωt. When considering a rectangular light pulse, i.e. a constant optical field that is turned on for a finite time of t_p, the unitless quantity Ωt_p is called the pulse area A. For an arbitrarily shaped optical pulse, the pulse area is defined as

$$A = \int dt \Omega_R(t) \tag{1.27}$$

and measures the angle by which the Bloch vector is rotated on the Bloch sphere. For example, when probing the population of the excited state while scanning the pulse area, oscillations can be observed. To differentiate these pulse area-dependent oscillations from the time-dependent oscillations, we call them Rabi rotations.

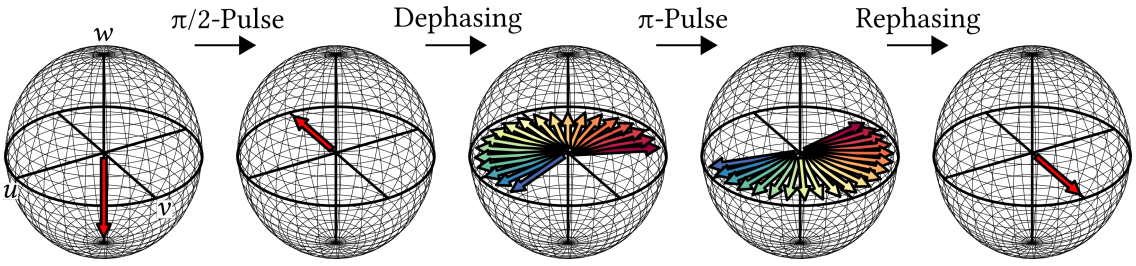

Figure 1.6: Vizualization of the ideal PE sequence in the regime of Rabi rotations. The first $\pi/2$ pulse excites all Bloch vectors to the equator plane. The subsequent dephasing dynamic is inverted by a second π pulse. A macroscopic polarization is thus reformed at twice the delay between the first and second pulse.

The effect of Rabi rotations on an inhomogeneously broadened ensemble of TLS can be observed in a PE sequence as is visualized in Figure 1.6. Here, the dynamics of the Bloch vectors are shown

on a sphere, which is called the Bloch sphere. For the PE, the ideal pulse sequence leading to a full reformation of macroscopical polarization consists of temporally separated $\pi/2$ and π pulses. The first pulse excites all Bloch vectors from the ground state ($w = -1$) to the equator plane of the Bloch sphere ($w = 0$), where the polarization is maximum. Subsequentially, the system dephases due to the different eigenfrequencies of the oscillators (represented by the different colors in Figure 1.6). Applying a π pulse inverts the phases of all oscillators which leads to a rephasing dynamic and a reformation of the macroscopic polarization. When sweeping the area of the first/second pulse (A_1/A_2), the amplitude of the PE oscillates as

$$E_{\mathrm{PE}} \propto \sin(A_1)\sin^2(A_2/2). \tag{1.28}$$

The oscillations of the amplitude of the PE pulse as a function of A_2 are visualized in Figure 1.5c. Equation (1.28) results from the assumption of short pulses with respect to the dephasing time of the ensemble, $t_p \ll T_2^*$. It should be noted that strong modifications of the temporal shape of the PE response can arise when the pulse duration is comparable to T_2^* [103], which is a key topic of Chapter 6.

2 Experimental methods

This chapter describes in detail the experimental setup for transient four-wave mixing (FWM) spectroscopy and provides relevant information about the studied material systems. The focus is set on the accurate description of the heterodyne technique (Section 2.1), which lies at the heart of the experimental method. Further, Section 2.2 describes a developed experimental approach to observe pronounced Rabi rotations using a flattop laser intensity profile. A description of the studied samples is given in Section 2.3.

2.1 Experimental setup for transient four-wave-mixing spectroscopy

A schematic picture of the experimental setup is shown in Figure 2.1. We use a mode-locked titan sapphire laser (MIRA900, Coherent) as a source of laser pulses that is optically pumped by a continuous wave laser providing 10 W at a photon energy of 2.33 eV (Verdi-V10, Coherent). Depending on two possible arrangements of the laser cavity, the MIRA900 delivers laser pulses with a duration of either ≈ 4 ps or ≈ 200 fs at a repetition rate of $f_{\mathrm{rep}} = T_{\mathrm{rep}}^{-1} = 75.75$ MHz, where $T_{\mathrm{rep}} \approx 13$ ns is the corresponding repetition period. The central photon energy of the laser pulses can be tuned between 1.13 eV and 1.77 eV. Using beam splitters, the pulses are split into the first, second, and third excitation pulses as needed for the three-pulse photon echo (PE) technique. A fourth part is used for the reference pulse that is needed for the time-resolved heterodyne detection as described below. Motorized delay lines are used to adjust the delays τ_{12}, τ_{13}, and τ_{ref} between all pulses relative to the first pulse. Here, the smallest temporal step is roughly 30 fs and the maximum temporal range covers the full repetition period T_{rep}. The FWM experiments are carried out in a non-colinear arrangement of the pulses, where however the optical paths of the second and third pulses are joined after passing the corresponding delay lines. In this way, the beams share the same wavevector $\mathbf{k}_2 = \mathbf{k}_3$ and thus the phase matching conditions of the three- and two-pulse PE are equal $\mathbf{k}_3 + \mathbf{k}_2 - \mathbf{k}_1 = 2\mathbf{k}_2 - \mathbf{k}_1$. The wavevectors of the first and second pulses correspond to angles of incidence on the sample of approximately 4° and 3°, respectively. The sample under study is placed in the variable temperature insert (VTI) of a helium bath cryostat, which is pumped to a pressure of roughly 15 mbar. At such pressures, helium reaches a superfluid phase with an approximate temperature of 1.5 K, which is the smallest temperature used in our experiments. Using a parabolic mirror with 50 cm focal length, the laser beams with an initial diameter of ≈ 3 mm are focussed down to a spot diameter of ≈ 100 µm on the sample surface. The FWM signal is captured in reflection geometry in the direction $2\mathbf{k}_2 - \mathbf{k}_1$ by the same parabolic mirror. Undesired reflections of the exciting pulses are blocked by an iris diaphragm. The signal beam and the reference beam are guided to the heterodyne detection scheme, whose working principle is explained in the following based on Reference [104].

The optical heterodyne technique relies on a measurement of the interference between a weak signal of interest $\mathcal{E}_{\mathrm{S}}$ at central optical frequency ω_{S} and a strong reference field $\mathcal{E}_{\mathrm{ref}}$ at frequency ω_{R}. Their interference contains a beating component at the difference frequency $\Delta\omega = \omega_{\mathrm{S}} - \omega_{\mathrm{R}}$ that

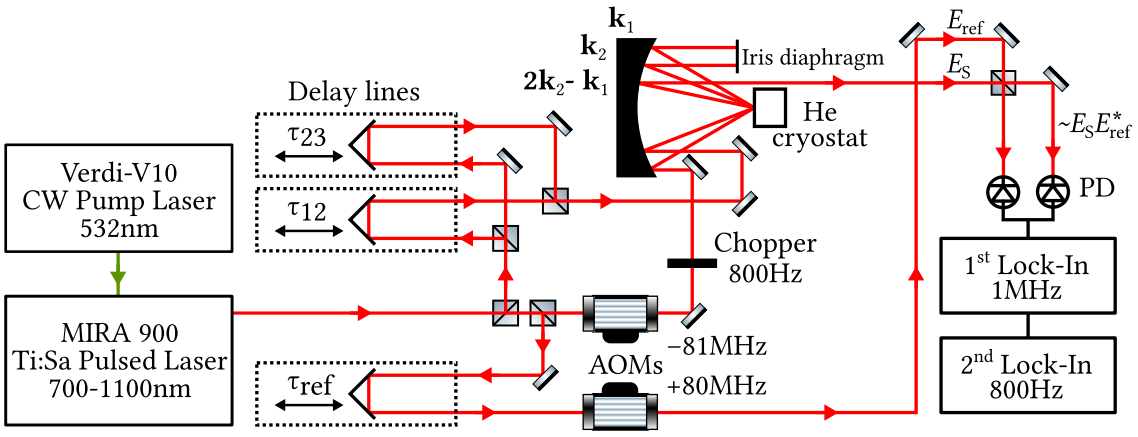

Figure 2.1: Scheme of the experimental setup for time-resolved four-wave-mixing spectroscopy as described in detail in the text. The scheme is adapted from [105]. Abbreviations: acousto-optical modulator (AOM), helium (He), photo-diode (PD).

is actively chosen to lie in the MHz-range. In this way, the beating signal can be resolved by slow photodetectors and subsequently filtered from noise components. Through the superposition with the strong reference beam, the beating component can strongly exceed the intensity of the original signal field. We show how exactly the magnitude and phase of the beating signal depend on signal and reference fields in the following. Both fields are pulse trains at a repetition rate of T_{rep}^{-1} and can be written as

$$\mathcal{E}_{\mathrm{S}} = \mathrm{e}^{i\omega_{\mathrm{S}}t+\varphi} \sum_{\mathrm{n}} E_{\mathrm{S}}(t - \mathrm{n}T_{\mathrm{rep}}) + \mathrm{c.c.} \tag{2.1a}$$

$$\mathcal{E}_{\mathrm{ref}} = \mathrm{e}^{i\omega_{\mathrm{ref}}(t-\tau_{\mathrm{ref}})} \sum_{\mathrm{n}} E_{\mathrm{ref}}(t - \tau_{\mathrm{ref}} - \mathrm{n}T_{\mathrm{rep}}) + \mathrm{c.c.}, \tag{2.1b}$$

where the arrival time of the reference pulses is shifted by τ_{ref} and signal and reference pulses may have in general a relative optical phase shift of φ. The functions $E_{\mathrm{S}}(t)$ and $E_{\mathrm{ref}}(t)$ denote the slowly varying temporal envelopes of each pulse within the pulse train. Note that the time domain description in Equations (2.1) is equivalent to a description in the frequency domain. In the frequency domain, the output of a mode-locked laser field is given by equidistant modes separated by the repetition rate of the laser f_{rep} multiplied with an envelope given by the Fourier transform of the temporal envelopes $E_{\mathrm{i}}(t)$. The signal and reference pulses are superimposed by a 50:50 non-polarizing beam splitter cube (see Figure 2.1), whose two output beams are focused on the two photo-diodes of a balanced photodetector (New Focus 2107). The output voltage of the balanced detector U_{PD} is proportional to the difference of photocurrents $\Delta I_{\mathrm{PD}} = I_{\mathrm{PD}}^{+} - I_{\mathrm{PD}}^{-}$ of the two diodes. As shown in Figure 2.1, the superposition in the beam splitter is arranged such that the intensities on the two photo-diodes are given by $|\mathcal{E}_{\mathrm{ref}} \pm \mathcal{E}_{\mathrm{S}}|^2$. The output voltage thus reads

$$\begin{aligned} U_{\mathrm{PD}} &\propto 2 \int_{T_{\mathrm{PD}}} \mathcal{E}_{\mathrm{S}} \mathcal{E}_{\mathrm{ref}}\, dt \\ &\propto \int_{T_{\mathrm{PD}}} dt\, \mathrm{e}^{i(\omega_{\mathrm{S}}-\omega_{\mathrm{ref}})t - i\omega_{\mathrm{ref}}\tau_{\mathrm{ref}} + i\varphi} \sum_{\mathrm{n}} E_{\mathrm{ref}}^{*}(t - \tau_{\mathrm{ref}} - \mathrm{n}T_{\mathrm{rep}}) E_{\mathrm{S}}(t - \mathrm{n}T_{\mathrm{rep}}) + \mathrm{c.c.}, \end{aligned} \tag{2.2}$$

where all terms that are oscillating at optical frequencies are neglected due to the slow integration time T_{PD} of the detector. The use of a balanced detection is advantageous since common noise components arising from the individual optical fields, especially from the strong reference beam

$\propto \mathcal{E}_{\mathrm{ref}}^2$, are suppressed while the beating term $\mathcal{E}_{\mathrm{S}}\mathcal{E}_{\mathrm{ref}}$ is doubled. Expression (2.2) can be further rearranged to

$$U_{\mathrm{PD}} \propto \int_{T_{\mathrm{PD}}} dt\, \mathrm{e}^{i(\omega_{\mathrm{S}}-\omega_{\mathrm{ref}})t - i\omega_{\mathrm{ref}}\tau_{\mathrm{ref}}+i\varphi} \int dt' E^*_{\mathrm{ref}}(t'-\tau_{\mathrm{ref}})E_{\mathrm{S}}(t') \sum_n \mathrm{e}^{i2\pi n\frac{t-t'}{T_{\mathrm{rep}}}}. \tag{2.3}$$

Here, it can be seen that filtering the signal at the beating frequency (or higher harmonics separated by the repetition rate of the laser) results in a signal, which is proportional to the cross-correlation between the reference and signal field envelopes

$$U_{\mathrm{PD}}^{\Delta\omega} \propto \mathrm{e}^{-i\omega_{\mathrm{ref}}\tau_{\mathrm{ref}}+i\varphi} \int dt E^*_{\mathrm{ref}}(t-\tau_{\mathrm{ref}})E_{\mathrm{S}}(t') + \mathrm{c.c.}\,, \tag{2.4}$$

where the integration over T_{PD} is negelcted due to $T_{\mathrm{PD}} \ll 1/\Delta\omega$. Scanning the arrival time of the reference beam thus allows temporally resolving the signal field, which is of major importance for disentangling homogenous and inhomogeneous decoherence times as explained in Section 1.2.1. Moreover, information about the relative optical phase φ between signal and reference is in principle preserved.

The desired frequency shift $\Delta\omega$ between reference and signal is achieved by introducing acousto-optical modulators (AOMs) in the paths of the first and reference beam, as indicated in Figure 2.1. AOMs rely on the Doppler-shifted signal upon diffraction of light on a propagating sound wave that is created in a glass material by a piezo-electric transducer. The AOMs shift the optical frequency components of the first and reference pulses to $\omega_1 = \omega_0 - 81\,\mathrm{MHz}$ and $\omega_{\mathrm{ref}} = \omega_0 + 80\,\mathrm{MHz}$, where ω_0 is the unshifted optical frequency. Here, the difference in sign of the two frequency shifts is realized by choosing the wavevector of the incoming light to have a component either in the same or opposite direction of the propagating sound wave. As a result of the frequency shift of the first pulse, the FWM signal has an optical frequency of $\omega_{\mathrm{S}} = 2\omega_2 - \omega_1 = \omega_0 + 81\,\mathrm{MHz}$, where $\omega_2 = \omega_0$ is the unshifted central frequency of the second pulse. The beating frequency between reference and signal pulses is thus given by $\Delta\omega = \omega_{\mathrm{S}} - \omega_{\mathrm{ref}} = 1\,\mathrm{MHz}$. Importantly, the two AOMs are driven by the same control unit, which provides an electric reference signal at the frequency $\Delta\omega$ as an additional output. This is important to subsequentially extract the beating signal from broadband noise components using lock-in methods.

We use the digital lock-in amplifier UHFLI 600MHz (Zurich Instruments). In general, a lock-in amplifier is capable of extracting a signal with a known frequency from a noise background whose frequency-integrated amplitude may be orders of magnitude stronger than the signal of interest. This is achieved by electronically multiplying the input signal $U_{\mathrm{PD}}(t)$ with a carrier wave $U_{\mathrm{C}}(t) \propto \cos(\omega_{\mathrm{C}}t)$ with frequency ω_{C}. When the carrier frequency ω_{C} is set to the desired frequency component of $U_{\mathrm{PD}}(t)$, the product contains a DC component that can be filtered from other components using a low-pass filter. It is important to point out that the output signal of a lock-in is sensitive to the relative phase θ between the signal wave and carrier wave as $U_{\mathrm{out}} \propto |U_{\mathrm{S}}|\cos(\theta)$, where $|U_{\mathrm{S}}|$ is the amplitude of the extracted frequency component. In this sense, the measured signal is also directly sensitive to the relative optical phases between reference, first, and second pulses as can be seen from Equation (2.4). Since the optical pathways between the involved beams in our experiments differ, the relative optical phases are not temporally stable. Instabilities arise for example because of air flux fluctuations or mechanical vibrations. To overcome this problem, we use a dual-phase lock-in amplifier. The dual-phase technique enables us to measure the relative phase between the signal and carrier wave, as well as the absolute value of the signal. By multiplying the signal separately with a sine and cosine carrier wave two outputs are created, commonly denoted as $X = R\cos(\theta)$ and $Y = R\sin(\theta)$. In this way, the magnitude R of the signal can be obtained from $R = \sqrt{X^2 + Y^2}$ and the phase between carrier and signal waves

from $\theta = \arctan(Y/X)$. Thus, the quantity R is not affected by phase fluctuations and therefore serves as the observable that is proportional to the magnitude of the electric field of the FWM signal. A phase-sensitive measurement of the FWM response requires active stabilization of the relative optical phases of the involved laser pulses, which is not considered in this thesis.

We make use of a double lock-in technique to isolate the signal from undesired noise components. The first lock-in operates at a frequency of 1 MHz as given by the AOM controller, followed by a short-pass filter with a bandwidth of roughly 1 kHz, which strongly minimizes the effect of electronic $1/f$ noise. Subsequentially, the output R_1 of the first lock-in serves as input for a second lock-in. The second modulation stage is necessary because of two reasons. First, in the case of imperfect sample surfaces, diffusively scattered light of the exciting beams may not be efficiently filtered by the iris diaphragm that is used to isolate the FWM response in the direction $2\mathbf{k}_2-\mathbf{k}_1$. Such scattering components of the i-th pulse with electric field E_i^sc result in beating terms $\propto E_\mathrm{i}^\mathrm{sc}E_\mathrm{ref}^*$. Those spurious beating terms can be spectrally broad and thus have components at the very same frequency as the desired beating term $\propto E_\mathrm{S}E_\mathrm{ref}^*$ with comparable amplitude. We cannot eliminate those frequency components by a single lock-in stage. The effect arises most strongly from scattered light of the second and third beam as they are spatially close to the PE response and temporally overlap more strongly with the reference pulse in the range of small values of τ_{12} in a two- or three-pulse PE experiment. To eliminate these spurious signals, we modulate the amplitude of the first beam using a mechanical chopper at a frequency of $f_\mathrm{ch} = 800\,\mathrm{Hz}$. The amplitude modulation creates frequency sidebands of the beating component $\propto E_\mathrm{S}E_\mathrm{ref}^*$ shifted by $\pm f_\mathrm{ch}$ from Δ_ω, while not affecting the spurious signals $\propto E_2^\mathrm{sc}E_\mathrm{ref}^*$ and $\propto E_3^\mathrm{sc}E_\mathrm{ref}^*$. The frequency f_ch serves as a reference for the second lock-in with a short pass filter of roughly 3.2 Hz bandwidth. In this case, the spurious beating components from the scattered light are effectively subtracted. By introducing a second chopper for the path of the second beam, spurious signals arising from the first beam could be filtered by setting the lock-in to the difference or sum frequency of the two choppers.

A second contribution to the remaining noise after the first lock-in stage is given by imperfect filtering of intensity fluctuations of the strong reference beam. Such contributions can result from an imperfect balance of the balanced detector, for example, because of unequal dynamical efficiencies of the photo-diodes or a non-perfect phase difference between the beating terms resulting from the two outputs of the beam splitter. Consequently, the reference creates broadband noise fluctuations which may have significant contributions at $\Delta\omega = 1\,\mathrm{MHz}$. In the same way as for the scattered light contributions, this offset signal is substracted by the chopper modulation of the first beam.

Even in the case of perfect balance, a finite random noise is present within the bandwidth of the first lock-in that typically scales with the intensity of the reference beam. This noise component introduces an intrinsic non-linearity in the detection scheme as is carefully considered in the following. Due to the aforementioned phase fluctuations, we have to use the amplitude output of the first lock-in stage R_1 as input for the second lock-in. We suppose that the dual-phase outputs X_1 and Y_1 of the first lock-in are Gaussian distributed with a mean value x_0 and standard deviation σ. Then $R_1 = \sqrt{X_1^2 + Y_1^2}/\sqrt{2}$ has a distribution strongly deviating from a Gaussian when x_0 and σ are comparable. In the limiting case of $x_0 = 0$, R_1 is distributed as

$$p(r) = \frac{2r}{\sigma^2}\exp\left(-\frac{r^2}{\sigma^2}\right). \tag{2.5}$$

The distributions of X_1 and R_1 are vizualized in Figure 2.2a. Here, the distribution of R_1 has a non-zero mean value of $\sqrt{\pi}\sigma/2$. For arbitrary values of x_0, R_1 has a mean value of $\sqrt{x_0^2 + \pi/4\sigma^2}$.

Thus, the noise component effectively introduces an offset which is however added in a nonlinear manner to the signal. When applying the double lock-in technique, this offset is linearly subtracted leading to the dependence of the mean value of R_2 of the second lock-in stage given by

$$R_2 = \left| \sqrt{x_0^2 + \frac{\pi\sigma^2}{2}} - \frac{\sqrt{\pi}\sigma}{2} \right|. \tag{2.6}$$

R_2 is thus only propotional to x_0 for $x_0 \gg \sigma$. We theoretically consider an example where the discussed nonlinearity of the detection scheme is relevant. We assume that the mean value $x_0 = \exp(-t/T)$ decays exponentially as a function of a parameter t with decay constant T shown by the black dashed line in Figure 2.2b. A random Gaussian noise with mean value zero and $\sigma = 0.01$ is added to X_1 and Y_1, which results in the green curve for R_1 in Figure 2.2b. The output of the second lock-in is shown in red. Here, the signal strongly deviates from the exponential decay starting from roughly $t \approx 3T$ before the signal reaches a reduced noise level defined by the bandwidth of the second lock-in. It is of major importance to be aware of such non-linearities when interpreting for example the decay of the two-pulse PE amplitude as a function of τ_{12}. To extract the decoherence time T_2, a linear regime of the detector has to be identified to avoid a systematic correlation between the decoherence time and signal amplitude. The influence of the nonlinearity can be minimized by choosing a longer time constant of the first lock-in which however enlarges the total measurement time. Since the PE signal is usually measured as a function of many parameters, a tradeoff between signal-to-noise ratio and total measurement time has to be made. Typically, a signal-to-noise ratio of at least 100:1 is achieved with the described filtering techniques.

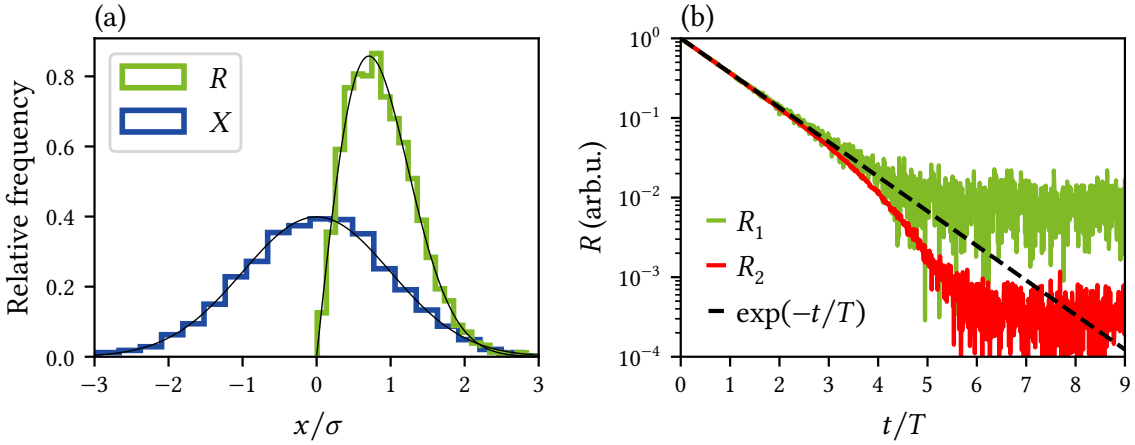

Figure 2.2: (a) Visualization of the distributions of X and R. (b) An example of the nonlinearity introduced by the double lock-in technique. The mean value of the signal (black) is assumed to decay exponentially with a time constant T. Adding a Gaussian noise results in the green and red curves for the outputs R_1 and R_2 of the first and second lock-in stages.

2.2 Realization of spatially flat laser pulses

As discussed in Section 1.3, Rabi oscillations refer to the time-dependent rotations of the Bloch vector when it is exposed to an optical field. When the optical field is in resonance with the two-level system, the frequency of the Rabi oscillations is given by $\Omega_R = \mu E/\hbar$, where μ is the dipole moment of the transition and E denotes the electric field amplitude of the optical field. A

direct manifestation of this phenomenon is given by intensity-dependent Rabi rotations when the two-level system (TLS) is excited by resonant laser pulses. Here, the final state of the Bloch vector is set by the pulse area A. In the PE experiment we can observe the effect of Rabi rotations in the form of oscillations of the PE amplitude as a function of the areas of the first and second pulse A_i according to

$$P \propto \sin(A_1) \sin^2\left(\frac{A_2}{2}\right). \tag{2.7}$$

Thus, the signal has local maxima for $A_1 = (2\mathrm{n}+1)\pi/2$ and $A_2 = (2\mathrm{n}+1)\pi$, where n is an integer. In the presented study, we focus on Rabi rotations as a function of the second pulse's area A_2. This choice is advantageous because of two reasons. First, the peak position of the echo emission is not influenced when sweeping A_2 and the Rabi oscillations can be analyzed at a fixed time delay of $\tau_{\mathrm{ref}} = 2\tau_{12}$ [62]. Second, because of the $\sin^2$ dependence in Equation (2.7), we can differentiate a decrease in the PE amplitude caused by the inhomogeneity of Rabi frequencies within the ensemble from a homogeneous excitation-induced decay of microscopic polarization. The former leads to a loss of contrast of the oscillation approaching a constant non-zero value, while the latter leads to a decay of the oscillation to zero without affecting the contrast.

One of the main problems in the observation of Rabi oscillations in intensity-dependent PEs from an ensemble of quantum dots (QDs) results from the Gaussian distribution of laser intensities within the finite spot size on the sample [62]. QDs that are located at the edges of the laser spot experience a smaller laser intensity compared to QDs in the center of the spot. The pulse area in Equation (2.7) therefore depends on the distance r from the center. The total signal measured by the interference of the signal field with the reference pulse may be written as

$$P \propto \int_0^\infty r\mathrm{e}^{-\frac{r^2}{\sigma^2}} \sin(A_1(r)) \sin^2(A_2(r)/2)\, dr, \tag{2.8}$$

where we assumed that all pulses (first, second, and reference) share the same radial symmetric Gaussian profile $A_i(r) \propto A_{i,0} \exp(-r^2/\sigma^2)$ with amplitude $A_{i,0}$ and width σ. The integration over the spatial coordinate r in Equation (2.8) thus represents an integration over a distribution of effective pulse areas, which results in a fading of the Rabi rotations, even when all QDs are identical and share the same dipole moment.

We aim to overcome the elaborated problem by introducing a more narrow distribution of intensities of the second pulse within the region of spatial overlap between the first and second pulse. The simplest realization of this condition relies on using a significantly larger spot diameter for the second beam such that the intensity is nearly constant in the region of spatial overlap, which was for example used in Reference [106]. In this case, however, a large portion of the available laser power is not used, which strongly limits the number of observable Rabi cycles. Therefore, a uniformly distributed intensity profile of the focussed beam is desired, which is ideally realized when using a flattop intensity profile for the second beam

$$E_2^{\mathrm{Flattop}}(r) = \begin{cases} E_{2,0} & r \leq R_0 \\ 0 & r > R_0 \end{cases}. \tag{2.9}$$

Here, the radius of the profile R_0 shall be chosen in the range of 100 µm comparable to the focussed Gaussian beam used in our experiments. The electric field distribution in the focus of a lens $E_{\mathrm{f}}(\mathrm{r})$ is given by the Fourier transform of the distribution before the lens $E_{\mathrm{in}}(\mathrm{r})$

$$E_{\mathrm{f}}(r) = \mathrm{FT}\left[E_{\mathrm{in}}(\rho)\right](r) = \int_0^\infty E_{\mathrm{in}}(\rho) J_0(2\pi r\rho)\rho \mathrm{d}\rho, \tag{2.10}$$

with the zero-order Bessel function of first kind J_0. A flattop intensity profile can be achieved by using an Airy disk pattern for $E_{\text{in}}(\text{r})$

$$E_{\text{in}}(r) \propto \frac{J_1(2\pi r)}{2\pi r} \tag{2.11}$$

where $J_1(r)$ is the first order Bessel function of the first kind. The task thus consists of realizing an approximation of the Airy disk pattern using the Gaussian beam provided by the laser system as an input.

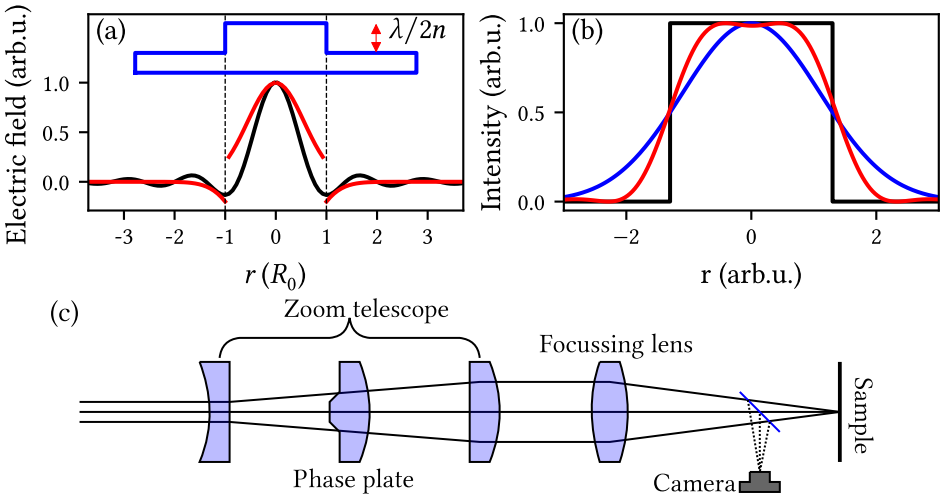

Figure 2.3: (a) Explanation of a simple realization of a focal refractive beam shaper. Here, a Gaussian beam passes an aspherical optical element (schematically sketched on top) with thicker width d within a radius R_0. The resulting radial electric field amplitude is shown in red in comparison to an Airy disk pattern (black). (b) Resulting radial intensity distribution in the focal plane from a Gaussian (blue), Airy disk pattern (black), and field distribution resulting from the refractive optical element described in (a) (red). (c) Schematic picture of the technical realization of the beam shaper AdlOptica Focal π-Shaper. Here, a similar refractive element as discussed in (a) and (b) is integrated into a zoom telescopic arrangement consisting of three lenses with adjustable distances. The resulting beam is focussed with a lens to the sample plane. To characterize the intensity profile, an optional mirror is introduced that guides the beam to a camera.

The Airy disk pattern for example results from the diffraction on a circular aperture that is sufficiently smaller than the width of the laser beam. Here, however, we meet again the problem that a big portion of the laser intensity is lost. Therefore, we aim to approximate the Airy disk pattern using refractive optics, which is a well-established approach in other fields of optics or engineering where flattop intensity profiles are needed [107, 108]. Refractive beam shapers that realize an Airy disk pattern are commercially available. In particular, we use the Focal π-Shaper 9HP from the company AdlOptica. The working principle of the shaper is briefly explained in the following. A simple refractive optical element that creates an approximation of the Airy disk pattern is given by an aspherical element whose thickness $d(r)$ as a function of distance r to the optical axis is given by

$$d(r) = \begin{cases} d_0 & r > R_0 \\ d_0 + N\frac{\lambda}{2n} & r \leq R_0 \end{cases}, \tag{2.12}$$

where d_0 is the thickness of the outer part ($r > R_0$), N is an odd number, λ is the wavelength of the laser beam, and n is the refractive index of the material. This binary phase plate is sketched in the top part of Figure 2.3a. The thickness of the thicker inner part ($r < R_0$) is chosen in such

a way that the phase of the radial electric field distribution within the radius R_0 is shifted by π relative to the outer part of the beam. Therefore, the sign of the electric field pattern is inverted. We show the resulting electric field of a Gaussian beam passing this phase plate in Figure 2.3a in comparison to the Airy disk pattern. Through the sign inversion of the wings of the Gaussian, the overshoot of the Airy disk is approximated. The resulting intensity profile in the focal plane, i.e. the absolute square of the Fourier transform of the electric field distributions in 2.3a, is shown in Figure 2.3b. For comparison, a Gaussian intensity profile is shown in red. It can be seen that the intensity profile from the phase plate exhibits a more flat intensity distribution in the inner part as well as sharper edges on the sides. More sophisticated refractive beam shapers optimize the discussed binary phase plate for a better approximation of the Airy disk. Here, a smoother transition between the inner and outer parts of the phase plate is chosen to prevent issues like overheating on the sharp edges, especially when using strong lasers. Furthermore, to optimize the beam pattern, the phase plate is integrated into a zoom telescopic arrangement as schematically shown in Figure 2.3c. Here, by shifting the relative distances between the three optical elements, the size of the input Gaussian beam relative to the size of the phase-shifting element can be adjusted. In this way, the flatness of the beam in the focal plane can be optimized. To precisely adjust the profile of the beam in the focal plane, the intensity profile in the focal plane has to be visualized. For this purpose, an optional mirror is introduced (Figure 2.3c) that guides the beams on a charge-coupled device (CCD) camera placed at the same distance as the sample plane.

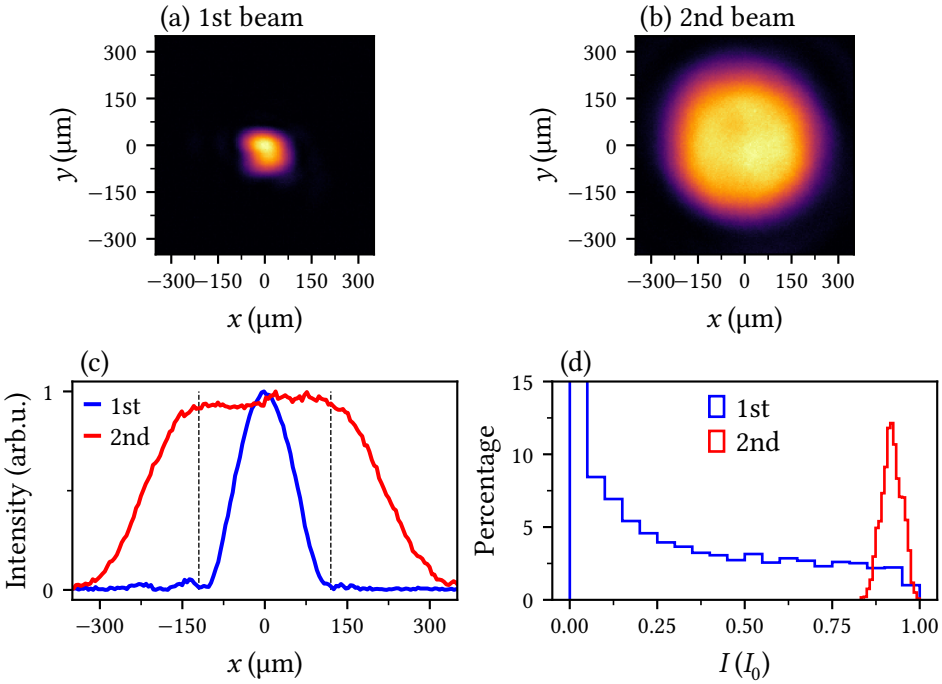

Figure 2.4: (a) Intensity profile of the first beam in the FWM experiment in the focal plane. The profile is approximately given by a 2D Gaussian distribution. (b) Intensity profile of the second beam, which was manipulated by the refractive beam shaper. (c) Cross-sections of the intensity distribution in (a) and (b) for $y = 0$. (d) Distribution of the intensities of the first and second beam within the region of spatial overlap, marked by vertical dashed lines in (c).

Figure 2.4a and 2.4b present the intensity profiles of the first and second beams that we use for the Rabi experiments. It can be seen that a more uniform distribution of the intensity profile in the inner part of the second beam is achieved. Figure 2.4c shows cross-sections of the two profiles for $y = 0$. The Gaussian profile of the first beam lies well inside the uniform part of the

flattop intensity profile of the second beam. To highlight the difference between the two intensity profiles, we examine the intensity distribution through histograms, as shown in Figure 2.4d. For the Gaussian profile, the area within which one can find the same intensities grows with the distance from the center of the spot. As a result, the intensities are distributed over the full range with an increasing trend towards zero. On the other hand, the shaped profile concentrates all intensities closely around a mean value near the maximum intensity I_0. By using a flat intensity profile for the second beam while keeping the first beam Gaussian, we expect to significantly reduce the damping of Rabi rotations as a function of A_2. The experimental results are presented in Chapter 5.

2.3 Description of samples

This section gives a brief description of the studied samples and how they were fabricated.

2.3.1 $MAPbI_3$ and $FA_{0.9}Cs_{0.1}PbI_{2.8}Br_{0.2}$ single crystals

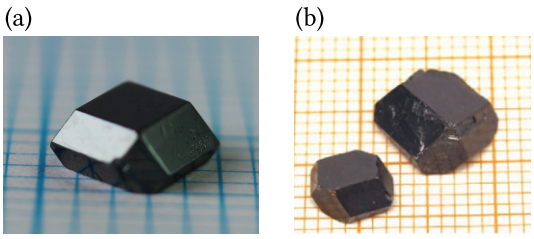

Figure 2.5: Images of (a) $MAPbI_3$ and (b) $FA_{0.9}Cs_{0.1}PbI_{2.8}Br_{0.2}$ single crystals. The lines on the paper below have a separation of 1 mm. The images are reprinted from References [63] and [109].

Figures 2.5a and 2.5b show images of the studied $MAPbI_3$ and $FA_{0.9}Cs_{0.1}PbI_{2.8}Br_{0.2}$ single crystals that were grown within the groups of Vladimir Dyakonov at the University of Würzburg and Maksym Kovalenko at ETH Zürich, respectively. Both crystals have sizes of roughly $3{\times}3\times2\,\mathrm{mm}^3$ and exhibit a black color. Facets of the crystals can be identified that correspond to diagonal planes of the cubic unit cell as discussed in Section 1.1. Both crystals are solution-grown. For the growth of the $MAPbI_3$ crystal, the components MAI and PbI_2 were dissolved in a solution consisting of γ-butyrolactone and an admixture of different alcohols. The solution was heated to a temperature of 85 °C, which led to the formation of perovskite crystals. For the growth of the $FA_{0.9}Cs_{0.1}PbI_{2.8}Br_{0.2}$ crystal, CsI, FAI, PbI_2, and $PbBr_2$ were dissolved in γ-butyrolactone and the growth temperature was set to 100 °C. A detailed description of the growth procedures of both systems can be found in References [110] and [109], respectively. The FWM experiments presented in Chapters 3 and 4 were performed in reflection geometry. To improve the surface quality of the crystals, the crystals were polished using a silk scarf and diamond dust.

2.3.2 (In,Ga)As quantum dot sample

A schematic side view of the studied (In,Ga)As quantum dot–cavity system is presented in Figure 2.6a. The sample was grown by molecular beam epitaxy within the research group of Sven Höfling at the University of Würzburg. A single layer of self-assembled quantum dots with a density of roughly $1.8\times10^9\,\mathrm{cm}^{-2}$ was grown through the deposition of InAs on GaAs using the Stranski-Krastanov method. Details of the growth mode can be found in Reference [112]. Figure 2.6b shows a scanning electron microscopy image of the quantum dots before the growth of additional layers. A silicon δ-layer is positioned 10 nm below the quantum dots within the

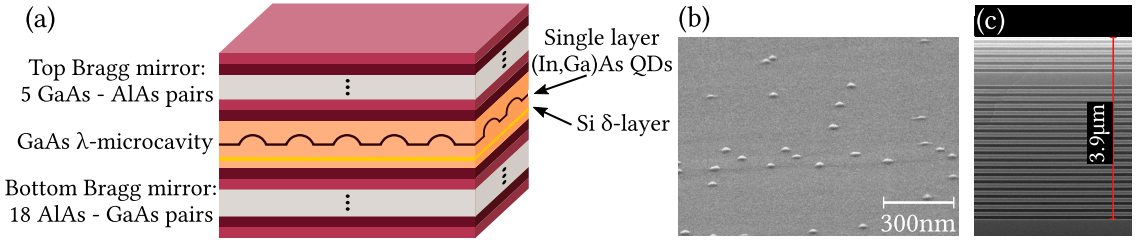

Figure 2.6: (a) Schematic side view of the quantum dot cavity system consisting of a single layer of self-assembled (In,Ga)As quantum dots embedded in a cavity formed by two AlAs GaAs distributed Bragg reflectors. A silicon δ-layer is used to form mainly charged quantum dots. Graphic from Reference [111]. (b) Scanning electron microscopy (SEM) image of the quantum dots before capping. (c) SEM image of the layers forming the DBRs for the cavity.

matrix material. It functions as an electron donor in the GaAs material, supplying electrons to form mainly charged quantum dots. An analysis of this property is given in Section 5.2. The quantum dots are placed in a λ-microcavity formed by two distributed Bragg reflectors (DBRs). These DBRs are formed by alternating layers of AlAs and GaAs with respective thicknesses of 82 nm and 68 nm. The top and bottom layers consist of five and eighteen layers of AlAs/GaAs pairs, respectively. A scanning electron microscopy image of the layers forming the cavity is presented in Figure 2.6c. The studied sample is a roughly $5\times5\,\mathrm{mm}^2$ piece of a round wafer that was rotated during the growth procedure. Therefore, the sample has a varying thickness that causes a radial gradient of the resonance energy of the cavity of roughly 5 meV/mm. As outlined in Reference [113], hill-like deformations of the cavity that are naturally self-aligned to the quantum dots can occur in the studied sample and further increase the light-matter coupling of the quantum dots. An optical characterization of the system using photoluminescence spectroscopy is given in Section 5.1.

Part I

Photon echo spectroscopy of organic-inorganic perovskites

Exciton coherence in $MAPbI_3$ and $FA_{0.9}Cs_{0.1}PbI_{2.8}Br_{0.2}$ – role of localization

3

The experiments presented in this chapter investigate the coherent optical properties of excitons in single crystals of $MAPbI_3$ and $FA_{0.9}Cs_{0.1}PbI_{2.8}Br_{0.2}$. In both samples, the exciton resonance is found to dominate the nonlinear spectrum. The transient four-wave mixing (FWM) signal is given by photon echos (PEs) which reveals the effect of crystallographic disorder. Applying the two- and three-pulse PE techniques, the decoherence time T_2 and the population decay time T_1 are extracted. For $MAPbI_3$, both values are found to be $\lesssim 1$ ps, whereas for $FA_{0.9}Cs_{0.1}PbI_{2.8}Br_{0.2}$, the relaxation times are by two orders of magnitude longer. By decomposing the decoherence time into contributions of pure decoherence and energy relaxation as a function of photon energy and temperature, signatures of exciton localization in the mixed crystal $FA_{0.9}Cs_{0.1}PbI_{2.8}Br_{0.2}$ are revealed that resemble the behavior of zero-dimensional systems with discrete energy spectra such as semiconductor quantum dots. The discrepancy found between ternary $MAPbI_3$ and quinternary $FA_{0.9}Cs_{0.1}PbI_{2.8}Br_{0.2}$ suggests that spatial fluctuations of the cation and halide content in mixed perovskites can lead to crystal potential fluctuations on the length scale comparable to the exciton Bohr radius. The results presented in this chapter were previously published in:

A. V. Trifonov, S. Grisard, A. N. Kosarev, I. A. Akimov, D. R. Yakovlev, J. Höcker, V. Dyakonov, and M. Bayer, "Photon echo polarimetry of excitons and biexcitons in a $CH_3NH_3PbI_3$ perovskite single crystal", ACS Photonics **9**, 621 (2022)
DOI: 10.1021/acsphotonics.1c01603, ©2022 American Chemical Society

S. Grisard, A. V. Trifonov, I. A. Solovev, D. R. Yakovlev, O. Hordiichuk, M. V. Kovalenko, M. Bayer, and I. A. Akimov, "Long-Lived Exciton Coherence in Mixed-Halide Perovskite Crystals", Nano Letters **23**, 7397 (2023)
DOI: 10.1021/acs.nanolett.3c01817, ©2023 American Chemical Society

3.1 Exciton coherence in $MAPbI_3$

As a first step of our study, we measure the FWM spectrum of the excitonic resonance in $MAPbI_3$ at a temperature of 1.5 K. Throughout the experiments, the sample is excited by the laser from the top surface which points towards the a-axis as characterized by X-Ray diffraction [110]. To gain high spectral resolution, we use the spectrally narrow picosecond pulses of the MIRA900 laser with a duration of 4 ps and spectral width of 0.3 meV. First and second pulses in the standard FWM geometry (Section 2.1) hit the sample simultaneously ($\tau_{12} = 0$) and the FWM response emitted in the direction $2\mathbf{k}_2 - \mathbf{k}_1$ is measured as a function of the central photon energy. The resulting spectral dependence, presented in Figure 3.1a, exhibits a broad resonance with full width at half maximum (FWHM) of 8 meV and a maximum at 1.639 eV. Both, peak position and width of the observed resonance are in agreement with those observed on the exciton resonance in Reference [42] where absorption spectroscopy was applied to a $MAPbI_3$ crystal revealing an exciton binding energy of roughly 10 meV [42]. Note that linear spectroscopic techniques such as

reflection and absorption spectroscopy do not allow to disentangle contributions of homogeneous and inhomogeneous broadening to the overall exciton linewidth. To address this issue, we make use of the time resolution of our FWM technique in the following. Throughout the rest of this section, we excite the sample at the maximum photon energy of 1.639 eV. Since the decoherence time is not resolved using the picosecond-pulses, we switch to the femtosecond regime of the Mira900 laser, which offers a higher temporal resolution. The spectrum of the 170 fs pulses has a FWHM of roughly 11 meV thus fully covering the exciton resonance.

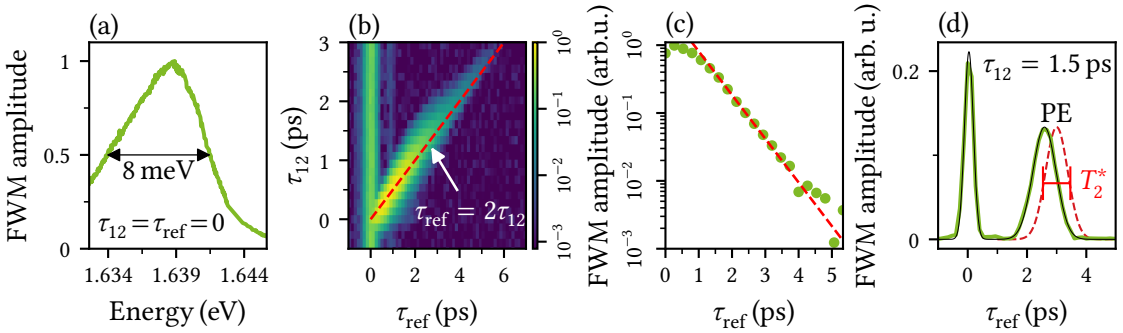

Figure 3.1: (a) FWM spectrum of the excitonic resonance in single crystal $MAPbI_3$ measured using the spectrally narrow picosecond-pulses. (b) Time-resolved FWM signal as a function of τ_{ref} and τ_{12} measured using the femtosecond-pulses. All pulses are linearly co-polarized. The red dashed line highlights the expected behavior of the PE $\tau_{ref} = 2\tau_{12}$. (c) Decay of the PE amplitude (green dots) and fit to a single exponential function (red line). (d) Temporal cross-section of the measured signal in (b) for $\tau_{12} = 1.5$ ps.

To analyze the temporal characteristic of the FWM response, we continuously scan the arrival time of the reference pulse for a set of values of the temporal gap τ_{12} between the first and second pulse. The resulting two-dimensional data set of the heterodyne signal is shown as a color map in Figure 3.1b. Here, the characteristic dependence of the PE following $\tau_{ref} = 2\tau_{12}$ can be observed as highlighted by the red dashed line. An additional signal at $\tau_{ref} = 0$, independent of τ_{12}, is an artifact from scattered light of the first pulse arising from an imperfect sample surface (as already discussed in Section 2.1). We can conclude that the exciton resonance in $MAPbI_3$ is inhomogeneously broadened. It is remarkable that even in a high-quality $MAPbI_3$ single crystal at 1.5 K, inhomogeneous broadening of the exciton transition represents a significant source of optical dephasing. The broadening might be associated with local crystal potential fluctuations potentially associated with random orientations of the organic cation. A discussion of this property within a broader context is given in the concluding section of this chapter.

To extract the homogeneous coherence time T_2, we consider the decay of the PE amplitude as a function of $\tau_{ref} = 2\tau_{12}$, as shown in Figure 3.1c. A fit to a single exponential, shown in red, results in $T_2 = (0.8 \pm 0.1)$ ps corresponding to a homogeneous exciton linewidth of $\Gamma_2 = 2\hbar/T_2 = 1.67$ meV. We note at this point that we reconsider the decay of the PE amplitude in Section 4.1.4 where we take the influence of the biexciton resonance into account. The deviation is here however of minor importance for the fitted value of T_2. To put the homogeneous broadening into context with the inhomogeneous broadening of the exciton ensemble, we analyze the temporal profile of the PE. Figure 3.1d shows a horizontal cross-section of the map in Figure 3.1b for $\tau_{12} = 1.5$ ps. The PE pulse is well described by a Gaussian with FWHM of (0.92 ± 0.12) ps. A deconvolution of the fitted curve from the temporal profile of the reference pulse results in the red dashed line. The width of the deconvoluted pulse corresponds to $T_2^* = (0.88 \pm 0.12)$ ps. Note that the PE peak position is shifted relative to $\tau_{ref} = 2\tau_{12} = 3$ ps. This effect occurs when the decoherence time

T_2 and dephasing time T_2^* are comparable since the temporal profile of the FWM response is described by

$$P(\tau_{\mathrm{ref}}) \propto \exp\left(-\frac{\tau_{\mathrm{ref}}}{T_2} - \frac{4\ln(2)(\tau_{\mathrm{ref}} - 2\tau_{12})^2}{T_2^{*2}}\right), \tag{3.1}$$

as previously discussed in Section 1.2.1. Consequently, the PE pulse has a maximum at

$$\tau_{\mathrm{ref}} = 2\tau_{12} - \frac{T_2^{*2}}{8\ln(2)T_2}, \tag{3.2}$$

which simplifies to $\tau_{\mathrm{ref}} = 2\tau_{12}$ in the limiting case of $T_2 \gg T_2^*$. Equation (3.2) predicts a constant shift of (0.18 ± 0.05) ps taking into account the aforementioned values of T_2 and T_2^*. From the fit using a Gaussian function, as shown by the black line in Figure 3.1d, we extract a shift of roughly (0.40 ± 0.02) ps. The deviation may be attributed to the influence of the biexciton resonance as will be discussed in Section 4.1.

An inhomogeneous broadening of the exciton transition due to crystallographic disorder may lead to spatial confinement of the exciton as a whole when the spatial extent of band gap fluctuations is comparable to the exciton Bohr radius. In this case, we expect an extended exciton population lifetime T_1. We therefore experimentally consider the population decay of the exciton in a three-pulse experiment. The second and third pulses share the same wavevector, such that the three- and two-pulse PE are emitted in the same direction $2\mathbf{k}_2 - \mathbf{k}_1$. Figure 3.2a visualizes the heterodyne signal as a function of τ_{12} and τ_{ref} for a fixed value of $\tau_{13} = 4.3$ ps. Here, we can observe the coexistence of two-pulse and three-pulse PE, where the two-pulse PE arising from the first and second pulse follows $\tau_{\mathrm{ref}} = 2\tau_{12}$ (red dashed line) and the three-pulse PE $\tau_{\mathrm{ref}} = \tau_{12} + \tau_{13}$ (white dashed line). The two-pulse PE arising from the interaction of the sample with the first and third pulse is not resolved in our experiments. The decay of the three-pulse PE as a function of $\tau_{\mathrm{ref}} = \tau_{12} + \tau_{13}$ for a fixed value of $\tau_{12} = 1$ ps is shown in Figure 3.2b. A fit to a single exponential gives the exciton population decay time $T_1 = (0.9 \pm 0.1)$ ps which is comparable to T_2.

The observed timescales are comparable to those found in other semiconductor structures such as GaAs, where excitons are effectively free [4]. Note that the decoherence time and population decay time in confined semiconductor systems such as (In,Ga)As semiconductor quantum dots lie in the order of 1 ns [64, 114]. Therefore, we conclude that excitons in the $MAPbI_3$ crystal are quasi-free, i.e. the characteristic length scale of band gap fluctuations that give rise to inhomogeneous broadening is significantly larger than the exciton Bohr radius. Although the exciton lifetime and coherence time are short, exciton-exciton interactions or the formation of multi-excitonic complexes such as trions or biexcitons may be favored by the effect of crystallographic disorder. We study this possibility in Section 4.1 by applying the PE polarimetry technique to the exciton resonance.

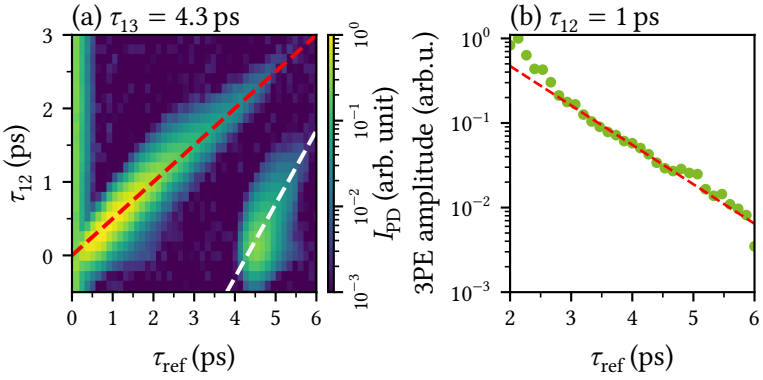

Figure 3.2: (a) Time-resolved heterodyne signal in a three-pulse PE experiment for a set of delays τ_{12} between first and second pulse. The delay between the first and third pulse is constant $\tau_{13} = 4.3$ ps. The dashed lines show the characteristic dependencies of the two- and three-pulse PE on the delay τ_{12}, as described in the main text. (b) Decay of the three-pulse PE amplitude as a function of $\tau_{\mathrm{ref}} = \tau_{12} + \tau_{13}$. Here, τ_{13} is scanned, while τ_{12} is set to 1 ps. The fit to a single exponential (red line) allows to extract the population decay time T_1.

3.2 Long-lived exciton coherence in $FA_{0.9}Cs_{0.1}PbI_{2.8}Br_{0.2}$

We commence our study of $FA_{0.9}Cs_{0.1}PbI_{2.8}Br_{0.2}$ following the same procedure as presented for $MAPbI_3$. In contrast to $MAPbI_3$, the transient FWM response of the quinternary alloy is well resolved using the picosecond-pulses of the MIRA900 that are applied throughout this section. Note that the use of spectrally narrow picosecond-pulses allows us to gain information about the homogeneous exciton linewidth with spectral resolution over the inhomogeneous broadening.

As a first step, we analyze the FWM spectrum of the $FA_{0.9}Cs_{0.1}PbI_{2.8}Br_{0.2}$ sample close to the band gap energy 1.52 eV as reported in Reference [115] for a crystal of the same composition. The spectral dependence is shown in Figure 3.3a where we observe an asymmetric lineshape with a peak at 1.515 eV. Here, the low energy part of the spectrum has a half width at half maximum (HWHM) of 8 meV, while the high energy part is significantly broader with a HWHM of 23 meV. Thus, the total FWHM amounts to 31 meV. The width on the low energy side coincides with the result of photoluminescence excitation (PLE) spectroscopy performed in Reference [115], whereas the broad high energy tail may be influenced by contributions from excited exciton states, which are not resolved in PLE. The large width as well as the asymmetry of the spectrum hint at a dominant contribution of inhomogeneous broadening [116]. The presence of inhomogeneous broadening of the exciton line can be confirmed by introducing a delay of $\tau_{12} = 26.5$ ps between the first and second pulse with a photon energy of 1.515 eV. In this case, as presented in Figure 3.3b, the FWM response of the sample is given by a PE pulse. The pulse is well described by a Gaussian function centered at $\tau_{\mathrm{ref}} = 2\tau_{12} = 53$ ps with a FWHM of 9 ps. A deconvolution of the fitted Gaussian from the temporal profile of the reference pulse is shown by the red curve in Figure 3.3b, revealing a FWHM of 7.5 ps of the PE pulse. Note that the laser spectrum with a width of 0.3 meV is narrower than the inhomogeneously broadened exciton resonance. Therefore, the duration of the PE pulse is approximately given by the duration of the laser pulses (6.5 ps associated with the FWHM of the electric field envelope).

Figure 3.3c presents the result of a T_2 measurement at a photon energy of 1.515 eV using the two-pulse PE. The two-pulse PE amplitude follows a single exponential decay $\propto \exp(-2\tau_{12}/T_2)$ with $T_2 = (83 \pm 1)$ ps corresponding to a narrow Lorentzian homogeneous line with FWHM of $\Gamma_2 = 2\hbar/T_2 = (15.9 \pm 0.2)\,\mu$eV. The FWM spectrum shown in Figure 3.3a is thus dominantly

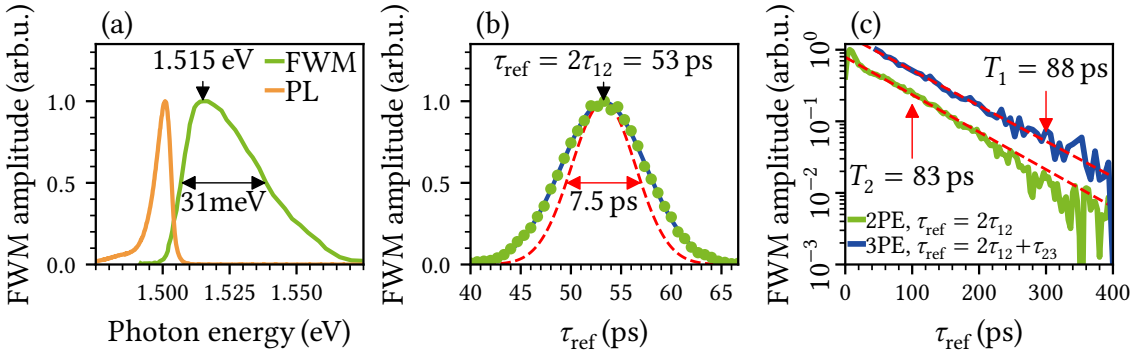

Figure 3.3: (a) FWM spectrum of the $FA_{0.9}Cs_{0.1}PbI_{2.8}Br_{0.2}$ crystal. Arrows indicate the peak position and FWHM. For comparison, we show the photoluminescence (PL) spectrum. (b) Time-resolved PE pulse, measured for $\tau_{12} = 26.5$ ps. The blue line is a fit to a Gaussian function, the red line is the calculated deconvolution from the reference pulse envelope. (c) Decays of the two- and three-pulse PE (2PE/3PE). Both decays are measured at a photon energy of 1.515 eV at $T = 1.5$ K. The dashed red lines represent fits to single exponential functions.

inhomogeneously broadened. In particular, the inhomogeneous broadening exceeds the homogeneous broadening by three orders of magnitude. It is remarkable that the coherence time of excitons in the $FA_{0.9}Cs_{0.1}PbI_{2.8}Br_{0.2}$ crystal is by two orders of magnitude longer as compared to the measured value in the ternary perovskite crystal $MAPbI_3$ presented in the previous section ($T_2 = 0.9$ ps). Instead, the observed value resembles results obtained in low-dimensional perovskites systems such nanocrystals of $CsPbBr_2Cl$ ($T_2 \approx 25$ ps measured at 5 K in Reference [117]) or $CsPbI_3$ ($T_2 \approx 10$ ps at 3 K in Reference [118]).

The long coherence time suggests a reduced interaction of excitons with their environment, which may be attributed to the localization of excitons in potentials formed by spatial fluctuations of the crystal composition. This idea is also encouraged by transient photoluminescence (PL) measurements published in Reference [119]. Here, it is found that the time-integrated PL, appearing at the low energy side of the exciton transition (shown in Figure 3.3a for comparison), is dominated by slow recombination dynamics of separately localized electrons and holes. We aim to understand if such localization sites give also rise to the localization of excitons as a whole which would explain the long-lived exciton coherence. Coherent laser spectroscopy was successfully used in the past to study various semiconductor systems that are subject to compositional or geometric disorder, such as GaAs/(Al,Ga)As quantum wells that exhibit spatial fluctuations of the well width [21]. Spatial disorder can lead to exciton localization and, consequently, to a reduction in their mobility accompanied by a narrowing of the homogeneous linewidth. Localized excitons in mixed semiconductor crystals were studied in a variety of semiconductors such as the II-VI alloys CdS_xSe_{1-x} [20, 120] or $ZnSe_{1-x}Te_x$ [121, 122]. The formation of quantized energy levels due to exciton localization in three dimensions can lead to a drastic reduction of phonon-assisted energy relaxation [123–127]. Further, the relative importance of purely elastic scattering events can be enhanced by the localization [54, 116, 128].

Figure 3.4 summarizes potential mechanisms that affect the decoherence of localized excitons in a spatially modulated potential energy landscape. As discussed in Section 1.2, the decay of coherence is mediated by both elastic and inelastic scattering events. The former is manifested in the population decay time T_1, the latter in the pure decoherence time T_2', such that $1/T_2 = 1/2T_1 + 1/T_2'$. The population decay time T_1 includes contributions of energy relaxation and recombination of excitons. The energy relaxation on a timescale τ_ε, case (i) in Figure 3.4, may result from the tunneling of excitons between localization sites of different energy or the relaxation

to lower energy levels within a single localization site. For excitons in the lower energy states, the population decay time is limited by the finite lifetime through the exciton recombination or non-radiative dissociation of electron and hole on a timescale τ_r, case (ii). Thus, the exciton population decay time can be written as

$$\frac{1}{T_1} = \frac{1}{\tau_\varepsilon} + \frac{1}{\tau_r}. \tag{3.3}$$

Pure decoherence processes involve, for example, elastic scattering events with phonons, as we show in case (iii) in Figure 3.4. Here, the exciton is excited to and deexcited from a virtual state, which leaves the energy and population unaffected, but changes the phase of the exciton wave function. We aim to quantify the discussed mechanisms to the exciton decoherence in the following.

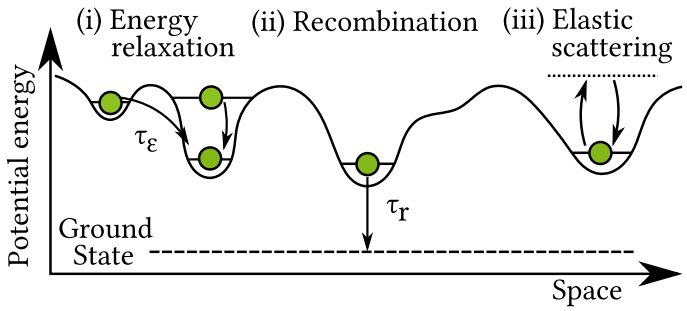

Figure 3.4: Visualization of possible contributions to the exciton linewidth in the context of localized excitons in a random potential. The population decay time T_1 involves contributions of (i) energy relaxation and (ii) recombination. Elastic scattering events as shown in (iii) represent a pure decoherence mechanism and only contribute to T_2.

We decompose the coherence time T_2 into contributions arising from population decay and purely elastic scattering. Therefore, we measure the decay of the three-pulse PE centered at $\tau_{ref} = 2\tau_{12} + \tau_{23}$ for a fixed value of $\tau_{12} = 20\,\text{ps}$. The three-pulse PE amplitude, shown in Figure 3.3c by a blue line, decays exponentially with $T_1 = (88 \pm 3)\,\text{ps}$. The measured value for $T_2 = (83 \pm 1)\,\text{ps}$ at a photon energy of 1.515 eV is noticeably smaller than $2T_1 \approx 176\,\text{ps}$ (as expected in lifetime limited case $T_2 = 2T_1$), which demonstrates a significant contribution of pure decoherence mechanisms. Using Equation (1.6), we obtain a value of $T_2' = (158 \pm 6)\,\text{ps}$ and the contribution to the homogeneous linewidth $\Gamma_2' = 2\hbar/T_2' = (8.3 \pm 0.3)\,\mu\text{eV}$. To gain insight into the origin of pure decoherence, we perform a temperature-dependent measurement. Figure 3.5a shows two contributions arising from pure decoherence rate Γ_2' and population decay rate $\Gamma_1/2 = \hbar/T_1$ as a function of temperature. In this representation, the sum of these quantities determines the homogeneous linewidth of the exciton $\Gamma_2 = 2\hbar/T_2$ (Equation (1.6)). The right axis in Figure 3.5a shows the corresponding inverted scale for the decay times. We observe that the pure decoherence rate Γ_2' grows faster compared to $\Gamma_1/2$ in a non-linear manner from 8 µeV at 1.5 K to 130 µeV at 10 K. $\Gamma_1/2$ in turn does not experience a significant rise and remains below 20 µeV in the observed temperature range. This observation is in agreement with the localization of excitons since the discrete energy spectrum of the localized excitons suppresses their energy relaxation, and in particular activation of higher energy states via phonon absorption. Such processes would lead to a rise of Γ_1 with increasing temperature [125, 126]. Pure elastic scattering events involving phonons in turn are more important for localized excitons due to the enhanced spread of the exciton wavefunction in momentum space [128]. In this way, pure decoherence is enhanced by the increasing phonon population with temperature.

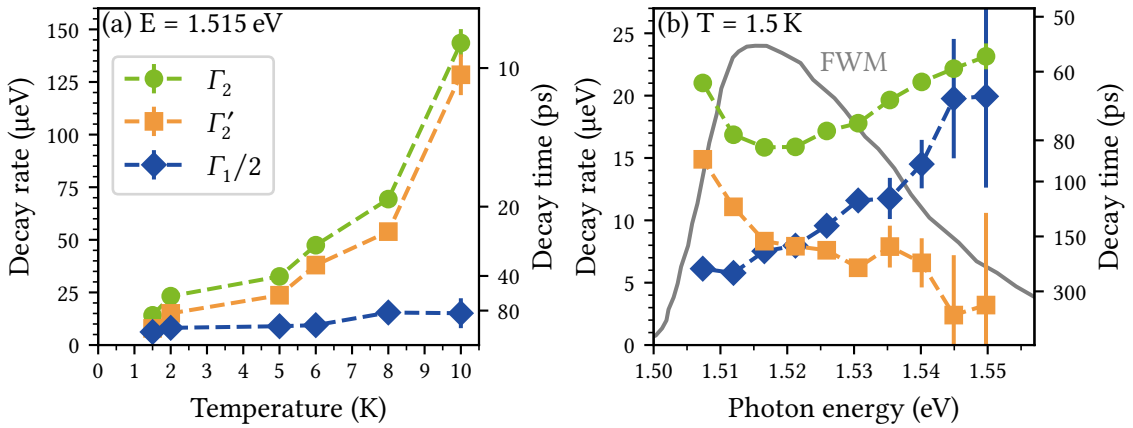

Figure 3.5: (a) Contributions to the homogeneous exciton linewidth $\Gamma_2 = 2\hbar/T_2$ associated with the population decay rate $\Gamma_1/2 = \hbar/T_1$ and pure decoherence rate $\Gamma_2' = 2\hbar/T_2'$ as a function of temperature, measured at a photon energy of 1.515 eV. Here, Γ_2 and Γ_1 result from the measurement of the PE decay as a function of τ_{12} and τ_{23}, respectively, whereas Γ_2' is calculated using Equation (1.6). (b) Dependence of Γ_2, $\Gamma_1/2$, and Γ_2' on the central photon energy of the ps-laser pulses, measured at a temperature of 1.5 K. The solid line shows the FWM spectrum for comparison in arbitrary units.

To address exciton states with different energies, we measure a spectral dependence of the exciton linewidth. Within an ensemble of excitons localized by compositional fluctuations, excitons contributing to the low energy side of the spectrum are stronger localized compared to excitons that contribute the high energy side. In Figure 3.5b we plot results for Γ_1 and Γ_2' as a function of the laser photon energy, measured at a temperature of 1.5 K. The FWM spectrum is shown in the same graph for orientation. We observe that the contribution of population decay to the homogeneous linewidth $\Gamma_1/2$ monotonically increases towards higher energies from roughly 5 μeV to 20 μeV, while the pure decoherence rate Γ_2' gradually decreases from 15 μeV to 3 μeV and becomes significantly smaller than $\Gamma_1/2$. Such behavior leads toward the limiting case at higher energies where the homogeneous linewidth is determined by the population decay, i.e. $\Gamma_2 = \Gamma_1/2 \approx 23$ μeV.

These observations are in agreement with the aforementioned correlation between the efficiency of energy relaxation and pure decoherence mechanisms for excitons with different degrees of localization. In particular, a decrease of the pure decoherence rate Γ_2' with increasing photon energy demonstrates that excitons with higher energies possess a smaller degree of localization because the elastic phonon scattering mechanism is significantly reduced (case (iii) in Figure 3.4). In contrast, the energy relaxation rate $1/\tau_\varepsilon$ is negligible for excitons in low-energy states due to the absence of lower energy states that can be accessed via phonon emission [124, 129]. Therefore, the population decay time measured on the low energy side of the spectrum at 1.510 eV, $T_1 = (108 \pm 4)$ ps, is the best estimate for the exciton lifetime τ_r, which takes place due to exciton recombination (case (ii) in Figure 3.4). At higher energies, the role of confined exciton states with larger quantum number as well as hopping of weakly localized excitons into the deeper potential sites accompanied by phonon emission starts to play an important role, i.e. $1/\tau_\varepsilon$ dominates the population decay rate (case (i) in Figure 3.4). In conclusion, we thus indeed find agreement between the expectations of the picture of excitons confined in a random potential and the measured temperature and energy dependences.

As a final step, we combine the results from the spectral and temperature dependencies to estimate the relevant size of exciton localization sites. For this purpose, we assume that the excitons are localized in a spherically symmetric potential well $V(r)$ with finite height U and diameter d

$$V(r) = \begin{cases} -U & r \leq \frac{d}{2} \\ 0 & r > \frac{d}{2}, \end{cases} \tag{3.4}$$

which is a well-known model from basic quantum mechanics in three dimensions [130]. The allowed energy levels ε_n in such potential have to obey the equation

$$\tan(z_\mathrm{n}) = -\frac{1}{\sqrt{\frac{z_0^2}{z_\mathrm{n}} - 1}}, \quad z_\mathrm{n} = \frac{\sqrt{2m(U+\varepsilon_\mathrm{n})}d}{2\hbar}, \quad z_0 = \frac{\sqrt{2mU}d}{2\hbar}, \tag{3.5}$$

where $m \approx 0.5m_0$ is the exciton mass [131–133]. Our best estimate for the mean depth of the potential is given by the inhomogeneous broadening of the exciton resonance $U = 16\,\mathrm{meV}$. At least one bound solution of Equation (3.5) can be found for all $z_0 \geq \pi/2$, which leads to a lower bound of the potential diameter [5]

$$d \geq \pi\hbar/\sqrt{2mU} \approx 7\,\mathrm{nm}. \tag{3.6}$$

An upper bound can be estimated from the following observation: Under resonant excitation with a photon energy of 1.515 eV, we do not observe the activation of higher energy states up to a temperature of 10 K, which would result in a significant rise of Γ_1 in Figure 3.5b. This means that the energy distance to the next higher-lying confinement state is larger than $k_\mathrm{B} \cdot 10\,\mathrm{K} \approx 1\,\mathrm{meV}$, where k_B is the Boltzmann constant. Using this value as the minimal energy spacing Δ_min between the two lowest states of excitons confined in the spherical potential, we can estimate the maximum diameter of the potential well. Taking into account that the potential height $U \approx 16\,\mathrm{meV}$ is significantly larger than Δ_min, we can approximate $z_1 \approx \pi$ and $z_2 \approx 2\pi$ in Equation (3.5), which leads to the upper bound

$$\varepsilon_2 - \varepsilon_1 = \frac{6\pi^2\hbar^2}{md^2} \geq \Delta_\mathrm{min} \Leftrightarrow d \leq \pi\hbar\sqrt{6/\Delta_\mathrm{min}m} \approx 95\,\mathrm{nm}. \tag{3.7}$$

Therefore, we estimate that potential fluctuations with a magnitude of about 16 meV take place in the $FA_{0.9}Cs_{0.1}PbI_{2.8}Br_{0.2}$ crystal on a scale of 7 nm to 95 nm.

3.3 Conclusions

This chapter presented two of the first applications of coherent spectroscopy to excitons in single crystals of organic-inorganic perovskites. The observation of photon echoes revealed the importance of crystallographic disorder on the transition energy of excitons in high-quality perovskite single crystals at cryogenic temperatures. As already mentioned in Section 1.1, the rotational degree of freedom of the organic cation introduces a possible source of spatial fluctuations of the band gap that may contribute to the large inhomogenous broadening in the order of 10 meV in both $MAPbI_3$ and $FA_{0.9}Cs_{0.1}PbI_{2.8}Br_{0.2}$. The drastic difference in exciton coherence times, $\approx 0.8\,\mathrm{ps}$ in $MAPbI_3$ versus $\approx 80\,\mathrm{ps}$ in $FA_{0.9}Cs_{0.1}PbI_{2.8}Br_{0.2}$, highlights that potential energy fluctuations in the two studied systems appear on different length scales. In the latter case, excitons show clear signatures of zero-dimensional systems in both energy and temperature dependences which demonstrates that excitons are confined as a whole and thus

exhibit extended coherence times. This observation suggests that random fluctuations of the alloy content in $FA_{0.9}Cs_{0.1}PbI_{2.8}Br_{0.2}$ introduce an additional mechanism that can lead to band gap fluctuation on the nanometer scale. To gain full insight into the microscopic origin of spatial disorder in mixed perovskite semiconductors, detailed studies of the exciton coherence time as a function of alloy composition are needed. In conclusion, the results presented in this chapter prove that coherent spectroscopy of excitons can provide valuable information about the non-trivial structural properties of organic-inorganic perovskites.

Spin-dependent exciton interactions in $MAPbI_3$ and $FA_{0.9}Cs_{0.1}PbI_{2.8}Br_{0.2}$

4

This chapter focusses on the role of exciton interactions in $MAPbI_3$ and $FA_{0.9}Cs_{0.1}PbI_{2.8}Br_{0.2}$. In both crystals, pronounced deviations from the assumption of non-interacting excitons are found in the dependences on the polarization of the exciting laser fields. For $MAPbI_3$ (Section 4.1), these deviations are found to be a result of the formation of biexcitons, a bound state of two excitons with opposite spins, upon excitation with broadband femtosecond-pulses. The biexciton binding energy of 2.4 meV is extracted using polarization beats of the photon echo. In the case of $FA_{0.9}Cs_{0.1}PbI_{2.8}Br_{0.2}$ (Section 4.2), strong deviations of the nonlinear exciton polarization selection rules as well as a polarization-dependent power dependence of the homogeneous linewidth are found to be a result of spin-dependent excitation-induced dephasing.

4.1 Biexciton formation in $MAPbI_3$

In this section, we observe the formation of a biexciton complex in $MAPbI_3$ for which we make use of quantum beatings of the PE polarization state. A detailed modeling of the transient polarization dependences of the exciton-biexciton system enables us to develop an experimental protocol to measure the biexciton binding energy of 2.4 meV. Remarkably, the presented approach allows us to measure the biexciton binding energy although the beating period is shorter than the exciton and biexciton decoherence times. Throughout this section, the exciton resonance in $MAPbI_3$ is resonantly excited at 1.639 eV using the femtosecond-pulses of the MIRA900 laser (FWHM 170 fs, 11 meV spectral width). The sample is cooled down to 1.5 K.

4.1.1 Photon echo polarimetry

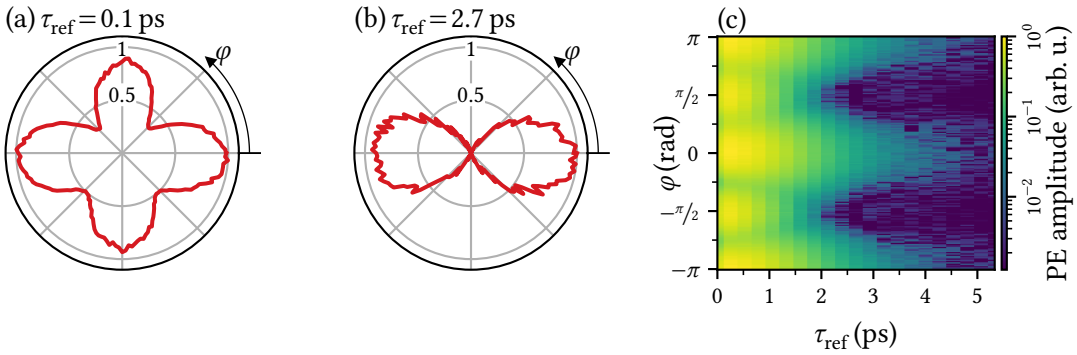

Figure 4.1: (a)/(b) Experimental polar rosettes, i.e. photon echo (PE) amplitude as a function of the linear polarization angle φ between first and second pulse, for two different values of $\tau_{ref} = 2\tau_{12}$ as indicated in the subfigure titles. (c) Measurement of the rosettes shown in (a) and (b) for a set of τ_{ref} values.

As discussed in Section 1.2.3, the PE polarimetry technique reveals the formation of multi-excitonic resonances such as charged excitons (trions) even when the inhomogeneous broadening exceeds the energetic splitting between such complexes and the single exciton resonance [63, 102]. For example, the dependence of the horizontally polarized component of the PE amplitude on the relative linear polarization angle φ between the horizontally polarized first pulse and second pulse (configuration referred to as HRH) allows us to conclude on the underlying energy level arrangement with corresponding dipole selection rules.

Interestingly, we observe that the qualitative shape of the measured rosettes in the HRH configuration in the studied $MAPbI_3$ sample depends on the temporal delay between the first and second pulse as presented in Figure 4.1a and 4.1b. For $\tau_{\mathrm{ref}} = 0.1\,\mathrm{ps}$, we observe a four-leave polar rosette with local maxima in the configurations HHH and HVH whereas for $\tau_{\mathrm{ref}} = 2.7\,\mathrm{ps}$, we only see two local maxima for co-polarized first and second pulse (HHH). To quantify this temporal dependence, we measure the rosettes for a series of delays and present the result as a color map in Figure 4.1c. The transition between a four- and two-leave behavior results from a faster decrease of the signal in HVH configuration on a time scale of approximately 0.5 ps. For a bare exciton resonance with a V-type energy level arrangement, as shown in Figure 4.2a, the continuous dependence of the PE signal on the angle φ reads as $\cos^2(\varphi)$ (Figure 4.2b). A signal in the configuration HVH is consequently not allowed. The observation in Figure 4.1c therefore represents a strong hint that on a short timescale of 0.5 ps, a multi-excitonic complex contributes to the coherent response of the $MAPbI_3$ crystal. Note that we use the linear polarization basis for the optical transitions in all the level schemes that we discuss within this section as it simplifies the discussion of the polarization dependences of the biexciton system (shown below).

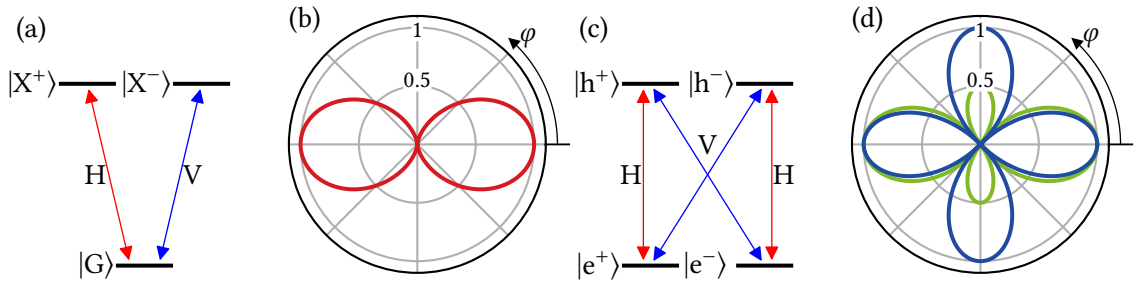

Figure 4.2: (a) Energy level scheme of the exciton with allowed optical transitions in linear polarization base. Here, $|\mathrm{G}\rangle$ is the ground state of the crystal and $|\mathrm{X}^{\pm}\rangle = 1/\sqrt{2}(|\mathrm{X}^{\uparrow}\rangle \pm |\mathrm{X}^{\downarrow}\rangle)$ are constructed from the optically bright spin up/down states $|\mathrm{X}^{\uparrow\downarrow}\rangle$ of the exciton. (b) Expected polar rosette for the exciton level scheme in (a). (c) Scheme of the trion, where $|\mathrm{e}^{\pm}\rangle = 1/\sqrt{2}(|\mathrm{e}^{\uparrow}\rangle \pm |\mathrm{e}^{\downarrow}\rangle)$ and $|\mathrm{h}^{\pm}\rangle = 1/\sqrt{2}(|\mathrm{h}^{\uparrow}\rangle \pm |\mathrm{h}^{\downarrow}\rangle)$ are ground states of the system with a resident electron with spin up/down and excited trion states with hole spin up/down. (d) Expected polar rosette of the trion scheme (blue) and interference of exciton and trion (green) as described in the text.

Taking into account recent studies of resident carrier spin dynamics in similar lead-halide perovskite materials [115, 134], it is a realistic scenario that trions may be formed spectrally close to the free exciton. For the trion with a four-level energy arrangement as shown in Figure 4.2c, a signal in HVH is allowed through the quantum path

$$\begin{array}{rcl} \mathbf{k}_2(\mathrm{V}) & \rightarrow & |\mathrm{e}^+\rangle\langle\mathrm{e}^+| \\ & & |\mathrm{e}^+\rangle\langle\mathrm{h}^+| \\ & & |\mathrm{h}^-\rangle\langle\mathrm{h}^+| \\ 2\mathbf{k}_2 - \mathbf{k}_1(\mathrm{H}) & \leftarrow & |\mathrm{h}^-\rangle\langle\mathrm{e}^-| \end{array} \begin{array}{l} \leftarrow \mathbf{k}_1(\mathrm{H}) \\ \\ \\ \rightarrow \mathbf{k}_2(\mathrm{V}) \end{array} . \tag{4.1}$$

Here, the polarization components are indicated in brackets for each interaction. The overall polar dependence is given by $|\cos(2\varphi)|$, which is shown by the blue line in Figure 4.2d. Therefore,

at first glance, the observed trend may be explained by the coexistence of excitons and trions. We consider carefully which polarimetric behavior can be expected from a mixed ensemble of excitons and trions. Here, the total temporal and polar dependence of the PE amplitude $P(\varphi, \tau_{\mathrm{ref}})$ results from the superposition of two independent polarizations P_X (exciton) and P_T (trion)

$$P(\varphi, \tau_{\mathrm{ref}}) \propto P_{\mathrm{X}}(\varphi) + r_{\mathrm{XT}} \cdot P_{\mathrm{T}}(\varphi) = \left(r_{\mathrm{XT}} \mathrm{e}^{-\frac{\tau_{\mathrm{ref}}}{T_2^{\mathrm{T}}}} + \frac{\mathrm{e}^{-\frac{\tau_{\mathrm{ref}}}{T_2^{\mathrm{X}}}}}{2} \right) \cos(2\varphi) + \frac{\mathrm{e}^{-\frac{\tau_{\mathrm{ref}}}{T_2^{\mathrm{X}}}}}{2}, \tag{4.2}$$

where r_{XT} denotes the ratio between the number of trions and neutral excitons and T_2^{T} and T_2^{X} are the respective decoherence times. We assumed that both transitions share the same dipole moment. Note that the expression in Equation (4.2) exhibits a zero crossing for any choice of r_{XT} and decoherence times since the sign of the trion polarization in HVH is negative relative to the exciton and trion polarization in HHH. The resulting polar rosette has a qualitative shape as shown by the green line in Figure 4.2d for $\tau_{\mathrm{ref}} = 0$ and $r_{\mathrm{XT}} = 1$. We observe a similar polar dependence of the PE amplitude on an ensemble of InGaAs semiconductor quantum dots where the ratio r_{XT} between charged and uncharged excitons is set by the applied optical power through a photo-charging effect. These results are presented in Section 5.2. However, the observed polar rosette on $MAPbI_3$ for $\tau_{\mathrm{ref}} = 0.1$ ps, Figure 4.1a, clearly deviates from this qualitative shape as a zero-crossing can not be observed. We thus conclude that the assumption of two independent subensembles (excitons and trions) cannot explain our observations. A more striking argument for this conclusion is given below by the experimental observation of quantum beats that cannot be caused by the interference of two independent polarizations.

In fact, all experimental observations that we present in this chapter turn out to be compatible with the formation of biexcitons. The biexciton is a bound state of two excitons with opposite spin, which is in a direct analogy to the hydrogen molecule H_2. As depicted in Figure 4.3a, the biexciton can be considered as a four-level diamond scheme. Here, $|\mathrm{G}\rangle$ is the ground state, $|\mathrm{X}^{\pm}\rangle$ denote the degenerate exciton states as discussed above and $|\mathrm{B}\rangle = |\mathrm{X}^{\uparrow}\mathrm{X}^{\downarrow}\rangle$ is the spin-zero biexciton state formed by two excitons of opposite spin. The energy of the biexciton state is lowered by the biexciton binding energy ε_{B} relative to the energy of two non-interacting excitons 2ε. In a four-wave mixing (FWM) experiment, the biexciton can be coherently excited when the spectral width of the resonant laser pulses (11 meV) is sufficiently larger than the biexciton binding energy ε_{B} [98]. In particular, a signal in the configuration HVH arises from the following quantum path

$$\begin{array}{rl} & |G\rangle\langle G| \\ \mathbf{k}_2(\mathrm{V}) \rightarrow & |G\rangle\langle \mathrm{X}^+| \\ \mathbf{k}_2(\mathrm{V}) \rightarrow & |\mathrm{X}^-\rangle\langle \mathrm{X}^+| \\ 2\mathbf{k}_2 - \mathbf{k}_1(\mathrm{H}) \leftarrow & |B\rangle\langle \mathrm{X}^+| \end{array} \leftarrow \mathbf{k}_1(\mathrm{H}) \tag{4.3}$$

With the final horizontally polarized emission from the biexciton to exciton transition. In this picture, a faster decay in HVH that we observed in the experiment could result from a shorter decoherence time of the exciton-biexciton coherence in comparison to the exciton-ground state coherence. Analytical modeling of the FWM response of the exciton-biexciton system is needed to confirm the hypothesis of biexciton formation, which we present in the following.

4.1.2 Exciton-biexciton model

To quantitatively model the polarimetric behavior of the exciton-biexciton system within the PE polarimetry method, we solve the optical Bloch equations in third-order perturbation theory using

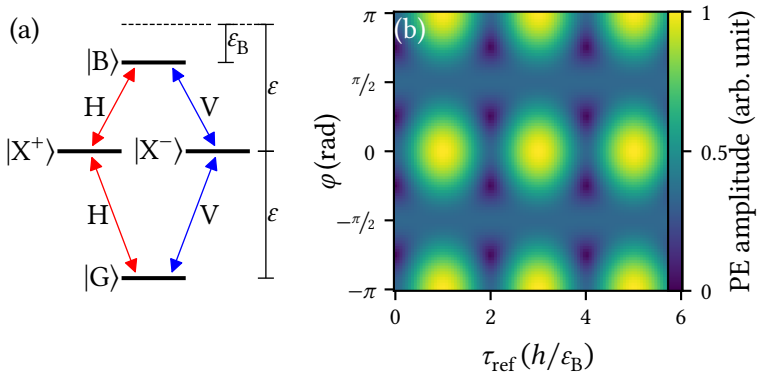

Figure 4.3: (a) Schematic of the exciton-biexciton system which expands the exciton scheme by an additional biexciton state $|\mathrm{B}\rangle$ that is energetically lowered by the biexciton binding energy ε_B from the two-exciton energy 2ε. (b) Colormap visualizing the temporal dynamics of the polar rosettes that results from the energy difference between transitions from biexciton to exciton and exciton to ground state.

the methods introduced in Section 1.2.2. The Hamiltonian of the unperturbed exciton-biexciton system reads as

$$H_0 = \mathrm{diag}(0, \varepsilon, \varepsilon, 2\varepsilon - \varepsilon_\mathrm{B}), \tag{4.4}$$

where we have chosen the representation of the eigenvectors as $|\mathrm{G}\rangle \hat{=} (1,0,0,0)^\top$, $|\mathrm{X}^+\rangle \hat{=} (0,1,0,0)^\top$, $|\mathrm{X}^-\rangle \hat{=} (0,0,1,0)^\top$, and $|\mathrm{B}\rangle \hat{=} (0,0,0,1)^\top$. Taking into account the dipole selection rules as indicated in Figure 4.3a, the matrix $\mathbf{V}$ accounting for the interaction of the system with light is given by

$$\mathbf{V} = -\mu \begin{pmatrix} 0 & E_\mathrm{H} & E_\mathrm{V} & 0 \\ E_\mathrm{H}^* & 0 & 0 & E_\mathrm{H} \\ E_\mathrm{V}^* & 0 & 0 & E_\mathrm{V} \\ 0 & E_\mathrm{H}^* & E_\mathrm{V}^* & 0 \end{pmatrix} \tag{4.5}$$

where μ denotes the dipole moment, that we assume to be equal for all transitions (we set $\mu = 1$ in the following) and E_H (E_V) is the horizontally (vertically) polarized component of the light field. We add decoherence times to the equation of motion for the density matrix elements of the system as

$$\frac{d}{dt}\boldsymbol{\rho} = \frac{i}{\hbar}\left[\boldsymbol{\rho}, \mathbf{H}_0 + \mathbf{V}\right] - \begin{pmatrix} 0 & \frac{\rho_{01}}{T_2^\mathrm{X}} & \frac{\rho_{02}}{T_2^\mathrm{X}} & 0 \\ \frac{\rho_{10}}{T_2^\mathrm{X}} & 0 & 0 & \frac{\rho_{13}}{T_2^\mathrm{B}} \\ \frac{\rho_{20}}{T_2^\mathrm{X}} & 0 & 0 & \frac{\rho_{23}}{T_2^\mathrm{B}} \\ 0 & \frac{\rho_{31}}{T_2^\mathrm{B}} & \frac{\rho_{32}}{T_2^\mathrm{B}} & 0 \end{pmatrix}, \tag{4.6}$$

where we denoted the decoherence times of the exciton-ground state coherence and exciton-biexciton coherence as T_2^X and T_2^B, respectively. All other decay times, such as the population decay times are ignored since they do not contribute to the considered two-pulse PE experiments. The temporal envelopes of the optical pulses are assumed to be delta functions. In Table 4.1 we show all time-ordered Feynman diagrams contributing to the four-wave mixing response in the phase-matched direction $2\mathbf{k}_2 - \mathbf{k}_1$ with the corresponding contribution to the third-order polarization on top. Table 4.1 enables us to model the PE response in arbitrary polarization configurations.

Table 4.1: Feynman diagrams contributing to the FWM response of the exciton-biexciton system in linear polarization base. Factors on top show the corresponding contribution to the third-order polarization.

(A) $E_{\mathrm{H},1}E^{*2}_{\mathrm{H},2}\mathrm{e}^{i\frac{\varepsilon}{\hbar}(2\tau_{12}-\tau_{\mathrm{ref}})+i\frac{\varepsilon_B}{\hbar}(\tau_{\mathrm{ref}}-\tau_{12})-\frac{\tau_{\mathrm{ref}}-\tau_{12}}{T_2^{\mathrm{B}}}-\frac{\tau_{12}}{T_2^{\mathrm{X}}}}$ 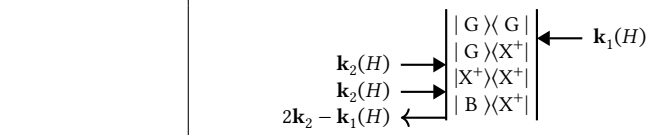	(B) $E_{\mathrm{V},1}E^{*2}_{\mathrm{V},2}\mathrm{e}^{i\frac{\varepsilon}{\hbar}(2\tau_{12}-\tau_{\mathrm{ref}})+i\frac{\varepsilon_B}{\hbar}(\tau_{\mathrm{ref}}-\tau_{12})-\frac{\tau_{\mathrm{ref}}-\tau_{12}}{T_2^{\mathrm{B}}}-\frac{\tau_{12}}{T_2^{\mathrm{X}}}}$ 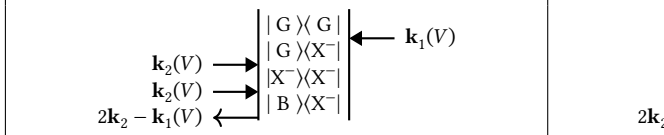	(C) $E_{\mathrm{V},1}E^{*2}_{\mathrm{V},2}\mathrm{e}^{i\frac{\varepsilon}{\hbar}(2\tau_{12}-\tau_{\mathrm{ref}})-\frac{\tau_{\mathrm{ref}}}{T_2^{\mathrm{X}}}}$
(D) $E_{\mathrm{V},1}E^{*2}_{\mathrm{V},2}\mathrm{e}^{i\frac{\varepsilon}{\hbar}(2\tau_{12}-\tau_{\mathrm{ref}})-\frac{\tau_{\mathrm{ref}}}{T_2^{\mathrm{X}}}}$ 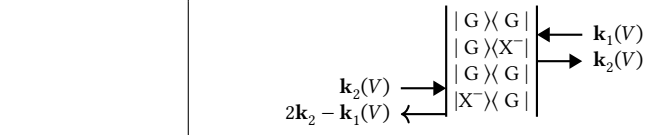	(E) $E_{\mathrm{H},1}E^{*2}_{\mathrm{H},2}\mathrm{e}^{i\frac{\varepsilon}{\hbar}(2\tau_{12}-\tau_{\mathrm{ref}})-\frac{\tau_{\mathrm{ref}}}{T_2^{\mathrm{X}}}}$ 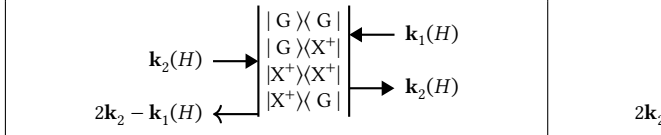	(F) $E_{\mathrm{H},1}E^{*2}_{\mathrm{H},2}\mathrm{e}^{i\frac{\varepsilon}{\hbar}(2\tau_{12}-\tau_{\mathrm{ref}})-\frac{\tau_{\mathrm{ref}}}{T_2^{\mathrm{X}}}}$
(G) $E_{\mathrm{H},1}E^{*}_{\mathrm{H},2}E^{*}_{\mathrm{V},2}\mathrm{e}^{i\frac{\varepsilon}{\hbar}(2\tau_{12}-\tau_{\mathrm{ref}})-\frac{\tau_{\mathrm{ref}}}{T_2^{\mathrm{X}}}}$ 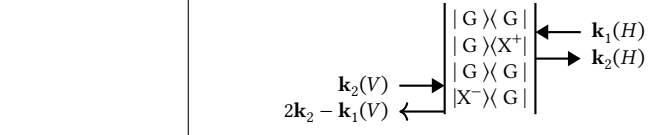	(H) $E_{\mathrm{H},1}E^{*}_{\mathrm{H},2}E^{*}_{\mathrm{V},2}\mathrm{e}^{i\frac{\varepsilon}{\hbar}(2\tau_{12}-\tau_{\mathrm{ref}})-\frac{\tau_{\mathrm{ref}}}{T_2^{\mathrm{X}}}}$ 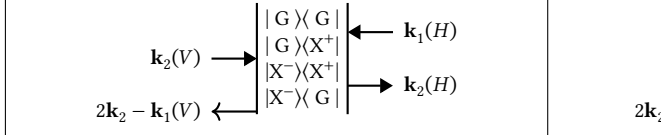	(I) $E_{\mathrm{H},1}E^{*2}_{\mathrm{V},2}\mathrm{e}^{i\frac{\varepsilon}{\hbar}(2\tau_{12}-\tau_{\mathrm{ref}})+i\frac{\varepsilon_B}{\hbar}(\tau_{\mathrm{ref}}-\tau_{12})-\frac{\tau_{\mathrm{ref}}-\tau_{12}}{T_2^{\mathrm{B}}}-\frac{\tau_{12}}{T_2^{\mathrm{X}}}}$
(J) $E_{\mathrm{V},1}E^{*2}_{\mathrm{H},2}\mathrm{e}^{i\frac{\varepsilon}{\hbar}(2\tau_{12}-\tau_{\mathrm{ref}})+i\frac{\varepsilon_B}{\hbar}(\tau_{\mathrm{ref}}-\tau_{12})-\frac{\tau_{\mathrm{ref}}-\tau_{12}}{T_2^{\mathrm{B}}}-\frac{\tau_{12}}{T_2^{\mathrm{X}}}}$ 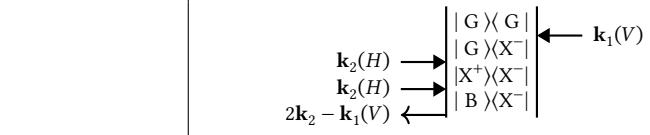	(K) $E_{\mathrm{V},1}E^{*}_{\mathrm{H},2}E^{*}_{\mathrm{V},2}\mathrm{e}^{i\frac{\varepsilon}{\hbar}(2\tau_{12}-\tau_{\mathrm{ref}})-\frac{\tau_{\mathrm{ref}}}{T_2^{\mathrm{X}}}}$ 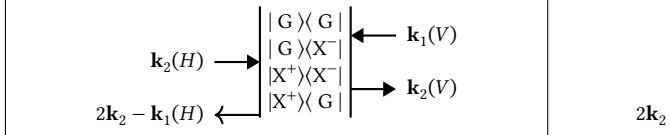	(L) $E_{\mathrm{V},1}E^{*}_{\mathrm{H},2}E^{*}_{\mathrm{V},2}\mathrm{e}^{i\frac{\varepsilon}{\hbar}(2\tau_{12}-\tau_{\mathrm{ref}})-\frac{\tau_{\mathrm{ref}}}{T_2^{\mathrm{X}}}}$

To calculate the signal in the configuration HRH as a function of τ_{ref}, we construct the polarization vector of first and second pulses in linear polarization base

$$\begin{pmatrix} E_{\mathrm{H},\,1} \\ E_{\mathrm{V},\,1} \end{pmatrix} \propto \mathrm{e}^{i\mathbf{k}_1} \begin{pmatrix} 1 \\ 0 \end{pmatrix}, \quad \begin{pmatrix} E_{\mathrm{H},\,2} \\ E_{\mathrm{V},\,2} \end{pmatrix} \propto \mathrm{e}^{i\mathbf{k}_2} \begin{pmatrix} \cos\varphi \\ \sin\varphi \end{pmatrix}, \tag{4.7}$$

and sum up the contributions of all Feynman diagrams with final horizontally polarized emission. In this way, we arrive at the temporal dependence of the polar rosettes

$$\left|E^{\mathrm{B}}_{\mathrm{HRH}}\right|(\varphi,\tau_{\mathrm{ref}}) \propto \sqrt{4\cos^4(\varphi)\,\mathrm{e}^{-\frac{2\tau_{\mathrm{ref}}}{T_{\mathrm{X}}}} + \mathrm{e}^{-\tau_{\mathrm{ref}}\left(\frac{1}{T_2^{\mathrm{X}}}+\frac{1}{T_2^{\mathrm{B}}}\right)} - 4\cos^2(\varphi)\cos\left(\frac{\varepsilon_{\mathrm{B}}}{2\hbar}\tau_{\mathrm{ref}}\right)\mathrm{e}^{-\tau_{\mathrm{ref}}\left(\frac{3}{2T_2^{\mathrm{X}}}+\frac{1}{2T_2^{\mathrm{B}}}\right)}}. \tag{4.8}$$

Two special cases are the configurations HHH ($\varphi = 0$) and HVH ($\varphi = \pi/2$)

$$\left|E^{\mathrm{B}}_{\mathrm{HHH}}\right|(\tau_{\mathrm{ref}}) \propto \sqrt{4\mathrm{e}^{-\frac{2\tau_{\mathrm{ref}}}{T_2^{\mathrm{X}}}} + \mathrm{e}^{-\tau_{\mathrm{ref}}\left(\frac{1}{T_2^{\mathrm{X}}}+\frac{1}{T_2^{\mathrm{B}}}\right)} - 4\cos\left(\frac{\varepsilon_{\mathrm{B}}}{2\hbar}\tau_{\mathrm{ref}}\right)\mathrm{e}^{-\tau_{\mathrm{ref}}\left(\frac{3}{2T_2^{\mathrm{X}}}+\frac{1}{2T_2^{\mathrm{B}}}\right)}} \tag{4.9a}$$

$$\left|E^{\mathrm{B}}_{\mathrm{HVH}}\right|(\tau_{\mathrm{ref}}) \propto \mathrm{e}^{-\frac{\tau_{\mathrm{ref}}}{2}\left(\frac{1}{T_2^{\mathrm{X}}}+\frac{1}{T_2^{\mathrm{B}}}\right)}. \tag{4.9b}$$

In the absence of decoherence, the function (4.8) can be simplified to

$$\left|E^{\mathrm{B}}_{\mathrm{HRH}}\right| \propto \sqrt{8\underbrace{\cos^2(\varphi)}_{\text{Two-leaves}}\sin^2\left(\frac{\varepsilon_{\mathrm{B}}}{4\hbar}\tau_{\mathrm{ref}}\right) + \underbrace{\cos^2(2\varphi)}_{\text{Four-leaves}}}, \tag{4.10}$$

which is visualized in Figure 4.3b. Here, it can be seen that the rosettes oscillate between a two-leave and four-leaf behavior at a frequency of $\varepsilon_{\mathrm{B}}/2h$, which is also highlighted in Equation (4.10) by the brackets. Although an experimental transition from a four-leaf to a two-leaf behavior was observed, the beating patterns could not be identified in the experimental trend shown in Figure 4.1c. This may be due to decoherence times that are shorter than the quantum beat period. A rough estimate for the expected quantum beat period results from an analogy to the H_2 molecule whose binding energy (4.7 eV) is about one-third of the Rydberg energy (13.6 eV). Given the exciton binding energy of 12 meV, we can therefore expect a beating period of approximately 1.1 ps, which is significantly longer than the observed decoherence times, both in HHH and HVH.

The observation of exciton-biexciton quantum beats would represent a direct proof of the biexciton formation and would allow to extract the biexciton binding energy. To overcome the limitations of short decoherence times, we considered polarization beats that turn out to allow for the observation of oscillations on a longer time scale as amplitude beats, which is discussed in detail in the next section.

4.1.3 Observation of polarization beats from the exciton-biexciton system

Oscillations of the polarization state of spectroscopic signals, such as FWM or photoluminescence, are discussed in various works as a sensitive tool to gain information about the optical characteristics of the quantum mechanical system under study [135–141]. Here, we consider polarization beats to place stringent constraints on the exciton-biexciton model and develop an experimental protocol that enables us to measure the biexciton binding energy with high confidence.

To induce polarization beats of the FWM response of the biexciton, we consider a modified polarization configuration where the first pulse is circularly polarized whereas the second pulse is horizontally polarized (called σ^+H for simplicity). Here, the first pulse simultaneously creates a superposition of the polarizations $|\mathrm{G}\rangle\langle\mathrm{X}^+|$ and $|\mathrm{G}\rangle\langle\mathrm{X}^-|$ with a relative phase shift of $\pi/2$. The interaction with the second H-polarized pulse leads to the emissions from $|\mathrm{X}^+\rangle \rightarrow |\mathrm{G}\rangle$ (H-polarized, paths E, F, K, L in Table 4.1), $|\mathrm{B}\rangle \rightarrow |\mathrm{X}^+\rangle$ (H-polarized, paths A, I), and $|\mathrm{B}\rangle \rightarrow |\mathrm{X}^-\rangle$ (V-polarized, path B) that interfere with each other. Due to the initial phase between H and V polarization of $\pi/2$ as set by the circularly polarized first pulse, the final emission will be in general elliptically polarized. Because of the energy difference between the transitions given by the biexciton binding energy, the polarization state will perform an oscillatory motion, which we can calculate by summing up the contributions of the Feynam diagrams from Table 4.1. To visualize the dynamic of the polarization state, we use the Poincaré sphere. The Poincaré sphere represents the polarization state of light defined through the Stokes parameters ρ_i

$$\rho_1 = \frac{I_\mathrm{H} - I_\mathrm{V}}{I_\mathrm{H} + I_\mathrm{V}}, \quad \rho_2 = \frac{I_\mathrm{D} - I_\mathrm{A}}{I_\mathrm{D} + I_\mathrm{A}}, \quad \rho_3 = \frac{I_{\sigma^+} - I_{\sigma^-}}{I_{\sigma^+} + I_{\sigma^-}} \tag{4.11}$$

where I_j (j = H, V, D, A, σ^+, σ^-) correspond to the intensity components of the light field with respect to the horizontal (H), vertical (V), diagonal (D), antidiagonal (A), and circular ($\sigma^\pm$) polarization projections. The polarization state of the PE amplitude in the configuration σ^+H describes a circular motion on the Poincaré sphere as we visualize in Figure 4.4a. Here, the green point marks the polarization state for $\tau_\mathrm{ref} = 0$ (σ^+ polarized in this case). The temporal dynamics of the three Stokes parameters are given by

$$\rho_1^{\sigma^\pm H} = \frac{\cos\left(\frac{\varepsilon_\mathrm{B}\tau_\mathrm{ref}}{2\hbar}\right) \mathrm{e}^{-\frac{\tau_\mathrm{ref}}{2T_\Delta}} - 1}{\cos\left(\frac{\varepsilon_\mathrm{B}\tau_\mathrm{ref}}{2\hbar}\right) \mathrm{e}^{-\frac{\tau_\mathrm{ref}}{2T_\Delta}} - \frac{1}{2}\mathrm{e}^{-\frac{\tau_\mathrm{ref}}{T_\Delta}} - 1} \tag{4.12a}$$

$$\rho_2^{\sigma^\pm H} = \pm\frac{\sin\left(\frac{\varepsilon_\mathrm{B}\tau_\mathrm{ref}}{2\hbar}\right) \mathrm{e}^{-\frac{\tau_\mathrm{ref}}{2T_\Delta}}}{\cos\left(\frac{\varepsilon_\mathrm{B}\tau_\mathrm{ref}}{2\hbar}\right) \mathrm{e}^{-\frac{\tau_\mathrm{ref}}{2T_\Delta}} - \frac{1}{2}\mathrm{e}^{-\frac{\tau_\mathrm{ref}}{T_\Delta}} - 1} \tag{4.12b}$$

$$\rho_3^{\sigma^\pm H} = \mp\frac{\cos\left(\frac{\varepsilon_\mathrm{B}\tau_\mathrm{ref}}{2\hbar}\right) \mathrm{e}^{-\frac{\tau_\mathrm{ref}}{2T_\Delta}} - \frac{1}{2}\mathrm{e}^{-\frac{\tau_\mathrm{ref}}{2T_\Delta}}}{\cos\left(\frac{\varepsilon_\mathrm{B}\tau_\mathrm{ref}}{2\hbar}\right) \mathrm{e}^{-\frac{\tau_\mathrm{ref}}{2T_\Delta}} - \frac{1}{2}\mathrm{e}^{-\frac{\tau_\mathrm{ref}}{T_\Delta}} - 1}, \tag{4.12c}$$

where $1/T_\Delta = 1/T_2^\mathrm{B} - 1/T_2^\mathrm{X}$ denotes the difference in decoherence rates of exciton and biexciton. Equations (4.12) also give the corresponding functions for excitation with a σ^- polarized first pulse, which will be important below. The three functions are shown for one quantum beat period in Figure 4.4b, where we first neglected the finite decoherence times. It can be seen that ρ_2 shows the highest effect amplitude which we therefore regard as the most informative Stokes parameter to observe quantum beats. An interesting property is given by the damping behavior of the oscillations on the polarization state when considering short decoherence times of excitons and biexcitons. In Figure 4.4c, we plot Equation (4.12b) in direct comparison to the decay of the amplitude decay of the PE amplitude in HHH and HVH for the same set of parameters $T_2^\mathrm{X} = 0.8\,\mathrm{ps}$, $T_2^\mathrm{B} = 0.6\,\mathrm{ps}$, and $\varepsilon_\mathrm{B} = 2.4\,\mathrm{meV}$. Here, it can be seen that the polarization beats offer a much higher sensitivity to observe beats since the envelope of the oscillation of ρ_2 decays with a rate given by the difference of decay rates between exciton and biexciton. In contrast, the amplitude beats decay with a weighted sum of the decay rates, compare Equation (4.8). Importantly, a full quantum beat cycle can be observed in ρ_2 within a temporal range during which the amplitude of the signal approximately drops by a factor of 1000, which lies in the dynamic range of our experimental setup.

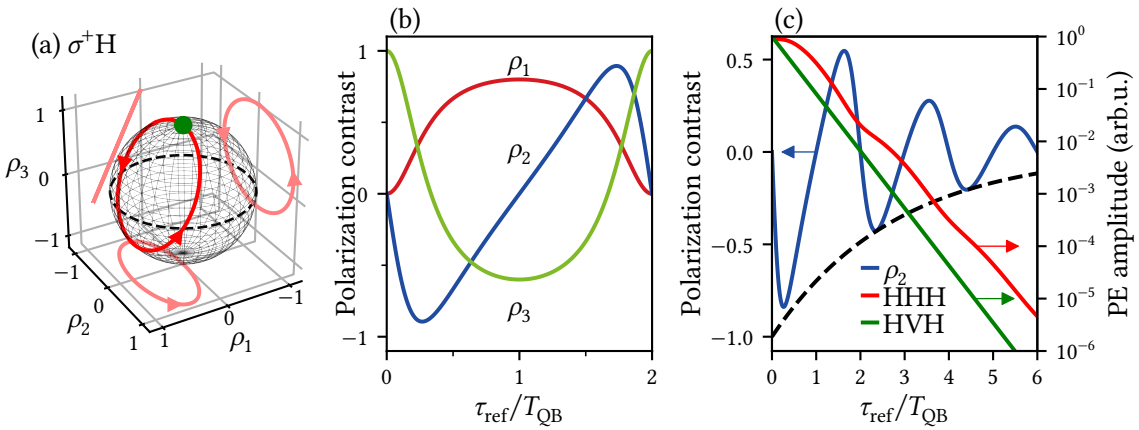

Figure 4.4: (a) Trajectory of the polarization state of the PE from the exciton-biexciton system upon excitation with a σ^+ polarized first pulse and H polarized second pulse, visualized on the Poincaré sphere. (b) Time dynamics of the three Stokes parameters ρ_i within one quantum beat period. (c) Comparison of the damping behavior of ρ_2 with the amplitude decay in the configurations HHH and HVH for the same set of parameters as given in the text.

We demonstrate quantum beats (QBs) using a method introduced by Koch et al. [22]. We define QBs as the quantum mechanical interference of two transitions with different energies that share one common state. In the case of the exciton-biexciton system, these two transitions are the biexciton to exciton and exciton to ground state transition with the exciton as a common state. Time-resolved FWM spectroscopy offers the unique possibility to distinguish QBs from the interference of two completely independent polarizations with different energy, which is denoted as polarization interference (PI) [22]. The idea of this distinction is described in the following. We consider two independent third-order polarizations P_1 and P_2 in a two-pulse PE experiment. Each third-order polarization P_j has a time dependence in the form of

$$P_j(\tau_{ref}, \tau_{12}) \propto \exp\left[i\omega_j(\tau_{ref} - 2\tau_{12})\right], \tag{4.13}$$

where ω_j denote the eigenfrequencies of the two transitions. The intensity signal $\propto |P_1 + P_2|^2$ on a detector will then produce a time-dependent polarization interference component

$$P_{PI}(\tau_{ref}, \tau_{12}) \propto \cos\left[\Delta_{12}(\tau_{ref} - 2\tau_{12})\right], \tag{4.14}$$

which is an oscillating signal with local extrema for $\tau_{ref} - 2\tau_{12} = n/\Delta_{12}$, where $\Delta_{12} = \omega_1 - \omega_2$. This behavior fundamentally deviates from a system where two transitions share one common state as in the case of the exciton-biexciton system. Here, an oscillating signal in the FWM results from quantum paths involving both transitions. The temporal dependence of the beating components is thus given by

$$P_{QB} \propto \exp\left[i\omega_1\tau_{12}\right] \cdot \exp\left[-i\omega_2(\tau_{ref} - \tau_{12})\right] = \exp\left[i\omega_1(2\tau_{12} - \tau_{ref})\right] \cdot \exp\left[i\Delta_{12}(\tau_{12} - \tau_{ref})\right], \tag{4.15}$$

which will produce an oscillating signal with local extrema for $\tau_{ref} - \tau_{12} = n/\Delta_{12}$. Measuring the FWM response as a function of τ_{ref} and τ_{12} thus allows us to unambiguously distinguish between the interference of two independent polarizations and QBs by analyzing the temporal dependence of local extrema of the oscillations.

To visualize the difference between QBs and PI in our experimental protocol, we calculated the expected PE signal in the HHH polarization configuration for the biexciton and exciton/trion system, which are shown in Figures 4.5b and 4.5c, respectively. The corresponding experimental

data is provided for comparison in Figure 4.5a. For the modeling, we assumed a biexciton binding energy of $\varepsilon_B = 2.5\,\text{meV}$ and a splitting Δ_{12} between the exciton and trion transition of the same magnitude. To observe several oscillation cycles in the theoretical color maps within the temporal width of the PE, we assumed a smaller inhomogeneous broadening of approximately 2 meV compared to the experiment. The crucial difference between QBs and PI lies in the functional course of the oscillation extrema in the τ_{12}-τ_{ref}-map. For the QBs, the extrema run parallel to the line $\tau_{\text{ref}} = \tau_{12}$ (red line), whereas for PI, they follow $\tau_{\text{ref}} = 2\tau_{12}$ (blue line). This property provides a simple way to determine whether our PE signal originates from the biexciton or an independent interference of two resonances. However, based on the data presented in Figure 4.5a, we cannot differentiate between QBs and PI since the involved decoherence times are too short to observe any oscillations of the PE amplitude. However, the influence of the quantum beats could explain the shifted position of the PE maximum that we mentioned in Section 3.1.

The same argument as for the extrema of the PE amplitude oscillations also holds for the extrema of any polarization contrast that exhibits oscillations due to QBs or PI. We modeled in Figures 4.5e and 4.5f the polarization contrast ρ_2 from biexciton and exciton/trion. Figure 4.5d shows the corresponding experimental data for comparison. Note, regardless of the inhomogeneous broadening, we can theoretically observe the polarization contrast for any positive values of τ_{12} and τ_{ref} due to an unlimited dynamic range. Again, in the case of QBs, the extrema run parallel to $\tau_{\text{ref}} = \tau_{12}$ (Figure 4.5e) and for PI parallel to $\tau_{\text{ref}} = 2\tau_{12}$ (Figure 4.5f). Because of the different damping behavior of the polarization contrast, we can observe oscillations in the experimental data for ρ_2. We identify that the extrema of the observed oscillations run parallel to $\tau_{\text{ref}} = \tau_{12}$ (red line), which rules out the possibility of polarization interference. This observation strongly supports the hypothesis of biexciton formation and strictly rules out the aforementioned coexistence of exciton and trion subensembles.

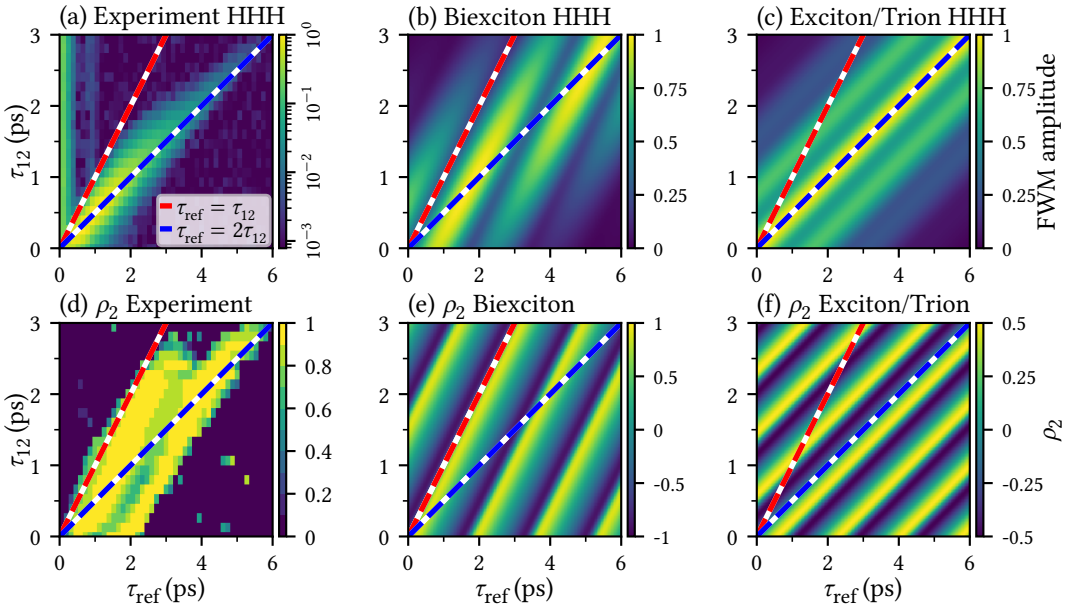

Figure 4.5: (a) Heterodyne signal as a function of τ_{12} and τ_{ref}, measured in the polarization configuration HHH. (b)/(c) Modeled data within the biexciton and exciton/trion models corresponding to (a). For the modeling, we neglected the finite decoherence times of the involved coherences and, for better visibility of the oscillating signal, assumed a more narrow inhomogeneous broadening. (d) Experimental polarization contrast ρ_2 as a function of τ_{12} and τ_{ref}. (e)/(f) Result of the calculation of ρ_2 within the two models.

4.1.4 Measurement of the biexciton binding energy by polarization beats

In this section, we describe the fitting procedure that we use to extract the biexciton binding energy ε_B as well as the decoherence times of exciton and biexciton, T_2^X and T_2^B being free parameters of the biexciton model as introduced above. To accurately access the biexciton binding energy, we measure transient polar rosettes involving one circular polarized pulse. This method enhances the potential of the PE polarimetry technique as introduced in Reference [102].

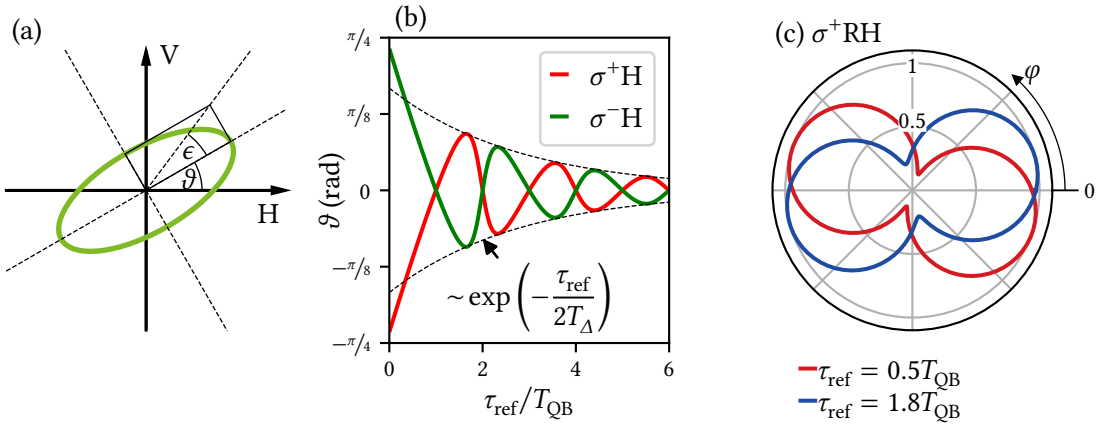

Figure 4.6: (a) Definition of the angles ϵ and ϑ as the ellipticity and the tilting angle of the polarization ellipse, respectively. (b) Time dynamics of ϑ for $\sigma^{\pm}$H excitation. The dashed black lines highlight that the oscillations of ϑ are damped by the difference of decoherence rates of exciton and biexciton T_Δ^{-1}. (c) Two theoretical polar dependences in the configuration σ^+RH for two different temporal positions within the quantum beat period T_{QB}.

The aforementioned beats of the PE polarization state can be translated into dynamics of the angles ϵ and ϑ characterizing the ellipticity and rotation angle of the polarization ellipse as defined in Figure 4.6a. We concentrate on the rotation angle ϑ as an easily accessible parameter in our experiments. An analytical expression for $\vartheta(\tau_{ref})$ within the exciton-biexciton model upon excitation with circularly polarized first and horizontally polarized second pulse directly results from the expressions given for the Stokes parameters in Equation (4.12)

$$\vartheta_{\sigma^\pm} = \arctan\left(\frac{\rho_2}{\rho_1}\right) = \pm\frac{1}{2}\arctan\left[\frac{\sin\left(\frac{\varepsilon_B\tau_{ref}}{2\hbar}\right)}{\cos\left(\frac{\varepsilon_B\tau_{ref}}{2\hbar}\right) - e^{\frac{\tau_{ref}}{2}\left(\frac{1}{T_2^B}-\frac{1}{T_2^X}\right)}}\right] \equiv \vartheta_{\sigma^\pm}(\tau_{ref}), \tag{4.16}$$

which describes damped anharmonic oscillations. The helicity of the first pulse results in a global sign of the function $\vartheta(\tau_{ref})$, which is a characteristic of the exciton-biexciton scheme that we test in our experiments below. We visualize Equation (4.16) for both helicities in Figure 4.6b, where we highlight the damping behavior of the oscillations by dashed lines. As can be seen by the exponential function in the denominator of the argument of the arctangent in Equation (4.16), the rotation angle ϑ experiences damped oscillations that decay proportional to $\exp(-\tau_{ref}/(2T_\Delta))$, i.e. on a time-scale set by the difference of decoherence rates of exciton and biexciton $1/T_\Delta = 1/T_2^B - 1/T_2^X \geq 0$. The angle ϑ shares the damping behavior of the polarization contrast ρ_2 and therefore represents a suitable parameter that allows to access the biexciton binding energy in the regime of short decoherence times.

Experimentally, $\vartheta_{\sigma^\pm}(\tau_{\mathrm{ref}})$ can be confidently extracted by measuring the PE amplitude as a function of linear polarization angle between the second pulse and reference pulse φ which is described by

$$\left|E^{\mathrm{B}}_{\sigma^\pm\mathrm{RH}}\right| \propto \Bigg[4\cos^2(\varphi)\, \mathrm{e}^{-2\frac{\tau_{\mathrm{ref}}}{T_2^{\mathrm{X}}}} + \mathrm{e}^{-\tau_{\mathrm{ref}}\left(\frac{1}{T_2^{\mathrm{X}}}+\frac{1}{T_2^{\mathrm{B}}}\right)} - 2\left[\cos\left(\frac{\varepsilon_{\mathrm{B}}}{2\hbar}\tau_{\mathrm{ref}}\right) + \cos\left(2\varphi \mp \frac{\varepsilon_{\mathrm{B}}}{2\hbar}\tau_{\mathrm{ref}}\right)\right] \mathrm{e}^{-\tau_{\mathrm{ref}}\left(\frac{3}{2T_2^{\mathrm{X}}}+\frac{1}{2T_2^{\mathrm{B}}}\right)} \Bigg]^{1/2}. \tag{4.17}$$

We call this experimental configuration $\sigma^\pm$RH. As can be seen by the red highlighted part of Equation (4.17), the quantum beats modulate the orientation of the polar rosettes. In Figure 4.6c, we plot two exemplary polar dependences given by Equation (4.17) for two different values of τ_{ref}. The orientation angle has a temporal dependence that is determined by $\vartheta(\tau_{\mathrm{ref}})$, which can be proven by calculating the angle that maximizes $P^{\mathrm{B}}_{\sigma^\pm\mathrm{RH}}$:

$$\frac{\mathrm{d}}{\mathrm{d}\varphi} E^{\mathrm{B}}_{\sigma^\pm\mathrm{RH}} = 0 \tag{4.18a}$$

$$\Leftrightarrow 0 = \sin\left(2\varphi \mp \frac{\varepsilon_{\mathrm{B}}}{2\hbar}\tau_{\mathrm{ref}}\right) \mathrm{e}^{-\tau_{\mathrm{ref}}\left(\frac{3}{2T_2^{\mathrm{X}}}+\frac{1}{2T_2^{\mathrm{B}}}\right)} - \sin(2\varphi)\, \mathrm{e}^{-2\frac{\tau_{\mathrm{ref}}}{T_{\mathrm{X}}}} \tag{4.18b}$$

$$\Leftrightarrow \varphi = \pm\frac{1}{2}\arctan\left[\frac{\sin\left(\frac{\varepsilon_{\mathrm{B}}\tau_{\mathrm{ref}}}{2\hbar}\right)}{\cos\left(\frac{\varepsilon_{\mathrm{B}}\tau_{\mathrm{ref}}}{2\hbar}\right) - \mathrm{e}^{\frac{\tau_{\mathrm{ref}}}{2}\left(\frac{1}{T_{\mathrm{B}}}-\frac{1}{T_{\mathrm{X}}}\right)}}\right] = \vartheta_{\sigma^\pm}(\tau_{\mathrm{ref}}). \tag{4.18c}$$

Figures 4.7a and 4.7b present the polar rosettes measured in the configurations σ^+RH and σ^-RH for $\tau_{\mathrm{ref}} = 0.8\,\mathrm{ps}$ and $\tau_{\mathrm{ref}} = 3.5\,\mathrm{ps}$. Here, we can observe the effect of the exciton-biexciton polarization beats as a time-dependent rotational behavior as well as the property that the sign of the rotation is set by the helicity of the circularly polarized first pulse. We measured such polar rosettes for a set of delays that we present in the form of color maps in Figures 4.7c and 4.7d for σ^+RH and σ^-RH. For each time step, we perform a fit to a simple $|\cos(\varphi - \vartheta)|$ function, to extract the orientation angle ϑ. In this way, we arrive at the dynamical behavior of the angle ϑ presented in Figure 4.8a. We can indeed identify an oscillatory dynamic of ϑ that enables us in the following to extract the biexciton binding energy.

Equation (4.16) predicts that the angle $\vartheta(\tau_{\mathrm{ref}})$ is mirrored on the τ_{ref}-axis upon change of helicity of the first pulse's polarization, i.e. $\vartheta_{\sigma^-}(\tau_{\mathrm{ref}}) = -\vartheta_{\sigma^+}(\tau_{\mathrm{ref}})$. Consequently, the sum of both curves vanishes. However, the sum of the experimental curves, plotted in Figure 4.8b, exhibits a non-zero offset. A fit to a constant function results in an offset of roughly 5°, shown as a blue line in Figure 4.8b. To account for this discrepancy between model and experiment, we phenomenologically expand the model (4.16) by an offset $\vartheta_0^\pm$

$$\vartheta_{\sigma^\pm}(\tau_{\mathrm{ref}}) = \pm\frac{1}{2}\arctan\left[\frac{\sin\left(\frac{\varepsilon_{\mathrm{B}}\tau_{\mathrm{ref}}}{2\hbar}\right)}{\cos\left(\frac{\varepsilon_{\mathrm{B}}\tau_{\mathrm{ref}}}{2\hbar}\right) - \mathrm{e}^{\frac{\tau_{\mathrm{ref}}}{2}\left(\frac{1}{T_{\mathrm{B}}}-\frac{1}{T_{\mathrm{X}}}\right)}}\right] + \vartheta_0^\pm. \tag{4.19}$$

Moreover, comparing the experimental data in Figure 4.8a with the modeled curves in Figure 4.6b, it is evident that the model does not accurately describe the experiment for $\tau_{\mathrm{ref}} < 0.8\,\mathrm{ps}$. Specifically, the first two data points (shaded in grey) deviate from the linear trend of the modeled

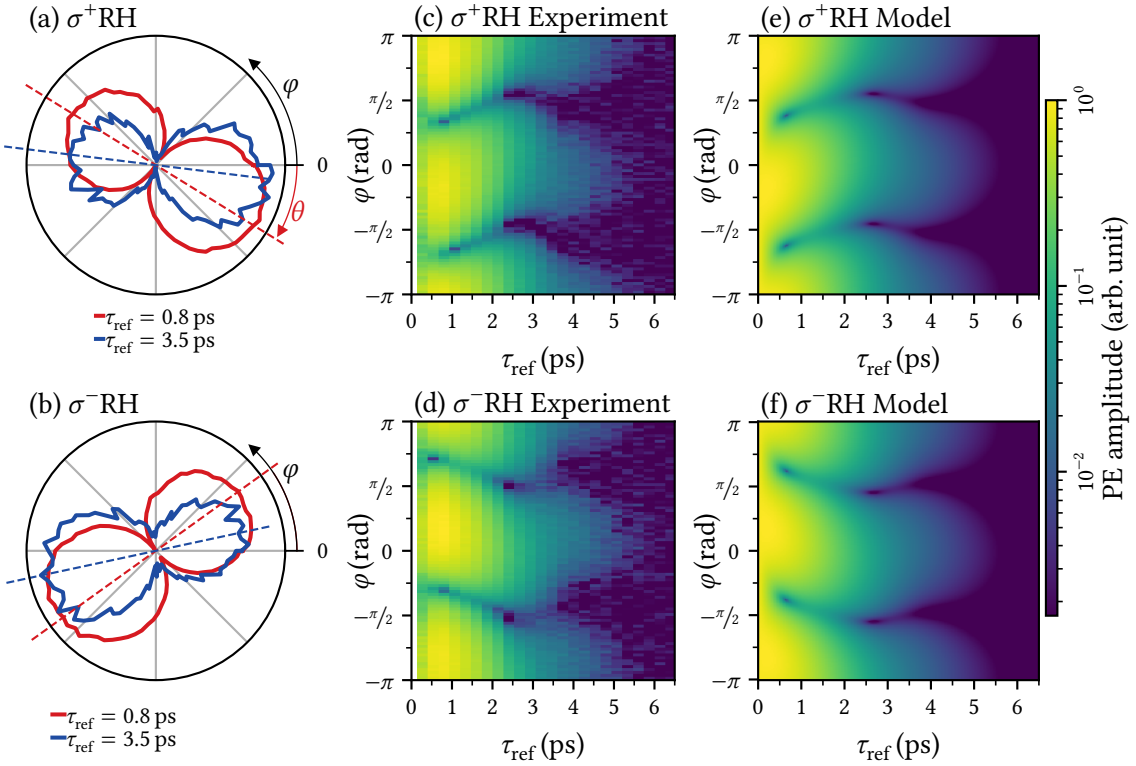

Figure 4.7: (a)/(b) Experimental polar rosettes in the configurations σ^+RH/σ^-RH for two different delays as indicated in the legends. (c)/(d) Measured rosettes as shown in (a)/(b) for a set of delays. (e)/(f) Modelled data corresponding to (c)/(d) including the fitted parameters of the exciton-biexciton model as presented in the text.

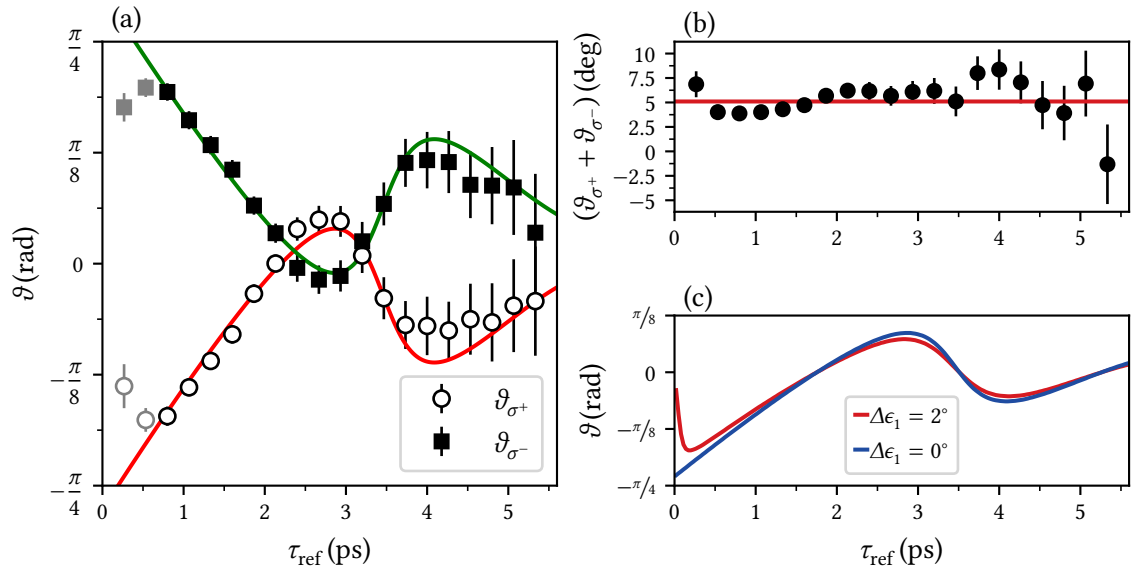

Figure 4.8: (a) Temporal dependence of the angle ϑ measured in the configuration σ^+RH and σ^-RH and corresponding fits to Equation (4.19). (b) Sum of the experimental curves shown in (a) and fit to a constant function. (c) Comparison of the modeled functions $\vartheta(\tau_{ref})$ for two different values of the ellipticity ϵ_1 of the first pulse.

functions. This deviation can be attributed to two influences. First, our model does not consider the temporal overlap of the optical pulses, which occurs in the range $\tau_{\mathrm{ref}} < 0.8\,\mathrm{ps}$. Second, our model assumes perfect circular polarization of the first pulse. However, in our experimental setup, the circular polarization created by a quarter-wave plate may be modified by the subsequent reflection on two silver mirrors. In Figure 4.8c, we numerically computed $\vartheta(\tau_{\mathrm{ref}})$ assuming a deviation of $\Delta\epsilon_1 = 2^\circ$ from a perfect circular polarization $\epsilon_1 = \pi/4$ of the first pulse. Here, the trend for small values of τ_{ref} corresponds well with the experimental observations. However, there is no closed solution for $\vartheta(\tau_{\mathrm{ref}})$ for a general elliptical polarization of the first pulse, making it computationally expensive and impractical to fit the data using standard fitting tools. Therefore, we use the idealized function (4.19) to fit our data in the following and exclude the first two data points from Figure 4.8a for simplicity.

To determine the value of ε_{B}, we merge the data for $\vartheta_{\sigma^+}(\tau_{\mathrm{ref}})$ and $\vartheta_{\sigma^-}(\tau_{\mathrm{ref}})$ by fitting $(\vartheta_{\sigma^+} - \vartheta_{\sigma^-})/2$ to Equation (4.19) for $\tau_{\mathrm{ref}} > 0.8\,\mathrm{ps}$. Additionally, the fit delivers the difference between decay rates T_Δ^{-1} and the difference between the offsets $\vartheta_0^+ - \vartheta_0^-$. A summary of all fitting parameters is provided in Table 4.2. The obtained value of $(2.4 \pm 0.2)\,\mathrm{meV}$ for the biexciton binding energy is discussed in the concluding section of this chapter.

Table 4.2: Summary of the parameters obtained from fit of the model (4.19) to experimental data for $\vartheta(\tau_{\mathrm{ref}})$ in the combined data of the polarization configurations σ^+RH and σ^-RH. The data and corresponding fits are shown in Figure 4.8.

ε_{B} (meV)	T_Δ^{-1} (THz)	ϑ_0^+ (deg)	ϑ_0^- (deg)
2.4 ± 0.2	0.45 ± 0.07	-9 ± 1	14 ± 1

As a next step, we utilize the experimental curve of the PE decay in the HHH configuration to determine the exciton decoherence time T_2^{X}, Figure 4.9a. Here, we take into account the values obtained for ε_{B} and T_Δ^{-1} and only allow T_2^{X} as a free fitting parameter. For this purpose, we express the function (4.9a) in terms of T_Δ^{-1}, ε_{B}, and T_2^{X}:

$$\left|E_{\mathrm{HHH}}^{\mathrm{B}}\right| \propto \mathrm{e}^{-\frac{\tau_{\mathrm{ref}}}{T_2^{\mathrm{X}}}} \sqrt{4 + \mathrm{e}^{-\frac{\tau_{\mathrm{ref}}}{T_\Delta}} - 4\cos\left(\frac{\varepsilon_{\mathrm{B}}}{2\hbar}\tau_{\mathrm{ref}}\right)\mathrm{e}^{-\frac{\tau_{\mathrm{ref}}}{2T_\Delta}}}. \tag{4.20}$$

The fit gives

$$T_2^{\mathrm{X}} = (0.79 \pm 0.03)\,\mathrm{ps} \tag{4.21}$$

and is visualized in Figure 4.9a. The corresponding homogeneous linewidth amounts to $(1.67 \pm 0.06)\,\mathrm{meV}$. Using the definition of the T_Δ^{-1}, we can calculate

$$T_2^{\mathrm{B}} = \left(\frac{1}{T_\Delta} + \frac{1}{T_2^{\mathrm{X}}}\right)^{-1} = (0.58 \pm 0.03)\,\mathrm{ps}, \tag{4.22}$$

corresponding to a linewidth of $(2.3 \pm 0.1)\,\mathrm{meV}$. Based on our model, the PE signal decays in the HVH configuration proportional to a single exponential function as given by Equation (4.9b). Figure 4.9b presents a comparison between the experimental decay and the model that uses the determined value of T_2^{B}. The measured decay dynamics in HVH slightly deviate from a single-exponential. Instead, the signal seems to decay in a Gaussian fashion. This observation may be linked to an inhomogeneity of the biexciton binding energy that could result from a correlation between the exciton transition energy and the biexciton binding energy [142]. Our model does not consider this effect. Apart from that, the model is in excellent agreement with all

measured polarization dependences. In particular, with the obtained parameters our model can accurately reproduce the temporal characteristics of the polar rosettes shown in 4.7e, 4.7f, and 4.9b.

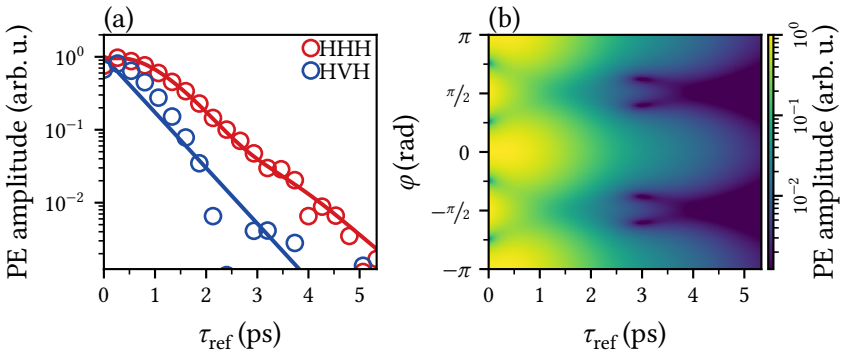

Figure 4.9: (a) Circles show the experimental decays of the PE amplitude in the polarization configurations HHH and HVH. Solid lines are the results of fits to the exciton-biexciton model. (b) Full dependence of the PE amplitude on linear polarization angle φ between first and second pulses and $\tau_{ref} = 2\tau_{12}$.

4.2 Spin-dependent excitation-induced dephasing in $FA_{0.9}Cs_{0.1}PbI_{2.8}Br_{0.2}$

The results presented in Chapter 3.2 demonstrate that lead halide perovskite semiconductors can have exceptionally long exciton coherence times associated with the localization of excitons in band gap fluctuations. In contrast to well-isolated semiconductor quantum dots, weakly localized excitons in a bulk material may be significantly affected by the coherent interaction with other photo-excited excitons or carriers [24]. The results presented in the following chapter show that even under moderate excitation densities, the assumption of isolated excitons in $FA_{0.9}Cs_{0.1}PbI_{2.8}Br_{0.2}$ leads to a strong deviation from the experimental observation within the PE polarimetry technique. In particular, a significant contribution resulting from excitation-induced dephasing (EID) is found in the PE signal. The EID effect is found to have a spin selectivity, that is, excitons interact more strongly with excitons of opposite spin. The exciton interactions have profound influences on the polarization dependence of non-linear optical spectra.

4.2.1 Photon echo polarimetry

Throughout this section, the exciton resonance in $FA_{0.9}Cs_{0.1}PbI_{2.8}Br_{0.2}$ is resonantly excited at 1.52 eV using the 4 ps pulses of the MIRA900 laser. As presented for $MAPbI_3$ in the previous section, we apply the PE polarimetry technique to investigate deviations from the picture of non-interacting excitons or the possible formation of multi-excitonic resonances. Therefore, we introduce a delay of $\tau_{12} = 20$ ps between the first and second pulse and measure the PE amplitude at $\tau_{ref} = 2\tau_{12} = 40$ ps in the configurations HRH. The resulting polar rosette is plotted in Figure 4.10a (red line). For direct comparison, we plot in Figure 4.10b the theoretical dependence given by $E_{HRH} = \cos^2(\varphi)$ resulting from the exciton V-scheme presented in Section 1.2.3. In the experiment, we observe a clear deviation from the $\cos^2(\varphi)$ dependence since a pronounced signal is emitted in the cross-polarized configuration $\varphi = \pi/2$ (HVH), which amounts to roughly one-third of the signal amplitude in co-polarized configuration $\varphi = 0$ (HHH). As highlighted by the green

line, the dependence is well described by a function of the form $\propto \cos^2\varphi + c$, where c is a signal component independent of the polarization between the first and second pulse. To investigate the polarization of the constant signal c, we repeat the measurement in the polarization configuration HRV. The experimental curve and the expectation for the V-scheme ($E_{\mathrm{HRH}} = |\sin(2\varphi)|/2$) are plotted in Figures 4.10a and 4.10b. Here, we can observe that the measured polar rosette in HRV does not qualitatively deviate from the $|\sin 2\varphi|$ dependence. Thus, the signal in the configuration HVH is fully horizontally polarized. The ratio between the maximum signal strength in HRH and HRV is larger than 1/2 as a result of the constant horizontally polarized offset c in the HRH dependence.

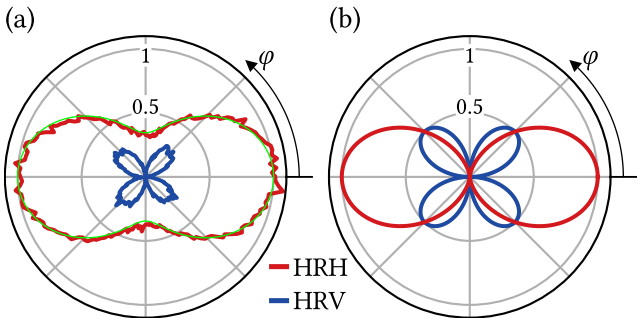

Figure 4.10: (a) Experimentally observed polar dependencies in the configurations HRH and HRV for a delay of $\tau_{12} = 20$ ps. The green line shows a fit of the HRH dependence to a function of the form $\cos^2\varphi + c$. (b) For comparison, theoretical polar dependencies of the PE amplitude in the configurations HRH and HRV assuming the V-scheme model of excitons.

Note that the observed polar trends are neither compatible with the formation of trions nor biexcitons. For the former, we expect qualitatively different polar dependencies as already discussed in Sections 1.2.3 and 4.1.1. For the latter, we expect quantum beats in the configuration HHH which are not observed (compare PE decay presented in Section 3.2). In Section 4.1, the biexciton binding energy in $MAPbI_3$ was found to be 2.4 meV, which we regard as a lower bound for the biexciton binding energy in $FA_{0.9}Cs_{0.1}PbI_{2.8}Br_{0.2}$ since localization typically leads to an increased biexciton binding energy [7]. Because our laser pulses are spectrally narrow ($\approx$ 0.3 meV), the formation of biexcitons is excluded. Instead of the formation of multi-excitonic resonances, spin-dependent excitation-induced nonlinearities can naturally describe the observed polar dependencies as we will motivate in the following.

4.2.2 Spin-dependent excitation-induced nonlinearities

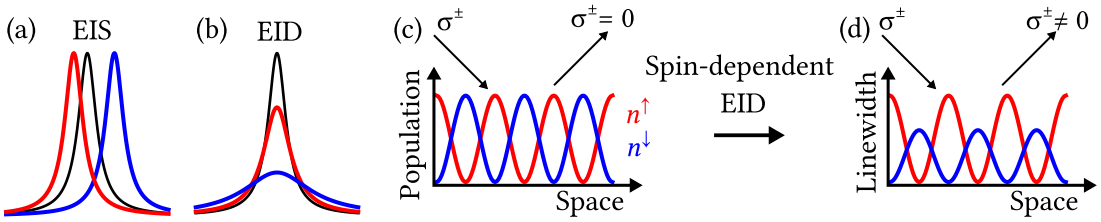

Figure 4.11: (a)/(b) Sketch of spin-dependent excitation induced shift and broadening of the exciton line. Upon excitation of an exciton population of one spin species, the exciton line for excitons with parallel (blue) and antiparallel (red) spin is differently affected. (c)/(d) Schematics of how the mechanisms shown in (a) and (b) give rise to a horizontally polarized FWM signal upon excitation with linearly cross-polarized pulses (HV).

We first qualitatively describe why spin-dependent excitation-induced shifts and broadening of the exciton resonance can explain our observations from the previous section. Subsequently, we perform a power-dependent measurement of the exciton coherence times in different polarization

configurations. Finally, we present two modeling approaches to account for the polarization dependence as well as the observed temporal dynamics.

In addition to the saturation upon excitation (phase-space filling, compare Section 1.2), an excitation-induced shift (EIS) or broadening (equivalent to EID in the time-domain) of the exciton resonance can give rise to a FWM signal [7, 143, 144]. FWM spectroscopy has been extensively employed in previous studies to investigate the impact of these nonlinearities on the coherent optical response of semiconductor structures, including GaAs single crystals [145], quantum wells [19], and transition metal dichalcogenides [146, 147]. As visualized in Figures 4.11a and 4.11b, both effects effectively lead to a decrease of the absorption at the unperturbed resonance energy. When first and second pulses in the FWM experiment interfere to form a spatial population grating, EID and EIS lead to a spatial modulation of the absorption coefficient which gives rise to a FWM signal diffracted in the phase-matched direction. Note that this discussion on signal formation can be equivalently conducted considering the spectral grating formed by the first and second pulse (compare Section 1.2.1). When EID and EIS are fully spin-independent, i.e. only depend on the total excitation level, no deviation from the polarization dependence resulting from the phase-space filling is expected. The situation changes when EID and EIS have a spin sensitivity, that is, the exciton linewidth/resonance frequency for spin up (down) excitons is differently affected by the number of excited excitons with the same or opposite spin. This case is visualized in Figures 4.11a and 4.11b by the two different lineshapes (blue and red). In this case, the symmetry of the exciton V-scheme that leads to the vanishing signal in the polarization configuration HVH is lifted as we explain in Figures 4.11c and 4.11d. In the absence of spin-dependent non-linearities, the population gratings $n^{\uparrow\downarrow}$ of spin-up and spin-down exciton states have the same magnitude but are out of phase for cross-linear excitation, compare blue and red spatial gratings in Figure 4.11c. Since the two exciton transitions are not two independent two-level systems but share a common ground state, σ^+ and σ^- light components effectively get diffracted on both gratings and the total FWM signal in both polarization channels vanishes. When however spin-dependent EIS or EID are considered, the relative amplitude of both gratings changes, Figure 4.11d. For example, σ^+ polarized light may diffract more strongly on the spin-up population grating than on the spin-down grating. Therefore, a finite FWM signal remains in both circular polarization channels.

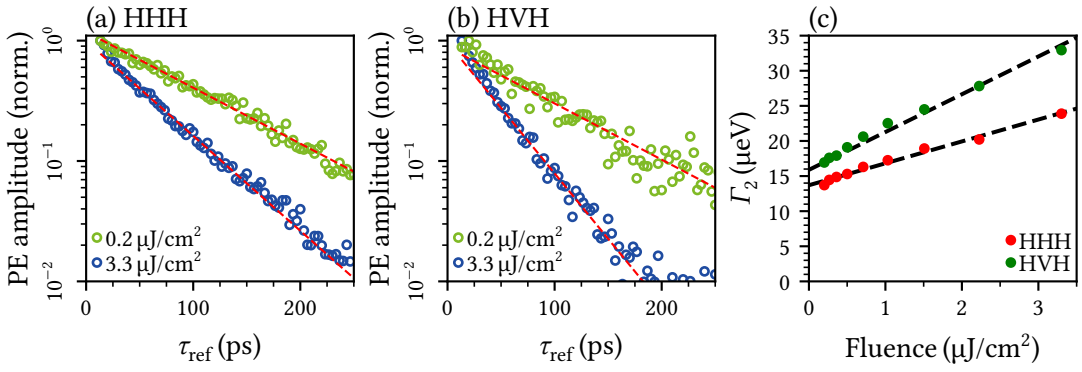

Figure 4.12: (a)/(b) Decay of the PE amplitude in HHH/HVH as a function of $\tau_{ref} = 2\tau_{12}$ for two different values of the applied laser fluence. Red dashed lines represent fits to a single exponential function. (c) Corresponding homogenous linewidth Γ_2 as a function of laser fluence. The black dashed line is a fit to a linear function.

The effect of EID on the exciton decoherence, in particular, is directly measurable with our technique. Therefore, we measure the exciton coherence time T_2 as a function of the total laser fluence (energy per pulse and area of the excitation spot). Figure 4.12a compares the decay

of the PE amplitude in HHH configuration as a function of $\tau_{\mathrm{ref}} = 2\tau_{12}$ for total laser fluences of $0.2\,\mu\mathrm{J/cm^2}$ and $3.3\,\mu\mathrm{J/cm^2}$. We can observe a notable decrease in the decoherence time from $T_2 = 85\,\mathrm{ps}$ to $T_2 = 60\,\mathrm{ps}$. As shown in Figure 4.12c, the homogeneous exciton linewidth $\Gamma_2 = 2\hbar/T_2$ linearly increases with the applied laser fluence, where the slope is given by roughly $3\,\mu\mathrm{eV}/\mu\mathrm{Jcm}^{-2}$. This finding suggests that the decoherence rate of excitons scales with the number of resonantly excited excitons. The measurement is repeated in HVH configuration, Figures 4.12b and 4.12c. Here, the decoherence time for low fluence is with $T_2 = 75\,\mathrm{ps}$ notably shorter than observed in HHH. This difference in decoherence times for the two polarization configurations increases when sweeping the total laser fluence as we present in Figure 4.12c, where the increase of the linewidth in HVH exhibits a larger slope of $5\,\mu\mathrm{eV}/\mu\mathrm{Jcm}^{-2}$. In this way, the ratio between the decoherence rates in HHH and HVH decreases from $\approx 85\,\%$ for zero fluence (linear dependence extrapolated to zero fluence) to roughly $\approx 70\,\%$ in the observed range of laser fluence. We can thus summarize that both the intrinsic linewidth as well as the strength of EID have a dependence on the relative polarization of the excitation pulses. The observed polarization-sensitive EID effect is a further indication of spin-dependent interactions between excitons that we mentioned above. However, it should be highlighted that EID represents a relatively small fraction of the exciton linewidth in the considered range of fluences. To quantify the influence of EID and EIS on the polarization dependence of the FWM signal, we introduce expanded Bloch equations for the exciton in the following.

Phenomenological expansion of Bloch equations

The non-linear optical response of non-interacting excitons can be calculated using the coupled equations of motion for the 3×3 density matrix $\boldsymbol{\rho}$ of the V-scheme consisting of the ground state $|\mathrm{G}\rangle$ and the two exciton states $|\mathrm{X}^{\uparrow\downarrow}\rangle$. The five independent elements of the density matrix are the two microscopic polarizations $p^{\pm} = \langle \mathrm{G}|\rho|\mathrm{X}^{\pm}\rangle$, the two occupations $n^{\pm} = \langle \mathrm{X}^{\pm}|\rho|\mathrm{X}^{\pm}\rangle$ of the excited states, and the spin polarization $s^{+} = \langle \mathrm{X}^{+}|\rho|\mathrm{X}^{-}\rangle = (s^{-})^{*}$. The equations of motion resulting from the Liouville-von Neumann equation (1.2) read as

$$\frac{d}{dt}p^{\pm} = i\Delta p^{\pm} - \Gamma_2 p^{\pm} - i\Omega^{\pm}(1 - n^{\mp} - 2n^{\pm}) + i\Omega^{\mp}s^{\mp} \tag{4.23a}$$

$$\frac{d}{dt}n^{\pm} = i\left(p^{\pm}\Omega^{\pm *} - p^{\pm *}\Omega^{\pm}\right) - \Gamma_1 n^{\pm} \tag{4.23b}$$

$$\frac{d}{dt}s^{+} = i(p^{-}\Omega^{+*} - p^{+*}\Omega^{-}). \tag{4.23c}$$

Here, $\Omega^{\pm} = \mu E^{\pm}(t)/\hbar$ are Rabi frequencies with respect to $\sigma^{\pm}$ polarized components of the slowly varying electric field amplitude $E^{\pm}(t)$. Note that the dipole moments μ of the two exciton transitions are assumed to be equal since the sample does not experience a static circular dichroism. Static circular dichroism can occur in organic-inorganic perovskite crystals that contain chiral molecules such as methylbenzylamine instead of formadinium or methylammonium [148]. A well-established phenomenological approach to account for excitation-induced effects is to introduce population-dependent decay rates and resonance frequencies [3, 4]. To further expand this approach for spin-dependent EID and EIS, we introduce population-dependent decay rates $\Gamma_2^{\pm}$ and resonance frequencies $\omega^{\pm}$ as

$$\Gamma_2^{\pm} = \Gamma_2 + \alpha_{\uparrow\uparrow}n^{\pm} + \alpha_{\uparrow\downarrow}n^{\mp} \tag{4.24a}$$

$$\omega^{\pm} = \omega_0 + \beta_{\uparrow\uparrow}n^{\pm} + \beta_{\uparrow\downarrow}n^{\mp}, \tag{4.24b}$$

where $\alpha_{\uparrow\uparrow}/\alpha_{\uparrow\downarrow}$ (real and positive) measure how strongly the exciton linewidth scales with the excitation level of excitons with the same/opposite spin. Analogously, $\beta_{\uparrow\uparrow}/\beta_{\uparrow\downarrow}$ (real) account for

excitation-induced shifts. We introduce the complex constants $V = \alpha + i\beta$ to compactly write the modified equation of motion for the polarizations $p^{\pm}$ (Equation (4.23a)) as

$$\frac{d}{dt}p^{\pm} = i\Delta p^{\pm} - \Gamma_2 p^{\pm} - i\Omega^{\pm}(1 - n^{\mp} - 2n^{\pm}) + i\Omega^{\mp}s^{\mp} - (V_{\uparrow\downarrow}n^{\mp} + V_{\uparrow\uparrow}n^{\pm})p^{\pm}. \tag{4.25}$$

To calculate the FWM response resulting from the third order polarization $p^{(3)} \propto E_1^* E_2^2$, we expand the density matrix elements in perturbative orders with respect to the electric field. Therefore, we have to solve the following set of equations

$$\frac{d}{dt}p^{\pm(1)} = i\Delta p^{\pm(1)} - \frac{p^{\pm(1)}}{T_2} - i\Omega^{\pm} \tag{4.26a}$$

$$\frac{d}{dt}n^{\pm(2)} = i\left(p^{\pm(1)}\Omega^{\pm *} - p^{\pm *(1)}\Omega^{\pm}\right) - \Gamma_1 n^{\pm(2)} \tag{4.26b}$$

$$\frac{d}{dt}s^{+(2)} = i(p^{-(1)}\Omega^{+*} - p^{+(1)*}\Omega^{-}) \tag{4.26c}$$

$$\begin{aligned}\frac{d}{dt}p^{\pm(3)} = {} & i\Delta p^{\pm(3)} - \Gamma_2 p^{\pm(3)} + i\Omega^{\pm}n^{\mp(2)} + 2i\Omega^{\pm}n^{\pm(2)} + i\Omega^{\mp}s^{\mp(2)} \\ & - (V_{\uparrow\downarrow}n^{\mp(2)} + V_{\uparrow\uparrow}n^{\pm(2)})p^{\pm(1)}.\end{aligned} \tag{4.26d}$$

In the equation for $p^{\pm(3)}$, it can be seen that through the excitation-induced effects, another source term for a third order polarization $\propto n^{(2)}p^{(1)}$ arises. Considering the phase-matching condition of our experiment, such third-order polarization can be interpreted as the scattering of the linear polarization created by the second pulse on the population grating created by the first and second pulses. For simplicity, we consider first and second pulses as delta pulses centered at $t = 0$ and $t = \tau_{12}$, i.e.

$$\Omega^{\pm}(t) = \Omega_1^{\pm}\delta(t) + \Omega_2^{\pm}\delta(t - \tau_{12}). \tag{4.27}$$

We thus arrive at the following solutions for the third-order polarizations that fulfill the phase-matching condition

$$\begin{aligned}p^{\pm(3)}(t) = {} & \mathrm{e}^{i\Delta(t-2\tau_{12})-\Gamma_2 t}\Bigg[(\Omega_2^{\pm})^2\Omega_1^{\pm *}\left(1 + \frac{V_{\uparrow\uparrow}}{2\Gamma_1}\left(1 - \mathrm{e}^{-\Gamma_1(t-\tau_{12})}\right)\right) \\ & + \Omega_2^{\pm}\Omega_2^{\mp}\Omega_1^{\mp *}\left(1 + \frac{V_{\uparrow\downarrow}}{2\Gamma_1}\left(1 - \mathrm{e}^{-\Gamma_1(t-\tau_{12})}\right)\right)\Bigg].\end{aligned} \tag{4.28}$$

The macroscopic response of an inhomogeneous ensemble is obtained from $P^{\pm(3)} \propto \int g(\Delta)p^{\pm(3)}(t, \Delta)$, where $g(\Delta)$ is assumed as a Gaussian distribution of detunings. Using Equation (4.28), we can construct the PE amplitude in the configurations HRH and HRV

$$|E_{\mathrm{HRH}}| \propto \frac{|\mu|^4}{\hbar^3}E_1^* E_2^2 \mathrm{e}^{-2\Gamma_2\tau_{12}}\left\{\cos^2(\varphi)\left(1 + \frac{V_{\uparrow\uparrow}}{2\Gamma_1}\left(1 - \mathrm{e}^{-\Gamma_1\tau_{12}}\right)\right) + \frac{V_{\uparrow\downarrow} - V_{\uparrow\uparrow}}{4\Gamma_1}\left(1 - \mathrm{e}^{-\Gamma_1\tau_{12}}\right)\right\} \tag{4.29a}$$

$$|E_{\mathrm{HRV}}| \propto \frac{|\mu|^4}{\hbar^3}E_1^* E_2^2 \mathrm{e}^{-2\Gamma_2\tau_{12}}\frac{|\sin(2\varphi)|}{2}\left\{1 + \frac{V_{\uparrow\uparrow}}{2\Gamma_1}\left(1 - \mathrm{e}^{-\Gamma_1\tau_{12}}\right)\right\}. \tag{4.29b}$$

Here, we can distinguish between spin-independent and spin-dependent excitation-induced effects. For spin-independent EID and EIS, i.e. $V_{\uparrow\uparrow} = V_{\uparrow\downarrow}$, the signal amplitudes are modified while the qualitative shape of the polar dependences is unchanged with respect to the model of non-interacting excitons. For spin-dependent EID and EIS, i.e. $V_{\uparrow\uparrow} \neq V_{\uparrow\downarrow}$, a horizontally polarized signal, solely arising from spin-dependent interaction is expected for linearly cross-polarized excitation $\propto V_{\uparrow\downarrow} - V_{\uparrow\uparrow}$ independent of φ which fits our observations presented above. We thus

can conclude that indeed spin-dependent exciton-exciton interactions can qualitatively explain the modified polarimetric behavior of the exciton resonance as we suggested above using the schematics shown in Figure 4.11. We discuss in the following if the simplified expansion of the Bloch equations can also quantitatively reproduce the polarimetric and temporal behavior that we observe.

The excitation-induced contributions predicted by Equations (4.29) scale with the ratio between the interaction constants V and the population decay rate Γ_1. Signals of comparable magnitude in the configuration HHH and HVH thus require a strong influence of EID/EIS. This prediction is a contradiction to the observation presented in Figure 4.12c where EID represents only a small correction to the intrinsic linewidth. Furthermore, all excitation-induced contributions in Equations (4.29) share a prefactor $\propto (1 - \exp(-\Gamma_1\tau_{12}))$ that rises on a timescale of $1/\Gamma_1 = T_1 \approx 100\,\mathrm{ps}$ [65]. In the experiment, no deviations from single exponential decays on that timescale are observed, compare photon-echo decays in Figure 4.12. Note that we neglected higher-order terms with respect to the external optical field which lead to a power-dependent decay of the excitation-induced signal. Even when high-order terms are taken into account, the described model is not capable of explaining the polarization-sensitive decoherence times that we observed in Figure 4.12. We thus can conclude that the simplified consideration of interaction effects between excitons through population-dependent linewidths and shifts (Equations (4.24)) is capable of accounting for the additional channels of signal formation, but results in wrong statements of the observed temporal dynamics as well as the relative amplitudes of signals in different polarization configurations. Before we present an alternative theoretical approach, we make use of Equations (4.28) and (4.29) in the limit $\tau_{12} \gg T_1$ to distinguish between EIS- and EID-induced contributions as well as the relative interaction strengths between excitons of the same or opposite spins.

The contribution of EID and EIS to the electric signal field in Equations (4.29) have a relative optical phase shift of $\pi/2$, which makes it possible, in principle, to distinguish both effects in a PE experiment [149]. However, when considering the absolute value of the signal field, as in our experiments, the indistinguishability is lifted when using excitation with circularly polarized pulses. Therefore, we investigate the polarization protocol that we already used in Section 4.1 for the identification of the biexciton, where the first pulse is circularly polarized ($\sigma^{\pm}$), and the second pulse is linearly polarized with variable polarization angle φ relative to the detected horizontal polarization component ($\sigma^{\pm}$RH). Taking into account both spin-dependent EID and EIS, the signal field in this configuration can be written as

$$|E_{\sigma^{\pm}\mathrm{RH}}| \propto \sqrt{\cos^2(\varphi \pm \vartheta) + \frac{\left(\tilde{V}_{\uparrow\uparrow} - \tilde{V}_{\uparrow\downarrow}\right)^2}{4\tilde{V}_{\uparrow\uparrow}\tilde{V}_{\uparrow\downarrow}}} \tag{4.30a}$$

$$\tilde{V}_j = \sqrt{\left(1 + \frac{\alpha_j}{2\Gamma_1}\right)^2 + \left(\frac{\beta_j}{2\Gamma_1}\right)^2}, \quad j = \uparrow\uparrow, \uparrow\downarrow \tag{4.30b}$$

$$\vartheta = \frac{1}{2}\arctan\left[\frac{\beta_{\uparrow\uparrow} - \beta_{\uparrow\downarrow}}{\left(2\Gamma_1 + \alpha_{\uparrow\uparrow}\right)\left(2\Gamma_1 + \alpha_{\uparrow\downarrow}\right) + \frac{\beta_{\uparrow\uparrow}\beta_{\uparrow\downarrow}}{2\Gamma_1}}\right]. \tag{4.30c}$$

In the absence of excitation-induced effects, the signal dependence reduces to $|E_{\sigma^{+}\mathrm{RH}}| \propto |\cos(\varphi)|$ with local extrema for $\varphi = 0, \pi$. This polar dependence is rotated by an angle ϑ depending on the imbalance between the EIS coefficients $\beta_{\uparrow\uparrow} - \beta_{\uparrow\downarrow}$. Such rotation is not expected for (spin-dependent) EID and therefore allows us to distinguish between spin-selective EID and EIS.

Experimentally, we can indeed observe a rotation of the polar dependences on a short timescale. As shown in Figure 4.13a, for $\sigma^{\pm}$RH and $\tau_{12} = 0$, we observe rotated polar dependences in opposite directions by an angle of roughly $\vartheta = 0.2\pi$. We measure ϑ as a function of $\tau_{\mathrm{ref}} = 2\tau_{12}$ in Figure 4.13b. Here, we see that ϑ decays to zero after roughly 15 ps. Note that in this regime, the optical pulses in our experiment temporally overlap as we highlight by plotting the cross-correlation between the reference and first pulse (red line), which represents a measure of the temporal overlap. This observation suggests that the EIS contribution may depend on the macroscopic polarization of the ensemble which is present for overlapping pulses in our experiments. However, there are other realistic contributions to the observed rotation of polar dependences such as the formation of a macroscopic spin polarization through the excitation with circularly polarized light or exciton fine structure splitting. To further discuss these findings, measurements with shorter pulses and magnetic field dependencies are required. Since a rotation angle of the polar dependence upon excitation with circularly polarized light is not observed on a timescale $\tau_{\mathrm{ref}} > 15$ ps, we conclude that the observed modification of exciton polarization dependences is a manifestation of spin-dependent EID.

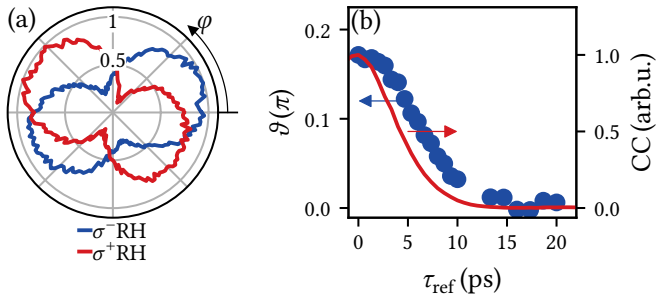

Figure 4.13: (a) Polar dependences of the FWM amplitude in the configurations $\sigma^{\pm}$RH measured for $\tau_{12} = 0$. (b) The rotation angle ϑ of the rosettes in (a) measured as a function of $\tau_{\mathrm{ref}} = 2\tau_{12}$. For comparison, we show in red the cross-correlation (CC) between the first and reference pulse being a measure for the temporal overlap of the pulses at a given value of τ_{12}.

We further comment on the relative size of the constants $\alpha_{\uparrow\downarrow}$ and $\alpha_{\uparrow\uparrow}$ using the qualitative shape of the HRH dependence in Figure 4.10a. In Figures 4.14a–c, we compare the qualitative shape of the polar rosettes in HRH configuration for the cases $\alpha_{\uparrow\downarrow} = \alpha_{\uparrow\uparrow}$, $\alpha_{\uparrow\downarrow} > \alpha_{\uparrow\uparrow}$, and $\alpha_{\uparrow\downarrow} < \alpha_{\uparrow\uparrow}$ according to Equation (4.29). The experimental curve is compatible with the case $\alpha_{\uparrow\downarrow} > \alpha_{\uparrow\uparrow}$. Here, no zero crossing is observed and thus the signals in co-polarized configuration (HHH) $\propto 1 + \frac{\alpha_{\uparrow\uparrow}+\alpha_{\uparrow\uparrow}}{4\Gamma_1}$ and cross-polarized configuration (HVH) $\frac{\alpha_{\uparrow\downarrow}-\alpha_{\uparrow\uparrow}}{4\Gamma_1}$ share the same sign, which requires $\alpha_{\uparrow\downarrow} - \alpha_{\uparrow\uparrow} > 0$. Based on this discussion, we can therefore conclude that the exciton linewidth is more strongly broadened in the presence of other excitons with opposite spin.

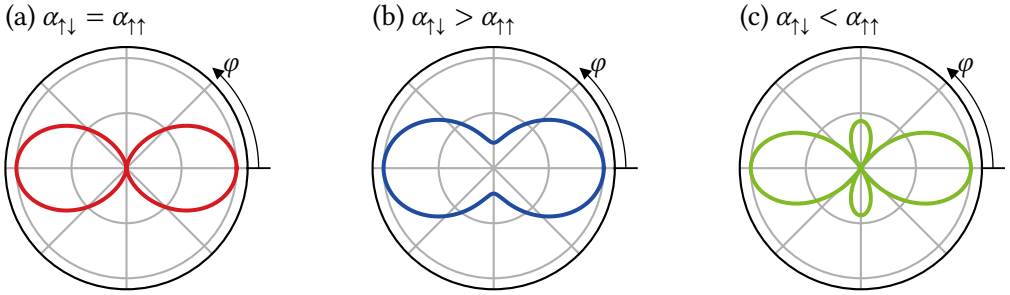

Figure 4.14: Qualitative shape of polar rosettes in the presence of excitation-induced dephasing for different cases of the relative size of the interaction constants $\alpha_{\uparrow\uparrow}$/ $\alpha_{\uparrow\downarrow}$.

Two-exciton model

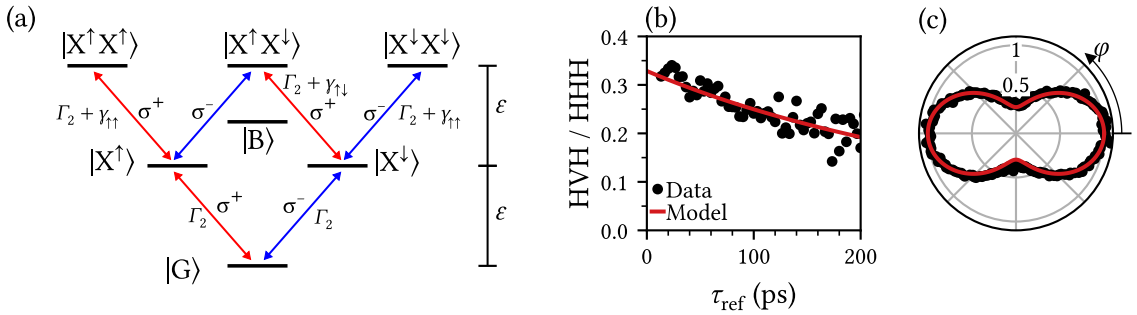

Figure 4.15: (a) Visualization of the two-exciton model as introduced in the text. (b) Dynamics of the ratio HVH/HHH as measured for a fluence of 0.2 µJcm^{-2} and fit to the model (4.34). (c) Comparison of the experimental and modeled polar rosette in the configuration HRH.

We present an alternative model based on References [150–153] that takes into account excitation-induced dephasing based on a correlated two-exciton model. As we will show below, the model makes statements about polarization-dependent linewidths and can quantitatively reproduce the experimentally observed polar rosettes in a regime of weak EID.

We consider a two-exciton model visualized in Figure 4.15a consisting of the ground state $|\mathrm{G}\rangle$, singly excited exciton states $|\mathrm{X}^{\uparrow}\rangle$ / $|\mathrm{X}^{\downarrow}\rangle$, as well as the three different spin configurations for unbound but correlated two-exciton states $|\mathrm{X}^{\uparrow}\mathrm{X}^{\uparrow}\rangle$, $|\mathrm{X}^{\uparrow}\mathrm{X}^{\downarrow}\rangle$, and $|\mathrm{X}^{\downarrow}\mathrm{X}^{\downarrow}\rangle$. The bound biexciton state $|\mathrm{B}\rangle$ is also shown in the scheme but is not excited in our experiments as discussed above. Note that higher correlated states with more than two excitons are not excited when we neglect nonlinear polarizations higher than FWM. In such consideration, many-body effects can be introduced phenomenologically as excitation-induced shifts or modified decoherence rates of the two-exciton to one-exciton states [150]. Based on our discussion in the previous section, we solely consider modified decoherence rates $\Gamma_2 \rightarrow \Gamma_2 + \gamma$, where we further distinguish between parallel and antiparallel spins ($\gamma_{\uparrow\uparrow}$ / $\gamma_{\uparrow\downarrow}$), as indicated in Figure 4.15a. The rates γ are assumed to depend on the laser fluence. Calculating the FWM signal of such a six-level system leads to the interference of quantum paths involving the two-exciton to one-exciton and one-exciton to ground state transitions. In this way, the polarization dependence as well as the decay dynamic of the system is modified with respect to the one-exciton model. Following References [150, 151], we construct the dipole moments of the transitions $|\mathrm{X}^{\uparrow\downarrow}\rangle \rightarrow |\mathrm{X}^{\uparrow\downarrow}\mathrm{X}^{\uparrow\downarrow}\rangle$ as $\sqrt{2}(1-\nu)\mu$ and of the transitions $|\mathrm{X}^{\uparrow\downarrow}\rangle \rightarrow |\mathrm{X}^{\uparrow}\mathrm{X}^{\downarrow}\rangle$ as $(1-\nu)\mu$, where μ is the dipole moment of the groundstate to one-exciton transitions. The parameter ν, with $0 \leq \nu \leq 1$, accounts for the relative importance of phase-space filling to the FWM response. In the case $\nu = 0$, space-filling is absent (no FWM response) and in the case $\nu = 1$ the system simplifies to the V-scheme describing fully independent excitons with saturable absorption. We discuss the impact of excitation-induced dephasing on the polarimetric and temporal characteristics of this model in the following. Using an analogous calculation procedure as shown for the biexciton system (Section 4.1.2), we arrive at the following temporal dependence of the PE signal measured in the configuration HRH

$$|E_{\mathrm{HRH}}| \propto \mathrm{e}^{-2\Gamma_2\tau_{12}} \left\{ \cos^2(\varphi) \left[1 - (1-\nu)^2 \mathrm{e}^{-\gamma_{\uparrow\uparrow}\tau_{12}} \right] + \frac{(1-\nu)^2}{2} \left[\mathrm{e}^{-\gamma_{\uparrow\uparrow}\tau_{12}} - \mathrm{e}^{-\gamma_{\uparrow\downarrow}\tau_{12}} \right] \right\}, \tag{4.31}$$

consisting of a term proportional to $\cos^2\varphi$ for $\nu \neq 0$ and a polarization-independent part for $\nu \neq 1$ and $\gamma_{\uparrow\uparrow} \neq \gamma_{\uparrow\downarrow}$. Two special cases are the configurations HHH and HVH

$$|E_{\mathrm{HHH}}| \propto \mathrm{e}^{-2\Gamma_2\tau_{12}}\left\{1 - \frac{(1-\nu)^2}{2}\left[\mathrm{e}^{-\gamma_{\uparrow\uparrow}\tau_{12}} + \mathrm{e}^{-\gamma_{\uparrow\downarrow}\tau_{12}}\right]\right\}. \tag{4.32a}$$

$$\left|E_{\mathrm{HVH}}\right| \propto \mathrm{e}^{-2\Gamma_2\tau_{12}}\frac{(1-\nu)^2}{2}\left\{\mathrm{e}^{-\gamma_{\uparrow\uparrow}\tau_{12}} - \mathrm{e}^{-\gamma_{\uparrow\downarrow}\tau_{12}}\right\}. \tag{4.32b}$$

Here, the signal in HHH configuration has a component arising from the one-exciton to ground state transitions, which decays at the unperturbed decoherence rate Γ_2. Instead, the signal in HVH solely stems from the two-exciton to one-exciton transitions and decays faster as given by the rates $\gamma_{\uparrow\uparrow}$ and $\gamma_{\uparrow\downarrow}$. Note however, due to the different signs of the contributions resulting from the anti-parallel and parallel spin configurations, a finite rise time or, depending on the relative size of $\gamma_{\uparrow\uparrow}$ and $\gamma_{\uparrow\downarrow}$, a sign inversion of the HVH signal at a non-zero delay τ_{12} is predicted by the model. As discussed in the previous section, the signal in HHH and HVH share the same sign. This behavior is compatible with the model if the term $\propto \mathrm{e}^{-\gamma_{\uparrow\uparrow}\tau_{12}}$ dominates over the term $\propto \mathrm{e}^{-\gamma_{\uparrow\downarrow}\tau_{12}}$ in Equation (4.32b). This condition is realized under the assumption that the correlated state of two excitons with opposite spins $|\mathrm{X}^{\uparrow}\mathrm{X}^{\downarrow}\rangle$ decays significantly faster as the ones with equal spins $|\mathrm{X}^{\uparrow}\mathrm{X}^{\uparrow}\rangle$ / $|\mathrm{X}^{\downarrow}\mathrm{X}^{\downarrow}\rangle$, i.e. $\gamma_{\uparrow\downarrow} \gg \gamma_{\uparrow\uparrow}$, which is in agreement with the picture of spin-dependent EID. In this limiting case, Equation (4.31) can be simplified to

$$|E_{\mathrm{HRH}}| \propto \mathrm{e}^{-2\Gamma_2\tau_{12}}\left\{\cos^2(\varphi)\left[1 - (1-\nu)^2\mathrm{e}^{-\gamma_{\uparrow\uparrow}\tau_{12}}\right] + \frac{(1-\nu)^2}{2}\mathrm{e}^{-\gamma_{\uparrow\uparrow}\tau_{12}}\right\}. \tag{4.33}$$

Here, the signal in HVH ($\varphi = 0$) decays with a rate of $\Gamma_2 + \gamma_{\uparrow\uparrow}/2$ whereas the main contribution of the signal in HHH ($\varphi = 0$) decays at the unperturbed rate Γ_2. A slow rise of the signal is not expected in both polarization configurations. In this way, the ratio HVH/HHH experiences a decaying dynamic given by

$$\mathrm{HVH\ /\ HHH} = \left[\frac{2\mathrm{e}^{\gamma_{\uparrow\uparrow}\tau_{12}}}{(1-\nu)^2} - 1\right]^{-1}. \tag{4.34}$$

Here it can be seen that the ratio between the signal in HVH and HHH for $\tau_{12} = 0$ is determined by the parameter ν whereas its decaying dynamic is defined by $\gamma_{\uparrow\uparrow}$. In this way, even in the case of weak EID ($\gamma_{\uparrow\uparrow} \ll \Gamma_2$), comparable magnitudes of the signals in HHH and HVH can be expected. This represents a strong difference to the previously presented model in which a strong signal in HVH configuration requires comparable magnitudes of the parameter α and the population decay rate Γ_1 (compare Equation (4.29)). The model (4.34) is fitted to the corresponding experimental data for a fluence of $0.3\,\mu\mathrm{Jcm}^{-2}$ which yields $\gamma_{\uparrow\uparrow} = (5.6 \pm 0.5)\,\mu\mathrm{eV}$ and $\nu = 0.30 \pm 0.01$. As shown in Figure 4.15b, the resulting curve can excellently describe the experimental data for the ratio HVH/HHH. In this way, also the polar rosette for $\tau_{\mathrm{ref}} = 20\,\mathrm{ps}$ is well described by Equation (4.33) with the obtained values for $\gamma_{\uparrow\uparrow}$ and ν, Figure 4.15c. The model thus is successful in describing both the polarization-dependent decoherence rates at a given laser fluence as well as the observed qualitative shape of the polar rosettes.

The agreement between the two-exciton model and the experimental observations is found under the assumption of a significantly faster decoherence of the two-exciton state with different spin, i.e. $\gamma_{\uparrow\downarrow} \gg \gamma_{\uparrow\uparrow}$. A microscopic explanation for this behavior might be the relaxation to the biexciton state. As shown in Figure 4.15a the biexciton state is energetically below the considered unbound two-exciton state. Relaxation of two excitons into this state, for example through phonon emission, may represent the additional scattering channel that could explain the spin-dependent exciton interactions presented in this section. The derived value of the

parameter ν, approximately 0.3, established a reasonable scenario wherein excitons are localized, thereby exhibiting a substantial space-space filling effect ($\nu \neq 0$), yet they are not entirely isolated ($\nu \neq 1$). This is in contrast to well-isolated excitons in (In,Ga)As quantum dots that are studied in Part II of the thesis.

4.3 Conclusions

This chapter demonstrated the important role of spin-dependent exciton interactions in the non-linear optical response of organic-inorganic perovskites. In $MAPbI_3$, under excitation with broadband femtosecond pulses, we observed the formation of biexcitons, a bound state of two excitons with opposite spins. The obtained value of the biexciton binding energy of 2.4 meV amounts to roughly 20 % of the exciton binding energy in this material, which is in agreement with the ratio found in conventional semiconductors [154]. Note that biexcitons can not be observed in all bulk semiconductors. Potentially, a certain localization of excitons in $MAPbI_3$ manifested in the inhomogeneous broadening studied in Section 3.1 favors the formation of biexcitons. Remarkably, the biexciton binding energy was extracted although the period of the quantum beats exceeds the decoherence time of the system. For this purpose, a measurement protocol based on polarization beats was developed whose resolution is limited only by the difference in decoherence rates of exciton and biexciton.

In $FA_{0.9}Cs_{0.1}PbI_{2.8}Br_{0.2}$, we discovered a different regime of exciton interactions that we interpret as a spin-dependent excitation-induced dephasing of excitons. We introduced two modeling approaches: one based on population-dependent decoherence rates, and a correlated two-exciton model. The former qualitatively described the polarization dependence of the photon echo signal but failed to account for polarization-dependent decoherence rates. Consequently, we presented an alternative framework involving correlated exciton states with varying decoherence times. This approach allowed us to understand both the polarimetric properties and the decay dynamics by considering an asymmetry between the decoherence rates for correlated exciton states with parallel and opposite spins. Importantly, the two-exciton model reproduces all experimental observations even in the case of weakly interacting excitons. These findings highlight the significant impact of exciton interactions in correctly interpreting the polarization dependences of non-linear optical spectra in organic-inorganic perovskites.

Part II

Coherent control of photon echoes from quantum dots

Observation of Rabi rotations of a quantum dot ensemble using spatially shaped laser pulses

5

The observation of collective Rabi rotations from a quantum dot (QD) ensemble is usually hampered by the inhomogeneity of the laser intensity profile that is used to excite the QDs. We tackle this problem in this chapter by introducing a flattop intensity profile of the refocussing pulse in a photon echo (PE) sequence. We show that this modification of the experimental scheme allows us to observe pronounced Rabi rotations up to a pulse area of 5.5π. Further, we compare Rabi rotations arising from neutral and charged QDs using the PE polarimetry technique. Here, it is demonstrated that a photo-induced charging of the QDs leads to a significant reduction of the number of neutral QDs under resonant excitation. Finally, we analyze the damping of Rabi rotations considering the interaction with acoustic phonons. The results presented in this chapter were previously published in:

S. Grisard, H. Rose, A. V. Trifonov, R. Reichhardt, D. E. Reiter, M. Reichelt, C. Schneider, M. Kamp, S. Höfling, M. Bayer, T. Meier, and I. A. Akimov, "Multiple Rabi rotations of trions in InGaAs quantum dots observed by photon echo spectroscopy with spatially shaped laser pulses", Physical Review B **106**, 205408 (2022)
DOI: 10.1103/PhysRevB.106.205408,

The results of a numerical modeling procedure, presented in Section 5.3, were obtained by Hendrik Rose within the research group of Torsten Meier at the University of Paderborn.

5.1 Characterization of the quantum dot–cavity system

For the first optical characterization of the QD–cavity system, we apply angle-resolved photoluminescence spectroscopy (ARPL) using an experimental setup described in Reference [155]. The technique allows to characterize the spectral position and width of the cavity mode as a function of the emission angle. The resonance energy of the cavity E_0 is expected to exhibit a quadratic dependence on the emission angle θ as follows from Bragg's law [156]

$$E_0(\theta) \propto \frac{1}{2d\cos(\theta)} \approx E_0(\theta = 0)\left(1 + \frac{\theta^2}{2n^2}\right), \tag{5.1}$$

where d is the thickness of the cavity and n is the refractive index of the cavity material (GaAs in our case). We test this prediction on the studied sample using the ARPL technique. As explained in Figure 5.1a, the basic principle of the technique is based on Fourier spectroscopy. The sample is placed in a helium flow cryostat and cooled down to a temperature of 5 K. We excite the sample from the top surface by a continuous wave laser with a photon energy of 2.3 eV, which is focussed using a microscope objective with a high numerical aperture of $N_A = 0.4$. Thus, the objective collects the photoluminesce light emitted within a wide range of angles $\pm \arcsin N_A/n \approx \pm 23.5°$, where $n \approx 1$ is the refractive index of air. The entrance slit of a spectrometer with a two-dimensional charge-coupled device (CCD) detector is placed in the

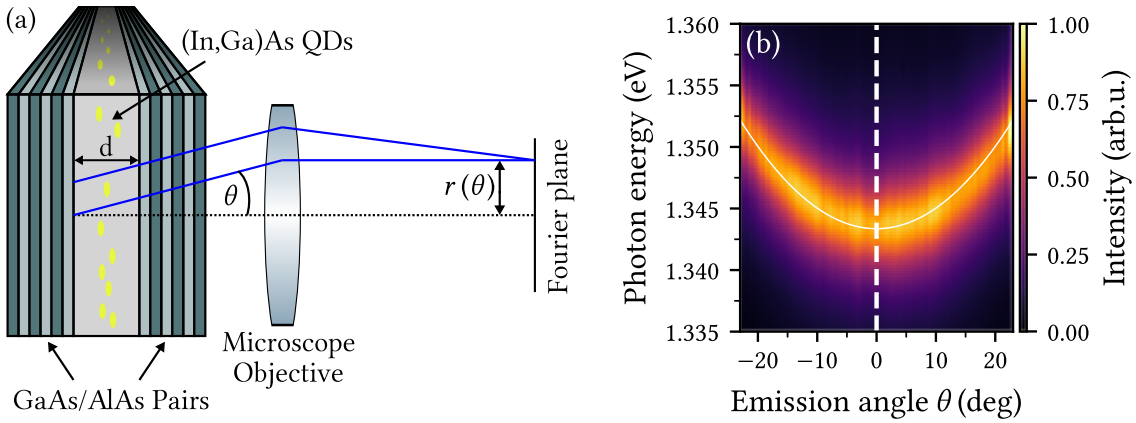

Figure 5.1: (a) Schematic view of the studied QD–cavity system and working principle of Fourier spectroscopy. The sample consists of a single layer of (In,Ga)As QDs that is embedded in a microcavity with thickness d formed by two Bragg mirrors. The Bragg mirrors consist of GaAs/AlAs pairs. (b) Angle-resolved photoluminescence spectrum measured at a temperature of 5 K. The angle dependence shows a parabolic behavior of the resonance frequency, which is a characteristic of planar microcavities.

Fourier plane of the microscope objective, i.e. at a distance $2f$ from the sample surface, where f is the focal length of the objective. In the Fourier plane, the emission angle θ is mapped to a radial position $r(\theta)$, as examplary shown in Figure 5.1a for one emission angle. Therefore, the dimension of the CCD detector parallel to the entrance slit of the spectrometer includes information about the emission angle whereas the perpendicular dimension is used for the spectral resolution.

The measured ARPL spectrum is presented in Figure 5.1b as a two-dimensional color map. For $\theta = 0$, the photoluminescence emission can be observed at 1.345 eV. The peak emission shifts in a quadratic manner towards higher energies as a function of the emission angle, which is a characteristic of the microcavity as explained above. The solid white line in Figure 5.1b shows the quadratic dependence according to Equation (5.1) taking into account the resonance energy at θ=0 and the refractive index of GaAs of 3.5 from Reference [157]. We can conclude that the cavity is in resonance with the emission spectrum of the QD ensemble. We further characterize the spectral width of the cavity mode using the cross-section of the ARPL spectrum for $\theta = 0$, plotted in Figure 5.2a. The spectrum can be well fitted by a Lorentzian function, which yields a full width at half maximum (FWHM) of 6 meV, resulting in a quality factor of roughly $Q \approx 200$. For comparison, we show the spectrum of the picosecond laser pulses that we incorporate in the following for the PE experiments. The spectral width of 0.3 meV is significantly narrower than the cavity width. Equivalently, the photon lifetime in the cavity is significantly shorter than the duration of the laser pulses. The main effect of the cavity is therefore to enhance the light-matter interaction of those QDs that are in resonance with the cavity mode whereas, for example, modifications of the laser spectrum can be neglected from the discussions presented in this chapter.

We move on to the time-resolved four-wave mixing (FWM) study of the sample at a temperature of 1.5 K using the experimental setup described in Section 2.1. For all experiments, we use the picosecond regime of the MIRA900 laser and tune the photon energy to the resonance of the sample at 1.345 eV. At first, the optical pulses are linearly co-polarized. The intensity profile of the laser pulses in the focus is a Gaussian with a FWHM of roughly 100 µm. Figure 5.2b depicts an exemplary PE sequence, where we set the delay between first and second pulse to $\tau_{12} = 40$ ps and individually measure the cross-correlations between the reference pulse and first, second, and PE

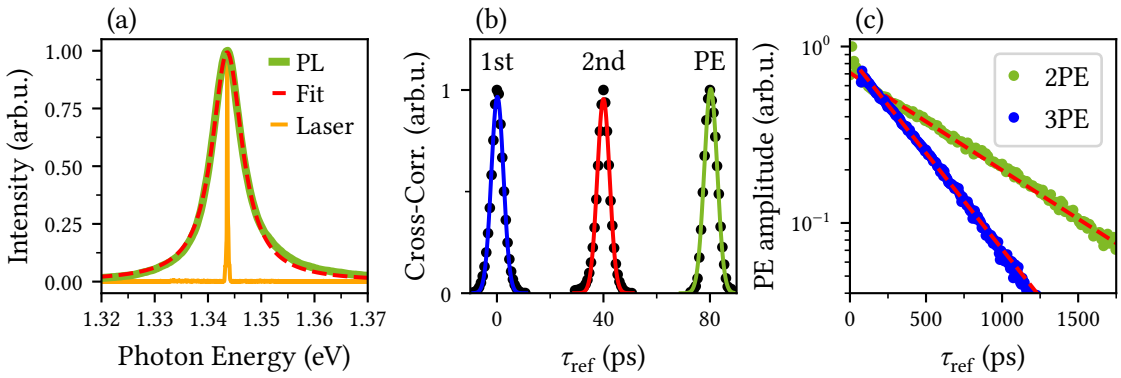

Figure 5.2: (a) Comparison of the photoluminescence (PL) spectrum of the QD cavity spectrum (green) and the laser spectrum (orange) of the picosecond laser pulses used for the transient experiments. (b) Exemplary PE sequence measured by the cross-correlation between reference pulse and first, second, and PE pulses, respectively. All pulses are well described by Gaussian functions (solid lines) with a width of roughly 4 ps. Note that the separately measured cross-correlations are normalized to the maximum value. (c) Decay of the two-pulse and three-pulse PE amplitude (2PE/3PE), measured for linearly co-polarized pulses. The red dashed lines show fit to exponential functions, which yields the decoherence time T_2 and population decay time T_1.

pulse. All pulses are fitted by a Gaussian (solid lines in Figure 5.2b), from which the respective durations can be extracted. First and second pulses share a duration of 3.8 ps, the PE pulse has a duration of roughly 4.3 ps. Note that the duration of the PE is mainly set by the duration of the laser pulses, since the spectrally narrow laser pulses only excite a subensemble of QDs as can be seen from the comparison of the spectra in Figure 5.2a.

Next, we extract the homogenous decoherence time T_2 by a measurement of the PE amplitude as a function of $\tau_{\mathrm{ref}} = 2\tau_{12}$, presented in Figure 5.2c. For $\tau_{\mathrm{ref}} > 100$ ps, the decay is well described by an exponential function with a decay constant of $T_2 = 790$ ps, corresponding to a homogeneous linewidth of $\Gamma_2 = 2\hbar/T_2 = 1.67\,\mu\mathrm{eV}$. We note that for $\tau_{\mathrm{ref}} < 100$ ps, we observe a faster decay of the PE amplitude that deviates from the single exponential. We comment on this behavior below where we discuss the interaction between the QDs and acoustic phonons. As typical for self-assembled QDs at cryogenic temperatures [53], the decoherence time T_2 is solely limited by the finite population lifetime, which we demonstrate by a comparison of the two-pulse PE decay with the three-pulse PE decay in Figure 5.2c. The latter is reprinted by permission from Reference [158]. The three-pulse PE decays exponentially with a time constant of $T_1 = 400$ ps, such that the condition of the limiting case $T_2 = 2T_1$ is roughly fulfilled (compare Equation (1.6)). The measured values of T_1 and T_2 coincide with those obtained on a sample resulting from the same wafer reported in Reference [159].

For the analysis of Rabi rotations from the QD ensemble, we incorporate the flattop intensity profile for the second beam as characterized in Section 2.2. Before we quantitatively compare the achieved improvement of the Rabi rotations, we apply the photon echo polarimetry technique to distinguish the Rabi rotations arising from charged and uncharged QDs.

5.2 Distinction of Rabi rotations from charged and uncharged quantum dots

In the context of collective Rabi rotations from QDs, a further source of dephasing results from the possible coexistence of various exciton complexes such as excitons and trions that may exhibit different dipole moments [160]. The excitation of biexcitons can be ruled out since the expected binding energy in the range of 3 meV, as reported in Reference [161], is significantly larger than the spectral width of the picosecond laser pulses. The PE polarimetry technique (Section 1.2.3) allows to identify the contributions from various exciton complexes and enables to independently address different subensembles by selecting appropriate polarizations of the involved laser pulses. For uncharged quantum dots (excitons), with a V-type energy level arrangement as shown in Figure 5.3a, we expect a $\cos^2(\varphi)$ dependence on the relative linear polarization angle between the first and second pulse. In contrast, for charged quantum dots (trions) with a four-level scheme as depicted in Figure 5.3b, we expect a $\cos(2\varphi)$ dependence. Both dependences are plotted in Figures 5.3c and 5.3d, respectively. Since the energetic splitting between exciton and trion is typically much smaller than the inhomogeneous broadening of the ensemble, these complexes cannot be spectroscopically distinguished by linear techniques or a FWM experiment with co-polarized optical pulses. However, when choosing $\varphi = \pi/2$ only the trion contributes to the detected signal, while only the exciton contributes for $\varphi = \pi/4$. We refer to these polarization contributions as HVH and HDH in the following.

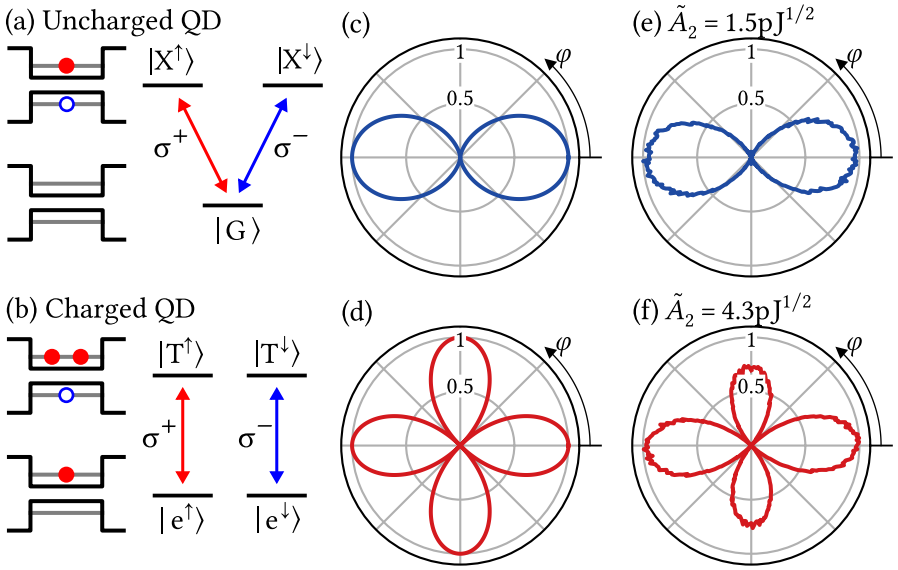

Figure 5.3: (a)/(b) Schematics of the energy level arrangement of excitons and trions. (c)/(d) Theoretical polar rosettes for the level schemes in (a) and (b). (e)/(f) Experimentally observed polar rosettes for two different values of the applied power of the second pulse as indicated in the figure titles, given in units of the square root of the energy per pulse, which is a measure for the pulse area.

We measure polar dependences of the PE amplitude for a delay of $\tau_{12} = 40\,\mathrm{ps}$. Interestingly, we find that the qualitative shape of the polar rosettes depends on the applied optical power, which is shown in Figures 5.3e and 5.3f. Here, we plot the measured polar rosettes for two values of the pulse area of the second beam, which is given in units of the square root of the energy per pulse $\tilde{A}_2$. For the value $\tilde{A}_2 = 1.5\,\mathrm{pJ}^{1/2}$, we observe a $\cos^2\varphi$ dependence indicating that the QDs are uncharged. For a higher pulse area of $\tilde{A}_2 = 4.3\,\mathrm{pJ}^{1/2}$, Figure 5.3f, we find also local

maxima in the cross-polarized HVH configuration, which is a characteristic of the four-level trion scheme. The observed power-dependent polarimetric behavior hints at a power-dependent ratio of charged and uncharged QDs within the ensemble.

To quantify the charging effect, we measure the signals in HVH and HDH continuously as a function of $\tilde{A}_2$, the result is presented in Figure 5.4a. In the HVH configuration, we observe clear Rabi rotations from the ensemble, with three distinct local maxima associated with pulse areas of $A_2 = \pi, 3\pi, 5\pi$, as well as two local minima for $A_2 = 2\pi, 4\pi$ (Equation (2.7)). In contrast, the Rabi rotations in the HDH configuration are more strongly damped, with only one observable local maximum. Additionally, we observe that the first maximum of the signal in HVH is shifted towards higher optical powers by a factor of 2.2 relative to the signal in HDH. This shift could be attributed to differences in dipole moments between the exciton and trion [160]. However, our analysis of the intensity dependence of the PE amplitude for the trion up to the first maximum indicates that the damping mechanism for the Rabi rotations of excitons and trions is different. Specifically, the signal for the exciton follows a $\sin^2(A_2/2)$ as highlighted by the red dashed line in Figure 5.4a. In contrast, we observe a significant deviation for the trion, which we highlight with the red area in Figure 5.4a. Instead, the signal for the trion in HVH configuration follows a polynomial function of a higher degree in the low power range, suggesting that another power-dependent contribution leads to an increase in the signal. We associate this finding with a photo-charging of the QDs [162], that occurs on a slower timescale than the decoherence times of excitons and trions [163]. Increasing the optical power leads to an increase in the number of singly charged QDs and a corresponding decrease in the number of neutral excitons, which explains the strong damping of the PE signal measured in the HDH configuration. Note that the process of QD discharging does not affect the temporal dynamics of the PE and its decay, but it does change the ratio between the number of excitons and trions contributing to the signal.

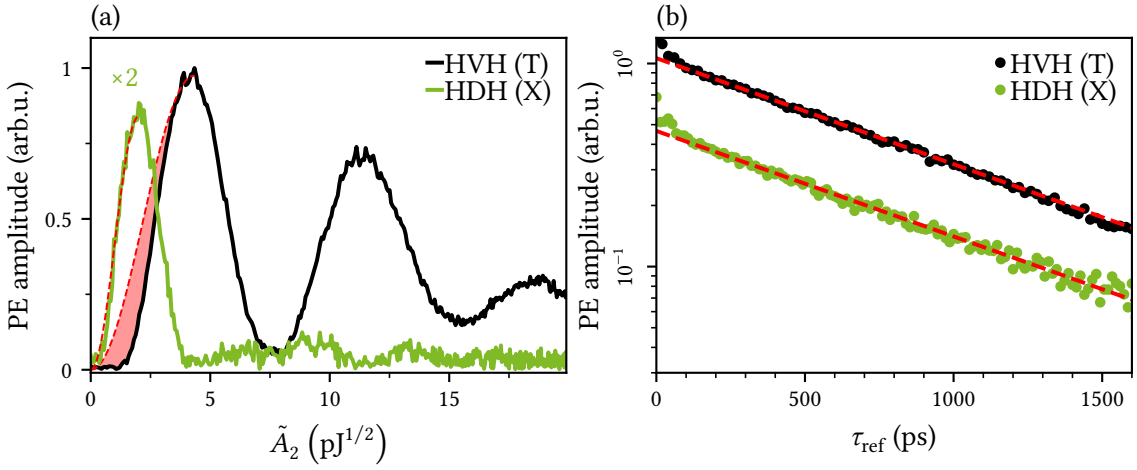

Figure 5.4: (a) PE amplitude as a function of the pulse area of the second beam captured in the polarization configurations HVH (trion/T) and HDH (exciton/X). The red dashed lines show the ideal $\sin^2(A_2/2)$ dependences, compare Equation (2.7). For HVH, the red area highlights the discrepancy between the ideal and measured dependence. (b) Decay of the PE amplitude for the configuration HVH and HDH. Red lines represent fits to exponential functions.

We compare the homogeneous linewidth associated with charged and uncharged QDs. In Figure 5.4b, we show the decays of the PE amplitude measured in the configurations HDH and HVH. For both resonances, we extract $T_2 = 0.83\,\text{ns}$, corresponding to a linewidth of 1.6 µeV. This observation suggests that both charged and uncharged QDs share the same dipole moment and the shift of the π-maxima in the Rabi rotations indeed stems from the photo charging effect. For

our discussion on the damping mechanisms of the Rabi rotations, we restrict ourselves to the polarization configuration HVH, where we exclusively detect charged QDs.

5.3 Analysis of damping mechanisms

The goal of this section is to gain insight into the underlying mechanisms that lead to a loss of the macroscopic coherence within the Rabi rotation experiment. Here, we distinguish between effects that arise from inhomogeneities of the ensemble and those that are intrinsic to a single QD. By comparing the experimental results with theoretical predictions, we discuss the relative importance of each decoherence channel.

First, we emphasize the crucial role of employing a flattop intensity profile to identify internal sources of decoherence. For this purpose, we compare in Figure 5.5a the Rabi rotations measured using the flattop intensity profile (blue) with those measured in an experiment where both pulses share the same Gaussian intensity profile (black). For the latter, the Rabi rotations are strongly faded as only one weakly pronounced local maximum and minimum are visible followed by a monotonic damping of the signal. Comparable weakly pronounced Rabi rotations were observed under similar conditions in References [62, 105, 158]. To quantify the remaining impact of the inhomogeneity of the flattop intensity profile, a numerical model was introduced in Reference [64]. Here, the measured laser intensity profiles serve as an input for a numerical solution of the optical Bloch equations. The resulting Rabi rotations are shown by a green dashed line in Figure 5.5a. No damping is observable within the measured intensity range. Therefore, we conclude that our experimental method allows to overcome the effect of spatial averaging. Note that the modeled PE has a lower amplitude for $A_2 = \pi$ than for $A_2 = 3\pi$. This deviation from the simplified $\sin^2(A_2/2)$-dependence, Equation (2.7), arises from the finite duration of the optical pulses. We conclude that the accomplished laser intensity profile (characterized in Section 2.2) does not introduce a significant influence on the fading of the Rabi rotations in the observed range of pulse areas. We thus proceed to explore additional potential contributions to intensity-dependent decoherence.

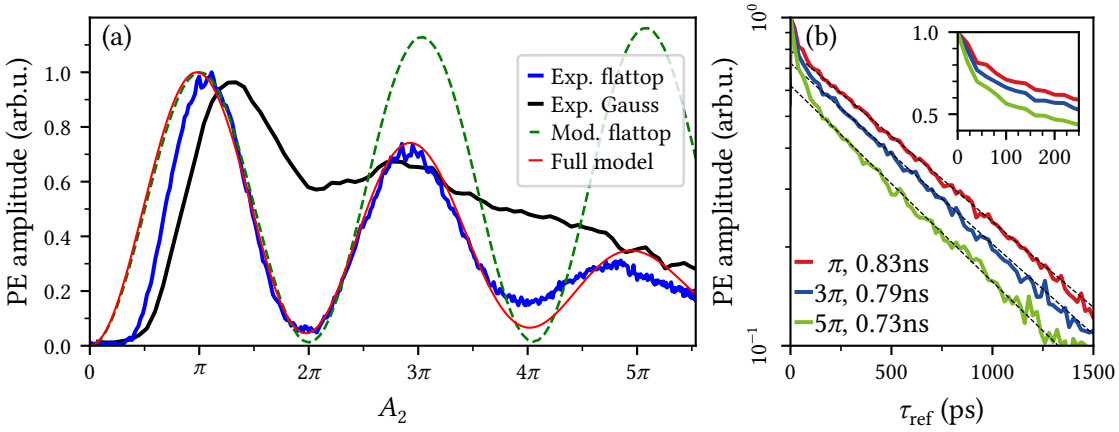

Figure 5.5: (a) Rabi rotations as a function of the pulse area of the second pulse A_2 for a Gaussian (black) and a flattop intensity profile (blue). The red and green lines show modeling results as described in the text. (b) Decay of the normalized PE amplitude for $A_2 = \pi, 3\pi, 5\pi$ (local maxima of the Rabi cycle in (a)). The inset highlights the temporal range where the decays deviate from a single exponential function.

A remaining damping effect, arising from the average over an ensemble, is a potential spread of dipole moments that are affected by the size and shape of the QDs. In a similar manner as the fading of Rabi rotations by a Gaussian intensity profile, the inhomogeneity of dipole moments gives rise to a modification of the total polarization described by

$$P(A_2) \propto \int_0^\infty \mu e^{-\frac{(\mu-\mu_0^2)^2}{2\sigma_\mu^2}} \sin^2\left(\frac{\mu}{\mu_0}\frac{A_{2,0}}{2}\right) \mathrm{d}\mu, \tag{5.2}$$

where we assumed a Gaussian distribution of dipole moments μ with mean value μ_0 and standard deviation σ_μ. $A_{2,0} = \mu_0/\hbar \int E_2(t)dt$ denotes the pulse area associated with the mean dipole moment. Equation (5.2) describes a loss of contrast of the Rabi rotations due to the superposition of individual Rabi rotations of the QDs within the ensemble. In the limit $A_{2,0} \to \infty$, the signal reaches a constant value of 50 % relative to the Rabi cycle associated with the mean dipole moment. In the experiment, we can indeed observe a strong loss of contrast in the rotations: The contrast between the π maximum and the 2π minimum is roughly 90 % whereas the contrast between the 4π minimum and 5π maximum amounts to only 30 %, which we can associate to a spread of dipole moments within the excited ensemble. However, the signal drops significantly below a constant value of 50 % relative to the maximum signal at π, since the amplitude for the local maximum at 5π is roughly given by 30 %. This loss of macroscopic coherence can not be explained by an effect associated with the inhomogeneity of the system. We therefore have to consider decoherence effects that are inherent to a single QD. Here, the coupling to acoustic phonons is relevant, whose characteristics will be reviewed in the following based on Reference [164].

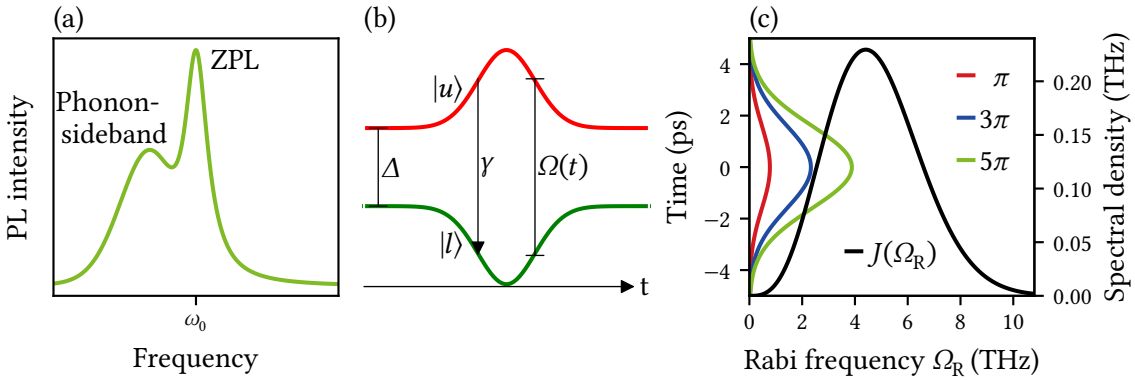

Figure 5.6: (a) Schematic photoluminescence (PL) spectrum of a QD interacting with acoustic phonons. The spectrum consists of a zero-phonon line (ZPL) and a phonon-sideband. (b) Sketch of the basic idea of the phonon model described in the text. Here, an optical (Gaussian) pulse leads to a time-dependent dressing of the two states (green, red). The dressing leads to phonon-assisted transitions between the dressed states at a rate γ. (c) Phonon spectral density resulting from the fitting procedure described in the text. Colored lines show the time-dependent Rabi frequency as set by the electric field pulses with area $\pi, 3\pi, 5\pi$.

The coupling of self-assembled (In,Ga)As QDs to their crystal surrounding in the form of carrier-phonon coupling has been subject to intense research efforts both experimentally and theoretically within the last 20 years [54, 165–169]. Since direct transitions between the QD states are typically not accomplished by phonon energies, pure decoherence effects via the coupling to longitudinal acoustic phonons are most relevant [166]. In the PL absorption spectrum of single QDs at low temperatures, the influence of phonons can be seen in the form of a phonon sideband on the low-energy side that superimposes a Lorentzian line at the resonance energy of the QD transition (zero-phonon line). A schematic spectrum is shown in Figure 5.6a. The phonon sideband typically shows a maximum at a non-zero detuning from the zero-phonon line, which is referred to as a

resonance phenomenon of the coupling efficiency between the QD exciton and the phonons [167]. The coupling efficiency can be described by the phonon spectral density $J(\omega)$ whose spectral characteristics result from the interplay of two properties of the (In,Ga)As QD system. First, the lattice parameters of InAs and GaAs are similar and the phonons can thus be considered as bulk modes, i.e. plane waves. Second, the spatial confinement of the charges restricts the coupling to acoustic phonons with small wavenumbers, i.e. sound waves with linear dispersion $\omega = ck$, with the speed of sound c. The carriers couple most strongly to the phonons whose wavelengths are equal to the width of the carrier wave function, i.e. the size of the QDs. For lower energies, $J(\omega)$ behaves as in the bulk material, whereas for higher energies the coupling drops due to the finite size of the QDs. Assuming that the QDs are spherical, $J(\omega)$ can be derived to

$$J(\omega) \propto A\omega^3 \exp\left(-\frac{\omega^2}{\omega_c^2}\right), \tag{5.3}$$

where A is a constant and ω_c is a cut-off frequency that is determined by the size of the spherical QDs [170]. The discussed spectral dependence of the homogeneous line of the QDs corresponds to a non-exponential decay of the polarization in the time domain, where the signal initially drops fast on a picosecond timescale corresponding to the emission of a phonon wave packet and partial loss of coherence [171]. In non-linear spectra, the homogeneous line can strongly depend on the applied optical power, which therefore results in an intensity-dependent damping mechanism for the Rabi oscillations. This can be understood by taking into account that the application of a strong laser field results in a dressing of ground and excited states between which direct phonon-assisted transitions are allowed. Strong excitation can therefore result in the efficient creation and emission of a phonon wave packet accompanied by a loss of exciton coherence on a picosecond-timescale [164, 172]. The coupling is strongest when the Rabi frequency, which corresponds to the splitting between the dressed states, matches the maximum of the phonon spectral density $J(\omega)$.

We experimentally investigate the effect of the applied laser intensity on the shape of the homogeneous line by a measurement of the PE decay as a function of the pulse area of the second pulse. Figure 5.5b presents the PE decays measured for $A_2 = \pi, 3\pi, 5\pi$ (maxima of the Rabi rotations). With increasing pulse area, we can observe a stronger influence of the aforementioned fast component in the range $\tau_{\mathrm{ref}} < 100\,\mathrm{ps}$. This temporal range is highlighted in the inset of Figure 5.5b. Further, the decoherence time T_2 corresponding to the subsequent exponential decay gradually drops from 830 ps for $A_2 = \pi$ over 790 ps for $A_2 = 3\pi$ to 730 ps for $A_2 = 5\pi$. This excitation-induced dephasing (EID) effect may be attributed for example to the coupling to wetting layer states as discussed in Reference [173]. Concerning the damping of Rabi rotations, the EID effect results in a damping of the PE amplitude by a factor $\exp[-\tau_{\mathrm{ref}}/T_2(A_2)]$, where $T_2(A_2)$ is the decoherence time as a function of A_2. However, since the Rabi rotations presented in Figure 5.5a are measured for a short delay $\tau_{\mathrm{ref}} = 80\,\mathrm{ps}$, the contribution of EID on the drop of amplitude is negligible as emerges from the estimation $\exp(-80\,\mathrm{ps}/T_2(5\pi))/\exp(-80\,\mathrm{ps}/T_2(\pi)) \approx 99\,\%$. Instead, the described loss of coherence is dominated by the fast drop of the PE amplitude, which results from the intensity-dependent coupling efficiency to acoustic phonons that we motivated above. To account for this effect in a quantitative model, we adopt a rate equation approach introduced in Reference [170] for the modeling of time-dependent Rabi oscillations and pump-probe spectra.

The idea of the model is visualized in Figure 5.6b. The interaction of the QD, considered as a two-level system (TLS), with a light pulse leads to a time-dependent dressing of the states such that the energy splitting is given by the generalized Rabi frequency (for the definition of the dressed state base see Equation (1.21)). Since both dressed states $|u\rangle$ and $|l\rangle$ include an excited state

component, the coupling to phonons, although being of pure type, results in direct transitions at a rate γ assisted by the emission of a phonon with energy Ω. The rate γ follows from Fermi's golden rule

$$\gamma = \frac{\pi}{2}\left(\frac{\Omega_\mathrm{R}}{\Omega}\right)^2 J(\Omega) \tag{5.4}$$

and therefore includes the non-monotonous efficiency of the coupling to phonons described by the spectral density $J(\omega)$ [170]. We use the frequency dependence of $J(\omega)$ from Equation (5.3) that assumes spherical QDs. The assumption of a spherical shape might be a strong simplification of the actual shape of the studied self-assembled QDs. However, by appropriate choice of the parameters A and ω_c in Equation (5.3), an arbitrary geometry of QDs can be approximated [171]. Therefore, A and ω_c serve as fitting parameters of our modeling procedure. Note that for a Gaussian temporal envelope of the light field, the dressed state base is time-dependent. For a qualitative discussion, we first present an analytical consideration of the model for which we assume rectangular-shaped pulses. Afterward, the numerical results obtained in Reference [64] are presented that take into account the Gaussian temporal envelope.

The phonon relaxation rate (5.4) enters the equations of motion of the density matrix in the dressed state base as

$$\frac{d}{dt}\rho_{uu} = -\gamma\rho_{uu}, \quad \frac{d}{dt}\rho_{ll} = +\gamma\rho_{uu}, \quad \frac{d}{dt}\rho_{lu} = -i\Omega\rho_{lu} - \frac{\gamma}{2}\rho_{lu}, \tag{5.5}$$

which are solved by

$$\rho_{uu}(t) = \rho_{uu}(0)\mathrm{e}^{-\gamma t} \tag{5.6a}$$

$$\rho_{ll}(t) = \rho_{ll}(0) + (1-\mathrm{e}^{-\gamma t})\rho_{uu}(0) \tag{5.6b}$$

$$\rho_{lu}(t) = \rho_{lu}(0)\mathrm{e}^{-(i\Omega+\frac{\gamma}{2})t}. \tag{5.6c}$$

This solution is transformed to formulate the action of a rectangular-shaped pulse of duration t_p on the Bloch vector using the transformation between dressed and undressed states from Equation (1.21) and the definition of the Bloch vector from Equation (1.23)

$$\begin{pmatrix} u \\ v \\ w \end{pmatrix} = \begin{pmatrix} \frac{\Omega_\mathrm{R}^2 e^{-\gamma t_p} + \Delta^2\cos(\Omega t_p)e^{-\frac{\gamma}{2}t_p}}{\Omega^2} & -\frac{\Delta}{\Omega}\sin(\Omega t_p)e^{-\frac{\gamma}{2}t_p} & \frac{\Delta\Omega_\mathrm{R}}{\Omega^2}\left[e^{-\gamma t_p} - \cos(\Omega t_p)e^{-\frac{\gamma}{2}t_p}\right] \\ \frac{\Delta}{\Omega}\sin(\Omega t_p)e^{-\frac{\gamma}{2}t_p} & \cos(\Omega t_p)e^{-\frac{\gamma}{2}t_p} & \frac{\Omega_\mathrm{R}}{\Omega}\sin(\Omega t_p)e^{-\frac{\gamma}{2}t_p} \\ -\frac{\Delta\Omega_\mathrm{R}}{\Omega^2}[e^{-\gamma t_p} - \cos(\Omega t_p)e^{-\frac{\gamma}{2}t_p}] & -\frac{\Omega_\mathrm{R}}{\Omega}\sin(\Omega t_p)e^{-\frac{\gamma}{2}t_p} & \frac{\Delta^2 e^{-\gamma t_p} + \Omega_\mathrm{R}^2\cos(\Omega t_p)e^{-\frac{\gamma}{2}t_p}}{\Omega^2} \end{pmatrix} \begin{pmatrix} u_\mathrm{b} \\ v_\mathrm{b} \\ w_\mathrm{b} \end{pmatrix} \tag{5.7}$$

$$+ \begin{pmatrix} \frac{\Omega_\mathrm{R}}{\Omega}\left(1 - e^{-\gamma t_p}\right) \\ 0 \\ \frac{\Delta}{\Omega}\left(1 - e^{-\gamma t_p}\right) \end{pmatrix},$$

where $(u_\mathrm{b}, v_\mathrm{b}, w_\mathrm{b})$ is the Bloch vector before pulse action. Multiple applications of Equation (5.7) are used to account for arbitrary sequences of rectangular-shaped pulses. Equation (5.7) represents an expansion of the equations given in Reference [170], where only the initial condition $(u_\mathrm{b}, v_\mathrm{b}, w_\mathrm{b}) = (0, 0, -1)$ (i.e. system in the ground state) is considered. Equation (5.7) manifests two distinct effects arising from the phonon interaction. First, the transition rate γ leads to a decay of all components of the Bloch vector, thus leading to both decoherence and population decay during pulse action. Since the decay rate depends on the detuning, this decoherence effect also affects the contrast of the Rabi oscillations. A second feature is given by the long-term steady state of the Bloch vector described by the last summand in (5.7), which is independent of

the initial Bloch vector. For a fixed Rabi frequency, the steady state on the Bloch sphere solely depends on the detuning Δ which was already discussed in Reference [174] using path integral formalism and was proposed as a possible state preparation scheme for QD qubits. Further, it should be noted that the transition rate γ shares the resonant nature of the phonon spectral density. Consequently, for pulses corresponding to a large or small Rabi frequency, as compared to the cut-off frequency ω_c in Equation (5.3), the influence of phonons is negligible, which is realized at a given pulse area for sufficiently short or long pulses, respectively.

As a final step, we aim to determine the free parameters of the phonon spectral density, being the amplitude A and cut-off frequency ω_c, by performing a fit to the observed Rabi rotations. For this purpose, a complete numerical model was introduced in Reference [64] that takes into account the Gaussian temporal profile of the pulses with a FWHM of 3.8 ps. To do so, the Gaussian pulses are approximated by piecewise constant functions with a stepwidth of 20 fs. For each step, the equations of motion are transformed to the dressed state base and the Equations of motion (5.5) are solved numerically. The final polarization in the undressed base is averaged over an inhomogeneous distribution of detunings and dipole moments. The inhomogeneous broadening of the dipole moments is assumed to be a Gaussian distribution whose width serves as a third fitting parameter. The best fit is given for $A = (0.012 \pm 0.002)\,\mathrm{ps}^2$, $\omega_c = (3.6 \pm 0.1)\,\mathrm{THz}$, and a dipole inhomogeneity of $(21 \pm 2)\,\%$ (FWHM). These parameters are in reasonable agreement with results obtained on similar QD samples [161, 175]. The corresponding damped Rabi cycle is plotted together with the experimental data in Figure 5.5a. Note that the modeling procedure does not take into account the photo charging effect that we discussed in the previous section. Therefore, the modeled curve deviates from the experimental data in the range $A_2 < \pi$. Excellent agreement between model and experiment is found in the range $\pi \leq A_2 \leq 3.5\pi$, whereas the contrast of the measured oscillations is less pronounced for $A_2 \geq 3.5\pi$ as described by our model. Nevertheless, the comparison between the experimental and modeled Rabi rotations in combination with the study of EID and the non-exponential decay of the PE amplitude allows us to conclude that the resonant coupling to acoustic phonons is the dominant mechanism for the loss of optical coherence inherent to a single QD. In Figure 5.6c we plot the time-dependent Rabi frequency Ω_R in direct comparison to the phonon spectral density. For the used pulse durations of 3.8 ps, the largest pulse areas in our experiment $\approx 5\pi$ feature a maximum Rabi frequency of roughly 4 THz, which is close to the maximum of the phonon spectral density with the found parameters. Consequently, the loss of coherence acts very efficiently in the regime of large pulse areas. Through the use of longer ($\approx$ 50 ps) or shorter ($\approx$ 100 fs) pulses, the coupling to phonons could be strongly reduced.

5.4 Conclusions

In this chapter, we observed collective Rabi rotations in an intensity-dependent PE experiment from an ensemble of (In,Ga)As QDs placed in a microcavity with a moderate quality factor of 200. Using the PE polarimetry technique, we independently considered charged and uncharged QDs. Charged QDs (trions) are found to be dominantly responsible for the coherent optical response of the sample which we attribute to a photo-charging effect. The main demonstration presented in this section is given by the successful expansion of the Rabi rotation protocol on an ensemble of charged QDs using a flattop intensity profile. By overcoming the effect of spatial inhomogeneity, pronounced Rabi rotations up to a pulse area of 5.5π were observed, which was so far not possible in experiments on an ensemble of exciton complexes in semiconductor structures [62, 103, 106]. A careful analysis of the damping behavior of the Rabi rotations as well as the qualitative shape of the homogenous line as a function of applied optical power, allowed

us to identify the resonant coupling to acoustic phonons as the major decoherence channel under resonant excitation. The excitation-induced spectral broadening of the zero-phonon line instead is negligible. We successfully employed an adequate modeling procedure to account for the resonant nature of the phonon coupling that results from the interaction between bulk phonons and localized excitations. We presented an analytical expansion of the effect on the Bloch vector assuming rectangular-shaped pulses and finally took into account the Gaussian temporal shape of the optical pulses to obtain parameters for the spectral density as well as the inhomogeneity of dipole moments. The discussed strong dependence of the phonon coupling on the duration of the resonant laser pulses motivates us to perform similar measurements using pulses in the femtosecond regime. Here, the effect of biexciton formation is expected to be negligible as the QDs are mainly charged.

Temporal sorting of optical multi-wave-mixing processes

6

The observation of well-pronounced Rabi rotations in Chapter 5 up to an area of 5.5π using a flattop intensity profile demonstrates the possibility of performing multiple unitary operations on the qubit ensemble realized in the studied (In,Ga)As quantum dot–cavity system. These findings motivate to study more complex pulse arrangements as used in nuclear magnetic resonance (NMR), where almost arbitrary logical operations can be realized by the combination of magnetic field pulses acting on qubits represented by nuclear spin states. In the optical regime, the interplay of multiple pulses with an optical emitter, such as an exciton in a quantum dot (QD), results in the formation of high-order multi-wave mixing (MWM) responses that allow to directly impact on the emitting optical coherence [159, 176]. Qubits realized by QDs offer advantages regarding the speed of control, polarization selectivity, and phase matching condition dictated by spin and photon momentum conservation. The experimental results presented in this chapter reveal the rich possibilities of all-optically controlling the emission properties of QD ensembles by manipulating their phase evolution. In particular, we expand the two-pulse photon echo (PE) sequence by two optical control pulses that operate on the phase evolution of the ensemble. The first and second pulse of the two-pulse PE sequence initialize a macroscopic coherence and reverse the phase evolution leading to PE formation, respectively. The areas of two additional control pulses serve as tuning knobs for adjusting the magnitude and timing of the coherent emission. Furthermore, we make use of the spin degeneracy of ground and excited state of charged QDs to control the polarization state of the emitted signal.

Additionally, we analyze the effect of finite duration of the resonant optical pulses on optical MWM signals. Usually, high-order MWM terms that share the same phase dependence on the fields are emitted at the same time and are indistinguishable using heterodyne techniques. Surprisingly, we reveal that the use of optical control pulses, whose durations are comparable to the dephasing time of the ensemble leads to a temporal sorting of the MWM processes of different order. This phenomenon is manifested in a significant modification of the temporal shape of the coherent optical response for strong optical fields. The results presented in this chapter were previously published in:

S. Grisard, A. V. Trifonov, H. Rose, R. Reichhardt, M. Reichelt, C. Schneider, M. Kamp, S. Höfling, M. Bayer, T. Meier, and I. A. Akimov, "Temporal Sorting of Optical Multiwave-Mixing Processes in Semiconductor Quantum Dots", ACS Photonics **10**, 3161 (2023)
DOI: 10.1021/acsphotonics.3c00530, ©2023 American Chemical Society

6.1 Theoretical description of control pulse experiment

In this section, we theoretically describe the coherent control scheme that we use to all-optically manipulate the phase evolution of an ensemble of singly charged (In,Ga)As QDs. Our approach is based on the interplay of temporally sorted high-order MWM signals in a PE experiment. All experiments are performed on the same QD ensemble embedded in an AlAs/GaAs microcavity

that was studied in Chapter 5. Importantly, we recall that the optical response of the sample upon moderate optical excitation is dominated by negatively charged QDs, i.e., trions. The trion scheme is made up of two separated two-level system (TLS) that can be independently addressed by the two circular light polarizations σ^+ and σ^-. Under excitation with linearly co-polarized pulses and in the absence of a magnetic field, the trion behaves effectively like a single TLS consisting of states $|0\rangle$ and $|1\rangle$. When, however, the relative amplitude or optical phase between σ^+ and σ^- components of the exciting light are varied, the spin degeneracy of the trion in the ground and excited state offers possibilities for the polarization control of the coherent optical response of the QD ensemble, as we will discuss below.

For the discussion of the general properties of the considered mechanisms, we analytically solve the optical Bloch equations assuming delta-like optical pulses (impulsive limit, Section 6.1.1). Afterwards in Section 6.1.2, we discuss the effect of a finite pulse duration on the temporal shape of the resulting PE response. The latter becomes crucial for distinguishing between MWM contributions that appear at the same temporal position in the case of delta-pulses.

6.1.1 Impulsive limit

Within this section, we consider all resonant optical fields as delta pulses (impulsive limit). Note that the finite duration of the pulses can only be safely neglected when the spectrum of the pulses is much broader than the inhomogeneous broadening of the ensemble, i.e. when the duration is much shorter than the reversible dephasing time T_2^*. Although this condition is not fulfilled in our experiments (compare discussions in Chapter 5), the consideration of the impulsive limit enables us to derive meaningful analytical expressions for MWM signals whose general properties remain valid even when the finite duration of the pulses is taken into account. The profound influence of the finite pulse duration on the temporal shape of the PE responses is discussed in the next section.

The excitation scheme is schematically presented in Figure 6.1a. Here, we expand the two-pulse PE sequence by two additional resonant control pulses, with electric field amplitudes E_{C1} and E_{C2}. The control pulses share the same wavevector $\mathbf{k}_{\mathrm{C}} \neq \mathbf{k}_2 \neq \mathbf{k}_1$ and are temporally split by a delay of τ_{C}. By exciting the ensemble temporally between the first and second pulse, the control pulses directly modify the dephasing dynamic of the ensemble after the action of the first pulse. Therefore, the two-pulse PE response is directly modified. The effect on the spectro-temporal shape of the PE field is analyzed by temporally resolving the signal using the heterodyne technique. Besides modifying the two-pulse PE response, the addition of two resonant laser pulses results in various PE signals formed at different temporal positions and emitted in different directions. For example, the combination of the first pulse E_1 and first control pulse E_{C1} creates a PE emitted in the direction $2\mathbf{k}_{\mathrm{C}} - \mathbf{k}_1$. The photon momentum conservation in combination with the heterodyne technique allows a selective study of those responses that fulfill the phase-matching condition $2\mathbf{k}_2 - \mathbf{k}_1$ and thus directly impact the two-pulse PE response. This means that we only consider MWM signals that are not affected by the spatial phase of the control pulses or only depend on the difference between the phases, which vanishes for the choice $\mathbf{k}_{\mathrm{C1}} = \mathbf{k}_{\mathrm{C2}}$.

To analyze the effect of the control pulses on the PE response when the area of the control pulses is driven in the Rabi regime, we analytically solve the optical Bloch equations for a TLS. Since the considered trion ensemble consists of two independent subensembles that can be addressed with circularly polarized light, the solution can be transferred to the four-level system by subdividing the optical fields into circularly polarized components

$$E_{\mathrm{j}}^{\pm}(t) = E_{0,\,\mathrm{j}}^{\pm}\delta(t - t_{\mathrm{j}})\mathrm{e}^{i\phi^{\pm}}. \tag{6.1}$$

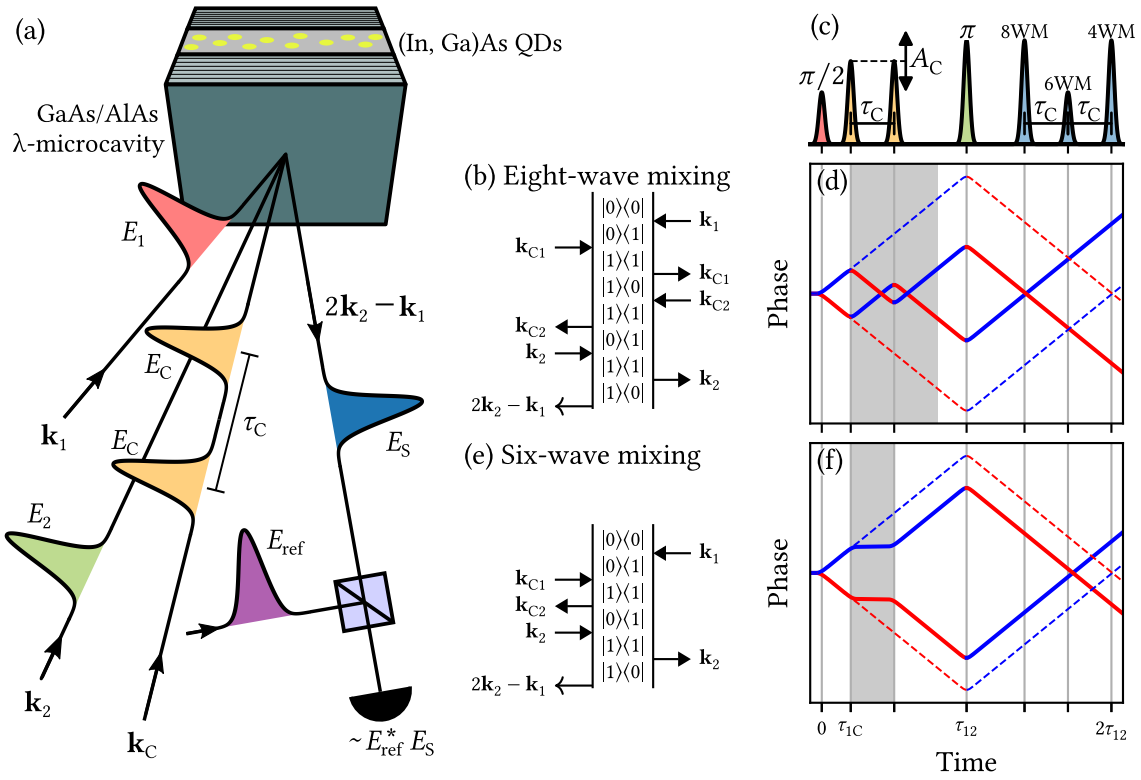

Figure 6.1: (a) Temporal and angular arrangement of the optical pulses for our experiments. The basis is set by the two-pulse PE experiment, where two pulses with wavevectors $\mathbf{k}_1$ and $\mathbf{k}_2$ generate a PE signal in the phase matched direction $2\mathbf{k}_2 - \mathbf{k}_1$. In between these two pulses, we introduce two control pulses sharing the same wavevector $\mathbf{k}_C$. The resulting coherent responses are temporally resolved using the heterodyne technique as introduced in Section 2.1. Note that all pulses possess the same photon energy and colors in the figure are chosen only for clarity. (b)/(e) Double-sided Feynman diagrams for the eight- and six-wave-mixing processes (EWM/SWM) as described in the text. (c) Temporal arrangement of optical pulses for reference on the time axis of the phase diagrams in (d) and (f). (d)/(f) Evolution of the phase of two individual TLS for the two different MWM processes in (b) and (e). Dashed lines show the phase evolution in the absence of the control pulses for comparison.

Here, $\phi^{\pm} = \mathbf{k}\cdot\mathbf{r} + \varphi^{\pm}$ denotes an optical phase including the spatial phase $\mathbf{k}\cdot\mathbf{r}$ and an individual optical phase $\varphi^{\pm}$ for the σ^+ and σ^- components, which makes it possible to construct arbitrary polarizations. The effect of a delta pulse on each TLS can be compactly written as a matrix operation on the elements of the density matrix $\rho^{\pm}_{ij}$ that transforms the density matrix elements before the action of the pulse (index b) into the density matrix elements after the action of the pulse (index a)

$$\begin{pmatrix}\rho^{\pm}_{00}\\ \rho^{\pm}_{11}\\ \rho^{\pm}_{01}\\ \rho^{\pm}_{10}\end{pmatrix}_a = \mathbf{M}^{\pm}(A^{\pm},\phi^{\pm})\begin{pmatrix}\rho^{\pm}_{00}\\ \rho^{\pm}_{11}\\ \rho^{\pm}_{01}\\ \rho^{\pm}_{10}\end{pmatrix}_b, \tag{6.2}$$

where the matrix $\mathbf{M}^{\pm}$ is given by [96]

$$\mathbf{M}^{\pm} = \frac{1}{2}\begin{pmatrix} 1+\cos(A^{\pm}) & 1-\cos(A^{\pm}) & i\sin(A^{\pm})e^{-i\phi} & -i\sin(A^{\pm})e^{+i\phi}\\ 1-\cos(A^{\pm}) & 1+\cos(A^{\pm}) & -i\sin(A^{\pm})e^{-i\phi} & i\sin(A^{\pm})e^{+i\phi}\\ i\sin(A^{\pm})e^{+i\phi} & -i\sin(A^{\pm})e^{+i\phi} & 1+\cos(A^{\pm}) & (1-\cos(A^{\pm}))e^{2i\phi}\\ -i\sin(A^{\pm})e^{-i\phi} & i\sin(A^{\pm})e^{-i\phi} & (1-\cos(A^{\pm}))e^{-2i\phi} & 1+\cos(A^{\pm})\end{pmatrix} \tag{6.3}$$

with the pulse area $A^{\pm} = \int \frac{\mu}{\hbar} E_0^{\pm} \delta(t-\tau) dt$. In this section, we intentionally avoid the Bloch vector representation of the density matrix elements, given that the incorporation of different wavevectors for the optical pulses makes this approach less insightful [96]. The free evolution of the density matrix elements during a temporal gap τ between two pulses can be analogously formulated as multiplication with the matrix

$$\mathbf{M}^0(\Delta, \tau) = \mathrm{diag}(1, 1, \mathrm{e}^{i\Delta\tau}, \mathrm{e}^{-i\Delta\tau}). \tag{6.4}$$

By combinations of the matrices given by Equations (6.3) and (6.4), the effect of an arbitrary sequence of delta pulses with different wavevectors can be modeled.

As a starting point, we use the modeling formalism to obtain the PE response resulting from two laser pulses. We assume that before the action of the pulses, all oscillators are in the ground state, i.e. $\boldsymbol{\rho}^{\pm}(0) = (1, 0, 0, 0)^{\top}$. The density matrix at observation time t is given by

$$\boldsymbol{\rho}^{\pm}(t) = \mathbf{M}^0(t-\tau_{12})\mathbf{M}^{\pm}(A_2^{\pm})\mathbf{M}^0(\tau_{12})\mathbf{M}^{\pm}(A_1^{\pm})\boldsymbol{\rho}^{\pm}(0). \tag{6.5}$$

From a full solution for the coherences $\rho_{01}^{\pm}$ being microscopic sources of $\sigma^{\pm}$ polarized light, we select only those terms with a spatial phase factor $\mathbf{k}_{\mathrm{S}} \cdot \mathbf{r} = (2\mathbf{k}_2 - \mathbf{k}_1) \cdot \mathbf{r}$. In this way, we arrive at the following expression of the two-pulse PE fields in σ^+ and σ^- polarization

$$E_{\mathrm{2PE}}^{\pm} \propto \sin\left(A_1^{\pm}\right) \sin^2\left(\frac{A_2^{\pm}}{2}\right) \exp\left[i(2\phi_2^{\pm} - \phi_1^{\pm}) + i\Delta(t - 2\tau_{12})\right]. \tag{6.6}$$

Due to the phase factor $\exp[i\Delta(t-2\tau_{12})]$, the integration over a distribution of detunings Δ in an inhomogeneous ensemble restricts the two-pulse PE signal to the temporal position where all relative phases equal zero. The formation of macroscopical polarization of the ensemble can thus be observed at $t = 2\tau_{12}$ in the form of a coherent light pulse. We elaborate in the following on how this PE field is influenced by the action of the control pulses.

When considering MWM responses from a TLS, the contribution of each control pulse with wavevector $\mathbf{k}_{\mathrm{Ci}}$ to the overall phasematching condition is 0, $\pm 2\mathbf{k}_{\mathrm{Ci}}$, or $\pm\mathbf{k}_{\mathrm{Ci}}$. Therefore, we can expect three distinct MWM contributions, for which we explicitly write the phasematching conditions as

$$\mathbf{k}_{\mathrm{S}} = 2\mathbf{k}_2 - \mathbf{k}_1 + \mathbf{k}_{\mathrm{C1}} - \mathbf{k}_{\mathrm{C1}} + \mathbf{k}_{\mathrm{C2}} - \mathbf{k}_{\mathrm{C2}}, \tag{6.7a}$$

$$\mathbf{k}_{\mathrm{S}} = 2\mathbf{k}_2 - \mathbf{k}_1 + 2\mathbf{k}_{\mathrm{C1}} - 2\mathbf{k}_{\mathrm{C2}}, \tag{6.7b}$$

$$\mathbf{k}_{\mathrm{S}} = 2\mathbf{k}_2 - \mathbf{k}_1 + \mathbf{k}_{\mathrm{C1}} - \mathbf{k}_{\mathrm{C2}}. \tag{6.7c}$$

For the choice $\mathbf{k}_{\mathrm{C1}} = \mathbf{k}_{\mathrm{C2}}$, all three phase matching conditions simplify to $\mathbf{k}_{\mathrm{S}} = 2\mathbf{k}_2 - \mathbf{k}_1$. Each response leads to a PE emitted at a well-defined temporal position relative to the two-pulse PE, as we discuss in the following.

The first case, Equation (6.7a), implies an insensitivity of the resulting signal to the optical phases of the control pulses and can be observed for any choice of $\mathbf{k}_{\mathrm{C1}}$ and $\mathbf{k}_{\mathrm{C2}}$ in the direction $2\mathbf{k}_2 - \mathbf{k}_1$. Within the impulsive limit, the temporal position of the resulting coherent emission will not be shifted relative to the two-pulse PE at $t = 2\tau_{12}$. As for the two-pulse PE, we derive the dependence of the signal fields in $\sigma^{\pm}$ polarizations on the involved pulse areas

$$E_{\mathrm{FWM}}^{\pm} = E_{\mathrm{2PE}}^{\pm} \cos^4\left(\frac{A_{\mathrm{C}}^{\pm}}{2}\right), \tag{6.8}$$

where the functional dependence of $E_{\mathrm{2PE}}^{\pm}$ on $A_1^{\pm}$ and $A_2^{\pm}$ is given by Equation (6.6). The signal is maximum for $A_{\mathrm{C}} = 2n\pi$ and zero for $A_{\mathrm{C}} = (2n+1)\pi$, where n is an integer. We indexed the signal

with FWM (four-wave mixing) corresponding to the lowest non-zero MWM order of the signal. We underline however, that Equation (6.8) is the exact solution including all possible higher-order MWM components that share the same phasematching condition and temporal characteristic. As can be seen in Equation (6.8), the pulse area A_C directly modulates the amplitude of the two-pulse PE, which may be also used to independently modify the contributions of σ^+ and σ^- components as we experimentally demonstrate in Section 6.4.

Next, we consider the phasematching condition $\mathbf{k}_S = 2\mathbf{k}_2 - \mathbf{k}_1 + 2\mathbf{k}_{C1} - 2\mathbf{k}_{C2}$, Equation (6.7b), which simplifies to the phase matching condition of the two-pulse PE for the special case $\mathbf{k}_{C1} = \mathbf{k}_{C2}$. This phasematching condition is realized, in lowest perturbative order, by an eight-wave mixing (EWM) process proportional to $E_1^* E_2^2 E_{C1}^2 E_{C2}^{*2}$ as depicted by an exemplary Feynman diagram in Figure 6.1b. Similar to the action of the refocussing pulse in the two-pulse PE sequence, here, each of the control pulses converts the polarization to its complex conjugate, i.e. $|i\rangle\langle j|$ to $|j\rangle\langle i|$. The effect of this process on the overall coherent response is represented by the phase diagram in Figure 6.1d in comparison to the two-pulse PE (dashed lines). The diagram plots the phase evolution of the field amplitude associated with two oscillators with opposite detuning (blue and red). A coherent emission of the whole ensemble will appear only at the temporal positions where the relative phase of the oscillators disappears (crossing points of blue and red lines). For clarity, Figure 6.1c on top of the phase diagram sketches the temporal arrangement of the pulses. The ensemble experiences a refocusing dynamic after the first control pulse that is again inverted by the second control pulse. In this way, the phases of individual oscillators are effectively unaffected for a time of $2\tau_C$ after the first control pulse, which we highlight by the grey area in Figure 6.1d. Consequently, the refocusing pulse, acting at τ_{12}, generates a coherent emission that is shifted by $-2\tau_C$ with respect to the two-pulse PE at $2\tau_{12}$. Note that the two other moments where the relative phase is zero within the grey area in Figure 6.1d lead to a coherent emission in the directions $2\mathbf{k}_C - \mathbf{k}_1$ and $\mathbf{k}_1$, respectively, and are therefore not detected in our experiments. We again derive an analytical expression for the electric fields as a function of the involved pulse areas

$$E_{EWM}^{\pm} = E_{2PE}^{\pm} \sin^4\left(\frac{A_C^{\pm}}{2}\right) \exp\left[2i\left(\phi_{C2}^{\pm} - \phi_{C1}^{\pm}\right) + 2i\Delta\tau_C\right]. \tag{6.9}$$

The dependence of the signal on A_C oscillates with the opposite phase as compared to the signal at $2\tau_{12}$ ($E_{FWM}^{\pm} \propto \cos^4\left(A_C^{\pm}/2\right)$), Equation (6.8). Maxima appear for $A_C^{\pm} = (2n+1)\pi$, minima for $A_C^{\pm} = 2n\pi$. Consequently, the area A_C acts as a control knob for the coherent transfer between the two PEs occurring at different temporal positions. For $A_C = \pi$, the control pulses function as a temporal gate for the coherent emission of the ensemble. Furthermore, the optical phase of the signal in Equation (6.9) depends on twice the relative phases between the control pulses $2(\phi_{C2}^{\pm} - \phi_{C1}^{\pm})$, which opens up the possibility of acquiring full control over the polarization of the coherent emission by suitable choice of the polarizations of the control pulses as we experimentally demonstrate below.

Lastly, we consider the phasematching condition $\mathbf{k}_S = 2\mathbf{k}_2 - \mathbf{k}_1 + \mathbf{k}_{C1} - \mathbf{k}_{C2} = 2\mathbf{k}_2 - \mathbf{k}_1$, Equation (6.7c), corresponding to a six-wave mixing (SWM) response $\propto E_1^* E_2^2 E_{C1} E_{C2}^*$ in the lowest-order perturbation theory. A corresponding Feynman diagram is presented in Figure 6.1e. We again show the phase evolution of two oscillators with opposite detuning in Figure 6.1f. Here, the dephasing after the action of the first pulse is effectively turned off within a duration of τ_C (grey area) as the control pulses convert polarization $|0\rangle\langle 1|$ to population $|1\rangle\langle 1|$ and back. Therefore, the coherent emission appears at $2\tau_{12} - \tau_C$. The functional dependence on the pulse areas is given by

$$E_{SWM}^{\pm} = -\frac{E_{2PE}^{\pm}}{2} \sin^2\left(A_C^{\pm}\right) \exp\left[i\left(\phi_{C2}^{\pm} - \phi_{C1}^{\pm}\right) + i\Delta\tau_C\right], \tag{6.10}$$

which runs through maxima for $A_C = (2n+1)\pi/2$. Again, the optical phase of the signal can be controlled by the relative phase between the control pulses.

In summary, we have introduced an arrangement of optical pulses that evoke different MWM contributions where two control pulses act as gates that can be used to control the amplitude, temporal position, and polarization of the coherent emission. The overall signal fields $E_S^{\pm}$ in the phase-matched direction $2\mathbf{k}_2 - \mathbf{k}_1$ can be written as the sum

$$E_S^{\pm} = E_{FWM}^{\pm} + E_{SWM}^{\pm} + E_{EWM}^{\pm}, \tag{6.11}$$

which is depicted in Figure 6.2a by means of a two-dimensional color map as a function of real-time and pulse area of the control pulses. Here, we assumed linearly co-polarized pulses, where the trion scheme works effectively as a TLS. The relative optical phase between the control pulses is set to zero. We further chose $\tau_{12} = 40\,\text{ps}$, $\tau_C = 15\,\text{ps}$, and a Gaussian inhomogeneous broadening of detunings $\Delta = 0.3\,\text{meV}$, equivalent to $T_2^* = 4\,\text{ps}$ corresponding to the experimental situation. For this choice, we can see well-separated Gaussian PE signals at $2\tau_{12} = 80\,\text{ps}$ (E_{FWM}), $2\tau_{12} - \tau_C = 65\,\text{ps}$ (E_{SWM}), and $2\tau_{12} - 2\tau_C = 50\,\text{ps}$ (E_{EWM}) that oscillate as a function of A_C.

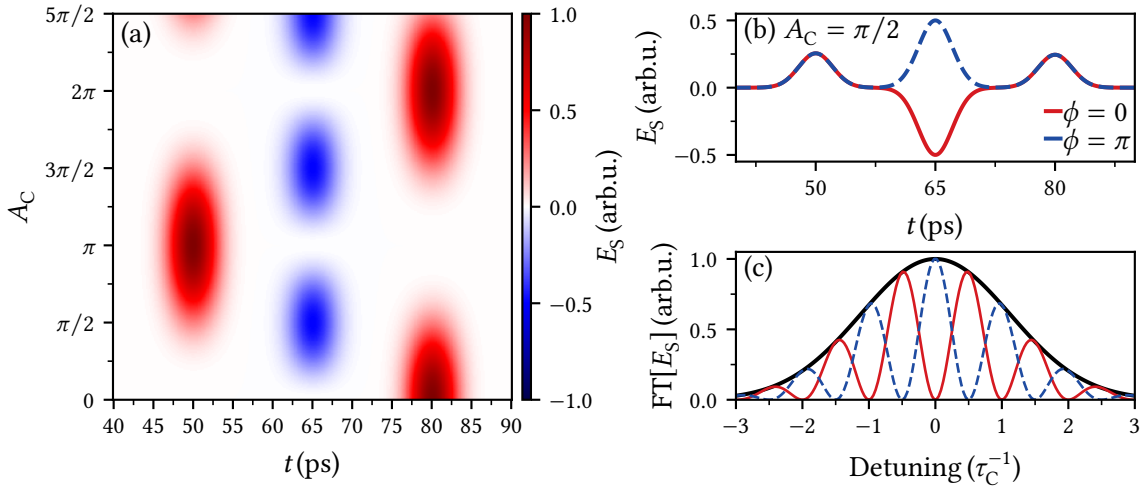

Figure 6.2: (a) Signal field amplitude E_S as a function of time t and the area of the control pulses A_C in impulsive limit according to Equation (6.11). (b) Temporal profile of the signal field E_S for $A_C = \pi/2$ and two different values of the relative phase ϕ between the two control pulses. (c) Amplitude of the Fourier spectra of the temporal profiles shown in (b). The black curve shows the distribution of detunings within the considered inhomogeneous ensemble of emitters.

The case $A_C = \pi/2$ is in direct analogy to a Ramsey fringe experiment. Ramsey fringes are commonly used in spectroscopy and atomic clock experiments to achieve high-precision measurements and control over quantum systems [177]. In a standard Ramsey fringe experiment, a TLS is exposed to two temporally separated $\pi/2$ pulses with a detuning Δ relative to the transition frequency of the QD. When probing, for example, the population of the excited state as a function of the detuning or the temporal delay between the pulses, oscillations can be observed that are known as Ramsey fringes. Maxima of the fringes arise when the product of detuning and temporal gap, i.e. the acquired optical phase between the two $\pi/2$ pulses, is a multiple of 2π, minima for an odd multiple of π. Such an experimental scheme was studied as a demonstration of coherent control over the quantum state of a single QD in References [178–180]. The combination of two $\pi/2$ pulses with the two-pulse PE sequence allows to observe Ramsey fringes from the inhomogeneous ensemble of emitters where different detunings are realized at once. Here, the Ramsey fringes manifest themselves in the time domain in the form of a temporal shape of

the emission deviating from a single Gaussian function. We show temporal cross sections for $A_C = \pi/2$ of the response of the QD ensemble in Figure 6.2b for two different values of the relative phase between the control pulses $\phi = 0$ and $\phi = \pi$. The overall response consists of three Gaussian pulses centered at $2\tau_{12} - 2\tau_C$, $2\tau_{12} - \tau_C$, and $2\tau_{12}$. As follows from Equation (6.10), the sign of the SWM response at $2\tau_{12} - \tau_C = 65$ ps is inverted for a phase shift of $\phi = \pi$ with respect to the case $\phi = 0$. In the Fourier spectrum, Figure 6.2c, these temporal cross sections correspond to Ramsey fringes with a period given by τ_C^{-1} modulated by the Gaussian distribution of detunings. The phase of the fringes is directly set by the relative phase between the control pulses.

6.1.2 Effect of finite pulse duration on multi-wave-mixing signals in the Rabi regime

In this section, we discuss how the results presented for the impulsive limit are modified when the pulse duration t_p is not significantly smaller than the dephasing time T_2^*. In this case, the dephasing of the TLS during pulse action has to be taken into account. For our discussion, we first consider an experiment with only one control pulse under otherwise the same conditions as in Section 6.1.1. In this way, we gain an intuitive understanding of the effect of finite pulse durations that can be expanded for more complex pulse arrangements.

We start again with an analytical expression for the full signal detected in the direction $2\mathbf{k}_2 - \mathbf{k}_1$ in the impulsive limit

$$E_S = E_{2PE} \cos^2\left(\frac{A_C}{2}\right), \tag{6.12}$$

which describes Rabi rotations of the PE as a function of the control pulse area A_C at the fixed temporal position $2\tau_{12}$. The signal field E_S as a function of real-time and pulse area A_C is visualized in Figure 6.3a according to Equation (6.12). Note that the time axis is normalized to the inhomogeneous dephasing time T_2^*.

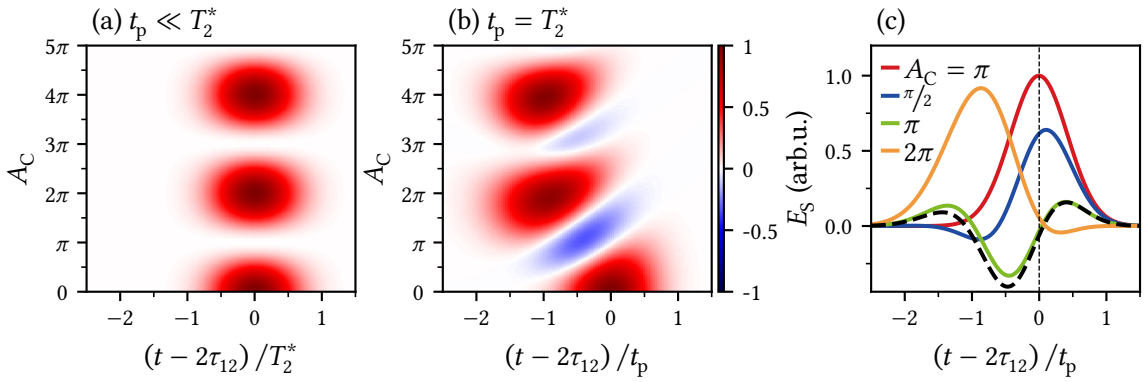

Figure 6.3: (a) Dependence of the signal amplitude E_S as a function of time t and the area of the single control pulse A_C in impulsive limit according to Equation (6.12). The time axis is shown relative to $2\tau_{12}$ in units of the dephasing time T_2^*. (b) Calculation of E_S for a single control pulse with finite duration t_p using optical Bloch equations. The time axis is shown in units of t_p. (c) Temporal cross sections of the map shown in (b) for selected values of the pulse area A_C. For comparison, the dashed black line shows the result of a perturbative expansion of the signal field for the case $A_C = \pi$ (corresponds to the black line in (c)).

Next, we model the effect of a control pulse with finite duration and therefore choose $t_p = T_2^*$, i.e., a pulse duration equal to the duration of the PE, which corresponds to the experimental situation presented later. The exciting and refocusing pulses are considered in the impulsive limit. For

simplicity, the temporal shape of the control pulse is considered rectangular. For a rectangular pulse shape, an analytical solution of the optical Bloch equations is well known [95] and can be used to model the dependence of the coherent response as a function of detuning Δ and pulse area A_C. For this purpose, the matrix describing the action of the optical pulse on the density matrix, given for delta pulses in Equation (6.3), has to be modified

$$\mathbf{M} = \begin{pmatrix} 1-\frac{\Omega_R^2(1-c)}{2\Omega^2} & \frac{\Omega_R^2(1-c)}{2\Omega^2} & \left(-\frac{\Delta\Omega_R(1-c)}{2\Omega^2}+i\frac{\Omega_R s}{2\Omega}\right)e^{-i\phi} & \left(-\frac{\Delta\Omega_R(1-c)}{2\Omega^2}-i\frac{\Omega_R s}{2\Omega}\right)e^{+i\phi} \\ \frac{\Omega_R^2(1-c)}{2\Omega^2} & 1-\frac{\Omega_R^2(1-c)}{2\Omega^2} & \left(\frac{\Delta\Omega_R(1-c)}{2\Omega^2}-i\frac{\Omega_R s}{2\Omega}\right)e^{-i\phi} & \left(\frac{\Delta\Omega_R(1-c)}{2\Omega^2}+i\frac{\Omega_R s}{2\Omega}\right)e^{+i\phi} \\ \left(-\frac{\Delta\Omega_R(1-c)}{2\Omega^2}+i\frac{\Omega_R s}{2\Omega}\right)e^{+i\phi} & \left(\frac{\Delta\Omega_R(1-c)}{2\Omega^2}-i\frac{\Omega_R s}{2\Omega}\right)e^{+i\phi} & c+\frac{\Omega_R^2(1-c)}{2\Omega^2}+i\frac{\Delta s}{\Omega} & \frac{\Omega_R^2(1-c)}{2\Omega^2}e^{2i\phi} \\ \left(-\frac{\Delta\Omega_R(1-c)}{2\Omega^2}-i\frac{\Omega_R s}{2\Omega}\right)e^{-i\phi} & \left(\frac{\Delta\Omega_R(1-c)}{2\Omega^2}+i\frac{\Omega_R s}{2\Omega}\right)e^{-i\phi} & \frac{\Omega_R^2(1-c)}{2\Omega^2}e^{-2i\phi} & c+\frac{\Omega_R^2(1-c)}{2\Omega^2}-i\frac{\Delta s}{\Omega} \end{pmatrix}, \quad (6.13)$$

with the Rabi frequency Ω_R, generalized Rabi frequency $\Omega = \sqrt{\Omega_R^2+\Delta^2}$, $c = \cos\Omega t_p$, and $s = \sin\Omega t_p$. Using this modified matrix, we obtain the dependence of the signal field emitted in direction $2\mathbf{k}_2 - \mathbf{k}_1$ as a function of the area A_C of a single control pulse and real-time t:

$$E_S \propto \int_{-\infty}^{\infty} d\Delta\, G(\Delta)\left\{\frac{\Delta}{\Omega_C}\sin\left(\Omega_C t_p\right) + i\left[\frac{\Omega_{R,C}^2}{\Omega_C^2}\sin^2\left(\frac{\Omega_C t_p}{2}\right)+\cos\left(\Omega_C t_p\right)\right]\right\}\exp\left[i\Delta\left(\tau_{ref}-2\tau_{12}+t_p\right)\right], \quad (6.14)$$

where $\Omega_C = \sqrt{\Omega_{R,C}^2+\Delta^2}$, $\Omega_{R,C} = A_C/t_p$, and the distribution of detunings $G(\Delta)$

$$G(\Delta) = \frac{\exp\left[-\frac{\Delta^2}{2\sigma^2}\right]}{\sqrt{2\pi}\sigma}, \quad \sigma = \frac{T_2^*}{\sqrt{8\ln 2}}. \quad (6.15)$$

The integral over detunings Δ is carried out numerically using the trapezoidal rule. The result is graphically presented in Figure 6.3b in direct comparison to the impulsive limit $t_p \ll T_2^*$ in 6.3a. As in the impulsive limit, we can observe Rabi rotations of the signal with maxima at $A_C = 2n\pi$. However, the maxima for $A_C = 2\pi,\ 4\pi$ appear advanced by the pulse duration with respect to the two-pulse PE for $A_C = 0$, as we highlight in Figure 6.3c where we plot the temporal envelope of the signal field for selected values of A_C. For non-zero pulse areas, below roughly $\pi/2$, the maximum of the coherent emission is shifted to positive delay times as shown in Figure 6.3c by the orange curve corresponding to $A_C = \pi/2$. We can observe an additional pronounced negative local extremum for $A_C = \pi$ where the signal equals zero in the impulsive limit, as given by Equation (6.12). The described advancement of PE pulse was observed previously in Reference [158] and can be explained by the fact that the action of a pulse with an area of $2n\pi$ and $\Omega_R \gg \Delta$ leaves the phases of individual TLS unaffected after a full Rabi rotation induced by the control pulse during t_p. Therefore, the overall phase evolution is effectively "frozen" for a duration of t_p and the coherent emission of the ensemble is shifted. However, the temporal shifts for arbitrary pulse areas and in particular for $A_C \leq \pi/2$, where a retardation of the signal is observed, remained so far unclear.

To gain insight into the non-trivial modification of the temporal shape of the PE profile by the effect of an additional control pulse with a finite duration, we propose in the following a perturbative expansion of the signal in MWM orders. As we will show, the effect of finite pulse duration leads to a temporal shift of the MWM fields that monotonously grows with the order of the MWM process. For the theoretical discussion, we make use of the perturbative MWM expansion of the non-linear polarization as introduced in Section 1.2.2. Here, we calculate the m-th order polarization $P^{(m)}$, being the source of a $(m+1)$-wave mixing response by constructing all contributing Feynman diagrams and subsequently apply the set of Equations (1.16). We only capture signals emitted in the direction $2\mathbf{k}_2 - \mathbf{k}_1$. Therefore, we take into account only those nonlinear terms that involve the same number of interactions with E_C and E_C^*, such as SWM

resulting from the fifths order polarization $P^{(5)} \propto E_1(E_2^*)^2 E_C E_C^*$. For the SWM process, four unique Feynman diagrams fulfill the time ordering and phase-matching condition. We show these diagrams in Table 6.1. The exciting and refocusing pulses are considered as delta-pulses in the lowest non-vanishing order, i.e. the first pulse in linear and the refocussing pulse in quadratic order. For the control pulse, we assume a rectangular-shaped envelope of duration t_p. All diagrams in Table 6.1 give the same contribution to the nonlinear polarization as a function of detuning Δ, that is

$$P^{(5)}(t,\Delta) \propto E_1(E_2^*)^2 \int_{-\infty}^{\tau_{12}} dt_{C2} \int_{-\infty}^{t_{C2}} dt_{C1} E_C(t_{C2}) E_C^*(t_{C1}) \exp\left[i\Delta(t-2\tau_{12}) + i\Delta(t_{C2}-t_{C1})\right], \quad (6.16)$$

where we labeled the integration variables corresponding to the control pulse field with t_{Cj}. Here, it can be seen that the control pulse has a direct impact on the phase evolution of the ensemble, as the usual phase factor $\exp(i\Delta(t-2\tau_{12}))$, that gives rise to a PE centered at $t = 2\tau_{12}$, is modified by the factor $\exp(i\Delta(t_{C2}-t_{C1}))$. To finally obtain the overall response of the inhomogeneous ensemble, we numerically average the nonlinear polarization over a Gaussian distribution of detuning as described above. In this way, we obtain the PE response of the ensemble in second-order perturbation with respect to the control pulse field, which is shown in Figure 6.4a (red dashed line), in comparison to the PE pulse in absence of the control pulse (blue line). Note that we normalized the signals that were calculated for a fixed value of the electric field E_C to their maximum. The global sign of the MWM signals alternates with increasing order. This effect was experimentally observed in Reference [181] where different orders of MWM processes in pump-probe experiments were compared. Interestingly, the temporal position is shifted towards negative delays in the case of SWM with respect to the four-wave mixing (FWM) PE pulse at $t = 2\tau_{12}$. To further analyze this effect, we calculate the PE pulses for higher-order interactions with the control pulse field. The next order is an EWM process including four interactions with the control pulse fields. For this perturbative order, there are 16 Feynman diagrams that we explicitly show in Table 6.2. Note that for higher orders than SWM, not all Feynman diagrams give necessarily the same contribution to the non-linear polarization. Compare for example in Table 6.2 the first and second diagram in the top row. Here, the phase evolution between the second and third interaction with the control pulse field is conjugated. As shown in Figure 6.4a, the PE pulse from the EWM response is shifted further toward negative delays. We plot the temporal shift Δt for up to twelve interactions (sixteen-wave-mixing) with the control pulse field in Figure 6.4b. Here, $|\Delta t|$ increases monotonically tending towards the pulse duration t_p (red line). Consequently, the temporal shift between two consecutive MWM orders approaches zero with increasing order.

We thus can understand the complex waveforms of the coherent response of the ensemble with increasing area of the control pulse in Figure 6.3c as an interference pattern of MWM orders that each give rise to a single PE pulse at a well-defined temporal position. Since the temporal shift is largest between consecutive low-order MWM components (Figure 6.4b), the interference pattern deviates most strongly from a single Gaussian PE pulse in the range of small pulse areas where low perturbative orders dominate the signal. As an example of the formation of non-Gaussian waveforms from the interference of different MWM orders, we plot in Figure 6.4c the MWM signals up to the sixth order in E_C for $A_C = E_C t_p \mu/\hbar = \pi$. The sum of the pulses with alternating signs results in the black solid curve that accurately reproduces the exact calculation as we highlight by directly comparing the exact and perturbative result (green and black line) in Figure 6.3c. The negative SWM signal (red dashed line in Figure 6.4c) has the largest amplitude and is therefore dominantly responsible for the negative signal at $A_C = \pi$ and the shift of the maximum signal towards positive delays for pulse areas $\lesssim \pi/2$ that we mentioned above.

Table 6.1: Unique Feynman diagrams for the six-wave-mixing process in a single control pulse experiment fulfilling the phase matching condition $2\mathbf{k}_2 - \mathbf{k}_1$ and time ordering of E_1, E_C, and E_2.

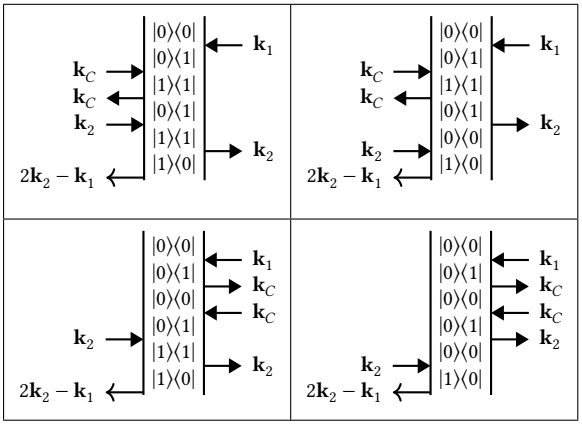

Table 6.2: Unique Feynman diagrams for the eight-wave mixing process in a single control pulse experiment fulfilling the phase matching condition $2\mathbf{k}_2 - \mathbf{k}_1$ and time ordering of E_1, E_C, and E_2.

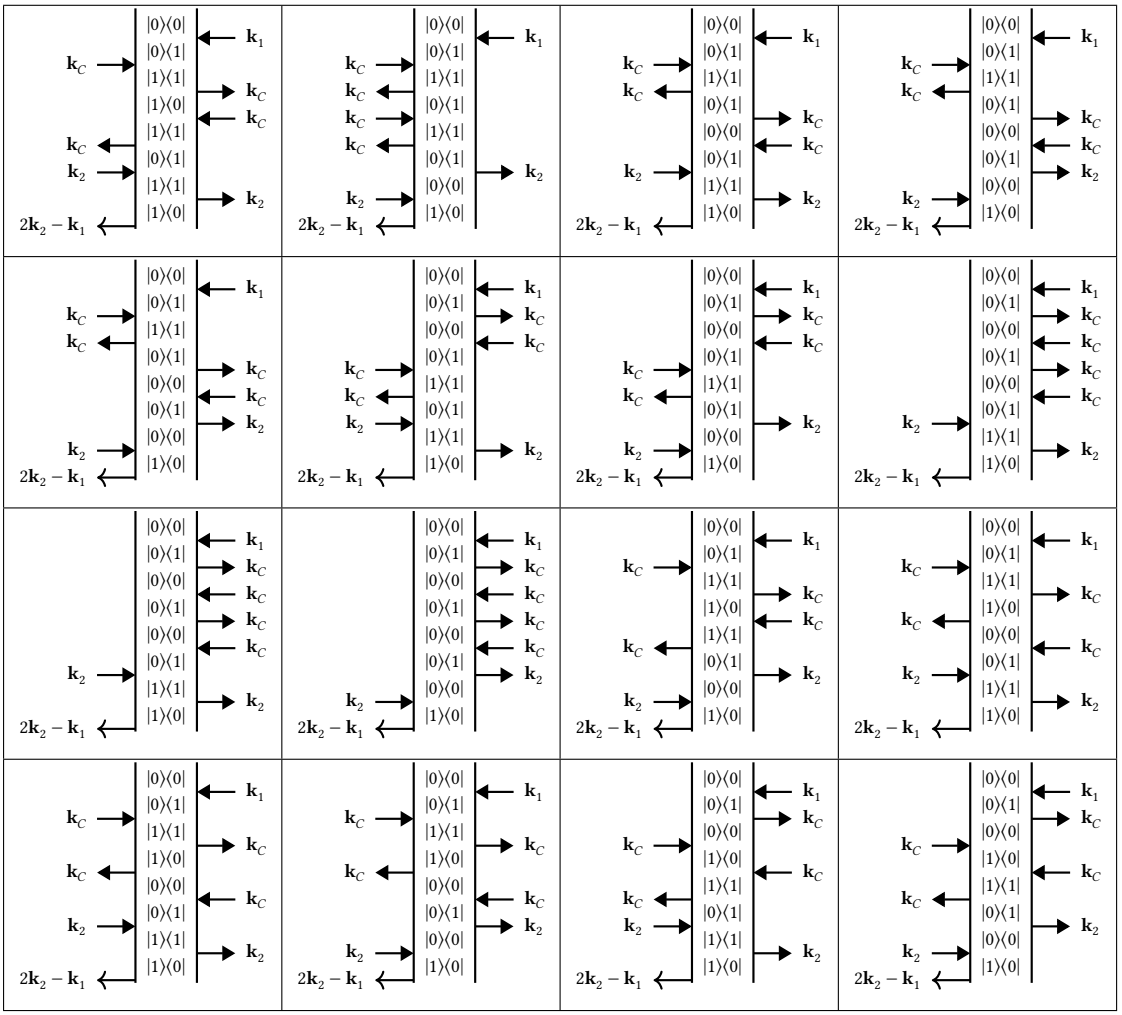

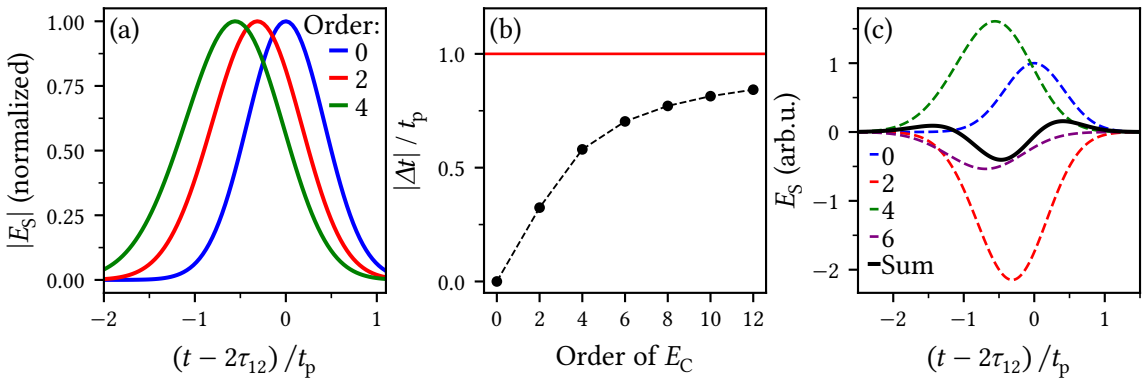

Figure 6.4: (a) PE signals calculated for different numbers of interactions with the control pulse field. (b) Temporal shifts of PEs calculated for different MWM orders. (c) Decomposition of total signal for $A_C = \pi$ in up to ten-wave mixing components.

In summary, we have discussed a nonlinear optical regime, where the expansion of Rabi rotations into MWM orders allows to gain meaningful insights into the non-trivial temporal shape of coherent emission caused by the finite duration of optical pulses. Within the impulsive limit, such expansion is not useful since all MWM orders appear simultaneously and result in Rabi rotations centered around a fixed emission time. We found that the finite pulse duration however lifts this temporal degeneracy and leads to a temporal sorting of MWM orders.

For the experiments including two control pulses, we expect similar modifications of the impulsive limit, i.e. temporal shifts of the PE signals and the occurrence of new local extrema evoked by higher-order MWM components. The modified closed expressions for the three signal fields are given by

$$\begin{aligned} E_{\mathrm{FWM}} \propto \int_{-\infty}^{\infty} \mathrm{d}\Delta\, G(\Delta) \Bigg\{ & \frac{\Omega_{R,C}^2 \Delta}{\Omega_C^3} \left[\sin(\Omega_C t_p)\cos(\Omega_C t_p) - \sin(\Omega_C t_p) \right] \\ & - \frac{\Delta}{\Omega_C} \sin(\Omega_C t_p)\cos(\Omega_C t_p) - i\frac{\Omega_{R,C}^4}{2\Omega_C^4} \sin^4\left(\frac{\Omega_C t_p}{2}\right) \\ & + i\frac{\Delta^2}{2\Omega_C^2} \sin^2(\Omega_C t_p) + i\frac{\Omega_{R,C}^2}{2\Omega_C^2} \cos(\Omega_C t_p)[\cos(\Omega_C t_p) - 1] \\ & - i\frac{1}{2} \cos^2(\Omega_C t_p) \Bigg\} \exp\left[i\Delta(\tau_{\mathrm{ref}} - 2\tau_{12} + 2t_p) \right] \end{aligned} \tag{6.17}$$

$$\begin{aligned} E_{\mathrm{SWM}} \propto \int_{-\infty}^{\infty} \mathrm{d}\Delta\, G(\Delta) \Bigg\{ & \frac{\Omega_{R,C}^2 \Delta}{2\Omega_C^3} [\sin(\Omega_C t_p) - \sin(\Omega_C t_p)\cos(\Omega_C t_p)] \\ & + i \left[\frac{\Omega_{R,C}^2}{4\Omega_C^2} \sin^2(\Omega_C t_p) - \frac{\Omega_{R,C}^2 \Delta^2}{\Omega_C^4} \sin^4\left(\frac{\Omega_C t_p}{2}\right) \right] \Bigg\} \times \\ & \times \exp\left[i\Delta(\tau_{\mathrm{ref}} - 2\tau_{12} + \tau_C + t_p) - i\phi \right] \end{aligned} \tag{6.18}$$

$$E_{\mathrm{EWM}} \propto \int_{-\infty}^{\infty} \mathrm{d}\Delta\, G(\Delta) \left\{ -i\frac{\Omega_{R,C}^4}{2\Omega_C^4} \sin^4\left(\frac{\Omega_C t_p}{2}\right) \right\} \exp\left[i\Delta(\tau_{\mathrm{ref}} - 2\tau_{12} + 2\tau_C) - i2\phi \right]. \tag{6.19}$$

These signal fields are plotted in Figures 6.5a–c.

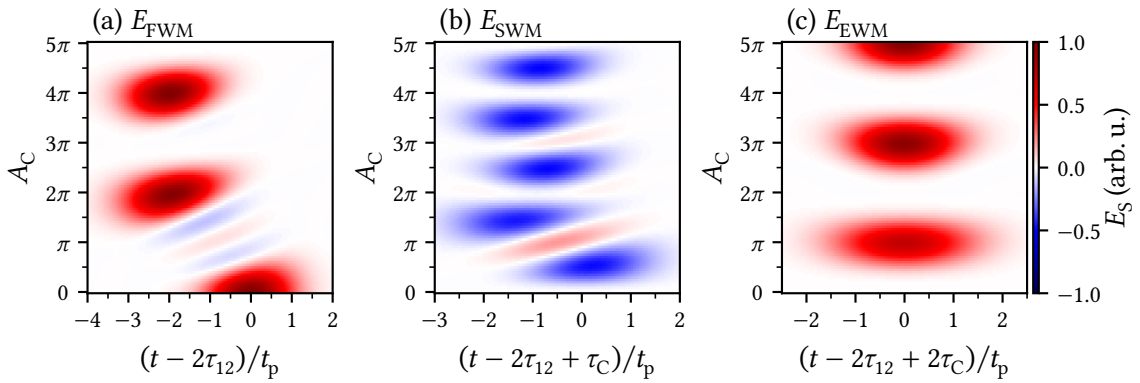

Figure 6.5: Temporal modifications of the three signals E_{FWM}, E_{SWM} and E_{EWM} as a function of A_{C} for finite duration of the control pulse fields.

6.2 Demonstration of control pulse experiment in co-polarized configuration

Within this section, we neglect the polarization degree of freedom by choosing linearly co-polarized pulses. As mentioned above, the trion scheme can be considered as a TLS under this condition. In this way, we first set the focus on the temporal characteristics of the discussed MWM signals.

The experiments were performed at a temperature of 2 K on the ensemble of (In,Ga)As QDs that was already characterized in Chapter 5. We excite the sample using 4 ps laser pulses that are tuned to the maximum of the photonic mode at 1.345 eV. As already discussed in Chapter 5, the spectral width of the pulses, 0.3 meV, is significantly narrower than the spectrum of the QD–cavity system, but still much broader than the homogeneous linewidth of the QDs ($\approx$ 1.6 µeV). Therefore, the laser pulses act on a macroscopic subensemble of emitters whose inhomogeneous broadening is governed by the laser spectrum. Note that this situation where the effective dephasing time T_2^* equals the pulse duration is ideal for studying the effect of finite pulse durations on the coherent response that we discussed in Section 6.1.2. The area of the laser pulses is adjusted by changing their intensity using combinations of $\lambda/2$ retardation plates and polarizers. Since we study MWM signals as a function of the pulse area, it is decisive to address all QDs with the same intensity. Therefore, we use spatially flat intensity profiles of the control pulses as proposed in Chapter 5. Under this condition, we circumvent a fading of the signal as a function of pulse area which is present for spatially Gaussian laser pulses.

We introduced a temporal delay between the exciting and refocusing pulse of $\tau_{12} = 40$ ps and between exciting and the first control pulse of $\tau_{1c} = 13$ ps. The temporal gap between the control pulses is $\tau_{\mathrm{C}} = 15.3$ ps. In this way, both control pulses interact with the sample temporally in between the exciting and refocusing pulse and the temporal overlap between all pulses is negligible. Note that all temporal gaps are here significantly smaller than the coherence time of the QDs $T_2 = 0.8$ ns. As already discussed in Chapter 2.1, the optical phases between all involved pulses are not actively stabilized. A phase-locked measurement of the signal fields is thus not subject to our studies. Instead, we capture the mean value of the modulus of the signal field $\langle |E_{\mathrm{S}}^c| \rangle$, where $\langle \cdot \rangle$ denotes here the average over a uniform distribution of optical phases of the involved pulses. When comparing experimental data with modeling results, we take this phase average into account.

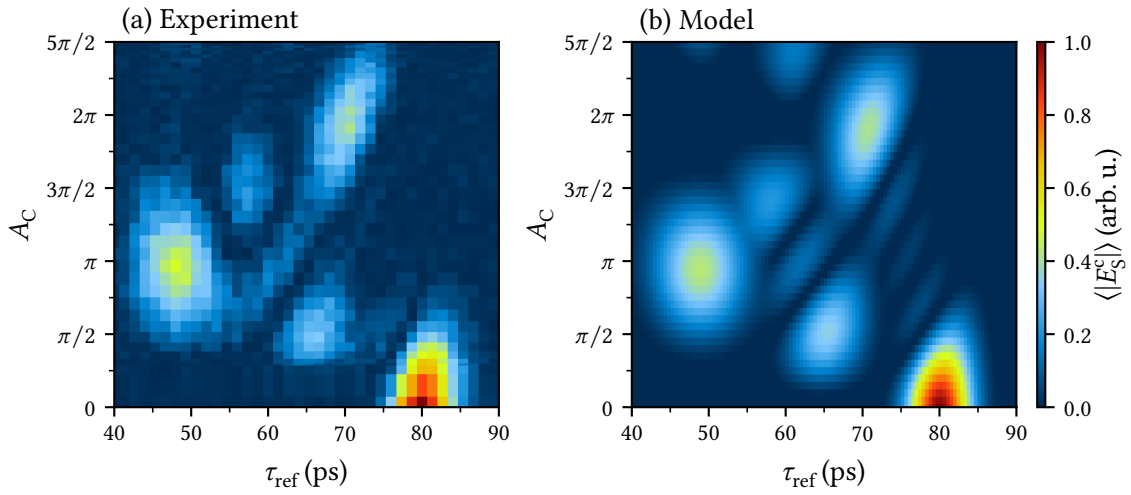

Figure 6.6: (a) Experimental dependence of the heterodyne signal on the area of the control pulses A_C and the reference time τ_{ref}. (b) Result of the calculation of $\langle |E_S^c| \rangle$ using optical Bloch equations assuming rectangular-shaped temporal envelopes of the control pulses. The intensity-dependent damping mechanisms were considered phenomenologically as described in the text.

To investigate the influence of the control pulses on the temporal shape of the coherent response, we measured the heterodyne signal as a function of the reference time τ_{ref} and the area of the control pulses A_C. For $A_C = 0$, the coherent response is given by the two-pulse PE pulse centered at $\tau_{ref} = 2\tau_{12} = 80$ ps. The control pulse area is varied by changing the intensity of the laser pulses. The areas of exciting and refocusing pulse were fixed at $A_1 = \pi/2$ and $A_2 = \pi$, respectively, corresponding to the maximum of the two-pulse PE, Equation (6.6). The experimental result is presented as a two-dimensional color map in Figure 6.6a. Next to the unshifted PE at 80 ps for $A_C = 0$, we can observe four local maxima of the signal within the temporal range between 50 ps and 80 ps occurring at multiples of $A_C = \pi/2$. This observation is in agreement with the modeling in the impulsive limit (see Figure 6.2a): For $A_C = \pi/2$, the maximum of the SWM response occurs at $\tau_{ref} = 2\tau_{12} - \tau_C \approx 65$ ps. Furthermore, at $A_C = \pi$, we can identify the local extremum of the EWM response located at $\tau_{ref} = 2\tau_{12} - 2\tau_C \approx 50$ ps. Due to the finite duration of the laser pulses, however, the overall temporal envelope of the heterodyne signal has a more complex shape as described by Equations (6.8) - (6.10). We can understand this observation using the approach presented in Section 6.1.2 as a non-trivial interference pattern of MWM contributions that experience a different temporal shift caused by the finite pulse duration. As a special case, when each control pulse area equals 2π, the emission appears at $\tau_{ref} = 2\tau_{12} - 2t_p \approx 72$ ps, which can be understood from our discussion of the finite duration of a single control pulse. Here, high-order MWM contributions appear advanced by the duration of each control pulse. Thus, the observations are a manifestation of the transition between perturbative and strong field limits as discussed in Section 6.1.2.

In addition to the temporal modification, we can observe a pulse-area-dependent damping of the signal. The amplitude of the signal's maximum for $A_C = 2\pi$ amounts to roughly 40 % of the PE amplitude in the absence of control pulses. In Chapter 5, we identified phonon-assisted relaxation processes during the action of the laser pulses as the main source for the loss of coherence with increasing pulse area. Within this chapter, we set the focus solely on the temporal characteristics of the observed PE signals and especially how they are influenced by the pulse area of the control pulses. To theoretically reproduce the experimental data, we use the non-perturbative modeling procedure as applied in Section 6.1.2. Closed expressions for the final modeling results are given

by Equations (6.17)–(6.19). We further take into account the cross-correlation with the reference pulse. To quantify the damping of the signal with increasing pulse area, the damping mechanisms discussed in Chapter 5 are phenomenologically considered by multiplying the modeled data with a function $\exp(-A_C/A_0)$, where the best agreement is found for $A_0 = 2.4\pi$. As shown in Figure 6.6b, we achieve excellent agreement between experimental and modeled data both regarding the temporal characteristics of the MWM response and the damping of the signal with increasing A_C. It is worth recalling that the control pulses in our model adopt a rectangular shape, demonstrating that the modified temporal response of the ensemble is predominantly influenced by the pulse area, rather than the precise temporal shape of the control pulses.

As mentioned above, the case $A_C = \pi/2$ is in analogy to a Ramsey fringe experiment. Figure 6.7a shows the temporal cross-sections of the color maps in Figures 6.6a and 6.6b for $A_C = \pi/2$ consisting mainly of three peaks. In the amplitude spectrum, this temporal shape corresponds to spectral fringes with a period of roughly $\tau_C^{-1} \approx 65\,\mathrm{GHz}$ as presented in Figure 6.7b. This observation is in agreement with our expectations if compared with Figures 6.2b and 6.2c. We thus demonstrate that the chosen geometry of optical control pulses realizes Ramsey fringes on a QD ensemble and thus enables to directly impact on the spectrum of the macroscopic emission. Note however that the phase of the signal field E_S is not resolved in our experiments. Therefore, we can experimentally control solely the frequency of the Ramsey fringes. Active stabilization of the optical phase between the two control pulses would allow to gain further control over the quantum states of the emitters within the ensemble, which we regard as a prospect for future studies. Apart from that, the importance of the relative optical phase is manifested in the possibility to control the polarization of emission from an ensemble of trions as will be demonstrated in the following section.

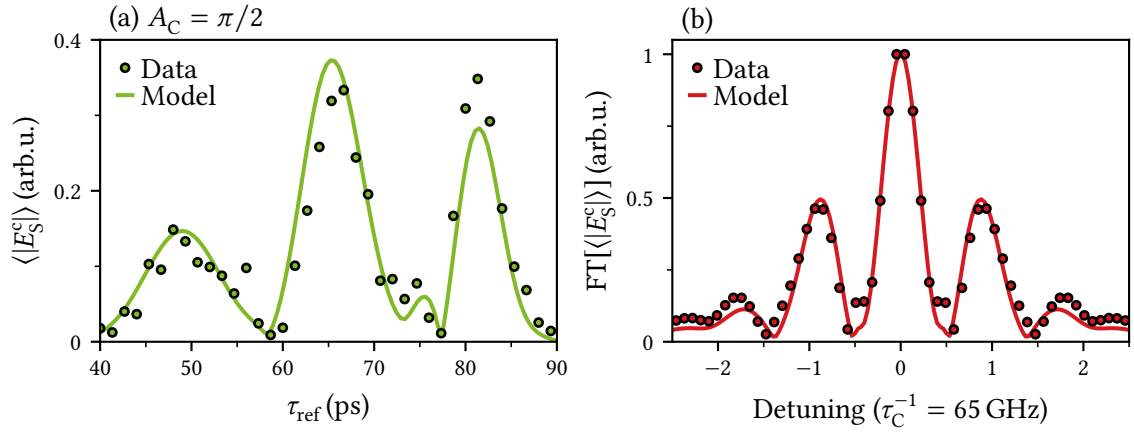

Figure 6.7: (a) Temporal cross-section of the color maps in Figure 6.6a and 6.6b for $A_C = \pi/2$. Dots and lines correspond to the experiment and model, respectively. (b) Absolute value of the Fourier transform of the temporal cross sections shown in (a).

6.3 Polarization-selective multi-wave mixing

As a next step, we take into account the spin degree of freedom in the QD sample to expand the possibilities of the presented control of MWM processes. In what follows, we present two possible polarization-resolved experiments, where we show that the selection rules for optical transitions in the four-level trion scheme open up new appealing possibilities to address the

polarization of the emitted photon PEs based on the sensitivity to the relative phase between the two optical control pulses.

First, we demonstrate that we can use the mutual polarization between the two control pulses to modify the polarization of the different MWM processes. Therefore, we consider the same pulse arrangement as depicted in Figure 6.1a. In contrast to the measurements presented so far, the linear polarization angle of the second control pulse with respect to the linear polarization of all other pulses is considered as an additional degree of freedom. To account for polarization in the MWM processes from the trion scheme, we construct the electric fields of the linearly polarized pulses E_j with linear polarization angle φ_j in circular polarization basis

$$E_\mathrm{j}(\varphi_\mathrm{j}) = \mathrm{e}^{-i\varphi_\mathrm{j}} E_\mathrm{j}^{+} + \mathrm{e}^{+i\varphi_\mathrm{j}} E_\mathrm{j}^{-}. \tag{6.20}$$

Without loss of generality, we choose the linear polarizations of exciting, refocussing, and first control pulse as $\varphi_\mathrm{j} = 0$ (horizontally polarized) and introduce φ as the relative rotation of the polarization of the second control pulse. We use Equations (6.8) - (6.10) to calculate the EWM response at $t = 2\tau_{12} - 2\tau_\mathrm{C}$ and the SWM response at $t = 2\tau_{12} - \tau_\mathrm{C}$ as a function of φ and the polarization φ_ref of the reference pulse, which defines the detected polarization component of the signal

$$E_\mathrm{EWM}(\varphi, \varphi_\mathrm{ref}) \propto \sin^4\left(\frac{A_\mathrm{C}}{2}\right) \cos\left(2\varphi + \varphi_\mathrm{ref}\right) \tag{6.21a}$$

$$E_\mathrm{SWM}(\varphi, \varphi_\mathrm{ref}) \propto \sin^2\left(A_\mathrm{C}\right) \cos\left(\varphi + \varphi_\mathrm{ref}\right). \tag{6.21b}$$

EWM and SWM thus differ by their dependence on the angle φ. To experimentally demonstrate this property, we choose $\varphi = \pi/2$, i.e. the control pulses are linearly cross-polarized, which we set as horizontally (H) and vertically (V) polarized. According to Equations (6.21a) and (6.21b), under this condition the EWM response is H-polarized whereas the SWM signal is V-polarized. The polarization contrast between both components is thus maximized in the configuration $\varphi = \pi/2$. Note that the third main contribution to the overall signal E_FWM, as follows from Equation (6.8), is insensitive to phases of the control pulses and therefore does not depend on the linear polarization angle φ. The signal E_FWM is therefore expected to be horizontally polarized as defined by the polarizations of exciting and refocusing pulse.

In Figure 6.8 we measured the signal field amplitude as a function of τ_ref and A_C, where we additionally distinguished between $\varphi_\mathrm{ref} = 0$ (Figure 6.8a, H-detection) and $\varphi_\mathrm{ref} = \pi/2$ (Figure 6.8b, V-detection). By comparing the color maps with the results obtained for co-polarized pulses, Figure 6.6a, we can observe that we achieved to decompose the MWM response in H- and V-polarized components. For horizontal detection ($\varphi_\mathrm{ref} = 0$), Figure 6.8a, we observe the two-pulse PE at $\tau_\mathrm{ref} = 2\tau_{12}$, the EWM response at $A_\mathrm{C} = \pi$, $\tau_\mathrm{ref} = 2\tau_{12} - 2\tau_\mathrm{C} = 45\,\mathrm{ps}$, and the signal at $A_\mathrm{C} = 2\pi$, $\tau_\mathrm{ref} = 2\tau_{12} - 2t_p = 70\,\mathrm{ps}$. The SWM response at $A_\mathrm{C} = \pi/2$, $\tau_\mathrm{ref} - \tau_\mathrm{C} \approx 62\,\mathrm{ps}$ can be observed solely in vertically polarized detection configuration ($\varphi_\mathrm{ref} = \pi/2$), see Figure 6.8b. Both color maps 6.8a and 6.8b can be accurately reproduced by our modeling procedure as discussed above using the optical Bloch equations for the trion scheme in Figures 6.8c and 6.8d.

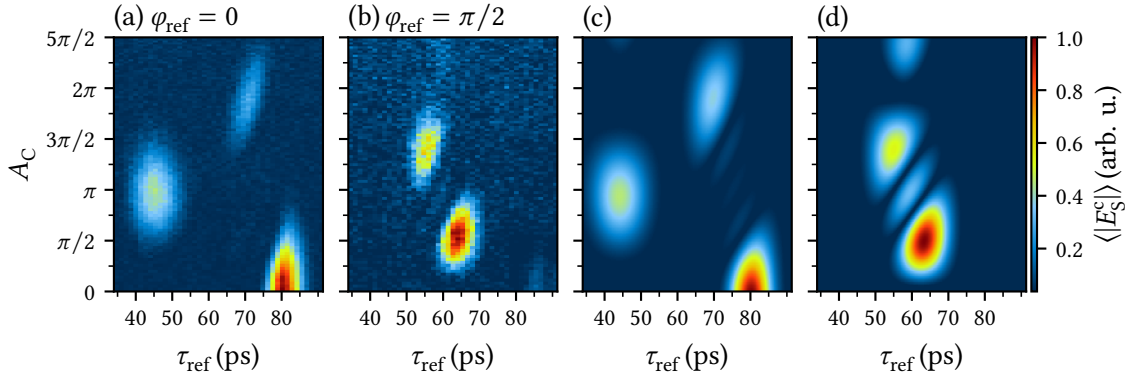

Figure 6.8: (a)/(b) Heterodyne signal as a function of control pulse area and reference time. In contrast to the measurement in Figure 6.6a, the two control pulses are cross-polarized, i.e. horizontally (H) and vertically (V) polarized. The signal is detected in H polarization (a) and V polarization (b). (c)/(d) Modeling results corresponding to experimental data in (a) and (b).

6.4 Temporal splitting of photon echoes

As a second example, we elaborate on the possibility to independently modify the coherent emission from the two TLS that form the trion scheme using circularly polarized control pulses. In particular, we use circularly polarized control pulses to independently evoke temporal shifts of the coherent emission in σ^+ and σ^- polarization. For this purpose, we modify the temporal arrangement of the optical pulses as sketched in Figure 6.9a. Here, the exciting and refocusing pulses are horizontally polarized, while the control pulses have opposite circular polarizations. The refocusing pulse is temporally located in between the two control pulses. This situation corresponds to an experiment with only one control pulse for each of the TLS that we considered in Section 6.1.2. When the area of each control pulse equals 2π, the phase evolution of each subensemble is frozen for a period of t_{p}, which is schematically shown by the phase diagram in Figure 6.9a. However, for one subensemble, the freezing takes place during the dephasing motion, while for another one during the rephasing motion. Consequently, the coherent emission is temporally split into two cross-polarized components arising at $2\tau_{12} \pm t_{\mathrm{p}}$.

We experimentally demonstrate the described effect in Figure 6.9 by continuously sweeping the pulse area A_{C} and temporally resolving the coherent emission in σ^- (Figure 6.9a) and σ^+ detection (Figure 6.9b). For a control pulse area of 2π, the σ^- component is shifted by -4 ps, whereas the σ^+ component is shifted by $+4$ ps relative to the two-pulse PE emission at $2\tau_{12} = 80$ ps as highlighted by white arrows. The experiments further allow to observe the signal at $A_{\mathrm{C}} = \pi$ that is dominated by a SWM contribution as discussed in Section 6.1.2 and therefore represents a further demonstration of lifting the degeneracy of MWM orders in the strong field limit by using finite pulse durations. The overall dependence on A_{C} and τ_{ref} is well reproduced by the modelled data in Figure 6.3b.

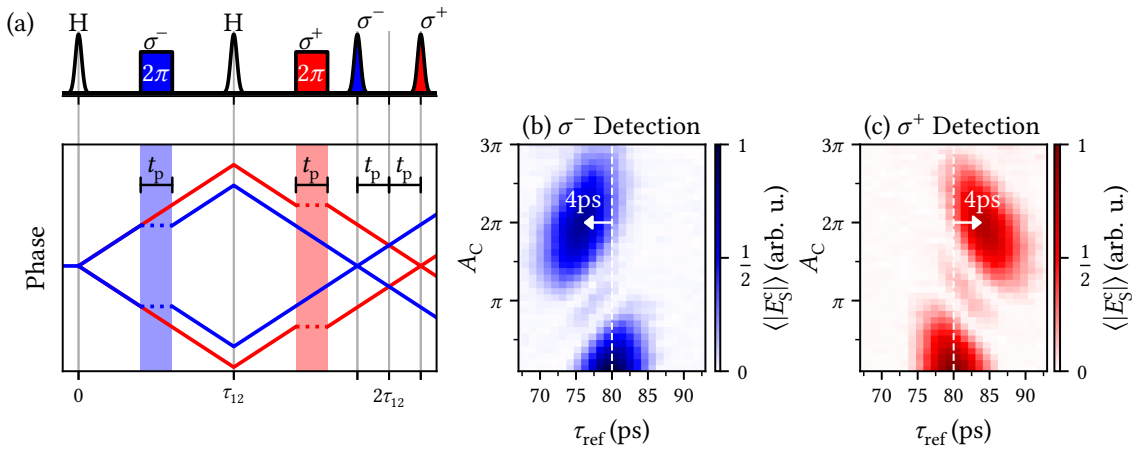

Figure 6.9: (a) Schematic illustration of the approach for the temporal splitting of linearly polarized PE in two cross-polarized components. The phase evolution of two oscillators within the σ^- (σ^+) subensemble is shown by blue (red) lines. As indicated on top, the first σ^- polarized control pulse is temporally located between the exciting and refocussing pulse, whereas the second σ^+ polarized control pulse acts between the refocussing and PE pulse. When the respective areas of the control pulses equal 2π, the phase evolution of the two subensembles (σ^+ and σ^-) is effectively frozen for the pulse duration t_p. In this way, the coherent response is temporally split into two circularly cross-polarized components. Note that all pulses in the experiment have the same temporal shape and duration, the two control pulses are schematically shown as rectangular pulses. (b)/(c) Experimental demonstration of the temporal splitting as discussed in (a). For $A_C = 2\pi$, we can observe a shift of the maximum coherent emission by $\mp t_p = \mp 4$ ps for the σ^- (b) and σ^+ (c) polarized components as highlighted by the horizontal arrows.

6.5 Conclusions

We demonstrate coherent optical control over the phase evolution of an ensemble of trions in charged (In,Ga)As QDs by employing temporally sorted MWM processes that are driven under resonant excitation in the regime of Rabi rotations. We have chosen a temporal and angular arrangement of four optical pulses, where two pulses act as control knobs of the trion qubits, whereas the other two pulses serve as a PE protocol to monitor the phase evolution of the inhomogeneously broadened ensemble. Using the energy and momentum conservation, we select three PE signals that are generated by degenerate four-, six-, and eight-wave-mixing processes in the lowest non-vanishing perturbative order. The temporal delay between the three distinct PE signals is given by the temporal delay between the control pulses. Depending on the area of the control pulses A_C, the phase evolution of trion ensemble can be modified in several ways. Ramsey fringes in the trion ensemble can be observed when the area of the control pulses equals $\pi/2$ which is manifested in the time domain as a coexistence of all three discussed PE signals. Further, the phases of trions can be fully inverted by each of the control pulses with area of π which results in a complete transfer of the macroscopic coherence from the FWM-PE to the EWM-PE.

As a next step, we exploited the spin degree of freedom in a four-level trion scheme to manipulate the polarization state of the coherent optical response. These findings demonstrate the importance of the relative optical phase between the control pulses, offering the possibility for arbitrary manipulation of the addressed trion states. Further, we demonstrate the splitting of the PE into two cross-polarized pulses, which has potential applications for the transformation between polarization and time-bin qubits in integrated semiconductor devices. Our demonstrations push

forward the realization of arbitrary pulse sequences, as widely used in NMR, for quantum memory protocols or information processing in ensembles of QDs by optical methods. We furthermore suggest new possibilities for coherent control that are not subject to NMR, such as polarization and wavevector selectivity.

We considered the importance of the frequency detuning of the driving optical field during the action of the control pulses. Here, using a perturbative MWM expansion we gained insight into how the coherent emission is modified when the inhomogeneous broadening of the excited ensemble and the width of the laser spectrum are comparable. Surprisingly, we revealed that different orders of MWM lead to an additional temporal sorting of the optical response, which can be interpreted in terms of additional modifications of the phase evolution. Lifting of the temporal degeneracy between different MWM processes allows to observe a transition from the perturbative to strong field regime with Rabi rotations. The strong temporal modification of the temporal MWM response potentially represents new spectroscopic signatures for investigations of complex energy structures in unexplored material systems, e.g. excitons in transition metal dichalcogenides [182, 183] or low-dimensional lead-halide perovskites [33, 184].

Summary and Outlook

In the first part of this thesis, photon echoes were employed as a spectroscopic tool to compare so far unexplored decoherence and interaction mechanisms of excitons in two representative organic-inorganic perovskite single crystals, $MAPbI_3$ and $FA_{0.9}Cs_{0.1}PbI_{2.8}Br_{0.2}$. The experimental studies presented in Chapter 3 revealed that, even at cryogenic temperatures, the exciton resonance in a high-quality $MAPbI_3$ crystal is subject to inhomogeneous broadening on the order of 10 meV. The inhomogeneity might be an intrinsic property of perovskites with organic cations, whose random orientation introduces a source of spatial band gap fluctuations that is absent in purely inorganic perovskites. Using the capability of time-resolved photon echo spectroscopy to overcome inhomogeneous broadening, the coherence time T_2 of excitons in $MAPbI_3$ was found to be $\lesssim 1$ ps, indicating that excitons are nearly free. In contrast, the mixed perovskite $FA_{0.9}Cs_{0.1}PbI_{2.8}Br_{0.2}$ possesses exciton coherence time extended by two orders of magnitude, although the inhomogeneous broadening is found in a similar range as in $MAPbI_3$. Combining the two- and three-pulse photon echo techniques, the decoherence time was disentangled into contributions from elastic and inelastic scattering. Their energy and temperature dependence confirmed that the extended coherence time arises from the localization of excitons as a whole on band gap fluctuations at the nanometer scale. Since band gap fluctuations are directly connected to charge transport, absorption, and emission properties of the system, the findings are relevant for the optimal design of photovoltaic and light-emitting devices. As a next step, the presented study should be expanded to different perovskite compositions to study how the property of exciton localization in mixed perovskites can be optimized or diminished.

Chapter 4 made use of the sensitivity of non-linear spectroscopy to study exciton-exciton interactions in both perovskite crystals. Here, special emphasis was put on the interconnection with the spin degree of freedom and corresponding polarization dependences of non-linear optical spectra. For $MAPbI_3$, the exciton resonance was excited with broadband femtosecond pulses which allowed observing the formation of biexcitons, a bound state of two excitons with opposite spin. An experimental protocol accompanied by detailed modeling, based on quantum beats of the photon echo polarization state, was developed that offers high sensitivity to extract the biexciton binding energy of 2.4 meV. The presented technique will be useful to study other exciton systems with energy splittings that are comparable to the homogeneous linewidth. In $FA_{0.9}Cs_{0.1}PbI_{2.8}Br_{0.2}$, under narrowband excitation with picosecond laser pulses the effect of weak exciton interactions on the μeV energy scale between localized excitons was studied. In particular, the polarization dependence of photon echo amplitude and its decay dynamic suggested that excitation-induced dephasing has a spin sensitivity. The experimental results were reproduced by an effective two-exciton model where exciton-exciton correlations are taken into account. In this way, a more detailed picture of localized but weakly interacting exciton in the $FA_{0.9}Cs_{0.1}PbI_{2.8}Br_{0.2}$ crystal was developed. These results suggest that the $FA_{0.9}Cs_{0.1}PbI_{2.8}Br_{0.2}$ crystal, exhibiting prolonged coherence times while maintaining significant correlation effects among excitons, could be an interesting system for fundamental research in the field of quantum optics, particularly for generating non-classical light states.

In the second part, the focus shifted to the coherent control of the photon echo response of an ensemble of self-assembled (In, Ga)As quantum dots embedded in a planar microcavity. In

Chapter 5, the experimental setup was expanded by refractive beam shaping optics to establish a flattop intensity profile of the exciting laser pulses. In this way, the major source of dephasing in coherent control experiments, which is associated with the inhomogeneity of applied laser intensity, was overcome. Consequently, pronounced collective Rabi rotations up to an area of 5.5π were observed, which was previously only possible on the single quantum dot level. Through the application of the photon echo polarimetry technique, optically charged quantum dots were identified as the main source of photon echo response. Through a quantitative analysis of the remaining damping of the Rabi rotations, it was shown that the pulse-area-dependent coupling to acoustic phonons represents the main source of decoherence in the system. Since this decoherence channel sensitively depends on the duration of the applied laser pulses, it would be interesting to drive the system with significantly shorter or longer optical pulses to minimize the effect of phonon coupling.

Chapter 6 built up on the possibilities introduced by the flattop intensity profiles to implement a more complex arrangement of optical pulses to coherently control the optical response of the quantum dot ensemble. In particular, it was theoretically predicted and experimentally demonstrated how a set of two optical control pulses can be used to either temporally shift the emission of the ensemble or modify its spectrum using Ramsey interference. The possibilities of this approach were expanded using the spin degeneracy of ground and excited state of the charged quantum dots. Here, utilizing the polarization of the control pulses, the polarization of the macroscopic emission was modified and the photon echo was temporally split into circularly cross-polarized components. These demonstrations push forward the realization of arbitrary pulse sequences for quantum memory protocols or information processing in ensembles of quantum dots by all-optical methods. Further, the importance of the frequency detuning during the action of the control pulses was theoretically considered using a multi-wave-mixing expansion. It was found that multi-wave-mixing orders that share the same phase dependence on the exciting optical fields become temporally sorted. In this way, the temporal shape of the photon echoes of the system are strongly modified, which potentially offers new spectroscopic signatures for the investigation of complex energy structures of unexplored material systems.

Bibliography

[1] S. Sze and K. K. Ng, *Physics of Semiconductor Devices*, 3rd ed. (John Wiley & Sons, Ltd, Hoboken, 2006),
DOI: 10.1002/0470068329.

[2] K. W. Böer and U. W. Pohl, *Semiconductor Physics* (Springer International Publishing, Cham, 2018),
DOI: 10.1007/978-3-319-69150-3.

[3] J. Shah, *Ultrafast spectroscopy of semiconductors and semiconductor nanostructures*, 2nd ed. (Springer, Berlin, Heidelberg, 1999),
DOI: 10.1007/978-3-662-03770-6.

[4] W. Schäfer and M. Wegener, *Semiconductor Optics and Transport Phenomena*, Advanced Texts in Physics (Springer, Berlin, Heidelberg, 2002),
DOI: 10.1007/978-3-662-04663-0.

[5] C. F. Klingshirn, *Semiconductor optics*, 4th ed. (Springer, Berlin, Heidelberg, 2012),
DOI: 10.1007/978-3-642-28362-8.

[6] M. T. Asaki, C.-P. Huang, D. Garvey, J. Zhou, H. C. Kapteyn, and M. M. Murnane, "Generation of 11-fs pulses from a self-mode-locked Ti:sapphire laser", Optics Letters **18**, 977 (1993)
DOI: 10.1364/OL.18.000977.

[7] S. T. Cundiff, "Coherent spectroscopy of semiconductors", Optics Express **16**, 4639 (2008)
DOI: 10.1364/OE.16.004639.

[8] M. Aßmann and M. Bayer, "Chapter Five - Quantum optics with quantum dot ensembles", in *Semiconductors and Semimetals*, Vol. 105, edited by S. T. Cundiff and M. Kira, Semiconductor Quantum Science and Technology (Elsevier, 2020), pp. 235–267,
DOI: 10.1016/bs.semsem.2020.10.003.

[9] A. Zrenner, E. Beham, S. Stufler, F. Findeis, M. Bichler, and G. Abstreiter, "Coherent properties of a two-level system based on a quantum-dot photodiode", Nature **418**, 612 (2002)
DOI: 10.1038/nature00912.

[10] W. Tittel, M. Afzelius, T. Chaneliére, R. Cone, S. Kröll, S. Moiseev, and M. Sellars, "Photon-echo quantum memory in solid state systems", Laser & Photonics Reviews **4**, 244 (2010)
DOI: 10.1002/lpor.200810056.

[11] A. I. Lvovsky, B. C. Sanders, and W. Tittel, "Optical quantum memory", Nature Photonics **3**, 706 (2009)
DOI: 10.1038/nphoton.2009.231.

[12] N. A. Kurnit, I. D. Abella, and S. R. Hartmann, "Observation of a Photon Echo", Physical Review Letters **13**, 567 (1964)
DOI: 10.1103/PhysRevLett.13.567.

[13] R. L. Fork, B. I. Greene, and C. V. Shank, "Generation of optical pulses shorter than 0.1 psec by colliding pulse mode locking", Applied Physics Letters **38**, 671 (1981)
DOI: 10.1063/1.92500.

[14] L. Schultheis, J. Kuhl, A. Honold, and C. W. Tu, "Picosecond Phase Coherence and Orientational Relaxation of Excitons in GaAs", Physical Review Letters **57**, 1797 (1986)
DOI: 10.1103/PhysRevLett.57.1797.

[15] P. C. Becker, H. L. Fragnito, C. H. B. Cruz, R. L. Fork, J. E. Cunningham, J. E. Henry, and C. V. Shank, "Femtosecond Photon Echoes from Band-to-Band Transitions in GaAs", Physical Review Letters **61**, 1647 (1988)
DOI: 10.1103/PhysRevLett.61.1647.

[16] J. Hegarty, M. D. Sturge, A. C. Gossard, and W. Wiegmann, "Resonant degenerate four-wave mixing in GaAs multiquantum well structures", Applied Physics Letters **40**, 132 (1982)
DOI: 10.1063/1.93013.

[17] L. Schultheis, M. D. Sturge, and J. Hegarty, "Photon echoes from two-dimensional excitons in GaAs-AlGaAs quantum wells", Applied Physics Letters **47**, 995 (1985)
DOI: 10.1063/1.95955.

[18] L. Schultheis, A. Honold, J. Kuhl, K. Köhler, and C. W. Tu, "Optical dephasing of homogeneously broadened two-dimensional exciton transitions in GaAs quantum wells", Physical Review B **34**, 9027 (1986)
DOI: 10.1103/PhysRevB.34.9027.

[19] A. Honold, L. Schultheis, J. Kuhl, and C. W. Tu, "Collision broadening of two-dimensional excitons in a GaAs single quantum well", Physical Review B **40**, 6442 (1989)
DOI: 10.1103/PhysRevB.40.6442.

[20] G. Noll, U. Siegner, S. G. Shevel, and E. O. Göbel, "Picosecond stimulated photon echo due to intrinsic excitations in semiconductor mixed crystals", Physical Review Letters **64**, 792 (1990)
DOI: 10.1103/PhysRevLett.64.792.

[21] S. Cundiff and D. Steel, "Coherent transient spectroscopy of excitons in GaAs-AlGaAs quantum wells", IEEE Journal of Quantum Electronics **28**, 2423 (1992)
DOI: 10.1109/3.159549.

[22] M. Koch, J. Feldmann, G. von Plessen, E. O. Göbel, P. Thomas, and K. Köhler, "Quantum beats versus polarization interference: An experimental distinction", Physical Review Letters **69**, 3631 (1992)
DOI: 10.1103/PhysRevLett.69.3631.

[23] K. Leo, M. Wegener, J. Shah, D. Chemla, E. Göbel, T. Damen, S. Schmitt-Rink, and W. Schäfer, "Effects of coherent polarization interactions on time-resolved degenerate four-wave mixing", Physical Review Letters **65**, 1340 (1990)
DOI: 10.1103/PhysRevLett.65.1340.

[24] D. S. Chemla and J. Shah, "Many-body and correlation effects in semiconductors", Nature **411**, 549 (2001)
DOI: 10.1038/35079000.

[25] E. Mayer, G. Smith, V. Heuckeroth, J. Kuhl, K. Bott, A. Schulze, T. Meier, D. Bennhardt, S. Koch, P. Thomas, R. Hey, and K. Ploog, "Evidence of biexcitonic contributions to four-wave mixing in GaAs quantum wells", Physical Review B **50**, 14730 (1994)
DOI: 10.1103/PhysRevB.50.14730.

[26] P. Borri, W. Langbein, J. Mørk, J. M. Hvam, F. Heinrichsdorff, M.-H. Mao, and D. Bimberg, "Dephasing in InAs/GaAs quantum dots", Physical Review B **60**, 7784 (1999)
DOI: 10.1103/PhysRevB.60.7784.

[27] P. Borri, W. Langbein, S. Schneider, U. Woggon, R. Sellin, D. Ouyang, and D. Bimberg, "Ultralong Dephasing Time in InGaAs Quantum Dots", Physical Review Letters **87**, 157401 (2001)
DOI: 10.1103/PhysRevLett.87.157401.

[28] W. Langbein, P. Borri, U. Woggon, V. Stavarache, D. Reuter, and A. Wieck, "Radiatively limited dephasing in InAs quantum dots", Physical Review B **70**, 033301 (2004)
DOI: 10.1103/PhysRevB.70.033301.

[29] W. Langbein and B. Patton, "Heterodyne spectral interferometry for multidimensional nonlinear spectroscopy of individual quantum systems", Optics Letters **31**, 1151 (2006)
DOI: 10.1364/OL.31.001151.

[30] J. D. Hybl, A. W. Albrecht, S. M. G. Faeder, and D. M. Jonas, "Two-dimensional electronic spectroscopy", Chemical Physics Letters **297**, 307 (1998)
DOI: https://doi.org/10.1016/S0009-2614(98)01140-3.

[31] K. Hao, J. F. Specht, P. Nagler, L. Xu, K. Tran, A. Singh, C. K. Dass, C. Schüller, T. Korn, M. Richter, A. Knorr, X. Li, and G. Moody, "Neutral and charged inter-valley biexcitons in monolayer $MoSe_2$", Nature Communications **8**, 15552 (2017)
DOI: 10.1038/ncomms15552.

[32] N. Takemura, S. Trebaol, M. D. Anderson, V. Kohnle, Y. Léger, D. Y. Oberli, M. T. Portella-Oberli, and B. Deveaud, "Two-dimensional Fourier transform spectroscopy of exciton-polaritons and their interactions", Physical Review B **92**, 125415 (2015)
DOI: 10.1103/PhysRevB.92.125415.

[33] A. Liu, D. B. Almeida, L. G. Bonato, G. Nagamine, L. F. Zagonel, A. F. Nogueira, L. A. Padilha, and S. T. Cundiff, "Multidimensional coherent spectroscopy reveals triplet state coherences in cesium lead-halide perovskite nanocrystals", Science Advances **7**, eabb3594 (2021)
DOI: 10.1126/sciadv.abb3594.

[34] H. Min, M. Kim, S.-U. Lee, H. Kim, G. Kim, K. Choi, J. H. Lee, and S. I. Seok, "Efficient, stable solar cells by using inherent bandgap of α-phase formamidinium lead iodide", Science **366**, 749 (2019)
DOI: 10.1126/science.aay7044.

[35] H. Chen, Y. Chen, T. Zhang, X. Liu, X. Wang, and Y. Zhao, "Advances to high-performance black-phase $FAPbI_3$ perovskite for efficient and stable photovoltaics", Small Structures **2**, 2000130 (2021)
DOI: 10.1002/sstr.202000130.

[36] Z. Zheng, S. Wang, Y. Hu, Y. Rong, A. Mei, and H. Han, "Development of formamidinium lead iodide-based perovskite solar cells: efficiency and stability", Chemical Science **13**, 2167 (2022)
DOI: 10.1039/D1SC04769H.

[37] P. Docampo and T. Bein, "A long-term view on perovskite optoelectronics", Accounts of Chemical Research **49**, 339 (2016)
DOI: 10.1021/acs.accounts.5b00465.

[38] A. Kojima, K. Teshima, Y. Shirai, and T. Miyasaka, "Organometal Halide Perovskites as Visible-Light Sensitizers for Photovoltaic Cells", Journal of the American Chemical Society **131**, 6050 (2009)
DOI: 10.1021/ja809598r.

[39] H. Min, D. Y. Lee, J. Kim, G. Kim, K. S. Lee, J. Kim, M. J. Paik, Y. K. Kim, K. S. Kim, M. G. Kim, T. J. Shin, and S. Il Seok, "Perovskite solar cells with atomically coherent interlayers on SnO_2 electrodes", Nature **598**, 444 (2021)
DOI: 10.1038/s41586-021-03964-8.

[40] K. Lin, J. Xing, L. N. Quan, F. P. G. de Arquer, X. Gong, J. Lu, L. Xie, W. Zhao, D. Zhang, C. Yan, W. Li, X. Liu, Y. Lu, J. Kirman, E. H. Sargent, Q. Xiong, and Z. Wei, "Perovskite light-emitting diodes with external quantum efficiency exceeding 20 per cent", Nature **562**, 245 (2018)
DOI: 10.1038/s41586-018-0575-3.

[41] Y. Jiang, X. Wang, and A. Pan, "Properties of Excitons and Photogenerated Charge Carriers in Metal Halide Perovskites", Advanced Materials **31**, 1806671 (2019)
DOI: 10.1002/adma.201806671.

[42] M. Baranowski and P. Plochocka, "Excitons in Metal-Halide Perovskites", Advanced Energy Materials **10**, 1903659 (2020)
DOI: 10.1002/aenm.201903659.

[43] L. Wang, N. E. Williams, E. W. Malachosky, J. P. Otto, D. Hayes, R. E. Wood, P. Guyot-Sionnest, and G. S. Engel, "Scalable Ligand-Mediated Transport Synthesis of Organic–Inorganic Hybrid Perovskite Nanocrystals with Resolved Electronic Structure and Ultrafast Dynamics", ACS Nano **11**, 2689 (2017)
DOI: 10.1021/acsnano.6b07574.

[44] S. A. March, D. B. Riley, C. Clegg, D. Webber, I. G. Hill, Z.-G. Yu, and K. C. Hall, "Ultrafast acoustic phonon scattering in $CH_3NH_3PbI_3$ revealed by femtosecond four-wave mixing", The Journal of Chemical Physics **151**, 144702 (2019)
DOI: 10.1063/1.5120385.

[45] A. Liu, D. B. Almeida, L. A. Padilha, and S. T. Cundiff, "Perspective: multi-dimensional coherent spectroscopy of perovskite nanocrystals", Journal of Physics: Materials **5**, 021002 (2022)
DOI: 10.1088/2515-7639/ac4fa5.

[46] B. J. Bohn, T. Simon, M. Gramlich, A. F. Richter, L. Polavarapu, A. S. Urban, and J. Feldmann, "Dephasing and Quantum Beating of Excitons in Methylammonium Lead Iodide Perovskite Nanoplatelets", ACS Photonics **5**, 648 (2018)
DOI: 10.1021/acsphotonics.7b01292.

[47] L. Jacak, A. Wójs, and P. Hawrylak, *Quantum Dots* (Springer Berlin Heidelberg, Berlin, Heidelberg, 1998),
DOI: 10.1007/978-3-642-72002-4.

[48] Y. Arakawa and H. Sakaki, "Multidimensional quantum well laser and temperature dependence of its threshold current", Applied Physics Letters **40**, 939 (1982)
DOI: 10.1063/1.92959.

[49] H. Jung, N. Ahn, and V. I. Klimov, "Prospects and challenges of colloidal quantum dot laser diodes", Nature Photonics **15**, 643 (2021)
DOI: 10.1038/s41566-021-00827-6.

[50] X. Zhou, L. Zhai, and J. Liu, "Epitaxial quantum dots: a semiconductor launchpad for photonic quantum technologies", Photonics Insights **1**, R07 (2023)
DOI: 10.3788/PI.2022.R07.

[51] P. Senellart, G. Solomon, and A. White, "High-performance semiconductor quantum-dot single-photon sources", Nature Nanotechnology **12**, 1026 (2017)
DOI: 10.1038/nnano.2017.218.

[52] F. Henneberger and O. Benson, *Semiconductor Quantum Bits* (Pan Stanford Publishing, New York, 2016).

[53] D. Birkedal, K. Leosson, and J. M. Hvam, "Long Lived Coherence in Self-Assembled Quantum Dots", Physical Review Letters **87**, 227401 (2001)
DOI: 10.1103/PhysRevLett.87.227401.

[54] P. Borri, W. Langbein, U. Woggon, V. Stavarache, D. Reuter, and A. D. Wieck, "Exciton dephasing via phonon interactions in InAs quantum dots: Dependence on quantum confinement", Physical Review B **71**, 115328 (2005)
DOI: 10.1103/PhysRevB.71.115328.

[55] T. H. Stievater, X. Li, D. G. Steel, D. Gammon, D. S. Katzer, D. Park, C. Piermarocchi, and L. J. Sham, "Rabi Oscillations of Excitons in Single Quantum Dots", Physical Review Letters **87**, 133603 (2001)
DOI: 10.1103/PhysRevLett.87.133603.

[56] B. Patton, U. Woggon, and W. Langbein, "Coherent Control and Polarization Readout of Individual Excitonic States", Physical Review Letters **95**, 266401 (2005)
DOI: 10.1103/PhysRevLett.95.266401.

[57] D. Wigger, C. Schneider, S. Gerhardt, M. Kamp, S. Höfling, T. Kuhn, and J. Kasprzak, "Rabi oscillations of a quantum dot exciton coupled to acoustic phonons: coherence and population readout", Optica **5**, 1442 (2018)
DOI: 10.1364/OPTICA.5.001442.

[58] O. Davidson, O. Yogev, E. Poem, and O. Firstenberg, "Single-Photon Synchronization with a Room-Temperature Atomic Quantum Memory", Physical Review Letters **131**, 033601 (2023)
DOI: 10.1103/PhysRevLett.131.033601.

[59] L. Ma, O. Slattery, and X. Tang, "Optical Quantum Memory and its Applications in Quantum Communication Systems", Journal of Research of the National Institute of Standards and Technology **125**, 125002 (2020)
DOI: 10.6028/jres.125.002.

[60] L. Langer, S. V. Poltavtsev, I. A. Yugova, M. Salewski, D. R. Yakovlev, G. Karczewski, T. Wojtowicz, I. A. Akimov, and M. Bayer, "Access to long-term optical memories using photon echoes retrieved from semiconductor spins", Nature Photonics **8**, 851 (2014)
DOI: 10.1038/nphoton.2014.219.

[61] A. N. Kosarev, A. V. Trifonov, I. A. Yugova, I. I. Yanibekov, S. V. Poltavtsev, A. N. Kamenskii, S. E. Scholz, C. A. Sgroi, A. Ludwig, A. D. Wieck, D. R. Yakovlev, M. Bayer, and I. A. Akimov, "Extending the time of coherent optical response in ensemble of singly-charged InGaAs quantum dots", Communications Physics **5**, 144 (2022)
DOI: 10.1038/s42005-022-00922-2.

[62] S. V. Poltavtsev, M. Reichelt, I. A. Akimov, G. Karczewski, M. Wiater, T. Wojtowicz, D. R. Yakovlev, T. Meier, and M. Bayer, "Damping of Rabi oscillations in intensity-dependent photon echoes from exciton complexes in a CdTe/(Cd,Mg)Te single quantum well", Physical Review B **96**, 075306 (2017)
DOI: 10.1103/PhysRevB.96.075306.

[63] A. V. Trifonov, S. Grisard, A. N. Kosarev, I. A. Akimov, D. R. Yakovlev, J. Höcker, V. Dyakonov, and M. Bayer, "Photon echo polarimetry of excitons and biexcitons in a $CH_3NH_3PbI_3$ perovskite single crystal", ACS Photonics **9**, 621 (2022)
DOI: 10.1021/acsphotonics.1c01603, ©2022 American Chemical Society.

[64] S. Grisard, H. Rose, A. V. Trifonov, R. Reichhardt, D. E. Reiter, M. Reichelt, C. Schneider, M. Kamp, S. Höfling, M. Bayer, T. Meier, and I. A. Akimov, "Multiple Rabi rotations of trions in InGaAs quantum dots observed by photon echo spectroscopy with spatially shaped laser pulses", Physical Review B **106**, 205408 (2022)
DOI: 10.1103/PhysRevB.106.205408, ©2022 American Physical Society.

[65] S. Grisard, A. V. Trifonov, I. A. Solovev, D. R. Yakovlev, O. Hordiichuk, M. V. Kovalenko, M. Bayer, and I. A. Akimov, "Long-Lived Exciton Coherence in Mixed-Halide Perovskite Crystals", Nano Letters **23**, 7397 (2023)
DOI: 10.1021/acs.nanolett.3c01817, ©2023 American Chemical Society.

[66] S. Grisard, A. V. Trifonov, H. Rose, R. Reichhardt, M. Reichelt, C. Schneider, M. Kamp, S. Höfling, M. Bayer, T. Meier, and I. A. Akimov, "Temporal Sorting of Optical Multiwave-Mixing Processes in Semiconductor Quantum Dots", ACS Photonics **10**, 3161 (2023)
DOI: 10.1021/acsphotonics.3c00530, ©2023 American Chemical Society.

[67] S. Grisard, A. V. Trifonov, D. R. Yakovlev, O. Hordiichuk, M. V. Kovalenko, M. Bayer, and I. A. Akimov, "Spin-dependent excitation-induced dephasing of excitons in a $FA_{0.9}Cs_{0.1}PbI_{2.8}Br_{0.2}$ crystal", In preparation (2023).

[68] P. Y. Yu and M. Cardona, *Fundamentals of semiconductors: physics and materials properties*, 3rd ed. (Springer, Berlin, 2005).

[69] F. Brivio, K. T. Butler, A. Walsh, and M. van Schilfgaarde, "Relativistic quasiparticle self-consistent electronic structure of hybrid halide perovskite photovoltaic absorbers", Physical Review B **89**, 155204 (2014)
DOI: 10.1103/PhysRevB.89.155204.

[70] S. Boyer-Richard, C. Katan, B. Traore, R. Scholz, J.-M. Jancu, and J. Even, "Symmetry-Based Tight Binding Modeling of Halide Perovskite Semiconductors", The Journal of Physical Chemistry Letters **7**, 3833 (2016)
DOI: 10.1021/acs.jpclett.6b01749.

[71] D. P. McMeekin, G. Sadoughi, W. Rehman, G. E. Eperon, M. Saliba, M. T. Hörantner, A. Haghighirad, N. Sakai, L. Korte, B. Rech, M. B. Johnston, L. M. Herz, and H. J. Snaith, "A mixed-cation lead mixed-halide perovskite absorber for tandem solar cells", Science **351**, 151 (2016)
DOI: 10.1126/science.aad5845.

[72] T. Baikie, N. S. Barrow, Y. Fang, P. J. Keenan, P. R. Slater, R. O. Piltz, M. Gutmann, S. G. Mhaisalkar, and T. J. White, "A combined single crystal neutron/X-ray diffraction and solid-state nuclear magnetic resonance study of the hybrid perovskites $CH_3NH_3PbX_3$ (X = I, Br and Cl)", Journal of Materials Chemistry A **3**, 9298 (2015)
DOI: 10.1039/C5TA01125F.

[73] G. R. Berdiyorov, F. El-Mellouhi, M. E. Madjet, F. H. Alharbi, and S. N. Rashkeev, "Electronic transport in organometallic perovskite $CH_3NH_3PbI_3$: The role of organic cation orientations", Applied Physics Letters **108**, 053901 (2016)
DOI: 10.1063/1.4941296.

[74] W. Kong, Z. Ye, Z. Qi, B. Zhang, M. Wang, A. Rahimi-Iman, and H. Wu, "Characterization of an abnormal photoluminescence behavior upon crystal-phase transition of perovskite $CH_3NH_3PbI_3$", Physical Chemistry Chemical Physics **17**, 16405 (2015)
DOI: 10.1039/C5CP02605A.

[75] P. S. Whitfield, N. Herron, W. E. Guise, K. Page, Y. Q. Cheng, I. Milas, and M. K. Crawford, "Structures, Phase Transitions and Tricritical Behavior of the Hybrid Perovskite Methyl Ammonium Lead Iodide", Scientific Reports **6**, 35685 (2016)
DOI: 10.1038/srep35685.

[76] F. Brivio, A. B. Walker, and A. Walsh, "Structural and electronic properties of hybrid perovskites for high-efficiency thin-film photovoltaics from first-principles", APL Materials **1**, 042111 (2013)
DOI: 10.1063/1.4824147.

[77] T. Kazimierczuk, D. Fröhlich, S. Scheel, H. Stolz, and M. Bayer, "Giant Rydberg excitons in the copper oxide Cu_2O", Nature **514**, 343 (2014)
DOI: 10.1038/nature13832.

[78] P. Kapuściński, A. Delhomme, D. Vaclavkova, A. O. Slobodeniuk, M. Grzeszczyk, M. Bartos, K. Watanabe, T. Taniguchi, C. Faugeras, and M. Potemski, "Rydberg series of dark excitons and the conduction band spin-orbit splitting in monolayer WSe_2", Communications Physics **4**, 1 (2021)
DOI: 10.1038/s42005-021-00692-3.

[79] D. A. B. Miller, A. C. Gossard, W. Wiegmann, D. S. Chemla, and P. W. Smith, "Nonlinear optics with a diode-laser light source", Optics Letters **8**, 477 (1983)
DOI: 10.1364/OL.8.000477.

[80] D. A. B. Miller, D. S. Chemla, D. J. Eilenberger, P. W. Smith, A. C. Gossard, and W. T. Tsang, "Large room-temperature optical nonlinearity in GaAs/Ga_{1-x} Al_x As multiple quantum well structures", Applied Physics Letters **41**, 679 (1982)
DOI: 10.1063/1.93648.

[81] D.-S. Kim, J. Shah, J. E. Cunningham, T. C. Damen, W. Schäfer, M. Hartmann, and S. Schmitt-Rink, "Giant excitonic resonance in time-resolved four-wave mixing in quantum wells", Physical Review Letters **68**, 1006 (1992)
DOI: 10.1103/PhysRevLett.68.1006.

[82] C. Ciuti, V. Savona, C. Piermarocchi, A. Quattropani, and P. Schwendimann, "Role of the exchange of carriers in elastic exciton-exciton scattering in quantum wells", Physical Review B **58**, 7926 (1998)
DOI: 10.1103/PhysRevB.58.7926.

[83] I. A. Solovev, I. I. Yanibekov, Y. P. Efimov, S. A. Eliseev, V. A. Lovcjus, I. A. Yugova, S. V. Poltavtsev, and Y. V. Kapitonov, "Long-lived dark coherence brought to light by magnetic-field controlled photon echo", Physical Review B **103**, 235312 (2021)
DOI: 10.1103/PhysRevB.103.235312.

[84] B. Urbaszek, R. J. Warburton, K. Karrai, B. D. Gerardot, P. M. Petroff, and J. M. Garcia, "Fine Structure of Highly Charged Excitons in Semiconductor Quantum Dots", Physical Review Letters **90**, 247403 (2003)
DOI: 10.1103/PhysRevLett.90.247403.

[85] I. N. Stranski and L. Krastanow, "Zur Theorie der orientierten Ausscheidung von Ionenkristallen aufeinander", Monatshefte für Chemie und verwandte Teile anderer Wissenschaften **71**, 351 (1937)
DOI: 10.1007/BF01798103.

[86] P. Michler, ed., *Single Quantum Dots*, Topics in Applied Physics (Springer, Berlin, 2010).

[87] M. Bayer, "Bridging Two Worlds: Colloidal versus Epitaxial Quantum Dots", Annalen der Physik, 1900039 (2019)
DOI: 10.1002/andp.201900039.

[88] S. Reitzenstein, J.-P. Reithmaier, and A. Forchel, "Light-matter Interaction in Single Quantum Dot – Micropillar Cavity Systems", in *Semiconductor Quantum Bits*, edited by F. Henneberger and O. Benson (Pan Stanford Publishing, New York, 2016).

[89] D. Gammon, E. Snow, B. Shanabrook, S. Brown, T. Kennedy, D. Katzer, and D. Park, "Single quantum dot spectroscopy", in Conference Proceedings LEOS'96 9th Annual Meeting IEEE Lasers and Electro-Optics Society, Vol. 1 (1996),
DOI: 10.1109/LEOS.1996.565181.

[90] K. J. Vahala, "Optical microcavities", Nature **424**, 839 (2003)
DOI: 10.1038/nature01939.

[91] S. M. Spillane, T. J. Kippenberg, and K. J. Vahala, "Ultralow-threshold Raman laser using a spherical dielectric microcavity", Nature **415**, 621 (2002)
DOI: 10.1038/415621a.

[92] M. Gryga, D. Ciprian, and P. Hlubina, "Distributed Bragg Reflectors Employed in Sensors and Filters Based on Cavity-Mode Spectral-Domain Resonances", Sensors **22**, 3627 (2022)
DOI: 10.3390/s22103627.

[93] J. Kasprzak, M. Richard, S. Kundermann, A. Baas, P. Jeambrun, J. M. J. Keeling, F. M. Marchetti, M. H. Szymańska, R. André, J. L. Staehli, V. Savona, P. B. Littlewood, B. Deveaud, and L. S. Dang, "Bose–Einstein condensation of exciton polaritons", Nature **443**, 409 (2006)
DOI: 10.1038/nature05131.

[94] H. Haug and S. W. Koch, *Quantum theory of the optical and electronic properties of semiconductors*, 4th ed (World Scientific, Singapore, River Edge, 2004), 453 pp.

[95] L. Allen and J. H. Eberly, *Optical resonance and two-level atoms*, Interscience monographs & texts in physics & astronomy (John Wiley & Sons, Nashville, 1975).

[96] P. R. Berman and V. S. Malinovsky, *Principles of laser spectroscopy and quantum optics* (Princeton University Press, Princeton, 2011), 519 pp.

[97] T. Meier, P. Thomas, and S. W. Koch, *Coherent semiconductor optics: from basic concepts to nanostructure applications* (Springer, Berlin, New York, 2007).

[98] T. Suzuki, R. Singh, M. Bayer, A. Ludwig, A. D. Wieck, and S. T. Cundiff, "Coherent Control of the Exciton-Biexciton System in an InAs Self-Assembled Quantum Dot Ensemble", Physical Review Letters **117**, 157402 (2016)
DOI: 10.1103/PhysRevLett.117.157402.

[99] R. W. Boyd, *Nonlinear optics*, 4th ed. (Academic Press is an imprint of Elsevier, San Diego, 2019).

[100] S. Mukamel, *Principles of nonlinear optical spectroscopy* (Oxford University Press, Oxford, 1999).

[101] C. L. Smallwood, T. M. Autry, and S. T. Cundiff, "Analytical solutions to the finite-pulse Bloch model for multidimensional coherent spectroscopy", Journal of the Optical Society of America B **34**, 419 (2017)
DOI: 10.1364/JOSAB.34.000419.

[102] S. V. Poltavtsev, Y. V. Kapitonov, I. A. Yugova, I. A. Akimov, D. R. Yakovlev, G. Karczewski, M. Wiater, T. Wojtowicz, and M. Bayer, "Polarimetry of photon echo on charged and neutral excitons in semiconductor quantum wells", Scientific Reports **9**, 5666 (2019)
DOI: 10.1038/s41598-019-42208-8.

[103] S. V. Poltavtsev, M. Salewski, Y. V. Kapitonov, I. A. Yugova, I. A. Akimov, C. Schneider, M. Kamp, S. Höfling, D. R. Yakovlev, A. V. Kavokin, and M. Bayer, "Photon echo transients from an inhomogeneous ensemble of semiconductor quantum dots", Physical Review B **93**, 121304 (2016)
DOI: 10.1103/PhysRevB.93.121304.

[104] P. Borri and W. Langbein, "Transient four-wave mixing of excitons in quantum dots from ensembles and individuals", in *Semiconductor Quantum Bits*, edited by F. Henneberger and O. Benson (Pan Stanford Publishing, New York, 2016).

[105] S. V. Poltavtsev, I. A. Yugova, I. A. Akimov, D. R. Yakovlev, and M. Bayer, "Photon Echo from Localized Excitons in Semiconductor Nanostructures", Physics of the Solid State **60**, 1635 (2018)
DOI: 10.1134/S1063783418080188.

[106] T. Suzuki, R. Singh, M. Bayer, A. Ludwig, A. D. Wieck, and S. T. Cundiff, "Detuning dependence of Rabi oscillations in an InAs self-assembled quantum dot ensemble", Physical Review B **97**, 161301 (2018)
DOI: 10.1103/PhysRevB.97.161301.

[107] V. Nasrollahi, P. Penchev, A. Batal, H. Le, S. Dimov, and K. Kim, "Laser drilling with a top-hat beam of micro-scale high aspect ratio holes in silicon nitride", Journal of Materials Processing Technology **281**, 116636 (2020)
DOI: 10.1016/j.jmatprotec.2020.116636.

[108] H.-C. Chuang, "Laser Scribing on Silver Flexible Substrate with Beam Shaping Technology", Journal of Laser Micro/Nanoengineering **9**, 198 (2014)
DOI: 10.2961/jlmn.2014.03.0003.

[109] O. Nazarenko, S. Yakunin, V. Morad, I. Cherniukh, and M. V. Kovalenko, "Single crystals of caesium formamidinium lead halide perovskites: solution growth and gamma dosimetry", NPG Asia Materials **9**, e373 (2017)
DOI: 10.1038/am.2017.45.

[110] J. Höcker, F. Brust, M. Armer, and V. Dyakonov, "A temperature-reduced method for the rapid growth of hybrid perovskite single crystals with primary alcohols", CrystEngComm **23**, 2202 (2021)
DOI: 10.1039/D0CE01759K.

[111] R. Reichhardt, "Rabi rotations of photon echo in (In, Ga)As qunatum odts using spatially shaped laser pulses", Master's thesis (Technische Universität Dortmund, 2022).

[112] J. M. Garcia, T. Mankad, P. O. Holtz, P. J. Wellman, and P. M. Petroff, "Electronic states tuning of InAs self-assembled quantum dots", Applied Physics Letters **72**, 3172 (1998)
DOI: 10.1063/1.121583.

[113] S. Maier, P. Gold, A. Forchel, N. Gregersen, J. Mørk, S. Höfling, C. Schneider, and M. Kamp, "Bright single photon source based on self-aligned quantum dot–cavity systems", Optics Express **22**, 8136 (2014)
DOI: 10.1364/OE.22.008136.

[114] D. Birkedal, K. Leosson, and J. M. Hvam, "Long coherence times in self-assembled semiconductor quantum dots", Superlattices and Microstructures **31**, 97 (2002)
DOI: 10.1006/spmi.2002.1031.

[115] E. Kirstein, D. R. Yakovlev, M. M. Glazov, E. Evers, E. A. Zhukov, V. V. Belykh, N. E. Kopteva, D. Kudlacik, O. Nazarenko, D. N. Dirin, M. V. Kovalenko, and M. Bayer, "Lead-Dominated Hyperfine Interaction Impacting the Carrier Spin Dynamics in Halide Perovskites", Advanced Materials **34**, 2105263 (2022)
DOI: 10.1002/adma.202105263.

[116] G. Moody, M. E. Siemens, A. D. Bristow, X. Dai, D. Karaiskaj, A. S. Bracker, D. Gammon, and S. T. Cundiff, "Exciton-exciton and exciton-phonon interactions in an interfacial GaAs quantum dot ensemble", Physical Review B **83**, 115324 (2011)
DOI: 10.1103/PhysRevB.83.115324.

[117] M. A. Becker, L. Scarpelli, G. Nedelcu, G. Rainò, F. Masia, P. Borri, T. Stöferle, M. V. Kovalenko, W. Langbein, and R. F. Mahrt, "Long exciton dephasing time and coherent phonon coupling in $CsPbBr_2Cl$ perovskite nanocrystals", Nano Letters **18**, 7546 (2018)
DOI: 10.1021/acs.nanolett.8b03027.

[118] Y. Lv, C. Yin, C. Zhang, W. W. Yu, X. Wang, Y. Zhang, and M. Xiao, "Quantum Interference in a Single Perovskite Nanocrystal", Nano Letters **19**, 4442 (2019)
DOI: 10.1021/acs.nanolett.9b01237.

[119] N. E. Kopteva, D. R. Yakovlev, E. Yalcin, I. A. Akimov, M. O. Nestoklon, M. M. Glazov, M. Kotur, D. Kudlacik, E. A. Zhukov, E. Kirstein, O. Hordiichuk, D. N. Dirin, M. V. Kovalenko, and M. Bayer, "Giant optical orientation of exciton spins in lead halide perovskite crystals", arXiv, 2305.10875 (2023)
DOI: 10.48550/arXiv.2305.10875.

[120] S. Permogorov, A. Reznitskii, V. Travnikov, S. Verbin, G. O. Müller, P. Flögel, and M. Nikiforova, "Emission of localized excitons in mixed $CdS_{1-x}Se_x$ crystals", Physica Status Solidi (b) **106**, K57 (1981)
DOI: 10.1002/pssb.2221060157.

[121] H. Stolz, W. von der Osten, S. Permogorov, and A. Reznitsky, "Selective excitation of localised excitons in $ZnSe_{1-x}Te_x$ solid solutions", Journal of Physics C: Solid State Physics **21**, 5139 (1988)
DOI: 10.1088/0022-3719/21/29/011.

[122] S. Permogorov, A. Reznitsky, A. Naumov, H. Stolz, and W. von der Osten, "Localisation of excitons at small Te clusters in diluted $ZnSe_{1-x}Te_x$ solid solutions", Journal of Physics: Condensed Matter **1**, 5125 (1989)
DOI: 10.1088/0953-8984/1/31/011.

[123] A. V. Uskov, A.-P. Jauho, B. Tromborg, J. Mørk, and R. Lang, "Dephasing times in quantum dots due to elastic LO phonon-carrier collisions", Physical Review Letters **85**, 1516 (2000)
DOI: 10.1103/PhysRevLett.85.1516.

[124] H. Benisty, C. M. Sotomayor-Torrès, and C. Weisbuch, "Intrinsic mechanism for the poor luminescence properties of quantum-box systems", Physical Review B **44**, 10945 (1991)
DOI: 10.1103/PhysRevB.44.10945.

[125] H. Yu, S. Lycett, C. Roberts, and R. Murray, "Time resolved study of self-assembled InAs quantum dots", Applied Physics Letters **69**, 4087 (1996)
DOI: 10.1063/1.117827.

[126] C. Bardot, M. Schwab, M. Bayer, S. Fafard, Z. Wasilewski, and P. Hawrylak, "Exciton lifetime in InAs/GaAs quantum dot molecules", Physical Review B **72**, 035314 (2005)
DOI: 10.1103/PhysRevB.72.035314.

[127] T. Takagahara, "Theory of exciton dephasing in semiconductor quantum dots", Physical Review B **60**, 2638 (1999)
DOI: 10.1103/PhysRevB.60.2638.

[128] X. Fan, T. Takagahara, J. E. Cunningham, and H. Wang, "Pure dephasing induced by exciton-phonon interactions in narrow GaAs quantum wells", Solid State Communications **108**, 857 (1998)
DOI: https://doi.org/10.1016/S0038-1098(98)00461-X.

[129] U. Bockelmann, "Exciton relaxation and radiative recombination in semiconductor quantum dots", Physical Review B **48**, 17637 (1993)
DOI: 10.1103/PhysRevB.48.17637.

[130] D. Griffiths, *Introduction to Quantum Mechanics*, Pearson international edition (Pearson Prentice Hall, Upper Saddle River, 2005).

[131] K. Galkowski, A. Mitioglu, A. Miyata, P. Plochocka, O. Portugall, G. E. Eperon, J. T.-W. Wang, T. Stergiopoulos, S. D. Stranks, H. J. Snaith, and R. J. Nicholas, "Determination of the exciton binding energy and effective masses for methylammonium and formamidinium lead tri-halide perovskite semiconductors", Energy & Environmental Science **9**, 962 (2016)
DOI: 10.1039/C5EE03435C.

[132] Z. Yang, A. Surrente, K. Galkowski, A. Miyata, O. Portugall, R. J. Sutton, A. A. Haghighirad, H. J. Snaith, D. K. Maude, P. Plochocka, and R. J. Nicholas, "Impact of the halide cage on the electronic properties of fully inorganic cesium lead halide perovskites", ACS Energy Letters **2**, 1621 (2017)
DOI: 10.1021/acsenergylett.7b00416.

[133] M. Baranowski, P. Plochocka, R. Su, L. Legrand, T. Barisien, F. Bernardot, Q. Xiong, C. Testelin, and M. Chamarro, "Exciton binding energy and effective mass of $CsPbCl_3$: a magneto-optical study", Photonics Research **8**, A50 (2020)
DOI: 10.1364/PRJ.401872.

[134] V. V. Belykh, D. R. Yakovlev, M. M. Glazov, P. S. Grigoryev, M. Hussain, J. Rautert, D. N. Dirin, M. V. Kovalenko, and M. Bayer, "Coherent spin dynamics of electrons and holes in $CsPbBr_3$ perovskite crystals", Nature Communications **10**, 673 (2019)
DOI: 10.1038/s41467-019-08625-z.

[135] J. A. Bolger, A. E. Paul, and A. L. Smirl, "Ultrafast ellipsometry of coherent processes and exciton-exciton interactions in quantum wells at negative delays", Physical Review B **54**, 11666 (1996)
DOI: 10.1103/PhysRevB.54.11666.

[136] A. E. Paul, J. A. Bolger, A. L. Smirl, and J. G. Pellegrino, "Time-resolved measurements of the polarization state of four-wave mixing signals from GaAs multiple quantum wells", Journal of the Optical Society of America B **13**, 1016 (1996)
DOI: 10.1364/JOSAB.13.001016.

[137] A. Tookey, D. J. Bain, I. J. Blewett, I. Galbraith, A. K. Kar, B. S. Wherrett, B. Vögele, K. A. Prior, and B. C. Cavenett, "Polarization-state beating in four-wave-mixing experiments on ZnSe epilayers", Journal of the Optical Society of America B **15**, 64 (1998)
DOI: 10.1364/JOSAB.15.000064.

[138] A. L. Smirl, X. Chen, and O. Buccafusca, "Ultrafast time-resolved quantum beats in the polarization state of coherent emission from quantum wells", Optics Letters **23**, 1120 (1998)
DOI: 10.1364/OL.23.001120.

[139] T. Aoki, G. Mohs, Y. P. Svirko, and M. Kuwata-Gonokami, "Time-integrated four-wave mixing in GaN and ZnSe: Polarization-sensitive phase shift of the excitonic quantum beats", Physical Review B **64**, 045212 (2001)
DOI: 10.1103/PhysRevB.64.045212.

[140] A. P. Heberle, W. W. Rühle, and K. Ploog, "Quantum beats of electron Larmor precession in GaAs wells", Physical Review Letters **72**, 3887 (1994)
DOI: 10.1103/PhysRevLett.72.3887.

[141] I. A. Akimov, R. I. Dzhioev, V. L. Korenev, Y. G. Kusrayev, E. A. Zhukov, D. R. Yakovlev, and M. Bayer, "Electron-spin dynamics in Mn-doped GaAs using time-resolved magneto-optical techniques", Physical Review B **80**, 081203 (2009)
DOI: 10.1103/PhysRevB.80.081203.

[142] G. Moody, R. Singh, H. Li, I. A. Akimov, M. Bayer, D. Reuter, A. D. Wieck, A. S. Bracker, D. Gammon, and S. T. Cundiff, "Influence of confinement on biexciton binding in semiconductor quantum dot ensembles measured with two-dimensional spectroscopy", Physical Review B **87**, 041304 (2013)
DOI: 10.1103/PhysRevB.87.041304.

[143] P. Borri, W. Langbein, D. Birkedal, V. G. Lyssenko, and J. M. Hvam, "Nonlinear Response of Localized Excitons: Effects of the Excitation-Induced Dephasing", physica status solidi (a) **164**, 61 (1997)
DOI: 10.1002/1521-396X(199711)164:1<61::AID-PSSA61>3.0.CO;2-R.

[144] H. Wang, K. B. Ferrio, D. G. Steel, P. R. Berman, Y. Z. Hu, R. Binder, and S. W. Koch, "Transient four-wave-mixing line shapes: Effects of excitation-induced dephasing", Physical Review A **49**, R1551 (1994)
DOI: 10.1103/PhysRevA.49.R1551.

[145] H. Wang, K. Ferrio, D. G. Steel, Y. Z. Hu, R. Binder, and S. W. Koch, "Transient nonlinear optical response from excitation induced dephasing in GaAs", Physical Review Letters **71**, 1261 (1993)
DOI: 10.1103/PhysRevLett.71.1261.

[146] G. Moody, C. Kavir Dass, K. Hao, C.-H. Chen, L.-J. Li, A. Singh, K. Tran, G. Clark, X. Xu, G. Berghäuser, E. Malic, A. Knorr, and X. Li, "Intrinsic homogeneous linewidth and broadening mechanisms of excitons in monolayer transition metal dichalcogenides", Nature Communications **6**, 8315 (2015)
DOI: 10.1038/ncomms9315.

[147] C. Boule, D. Vaclavkova, M. Bartos, K. Nogajewski, L. Zdražil, T. Taniguchi, K. Watanabe, M. Potemski, and J. Kasprzak, "Coherent dynamics and mapping of excitons in single-layer $MoSe_2$ and WSe_2 at the homogeneous limit", Physical Review Materials **4**, 034001 (2020)
DOI: 10.1103/PhysRevMaterials.4.034001.

[148] Y. Dang, X. Liu, Y. Sun, J. Song, W. Hu, and X. Tao, "Bulk Chiral Halide Perovskite Single Crystals for Active Circular Dichroism and Circularly Polarized Luminescence", The Journal of Physical Chemistry Letters **11**, 1689 (2020)
DOI: 10.1021/acs.jpclett.9b03718.

[149] J. M. Shacklette and S. T. Cundiff, "Nonperturbative transient four-wave-mixing line shapes due to excitation-induced shift and excitation-induced dephasing", Journal of the Optical Society of America B **20**, 764 (2003)
DOI: 10.1364/JOSAB.20.000764.

[150] R. Singh, T. Suzuki, T. M. Autry, G. Moody, M. E. Siemens, and S. T. Cundiff, "Polarization-dependent exciton linewidth in semiconductor quantum wells: A consequence of bosonic nature of excitons", Physical Review B **94**, 081304 (2016)
DOI: 10.1103/PhysRevB.94.081304.

[151] Y. P. Svirko, M. Shirane, H. Suzuura, and M. Kuwata-Gonokami, "Four-Wave Mixing Theory at the Excitonic Resonance: Weakly Interacting Boson Model", Journal of the Physical Society of Japan **68**, 674 (1999)
DOI: 10.1143/JPSJ.68.674.

[152] D. B. Turner and K. A. Nelson, "Coherent measurements of high-order electronic correlations in quantum wells", Nature **466**, 1089 (2010)
DOI: 10.1038/nature09286.

[153] D. Karaiskaj, A. D. Bristow, L. Yang, X. Dai, R. P. Mirin, S. Mukamel, and S. T. Cundiff, "Two-Quantum Many-Body Coherences in Two-Dimensional Fourier-Transform Spectra of Exciton Resonances in Semiconductor Quantum Wells", Physical Review Letters **104**, 117401 (2010)
DOI: 10.1103/PhysRevLett.104.117401.

[154] C. F. Klingshirn and H. Haug, "Optical properties of highly excited direct gap semiconductors", Physics Reports **70**, 315 (1981).

[155] F. Spitzer, "Magneto-Optical Intensity Effects in Hybrid Plasmonic Structures", Dissertation (TU Dortmund University, 2019),
DOI: 10.17877/DE290R-19898.

[156] G. Björk, H. Heitmann, and Y. Yamamoto, "Spontaneous-emission coupling factor and mode characteristics of planar dielectric microcavity lasers", Physical Review A **47**, 4451 (1993)
DOI: 10.1103/PhysRevA.47.4451.

[157] K. Papatryfonos, T. Angelova, A. Brimont, B. Reid, S. Guldin, P. R. Smith, M. Tang, K. Li, A. J. Seeds, H. Liu, and D. R. Selviah, "Refractive indices of MBE-grown $Al_xGa_{(1-x)}As$ ternary alloys in the transparent wavelength region", AIP Advances **11**, 025327 (2021)
DOI: 10.1063/5.0039631.

[158] A. N. Kosarev, H. Rose, S. V. Poltavtsev, M. Reichelt, C. Schneider, M. Kamp, S. Höfling, M. Bayer, T. Meier, and I. A. Akimov, "Accurate photon echo timing by optical freezing of exciton dephasing and rephasing in quantum dots", Communications Physics **3**, 1 (2020)
DOI: 10.1038/s42005-020-00491-2.

[159] F. Fras, Q. Mermillod, G. Nogues, C. Hoarau, C. Schneider, M. Kamp, S. Höfling, W. Langbein, and J. Kasprzak, "Multi-wave coherent control of a solid-state single emitter", Nature Photonics **10**, 155 (2016)
DOI: 10.1038/nphoton.2016.2.

[160] J. D. Mar, J. J. Baumberg, X. L. Xu, A. C. Irvine, and D. A. Williams, "Precise measurements of the dipole moment and polarizability of the neutral exciton and positive trion in a single quantum dot", Physical Review B **95**, 201304 (2017)
DOI: 10.1103/PhysRevB.95.201304.

[161] P. Borri, W. Langbein, S. Schneider, U. Woggon, R. L. Sellin, D. Ouyang, and D. Bimberg, "Rabi oscillations in the excitonic ground-state transition of InGaAs quantum dots", Physical Review B **66**, 081306 (2002)
DOI: 10.1103/PhysRevB.66.081306.

[162] Ł. Dusanowski, C. Nawrath, S. L. Portalupi, M. Jetter, T. Huber, S. Klembt, P. Michler, and S. Höfling, "Optical charge injection and coherent control of a quantum-dot spin-qubit emitting at telecom wavelengths", Nature Communications **13**, 748 (2022)
DOI: 10.1038/s41467-022-28328-2.

[163] A. Kurzmann, A. Ludwig, A. D. Wieck, A. Lorke, and M. Geller, "Auger Recombination in Self-Assembled Quantum Dots: Quenching and Broadening of the Charged Exciton Transition", Nano Letters **16**, 3367 (2016)
DOI: 10.1021/acs.nanolett.6b01082.

[164] D. E. Reiter, T. Kuhn, and V. M. Axt, "Distinctive characteristics of carrier-phonon interactions in optically driven semiconductor quantum dots", Advances in Physics: X **4**, 1655478 (2019)
DOI: 10.1080/23746149.2019.1655478.

[165] A. Krügel, V. Axt, T. Kuhn, P. Machnikowski, and A. Vagov, "The role of acoustic phonons for Rabi oscillations in semiconductor quantum dots", Applied Physics B **81**, 897 (2005)
DOI: 10.1007/s00340-005-1984-1.

[166] B. Krummheuer, V. M. Axt, and T. Kuhn, "Theory of pure dephasing and the resulting absorption line shape in semiconductor quantum dots", Physical Review B **65**, 195313 (2002)
DOI: 10.1103/PhysRevB.65.195313.

[167] P. Machnikowski and L. Jacak, "Resonant nature of phonon-induced damping of Rabi oscillations in quantum dots", Physical Review B **69**, 193302 (2004)
DOI: 10.1103/PhysRevB.69.193302.

[168] E. A. Muljarov and R. Zimmermann, "Dephasing in Quantum Dots: Quadratic Coupling to Acoustic Phonons", Physical Review Letters **93**, 237401 (2004)
DOI: 10.1103/PhysRevLett.93.237401.

[169] A. J. Ramsay, A. V. Gopal, E. M. Gauger, A. Nazir, B. W. Lovett, A. M. Fox, and M. S. Skolnick, "Damping of Exciton Rabi Rotations by Acoustic Phonons in Optically Excited InGaAs / GaAs Quantum Dots", Physical Review Letters **104**, 017402 (2010)
DOI: 10.1103/PhysRevLett.104.017402.

[170] M. R. Klaßen and D. E. Reiter, "Optical Signals to Monitor the Dynamics of Phonon-Modified Rabi Oscillations in a Quantum Dot", Annalen der Physik **533**, 2100086 (2021)
DOI: 10.1002/andp.202100086.

[171] S. Lüker, T. Kuhn, and D. E. Reiter, "Phonon impact on optical control schemes of quantum dots: Role of quantum dot geometry and symmetry", Physical Review B **96**, 245306 (2017)
DOI: 10.1103/PhysRevB.96.245306.

[172] B. Krummheuer, V. M. Axt, T. Kuhn, I. D'Amico, and F. Rossi, "Pure dephasing and phonon dynamics in GaAs- and GaN-based quantum dot structures: Interplay between material parameters and geometry", Physical Review B **71**, 235329 (2005)
DOI: 10.1103/PhysRevB.71.235329.

[173] H. C. Schneider, W. W. Chow, and S. W. Koch, "Excitation-induced dephasing in semiconductor quantum dots", Physical Review B **70**, 235308 (2004)
DOI: 10.1103/PhysRevB.70.235308.

[174] M. Glässl, A. Vagov, S. Lüker, D. E. Reiter, M. D. Croitoru, P. Machnikowski, V. M. Axt, and T. Kuhn, "Long-time dynamics and stationary nonequilibrium of an optically driven strongly confined quantum dot coupled to phonons", Physical Review B **84**, 195311 (2011)
DOI: 10.1103/PhysRevB.84.195311.

[175] J. H. Quilter, A. J. Brash, F. Liu, M. Glässl, A. M. Barth, V. M. Axt, A. J. Ramsay, M. S. Skolnick, and A. M. Fox, "Phonon-Assisted Population Inversion of a Single InGaAs / GaAs Quantum Dot by Pulsed Laser Excitation", Physical Review Letters **114**, 137401 (2015)
DOI: 10.1103/PhysRevLett.114.137401.

[176] T. Hahn, D. Vaclavkova, M. Bartos, K. Nogajewski, M. Potemski, K. Watanabe, T. Taniguchi, P. Machnikowski, T. Kuhn, J. Kasprzak, and D. Wigger, "Destructive Photon Echo Formation in Six-Wave Mixing Signals of a $MoSe_2$ Monolayer", Advanced Science **9**, 2103813 (2022)
DOI: 10.1002/advs.202103813.

[177] P. Ester, S. Stufler, S. de Michaelis Vasconcellos, M. Bichler, and A. Zrenner, "Ramsey fringes in a single InGaAs/GaAs quantum dot", physica status solidi (b) **243**, 2229 (2006)
DOI: 10.1002/pssb.200668028.

[178] S. Stufler, P. Ester, A. Zrenner, and M. Bichler, "Ramsey Fringes in an Electric-Field-Tunable Quantum Dot System", Physical Review Letters **96**, 037402 (2006)
DOI: 10.1103/PhysRevLett.96.037402.

[179] S. Michaelis de Vasconcellos, S. Gordon, M. Bichler, T. Meier, and A. Zrenner, "Coherent control of a single exciton qubit by optoelectronic manipulation", Nature Photonics **4**, 545 (2010)
DOI: 10.1038/nphoton.2010.124.

[180] I. Khanonkin, O. Eyal, J. P. Reithmaier, and G. Eisenstein, "Room-temperature coherent revival in an ensemble of quantum dots", Physical Review Research **3**, 033073 (2021)
DOI: 10.1103/PhysRevResearch.3.033073.

[181] T. Meier, S. W. Koch, P. Brick, C. Ell, G. Khitrova, and H. M. Gibbs, "Signatures of correlations in intensity-dependent excitonic absorption changes", Physical Review B **62**, 4218 (2000)
DOI: 10.1103/PhysRevB.62.4218.

[182] K. Hao, G. Moody, F. Wu, C. K. Dass, L. Xu, C.-H. Chen, L. Sun, M.-Y. Li, L.-J. Li, A. H. MacDonald, and X. Li, "Direct measurement of exciton valley coherence in monolayer WSe_2", Nature Physics **12**, 677 (2016)
DOI: 10.1038/nphys3674.

[183] F. Katsch and A. Knorr, "Optical Preparation and Coherent Control of Ultrafast Nonlinear Quantum Superpositions in Exciton Gases: A Case Study for Atomically Thin Semiconductors", Physical Review X **10**, 041039 (2020)
DOI: 10.1103/PhysRevX.10.041039.

[184] G. Rainò, M. A. Becker, M. I. Bodnarchuk, R. F. Mahrt, M. V. Kovalenko, and T. Stöferle, "Superfluorescence from lead halide perovskite quantum dot superlattices", Nature **563**, 671 (2018)
DOI: 10.1038/s41586-018-0683-0.

List of Abbreviations

AOM acousto-optical modulator.

ARPL angle-resolved photoluminescence spectroscopy.

CCD charge-coupled device.

DBR distributed Bragg reflector.

EID excitation-induced dephasing.

EIS excitation-induced shift.

EWM eight-wave mixing.

FWHM full width at half maximum.

FWM four-wave mixing.

HWHM half width at half maximum.

MWM multi-wave mixing.

NMR nuclear magnetic resonance.

PE photon echo.

PI polarization interference.

PL photoluminescence.

PLE photoluminescence excitation.

QB quantum beat.

QD quantum dot.

SWM six-wave mixing.

TLS two-level system.

VTI variable temperature insert.

Acknowledgements

I would like to express my gratitude to everyone who helped during the work on this thesis. First, I thank my supervisor Ilya Akimov for offering me the possibility to work in his research group. With his expertise and helpfulness, he always found the perfect balance between guiding our research in the right direction and giving me the freedom to develop ideas on my own. Special thanks for allowing me to present our results at various conferences. I am grateful to all other leaders of the E2 chair, Manfred Bayer, Marc Aßmann, and Dmitri Yakovlev, for offering such an amazing research environment. Special thanks to Dmitri Yakovlev for helping us with our work on perovskites. I acknowledge Doris Reiter for taking over the second review of my thesis and for the pleasant collaboration on joint projects. I was lucky to have Artur Trifonov as a second supervisor. I think we shared the same enthusiasm for all the details of the experiment and related theoretical models. I want to especially thank for answering countless questions and for our interesting discussions that helped us to understand something about our experiments. Thanks to everyone I worked together with in the lab: Alexander Kosarev, Rilana Reichhardt, Ivan Solovev, Alex Hollberg, and Lars Klompmaker. An extra note of gratitude to Alexander for patiently showing me everything at the beginning of my work. I am also grateful to our theory colleagues from Paderborn, Torsten Meier and Hendrik Rose, for the productive and pleasant work on the quantum dots. Thanks to Dennis Kudlacik and Lars Wieschollek for answering many questions regarding the experimental equipment and to Michaela Wäscher for administrative support. I thank all other members of E2 for the friendly environment. Thanks to all those who were brave enough to join the E2 football group, it was always a big fun on Fridays. I thank Andreas Farenbruch for the great company in the office and the amazing time in Australia. Immense thanks to everyone who helped me with proofreading the thesis: Carolin Harkort, Sebastian Pape, Sophie Bork, Artur Trifonov, Alex Hollberg, Jonah Nitschke, Andreas Farenbruch, Steven Becker, and Karl Schiller. I thank all my other friends who made my studies so enjoyable. Finally, and most importantly, I am very grateful to my family, especially my girlfriend Carolin and my parents Dagmar and Uwe, for their unconditional support in my life.

Eidesstattliche Versicherung

Ich versichere hiermit an Eides statt, dass ich die vorliegende Dissertation mit dem Titel „From Spectroscopy to Coherent Control: Photon Echoes of Excitons in Organic-Inorganic Perovskites and (In, Ga)As Quantum Dots“selbstständig und ohne unzulässige fremde Hilfe erbracht habe. Ich habe keine anderen als die angegebenen Quellen und Hilfsmittel benutzt, sowie wörtliche und sinngemäße Zitate kenntlich gemacht. Die Arbeit hat in gleicher oder ähnlicher Form noch keiner Prüfungsbehörde vorgelegen.

Ort, Datum

Unterschrift

Belehrung

Wer vorsätzlich gegen eine die Täuschung über Prüfungsleistungen betreffende Regelung einer Hochschulprüfungsordnung verstößt, handelt ordnungswidrig. Die Ordnungswidrigkeit kann mit einer Geldbuße von bis zu 50 000.00 € geahndet werden. Zuständige Verwaltungsbehörde für die Verfolgung und Ahndung von Ordnungswidrigkeiten ist der Kanzler/die Kanzlerin der Technischen Universität Dortmund. Im Falle eines mehrfachen oder sonstigen schwerwiegenden Täuschungsversuches kann der Prüfling zudem exmatrikuliert werden (§ 63 Abs. 5 Hochschulgesetz).

Die Abgabe einer falschen Versicherung an Eides statt wird mit Freiheitsstrafe bis zu 3 Jahren oder mit Geldstrafe bestraft.

Die Technische Universität Dortmund wird ggf. elektronische Vergleichswerkzeuge (wie z. B. die Software „turnitin“) zur Überprüfung von Ordnungswidrigkeiten in Prüfungsverfahren nutzen.

Die oben stehende Belehrung habe ich zur Kenntnis genommen.

Ort, Datum

Unterschrift